



HAL
open science

Photodegradation of polymer nanocomposites for encapsulation of organic solar cells

Ievgeniia Topolniak

► **To cite this version:**

Ievgeniia Topolniak. Photodegradation of polymer nanocomposites for encapsulation of organic solar cells. Other. Université Blaise Pascal - Clermont-Ferrand II, 2015. English. NNT : 2015CLF22630 . tel-03270840

HAL Id: tel-03270840

<https://theses.hal.science/tel-03270840>

Submitted on 25 Jun 2021

HAL is a multi-disciplinary open access archive for the deposit and dissemination of scientific research documents, whether they are published or not. The documents may come from teaching and research institutions in France or abroad, or from public or private research centers.

L'archive ouverte pluridisciplinaire **HAL**, est destinée au dépôt et à la diffusion de documents scientifiques de niveau recherche, publiés ou non, émanant des établissements d'enseignement et de recherche français ou étrangers, des laboratoires publics ou privés.

N° D'ordre : D.U. 2630

UNIVERSITE BLAISE PASCAL

U.F.R. Sciences et Technologies

ECOLE DOCTORALE DES SCIENCES FONDAMENTALES

N° 842

THESE

présentée pour obtenir le grade de

DOCTEUR D'UNIVERSITE

Spécialité : Chimie-Physique

Par **TOPOLNIAK Ievgeniia**

**PHOTODEGRADATION OF POLYMER
NANOCOMPOSITES FOR ENCAPSULATION OF
ORGANIC SOLAR CELLS**

Soutenue publiquement le 4 Decembre 2015, devant la commission d'examen.

Président :	GARDETTE Jean-Luc	Professeur des Universités
Rapporteurs :	AL-MALAIKA Sahar MAJKOVÁ Eva	Professeur des Universités Professeur des Universités
Examineur :	THERIAS Sandrine FRANTISEK Uherek VINCZE Andrej HAŠKO Daniel CROS Stéphane	Directeur de Recherche CNRS Directeur de thèse Professeur des Universités Chargé de Recherche Chargé de Recherche Ingénieur CEA

Acknowledgements

Firstly, I am deeply indebted my supervisors, Dr. Sandrine Therias and Prof. Jean-Luc Gardette, who guided me with their invaluable suggestions through all my Ph D. work. Without their constructive critiques and recommendations, this work would not have been the same. Thank you for your time and invaluable help.

My thanks go to my research supervisors from International Laser Centre, Prof. František Uherek and Dr. Andrej Vincze. I acknowledge Prof. František Uherek for accepting me as a graduate student, giving me a chance to work in his group and all the help he managed to do for me in the realisation of this work.

I would like to express my special appreciation and thanks to Dr. Andrej Vincze who guided me through my entire thesis. He has been supportive during my working since I went to ILC providing countless help in all the aspects of my stay.

I am very grateful to Dr. Andreas Distler and Dr. Simon Dowland for organising my stays at Belectric OPV and all their help in performing the experiments. I could constantly benefit to their supports and suggestions. Simon's guidance and expertise allowed me the chance to work efficiently. I am thankful to him and his time for making samples, answering my questions, and chatting with me.

I would like to acknowledge Dr. Pierre-Olivier Bussiere for the scientific discussions and the help in DMTA, DSC and AFM analysis.

I would like to thank Prof. Alexander Šatka for the caring he has provided in SEM images obtaining.

I am thankful to Dr. Daniel Haško and his time for helping me to perform AFM measurements, scientific discussions and his support.

I also would like to express my gratitude to Christelle Blavignac and Claire Szczepaniak from Centre d'Imagerie Cellulaire Sante (CICS, University of Auvergne) for support in TEM analysis.

I acknowledge Pascal Wong Wah Chung (ICCF, Photochimie team) for help with SPME-GC-MS experiments.

I wish to thank Dr. Hans-Joachim Metz and Clariant Produkte (Deutschland) GmbH for kindly supplied gratis zeolite samples used in this work.

For this dissertation, I would like to thank my reading committee members: Prof. Eva Majková and Prof Al-Malaika for their time, interest, and helpful comments.

I would like to thank all my colleagues from Photochimie team (ICCF) for their support and suggestions in my research. I would like to address special thanks to Anthony Chapel, Aurelien Tournebize, Romain Prulho, Alexis Colin, Anthony Perthué and Camille Rouillon whose inspired me and helped to find a solution even in the darkest situations.

A warm word for my colleague and a great friend Isabel Fraga Dominguez. I am not sure what would happen with me during these three years if I would not have her endless emotional, personal and friend support.

I am very grateful to "amazing" Carole Turpin, who made all administrative issues during my scientific displacement very easy

Last but not the least, I want to thank my friends, Alena, Joao and Dieter for their not giving up on me as someone who newer replays on the messages, and whatever mood would reach me, always cheer me up.

Thanks P.S. for always being here for me. I really appreciate it.

Most of all, I would like to express my appreciation to my parents for their encouragement, and endless love.

I gratefully acknowledge the funding sources that made my Ph.D. work possible. I thank the European Union Seventh Framework Program (FP7 / 2011 under grant agreement ESTABLIS n°290022) for the financial funding of this PhD work

TABLE OF CONTENTS

GENERAL INTRODUCTION	1
CHAPTER I: LITERATURE REVIEW	7
INTRODUCTION	9
1. ORGANIC SOLAR CELLS	10
1.1. Introduction to photovoltaics	10
1.2. Module structures	11
1.3. Degradation of organic solar cells	13
2. ENCAPSULATION OF OSCs	17
2.1. Properties of encapsulation materials. General requirements	17
2.2. Encapsulation systems	20
2.2.1. Single-layer thin-film encapsulation	20
2.2.2. Multilayer thin-film encapsulation	21
2.2.2.1. Inorganic materials	22
2.2.2.2. Organic-inorganic hybrid materials: state-of-the-art	23
2.2.2.3. Polymer/nanocomposites	28
2.3. Conclusions	29
3. NANOFILLERS	31
3.1. Processing of nanocomposites with clays	37
3.2. Properties of polymer/nanocomposites	38
3.3. EVOH copolymers and nanocomposites	41
3.4. Photodegradation of nanocomposites	47
3.4.1. Nanocomposites based on nanolayers	48
3.4.2. Nanocomposites based on nanotubes	50
3.4.3. Nanocomposites based on nanoparticles	51
3.5. Polymer/zeolite nanocomposites	53
CONCLUSIONS	55
CHAPTER II: EXPERIMENTAL METHODS	57
INTRODUCTION	59
1. MATERIALS AND SAMPLE PREPARATION	60
1.1. Materials	60

1.2. Sample Preparation	62
2. ACCELERATED AGEING	65
2.1. Accelerated photoageing	65
2.2. Damp heat experiment	66
3. CHARACTERISATION TECHNIQUES	67
3.1. Spectroscopy	67
3.2. Chemical derivatisation treatments	67
3.2.1. NH ₃ treatment	67
3.2.2. 2,4-DNPH treatment	68
3.3. Chromatographic analysis	69
3.3.1. Solid phase micro extraction gas chromatography coupled with mass spectrometry detection (HS-SPME-GC-MS)	69
3.3.2. Ionic chromatography	71
3.4. Microscopic analysis	71
3.4.1. Transmission electron microscopy	71
3.4.2. Scanning electron microscopy	72
3.4.3. Atomic force microscopy	72
3.5. Dynamic mechanical thermal analysis	75
3.6. Differential scanning calorimetry	78
3.7. Water permeability	79
3.7.1. Gravimetric immersion water uptake	82
3.7.2. Dynamic vapour sorption	83
3.7.3. Calcium test	83
3.8. Time-of-flight secondary ion mass spectrometry	85
CHAPTER III: INITIAL CHARACTERISATION OF EVOH/COMPOSITES	89
INTRODUCTION	91
1. CHARACTERISATION OF ZEOLITE PARTICLES	92
1.1. Morphology	92
1.2. Chemical structure	93
1.2.1. Elemental composition	93
1.2.2. IR analysis	93
2. EVOH/ZEOLITE NANOCOMPOSITES CHARACTERISATION	94

2.1. Spectroscopy analysis	94
2.1.1. IR analysis	94
2.1.2. UV-Visible analysis	97
2.2. Morphology characterisation	98
2.2.1. Surface morphology	98
2.2.2. Particles dispersion and distribution in film thickness	100
2.3. ToF-SIMS surface characterisation	109
2.4. Viscoelastic properties	116
2.5. Thermal properties	120
2.6. Water sorption properties	123
2.6.1. Gravimetric immersion water uptake (IWU)	123
2.6.2. Dynamic vapour sorption analysis (DVS)	127
CONCLUSIONS	128
CHAPTER IV: PHOTOCHEMICAL BEHAVIOR OF EVOH AND EVOH/COMPOSITES	131
INTRODUCTION	133
1. PHOTOCHEMICAL BEHAVIOUR OF EVOH	134
1.1. UV-Visible analysis	134
1.2. IR analysis	134
1.3. Identification of photooxidation products	136
1.3.1. IR analysis	136
1.3.2. Chemical treatment	137
1.3.3. Analysis of volatile photoproducts by SPME-GC-MS	139
1.3.4. Ionic chromatography	141
1.4. Photooxidation mechanism of EVOH	142
2. INFLUENCE OF ZEOLITE NANOPARTICLES ON EVOH	
PHOTOOXIDATION	148
2.1. Photooxidation of EVOH/NZL nanocomposites at $\lambda > 300$ nm	148
2.1.1. UV-Visible analysis	148
2.1.2. IR analysis	149
2.2. Influence of zeolite on photooxidation rate of EVOH	151
2.2.1. Influence of zeolite type	151
2.2.2. Influence of zeolite loading	152

2.2.3. Influence of processing method	153
2.3. Surface morphology	155
2.3.1. Scanning electron microscopy (SEM)	155
2.3.2. Atomic force microscopy (AFM)	158
2.4. TOF-SIMS surface analysis	165
2.5. Influence on viscoelastic properties	175
2.6. Thermal properties	178
2.7. Influence on water sorption properties	182
CONCLUSIONS	185
CHAPTER V: MATERIALS TESTING IN DAMP HEAT	
CONDITIONS	187
INTRODUCTION	189
1. Calcium test	190
1.1. Orthogonal diffusion	190
1.2. Lateral diffusion	196
2. Encapsulation of organic solar cells with nanocomposite layers	201
3. Testing of multistacks in damp heat conditions	206
CONCLUSIONS	208
GENERAL CONCLUSIONS AND OUTLOOK	209
APPENDIX	215
REFERENCES	219

GENERAL INTRODUCTION

GENERAL INTRODUCTION

Amongst alternative energy sources, photovoltaics hold a considerable promise, as it is a plentiful, easily accessible and renewable source of power. Organic thin films photovoltaic are an emerging economically competitive photovoltaic technology that combines manufacturing adaptability, low cost processing and a light-weight, flexible device end-product.

However, commercial use of organic photovoltaics is hindered by low conversion efficiency and poor overall stability of the devices. It is known that organic solar cells (OSCs), especially the active layer and electrodes, are sensitive to trace quantities of oxygen and humidity, which jointly with light can strongly decrease the performance and the lifetime of the device.

One solution to overcome this problem is the use of encapsulation for preventing oxygen and moisture from reaching the fragile components of the cell. Encapsulation with high barrier performance materials is then one of the key-ways to address these issues and improve device lifetime. In addition to the low permeability to water and oxygen, an encapsulant for OSC should be transparent over the wavelength range from 400 nm to 1000 nm, chemically inert and preferably based on simple and low-cost processes. Moreover, lightness and flexibility must be insured for “all” organic OSCs.

The development of encapsulation materials for the photovoltaic module protection with high barrier properties is then one of the challenges for OSC competitiveness in the market. The barrier requirement range for OSCs encapsulation is of $\sim 10^{-3} \text{ cm}^3 \text{ m}^{-2} \text{ day}^{-1}$ and $\sim 10^{-6} \text{ g m}^{-2} \text{ day}^{-1}$ for OTR and WVTR respectively. Moreover, these materials have to be stable within the operating life of the cells.

Among the polymers commonly used as barrier materials for applications such as food packaging, ethylene vinyl alcohol copolymers (EVOH) have good barrier property to oxygen, considerable chemical resistance and good transparency, which make them good candidates for encapsulation coatings. In terms of permeability coefficients, even the best polymeric barriers remain several orders of magnitude higher than the OPV requirements.

Improvement of barrier properties of the polymer is then required, which could be achieved through the incorporation of inorganic particles into the polymer. The resulting increase of the barrier effect caused by the introduction of such passive particles is well known. It is attributed for a large part to a lengthening of the permeation path due to the tortuous path provoked by the particles (passive particles usually do not interact with the permeating gases either through sorption or chemical processes). It has been shown that in the case of EVOH the barrier

properties can be increased by adding various kinds of nanofillers such as organoclays (montmorillonite), layered double hydroxides or carbon nanotubes.

An alternative approach to the “passive” nanocomposite is the use of active fillers which strongly interact with a permeating gas. These active fillers are commonly known as getters whose activity is either to consume a permeating gas through chemical reaction or to trap permeating gas via sorption processes. Among the common types of getters that can trap water through adsorption, are molecular sieves such as zeolites.

Zeolites are aluminosilicates that have an ordered highly porous structure, which allows for a high water sorption capacity. Of particular interest are zeolites as they have the ability to be synthesised as nanoparticles. Nanoparticles of zeolites have been well researched, however, their use in barrier composites has received only very limited attention.

However, a drawback of particles use is their negative impact on the photostability of the polymer. The addition of particles to polymers has been indeed shown many times to affect the photostability of the nanocomposites. While inorganic particles rarely experience significant photodegradation under sunlight exposure, they can change the mechanisms and/or the rate of photooxidation of the polymer matrix and must therefore always be accounted for when determining the photostability of the nanocomposite. For example, lamellar nanofillers such as clays are reported to have a prodegradant effect on the polymer photooxidation due to the presence of transition metal ions such as iron that can produce a catalytic decomposition of hydroperoxides.

The goal of the work reported in this manuscript was to develop EVOH/nanocomposites based on inorganic fillers such as zeolites for potential encapsulation for OSC and to study the durability of their functional properties. On one hand, the study focuses on the photooxidation of EVOH copolymers, which was studied through identification of the photoproducts, both in the solid and the gas phases, and on the other hand, on the photochemical behaviour of the EVOH/zeolite nanocomposites, which was characterised depending on the particle size and the zeolite loading of the materials.

To achieve this goal, the following work program was performed:

- a brief description of the literature dedicated to OSCs and an overview of currently available encapsulant materials are given in the first chapter of the manuscript. The background on the materials that were studied is also presented.
- In the second chapter, we describe the materials, the ageing conditions and the various analytical techniques used for materials characterisation.

- The third chapter is devoted to the characterisation of the initial properties of the materials, EVOH copolymers and EVOH/zeolites nanocomposites. The final goal was to determine the best candidate for encapsulation of organic solar cells.

- The ageing of those materials is reported in the fourth chapter. It aims to understand the impact of the zeolite particles on the photochemical behaviour of the polymer. The attention was focused on the chemical degradation mechanism and the photostability of pristine polymers and nanocomposites. The consequences of the polymer photooxidation on the degradation of the properties was then investigated.

- The last chapter describes some preliminary tests performed to evaluate the ability of the studied materials to be used as potential candidates for efficient and stable encapsulation coatings for OSCs applications.

The research work reported in this manuscript was performed in the frame of the Marie Curie Initial Training Network (Call: FP7-PEOPLE-2011-ITN) Establis (“Ensuring stability in organic solar cells”) European project in collaboration with three partners of Establis, Institute of Chemistry of Clermont-Ferrand (ICCF), International Laser Centre (ILC) in Slovakia and Belectric OPV GmbH in Germany.

The research leading to these results has received funding from the European Union Seventh Framework Programme (FP7/2011) under grant agreement ESTABLIS no. 290022.

ToF-SIMS, SEM characterisations and part of AFM analyses were performed at ILC (see chapters 3 and 4). The results reported in chapter 5 (Ca-tests and damp heat testing of OSCs) were obtained at Belectric OPV GmbH. All other experiments were performed at ICCF (Clermont-Ferrand).

CHAPTER I:
LITERATURE REVIEW

INTRODUCTION

In this chapter, we give a brief description of the literature dedicated to the operating principle, structure and materials of organic solar cells (OSCs). Since these devices still cannot fully reach industrial production due to their low efficiency and lifetime, a peculiar attention is also given in this chapter to the degradation of OSCs and to the stability issue.

The second part deals with the current materials and technologies for OSCs lifetime improvement by using encapsulation. This part aims to understand the current issues addressed by coating materials, the principles of OSC encapsulation engineering, and advantages/disadvantages of each of them. The different used materials, organic, inorganic or hybrid are described, as well as their properties, focusing on the water and oxygen barrier properties.

As a consequence of the reinforcement effect of nanofillers on polymer properties, the use of nanocomposites is a potential strategy to improve the quality of barriers and the overall durability of the device. The last part of this chapter is then dedicated to polymer/nanocomposite materials. The main processing methods, the currently used nanofillers and nanofillers with forecasted interesting functionalities, in particular the barrier properties, are described. A special attention is paid to their effect on the material properties. OSCs stability is highly depending on the durability of the encapsulation. An overview of the photodegradation of nanocomposites is then presented in the manuscript.

Concluding this chapter, potential strategies for new encapsulation and the choice of the materials studied herein are explained.

1. ORGANIC SOLAR CELLS

1.1. Introduction to photovoltaics

The term “photovoltaic”(PV) has been coined from the Greek “photo”, which means light, and “voltaic” that refers to electricity came from the name of the Italian physicist Volta. The photovoltaic effect was first recognised in 1839 by the French physicist Antoine-Henri Becquerel. He reported for the first time that exposure to electro-magnetic radiation of certain materials, namely platinum electrodes covered with silver chloride or silver bromide in water, could lead to the production of a small electric current (photochemical effect) [1].

The first photovoltaic cell was created by Charles Fritts in 1883 [2] and was composed by coating selenium with an extremely thin layer of gold. Later, Russell Ohl invented the first silicon solar cell in 1941 [3]. However, the era of modern solar cell technology just began in 1954, when G. L. Pearson, D. Shapin and C. Fuller demonstrated a silicon solar cell capable of 6% energy conversion efficiency with direct sunlight [4]. Since then, the research in the field of solar cells has reached a significant progress, which is illustrated by the curve of cell efficiencies evaluation in Fig.1.1.

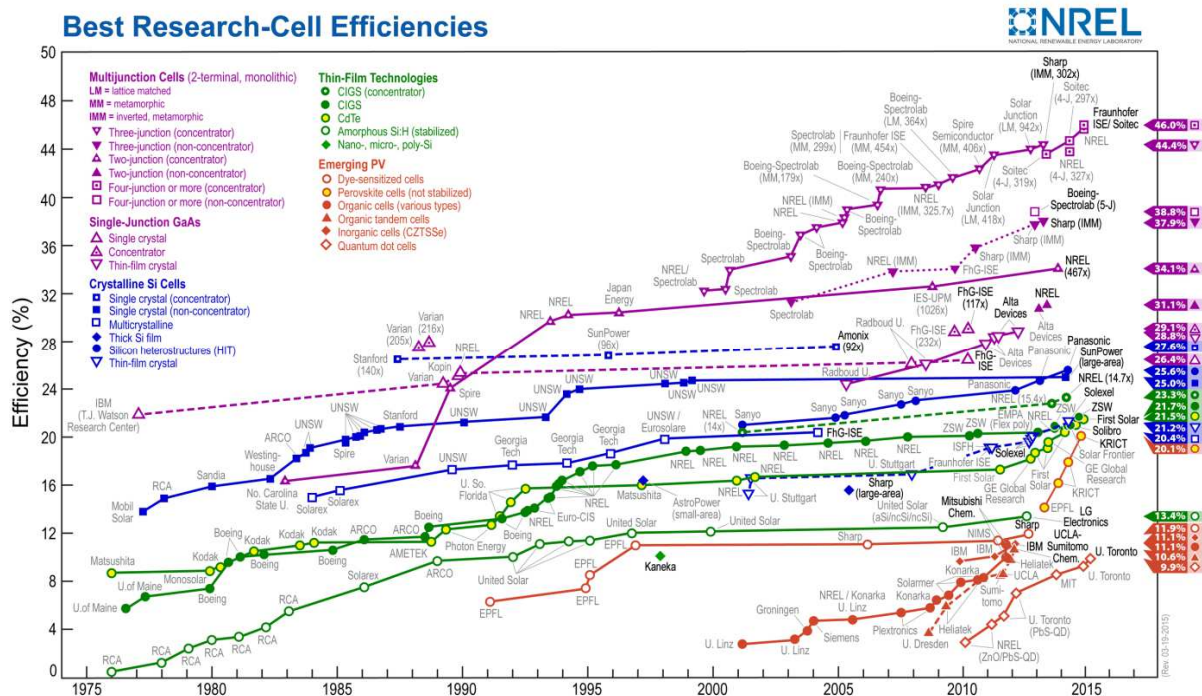


Fig.1.1. Best research solar efficiencies given by National Renewable Energy Laboratory (NREL).

Nowadays, crystalline Si-based solar cells have achieved quite high power conventional efficiency (PCE). However, the success of solar cells market cannot be based solely on high PCE values. This domain has to become also cost-competitive, which can be displayed by three followed key requirements^[5] (Fig.1.2.):

- *Cost*: to minimise the quantity and cost of materials as well as cost of processing;
- *Efficiency*: to maximise initial performance;
- *Stability*: to achieve maximum device lifetime.

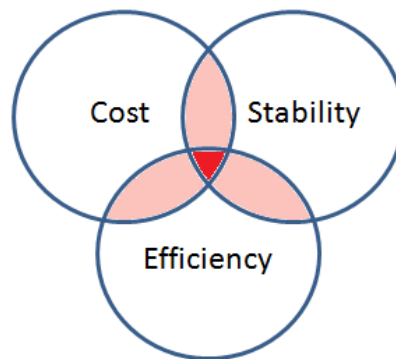


Fig.1.2. Overcrossing of requirements for marketing success.

Nevertheless, even with good stability (lifetime of over 25 years^[6]), Si-based solar cells are still far from being competitive with other conventional energy sources. High processing and installation expenses make the energy converted by these devices approximately five times more expensive than those produced by burning of fossil fuels^[7].

In contrast to heavy and expensive Si-based solar cells, organic thin films solar cells exhibit good factory additivity, flexibility and light-weight of end-products, which are cheap in manufacturing (possibility of simple solution coating and printing techniques^[8, 9]) and easily integrated. Hence, despite the long-term stability issue, organic photovoltaics (OPVs) are attractive as solar energy converting devices for application in new possible domains, particularly, for grid-off application.

1.2. Module structures

OPV technology is still in its early development stages. Due to continuous research to reach appropriate performance and stability, a clearly defined “typical” OPV cell composition and its design are not yet settled. A lot of different material compositions and their combinations are in the focus of intense research. The structure can be simplified to three main layers that

constitute the cell itself: the photoactive layer (PAL), where the conversion from light to electricity takes place; contact electrodes placed from both sides of PAL, at least one of which being transparent, and an encapsulation layer, placed on the top in order to protect the OPV module from degradation (see Fig.1.3.).

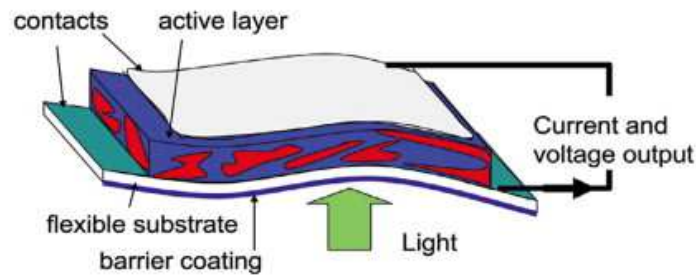


Fig.1.3. Schematic structure of an organic photovoltaic cell: a schematic representation of bulk heterojunction cell ^[10].

Nowadays the most common organic solar cells (OSCs) have mainly two architectures: conventional and inverted (Fig.1.4.a-b). The most “classic”, conventional cell composition, is as following ^[11, 12] (Fig.1.4.a):

- A transparent conductive oxide (TCO) sputtered onto a substrate in order to improve hole transport (so-called hole transport layer (HTL)). The most common TCO (especially in combination with PEDOT:PSS) is indium-tin oxide (ITO), which is a good conducting material and holes serving.
- A layer of polyethylenedioxythiophene:polystyrene sulphonate (PEDOT:PSS), which is a hole conductor, used both to ensure better separation and transport of charges between the active layer, and ITO.
- An active layer combining a donor (D) and an acceptor (A) of electrons. This heterojunction has a high donor–acceptor surface interface area distributed in the whole volume of the PAL in order to have a greater contact area between the donor and the acceptor and thus promote better charge separation.
- An electron transport layer (ETL) improves the separation and transfer of electrons to a cathode. Well-known and widely-used ETL materials are ZnO and TiO_x ^[13].
- A cathode, which can be made of a single material (Ca, Al) or a mixture of several compounds (LiF/Al, Ca/Al, Ba/Al, Ag/Ca, LiF/Al).

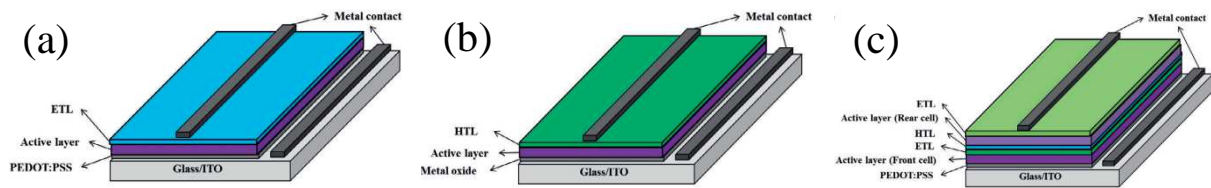


Fig.1.4. Device structures of (a) conventional single-junction cell, (b) inverted single-junction cell, and (c) conventional multi-junction tandem cells [14].

The similar structure with inversed polarity, shown in Fig.1.4.b, (Glass/ITO/metal oxide/photoactive blend layer/PEDOT:PSS/Ag), is now being widely studied due to the advantages in cell manufacturing (possibility to use roll-to-roll (R2R) process) [8], in increased protection against oxygen and moisture [15], and consequently, a better stability [16] in comparison to the normal geometry. Higher cell performance can be reached with multi-junction (tandem) cell [17]. Fig.1.4.c shows two sub-cells stacked together and separated by the electron transport layer and the hole transport layer, which can collect electrons from the front cell and holes from the rear cell respectively.

1.3. Degradation of organic solar cells

Three main parameters, efficiency, cost, and stability must be achieved to reach the commercial success for solar cells [5]. So far, the last one is a challenge for OPV. The degradation of OSCs occurs at various parts of the device (Fig.1.5.). The most significant processes take place in the PAL, electrodes and encapsulation layer [11]. Degradation issues are more important in the case of organic thin-film devices in comparison to more stable Si solar cells. The components of PAL, conjugated polymers or small molecules, are unstable in air having low resistance against oxygen and moisture [11, 18]. The chemical degradation can be classified into two types: intrinsic and extrinsic [5, 19].

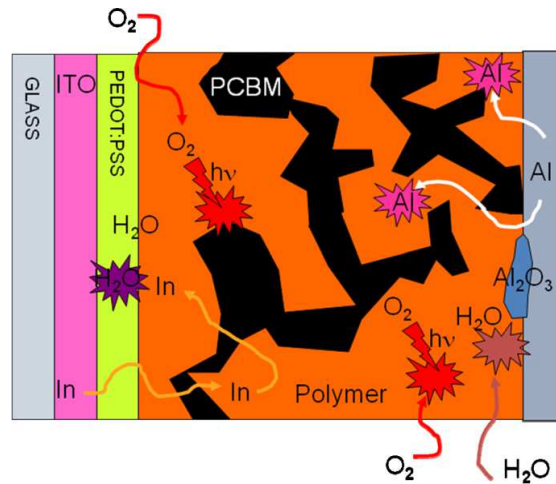


Fig.1.5. Sectional view of a cell and the various processes involved in the degradation of the device. A schematic illustration of some degradation processes that take place in a typical bulk heterojunction are shown [5].

Intrinsic degradation

This degradation implies changes in the morphological states of stacking layers and interface modifications due to inherent thermal characteristics of PAL materials. It comes from thermal diffusion of materials at interfaces. As a result, morphological changes in bulk heterojunction (BHJ) OSCs have been observed [20]. It also caused the phase separation at the organic-cathode interface [21], at semiconductor interfaces [22] and inter-diffusion at buffer-layer interfaces [23].

Extrinsic degradation

Extrinsic degradation is mainly focuses on the role of oxygen and water in the different parts of the device [11]. Still, the relative significance between these two factors is frequently argued in the literature.

Role of Oxygen in degradation

It is known that the combination of UV light and oxygen molecules results in photooxidation of polymers. Generally, most attention in the oxidative damage is focused on the PAL part of OSC [24-28]. UV light in the presence of oxygen molecules results in photooxidative reactions of organic components of the cell. Intensive light exposure also leads to an increase of the temperature which result in accelerated diffusion of water and oxygen into the device [29-31], and might accelerate the intrinsic degradation of the cell [22]. All these factors can have a crucial effect on cell lifetime.

Depending on the cell composition, oxygen can also play a dominant role in the degradation due to the following facts: i) oxygen promote the formation of dipoles at the interface of the metals which increase their work functions ^[32]; ii) due to hydrophilic nature of fullerene, electron transport properties of this acceptor suffer dominantly from oxygen exposure ^[33]; iii) consequently, in the presence of fullerene, aluminium can become passivated against water induced corrosion ^[34]. Oxygen presence can also result in degradation of PEDOT:PSS due to phase separation ^[35].

Role of water in degradation

Numerous publications have shown that water is likely to affect the properties of OSCs ^[36, 37, 38]. Penetrating into the device, water may cause a drop in short circuit current and fill factor due to the corrosion of active cathodes, and hence, a loss in contact area due to the formation of resistive metal oxides ^[39]. The effect of water on the performance of OPV was also shown to result in a decrease of charge generation ability due to the initiation of strong recombination of bulk polymers ^[40].

The main impact water-caused degradation has on hydrophilic components of OSCs, like commonly used PEDOT:PSS ^[29, 19]. It may result in material recrystallisations, or physical swelling. It was recently shown that the degradation of PEDOT:PSS hole selective contact is the major mechanism of device failure for inversed OPVs under accelerated ageing in humidity conditions ^[41].

Conceptions and methods for lifetime improving

Due to low stability of PV modules, different approaches have been developed and applied for improving the lifetime of PV modules.

First, the change of the cell architecture into an inverted one has shown better stability and allows using solution printing processing ^[8, 16]. Nonetheless, trying to find the most stable and efficient PAL composition is still a hot topic of research.

Second, the replacement of the moisture sensitive PEDOT:PSS by transition metal oxides as charge extraction interlayers ^[42] in order to avoid interface oxidation and delamination. The metals such as MoO₃ ^[43], V₂O₅ ^[44], WO₃ ^[45] and NiO ^[46] have been used as an HTL in OSC. The improved power conversional efficiencies with solution processed WO₃ compared to PEDOT:PSS-based devices have been reported ^[45]. Similarly, the increased device efficiency and stability was obtained for the cell with PC70BM as an acceptor, and low bandgap polymer, (poly[2,6-(4,4-bis-(2-ethylhexyl)-4*H*-cyclopenta [2,1-*b*;3,4-*b'*]dithiophene)-*alt*-

4,7(2,1,3-benzothiadiazole)] (PCBDTBT)) as a donor, where PEDOT:PSS was replaced by MoO₃ and NiO [46].

Another way to protect sensitive areas such as electrodes and interfaces is to introduce an ultrathin inorganic layer (Al₂O₃ [47], LiF [48], CrO_x [49], etc.) between metal electrode and PAL in order to prevent reactions at the interface. The commonly used TiO_x protective layer increases the device stability by preventing the diffusion of oxygen and moisture into PAL, thus, slowing the degradation [50]. Summarising, the possible methods for improving the device lifetime are presented in Fig.1.6.

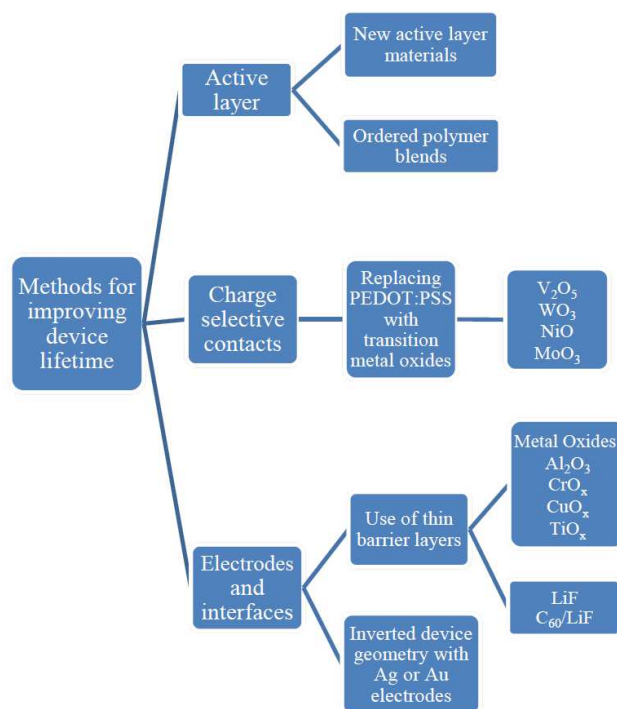


Fig.1.6. Main methods for improving device lifetime, classified according to the part of the device they applied to [51].

Nevertheless, even the improvement of PV module composition does not solve the main issue of degradation that initially comes from the ingress of permeants such as moisture and oxygen into the cell. Degradation can be avoided by encapsulation of the module by topcoat layer with barrier properties in order to prevent oxygen and water permeation. Encapsulation can also be used to protect the device from UV irradiation through the utilisation of UV filtering encapsulation [52]. The research on OSC encapsulation have shown the shift of device lifetime to many thousand hours using appropriate materials for rigid [53] as well as for

flexible ^[54, 55] coatings. Thus, encapsulation with high barrier performance is one of keys to address stability issues and improve device lifetime.

2. ENCAPSULATION OF OSC_S

It has been mentioned above that OSCs can be significantly affected by external factors such as moisture, oxygen, UV light, and temperature ^[5, 56], which lead to the device degradation. Encapsulation is thus required, paying attention to the fact that it should comply other aspects and properties of the desired end-product. For example, encapsulant has to block the diffusion of moisture and oxygen as well as to provide the structural support and resistance to the mechanical damage by absorbing the stress that prevents cracks and initiated fractures.

2.1. Properties of encapsulation materials. General requirements

To achieve high device stability, and meanwhile, to keep other important functional properties, different parameters should be taken into account during engineering of OSC encapsulation. The requirements to encapsulation depend on the used materials, technology, and the desired end-product properties. Some important aspects and properties have been outlined in recent papers ^[57, 58] and are summarised in Table 1.1.

Table 1.1. Specifications and requirements for encapsulant materials ^[58]

Characteristic	Requirement
WVTR	$10^{-3} - 10^{-6} \text{ g m}^{-2} \text{ day}^{-1}$
OTR	$10^{-3} - 10^{-5} \text{ cm}^3 \text{ m}^{-2} \text{ day}^{-1}$
Total light transmission over the wavelength range	>90 % of incident light
Hydrolysis	None (80 °C, 100 % RH)
Water absorption	< 0.5 wt % (20 °C/100 % RH)
Resistance to thermooxidation	Stable (up to 85 °C)
Tensile modulus	< 20.7 MPa (25 °C)

Optical properties. Light scattering/absorption by encapsulant layer lowers the light intensity absorbed by PAL, and consequently, decreases the efficiency. Thus, any absorption of light by the barrier film should be avoided. Moreover, optical clarity of the coating is a challenge to have a semi-transparent end-product that expands the frames of OPV application. The refractive index is another important characteristic of encapsulation, especially in the case of multiple components with different refractive indices.

Mechanical properties. Since flexibility is one of the key advantages of OPVs^[59], which brings new potential application opportunities and at the same time allows the use of cheap and easy processing methods (like roll-to-roll), the flexibility of encapsulant layer is an important property. Significant parameters required to design the coating are its resistance to mechanical damage and processing method, solvent solubility, water sorption, and etc.

Thermal and dimensional stability. The material stability at the temperatures that are reached during the processing of the device or at working conditions (temperature around 65 °C^[60]) of the device is critical. The differences in thermal expansion coefficient can be at the origin of the observed cracks and delamination between the different layers of the barrier material. In the case of a polymer layer, these changes are due to various factors such as mobility of the chains or/and ‘shrinkage’ or ‘expansion’ associated with the molecular relaxation of residual strain within the oriented parts of the film structure. These relaxations are strongly linked to the T_g of the polymer and are observed at the temperatures around or higher T_g . Hence, to obtain good dimensional stability, it is important to pay attention to T_g for the choice of materials^[61].

Moisture and chemical resistance. Moisture and solvent sorption ability affect the dimensional stability of the material, which becomes extremely important for processing including the use of solvents. Used solvents and chemicals for layer deposition may dissolve or damage already deposited functional layers of the cell or the substrate. The solvent of a layer must not dissolve the other layers of the device.

Surface quality. Surface roughness is essential since insufficient quality of the surface may lead to bad adhesion of the following layer and their delamination. Unfortunately, typical plastic substrates do not reach the requirement of ultrasurface (< 1 nm roughness)^[57] which obliges to “smooth over” the surface. This can be reached by including the planarising/smoothing layer^[62]. Corona treatment of the film surface is another approach which increases the surface energy and, therefore, improves the adhesion between the coatings^[63].

Barrier level. Water vapour and oxygen transition rates, named WVTR and OTR respectively, are the main parameters that define the level of material barrier properties and indicate the capability of moisture and oxygen to cross an encapsulating membrane. As reported by *Dennel et al.* [64], a targeted device lifetime of 10 000 h requires, in the case of OLEDs, WVTR and OTR of about 10^{-6} g m⁻² day⁻¹ and 10^{-3} – 10^{-5} cm³ m⁻² day⁻¹ atm⁻¹ respectively (Fig.1.7.).

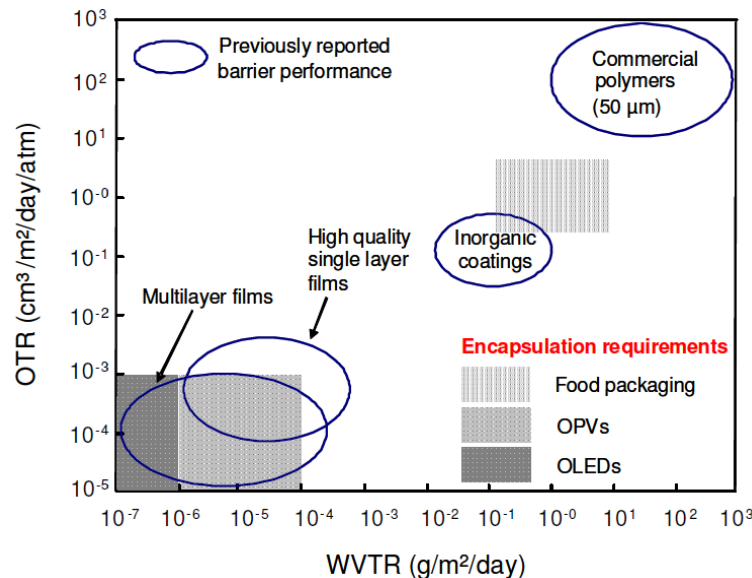


Fig.1.7. Oxygen and water vapour barrier requirements for various packaging applications (organic light-emitting device (OLED); organic photovoltaics (OPVs); food packaging) [64, 65].

However, organic photovoltaics (OPV), being based on more stable materials, need slightly lower protection level. It was shown by *Cros et al.* [66] that encapsulation with WVTR of 1×10^{-3} g m⁻² day⁻¹ would be sufficient to obtain device with lifetimes of several years.

It is worthy to note that the cell architecture, material composition, and expected cell lifetime are important in the estimation of required properties of used packaging. An overview of permeability values for some polymeric materials normalised to uniform thickness of 100 µm is shown in Fig.1.8. Comparing the barrier requirements (Fig.1.7.) with the achievable permeability values (Fig.1.8.), it can be noticed that liquid crystal polymers (LCP) and ethylene vinyl alcohol copolymer (EVOH) materials are potential candidates for encapsulation that may reach the demands from industry [67].

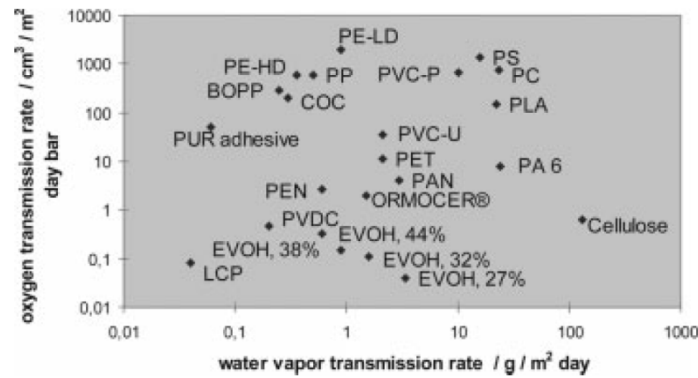


Fig.1.8. OTR and WVTR for selected polymers of 100µm thickness ^[67].

Durability properties. Besides all listed above characteristics, the durability of encapsulant properties is a key point that has to be addressed. The encapsulation must not deteriorate throughout the life of the cell to ensure its protection against environmental stresses.

2.2. Encapsulation systems

The different approaches to meet the assigned requirements using thin film encapsulation by single-layer or multilayer are described in this paragraph.

2.2.1. Single-layer thin-film encapsulation

Single layer encapsulation can be easily processed in comparison to multilayer encapsulation. The easiest solution is to cover the device with glass plates using an epoxy type sealant to hold them ^[68]. This configuration provides suitable protection, but obviously this way is not intended for flexible end-product.

In order to develop flexible and efficient single-layer thin film encapsulation, different materials can be used. Mainly, *inorganic materials* such as silicon (Si) ^[69, 70], SiN_x ^[71, 72], Al₂O₃ ^[73, 74], TiO_x have been proposed. Encapsulants based on *organic materials*, like polyacrylate (PA), parylene, ethylene vinyl acetate (EVA) ^[75, 76], europium doped EVA ^[77], polyvinyl butyral ^[78], ethylene methyl acrylate ^[79] and etc., are described in the literature.

The barrier properties of inorganic and organic layers are generally limited, due to the defects present in inorganic layers and to the fast diffusion rate of polymers ^[61, 70, 80]. In inorganic layers the pathways for external permeants come from pinhole defects formed during deposition, or from pores at the surface of films ^[64].

Due to present advantages and drawbacks of both, organic and inorganic encapsulants, silicon-based *inorganic-organic hybrid materials (IOH)*, like ORMOCER[®], have been developed to combine positive aspects of each component. The chemical structure of IOH materials is similar to glass model structure where organic groups are linked to silicon atom (Fig.1.9.).

ORMOCER[®] is synthesised by polycondensation (sol-gel chemistry), followed by organic crosslinking reaction, and combines in its structure organic and inorganic components [81]. The main characteristic of these materials is the incorporation of organic groups linked to the inorganic backbone formed by hydrolysis and condensation of alkoxides. The chemical structure of these materials, can be adjusted depending on the desired properties [82].

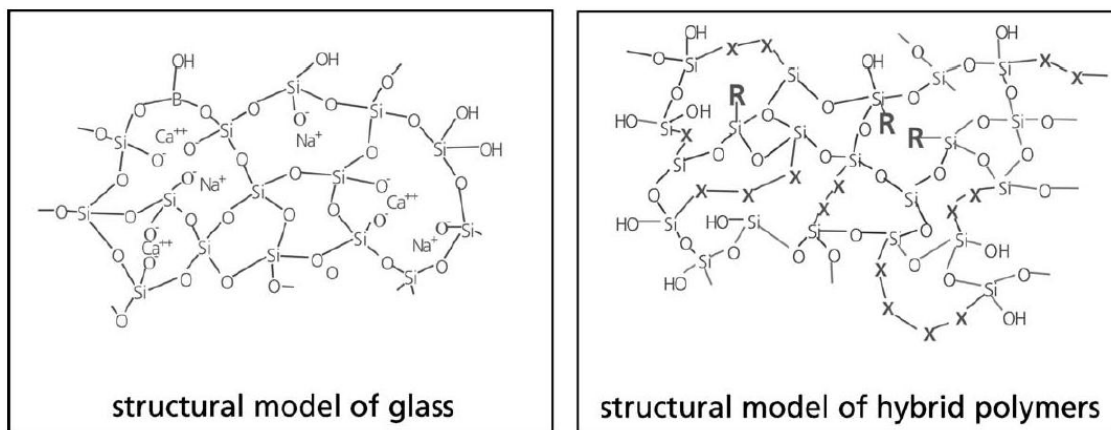


Fig.1.9. Comparison of the chemical structure of glass and hybrid polymer (R: organic groups) [83].

ORMOCER[®] coating on a glass plate reduces the reflection of substrate from 8 % to 1 % [84]. This hybrid material has antisoiling, antistatic and diffusion-inhibiting properties meanwhile keeping high transparency. The OTR and WVTR were measured below $10^{-2} \text{ cm}^3 \text{ m}^{-2} \text{ day}^{-1}$ and $10^{-2} \text{ g m}^{-2} \text{ day}^{-1}$ respectively [85].

2.2.2. Multilayer thin-film encapsulation

To overcome the drawbacks of single-layer films and to obtain high barrier properties, multilayer coatings alternating inorganic layers (oxide or nitride) and/or organic or hybrid layers can be realised. By applying multilayer films with alternating materials, the defects of the individual inorganic layers are interrupted and do not channel continuously through the film structure. Subsequently, this multilayer encapsulation can show excellent homogeneous

and conformal coverage without pinholes or microcracks, with tortuous diffusion pathways for oxygen and water vapour (Fig.1.10.) resulting in increased barrier properties of the coating ^[67]. An added advantage is that these films can be fabricated by roll-to-roll (R2R) process.

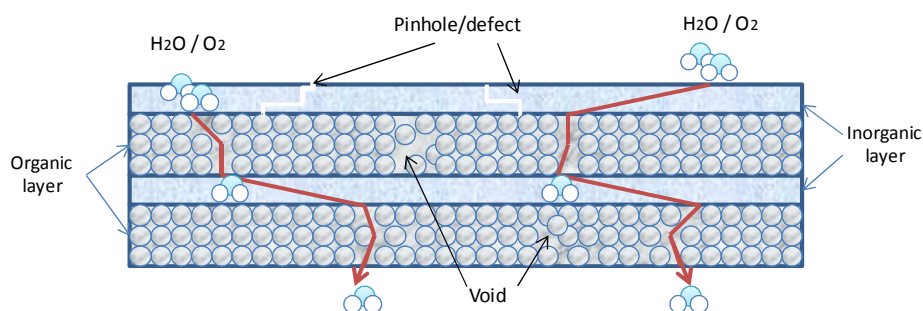


Fig.1.10. Tortuous penetration path through organic/inorganic multilayer structure.

2.2.2.1. Inorganic materials

Multilayer inorganic films consist of alternating inorganic materials such as a combination of $\text{SiN}_x/\text{SiO}_x$ deposited by PECVD or the alternation of Al_2O_3 and SiO_x deposited by ALD ^[86-88].

$\text{SiO}_x/\text{SiN}_x$. Combination of SiO_x and SiN_x has been tested for encapsulation purposes ^[87]. In comparison to single SiO_x structure, this system showed less reactivity to oxygen and water vapour. WVTR measured by Ca test (SiN_x - 6 pairs of $\text{SiO}_x/\text{SiN}_x$) was $3.1 \times 10^{-6} \text{ g m}^{-2} \text{ day}^{-1}$ (100 days at 25 °C and 40 % RH). Moreover, the value of permeation rate can still be kept below $3.54 \times 10^{-5} \text{ g m}^{-2} \text{ day}^{-1}$ after the cyclic bending test (5000 times) in a compressive mode.

Ta-Si-O/Ta-Si-N . A thin film of Ta-Si-O/Ta-Si-N combination was investigated as a protection of a copper–indium–2 selenide (CIS) solar cell ^[89]. It was found that 10 nm thick layer of Ta-Si-N deposited onto a Ta-Si-O layer reduces solar cell degradation in accelerated ageing conditions: the cells, encapsulated by a foil of 250 nm Ta-Si-O and 15 nm Ta-Si-N , kept more than 70 % of its initial efficiency after 1000 hours in accelerated aging test conditions. The weak point of this barrier coating is that Ta-Si-N film is unstable in the PV device even at low electrical current.

$\text{Al}_2\text{O}_3/\text{SiO}_2$. Even if a single Al_2O_3 layer deposited by ALD has good gas barrier properties ^[90, 74], an $\text{Al}_2\text{O}_3/\text{SiO}_2$ bilayer was developed that has better barrier performance, ^[88]. The system with layers of Al_2O_3 (26 nm) and SiO_2 (60 nm) shows a decrease of WVTR to

$1 \times 10^{-4} \text{ g m}^{-2} \text{ day}^{-1}$ in comparison to single layer of Al_2O_3 with WVTR of $1 \times 10^{-3} \text{ g m}^{-2} \text{ day}^{-1}$. However, there are some negative issues due to the corrosion of Al_2O_3 . To solve this drawback, $\text{Al}_2\text{O}_3/\text{ZrO}_2$ nanolaminate films have been investigated [91, 92]. In the structure, ZrO_2 was placed between layers of Al_2O_3 in order to stop the accumulation of unreacted Al-OH species [91]. Studied films stacks of 100-130 nm exhibit WVTR and OTR in the values about one-half and one-fifth of same thickness Al_2O_3 single layer [93]. WVTR and OTR for 100 nm thick $\text{Al}_2\text{O}_3/\text{ZrO}_2$ nanolaminate film were respectively found of $2.1 \times 10^{-2} \text{ g m}^{-2} \text{ day}^{-1}$ and $6.4 \times 10^{-5} \text{ cm}^3 \text{ m}^{-2} \text{ day}^{-1}$ determined under controlled conditions of 70 % RH and 70 °C [91].

2.2.2.2. Organic-inorganic hybrid materials: state-of-the-art

Nowadays, one of the most common approaches to obtain ultra-barrier materials is the alternation of organic and inorganic layers into encapsulation coating. As recalled above, inorganic layers have high barrier properties, but the pathway for permeants is provided by defects and pinholes present into the film. The permeation through polymers follows the mechanism of solution-diffusion where the permeants, first, get adsorbed onto the surface, dissolve in the polymer matrix and then diffuses in the polymer. One important parameter, regarding the diffusion rate, is the available free-volume between the molecular chains. The approach of sandwiching inorganic barriers between polymer layers results not only in a significant increase of barrier properties [94], but it also brings better resistance to mechanical damage, smoothing of the coated surface, and increased thermal stability of multilayer stacks.

BarixTM technologies

One of the first articles related to multilayer coatings for OLED displays protection showed the capability of using this approach by integrating BarixTM technologies, developed by Vitex System Inc [95]. BarixTM utilises “decoupling” layers of polymer deposited between multiple Al_2O_3 layers using organic acrylate evaporation and condensation, followed by an UV curing (Fig.1.11.a). A WVTR of $2 \times 10^{-6} \text{ g m}^{-2} \text{ day}^{-1}$ (20 °C/50 % RH) have been reached with this multilayer [96].

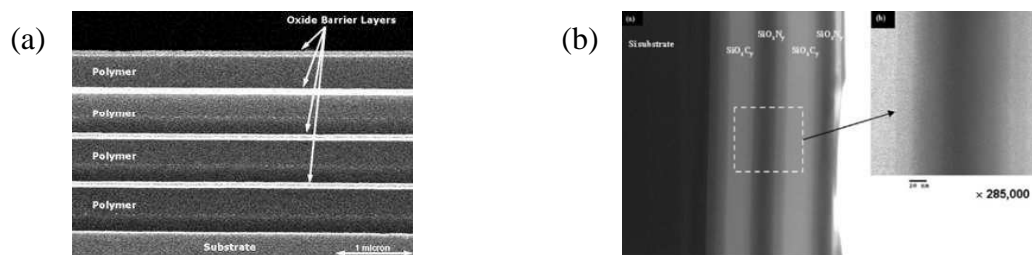


Fig.1.11. (a) Schematic cross section of a Barix™ encapsulation [95]; (b) TEM cross-section images of the graded UHB from General Electric [97].

Nowadays, Barix™ technology is commercialised for direct encapsulation and mainly used for OLED displays protection. This technology has been applied to protect as well inorganic [98] as organic PV [99]. It was shown that after 120 hours of storage in a climatic chamber at 30 °C/70 % RH P3HT:PCBM based devices still demonstrated a performance of 74 %, which indicated that the encapsulation extended the lifetime by more than two orders of magnitude [99].

SiO_x/organosilicon

Alternating SiO_x and organosilicon layers deposited by PECVD on a PEN substrate was proposed for OSCs encapsulation [100]. This was the first multilayer encapsulation applied to OSCs. Organosilicon was deposited in non-oxidised plasma with SiO_x produced from a volatile organosilicon precursor under oxidative plasma conditions. The system of five layers and total thickness of 500 nm kept good transparency and, in case of encapsulated OSC devices (MDMO-PPV:PCBM), increased lifetime from few hours up to 3000 h (V_{oc} was at about 90% of its initial value) in comparison to 175 μm PET coating, which provides 6 hours lifetime for the device.

Based on the same concept, an hybrid graded organic-inorganic ultra-high barrier (UHB) coating was developed by General Electric. Single graded SiO_xN_y-SiO_xC_y alternation layer deposited by PECVD with total thickness less than 1 μm exhibits WVTR value of $8.6 \times 10^{-6} \text{ g m}^{-2} \text{ day}^{-1}$ (25 °C/50 %RH). The cross-sectional TEM image of this thin film is shown in Fig.1.11.b.

The same system has been used by *Lungenschmied et al.* [54] to encapsulate polythiophene-based devices. The encapsulated cells composed of P3HT:PCBM active layer showed a shelf lifetime of 600h (storage in the dark under ambient air).

A SiO_x/organosilicon ultra-barrier system deposited onto PET substrate by PECVD was studied by *Wu et al.* [101]. It was shown that the WVTR of the PET substrate coated with 3-pairs organosilicon/SiO_x barrier structure was decreased to $4 \times 10^{-2} \text{ g m}^{-2} \text{ day}^{-1}$, which was

one order of magnitude smaller than that of the substrate coated with 1-pair of organosilicon/SiO_x multilayer barrier structure. For the barrier structure with six pairs, the WVTR was achieved below the detection limit of the used permeameter (MOCON Permatran-W3/61, 10⁻² g m⁻² day⁻¹).

SiO_x/SiN_x/parylene

The benefit of SiN_x over oxide or oxynitride as an effective transparent inorganic barrier coating material is that in the deposition process it does not require reactive oxygen atoms, which could react with the substrate. Deposition of parylene smooths inorganic layers by masking surface defects and consequently, improves permeation resistance. A SiN_x/parylene multilayer structure was introduced ^[102] and WVTR and OTR of the two pairs of parylene/SiN_x coating on the PC substrate can be maintained at a level near 10⁻² g m⁻² day⁻¹ and 10⁻¹ cm⁻³ m⁻² day⁻¹ respectively ^[103]. This indicates a good potential of this system for future use for encapsulation of organic electronics.

Calcium test performed by *Chen et al.* ^[104] showed that a system composed of one parylene and three SiO_x/SiN_x layers exhibit a WVTR of 2.5×10⁻⁷ g m⁻² day⁻¹ (25 C, 40 % RH for 75 days of experiment).

The first results of the deposition of parylene single layer showed insufficient protection of P3HT:PCBM based devices even at 10 μm thick layer ^[105]. In order to improve the protection of the cell, a multilayer made of alternating parylene (5 μm) and Al₂O₃ (~350 Å) layers has been developed. It has been shown that parylene/Al₂O₃ multilayers encapsulated device displays 50% in efficiency loss occurred after 40 hours of exposure to air, meanwhile, a non-encapsulated cell was completely degraded after only 8 hours of keeping them in air.

Lately, the multilayer system based on 100 nm thick SiO_x or SiN_x layer (PECVD) followed by a layer of 10–50 nm Al₂O₃ (ALD) and 1 μm thick parylene layer (chemical vapour deposition (CVD)) has been used for encapsulation of pentacene/C₆₀ solar cells ^[106]. The WVTR of this encapsulation reached (2±1)×10⁻⁵ g m⁻² day⁻¹ (at 20 °C/50 % RH) (it is worthy to note that encapsulated cells showed no decrease in conversion efficiency after 5800 hours of exposure with a xenon lamp (Fig.1.12.)).

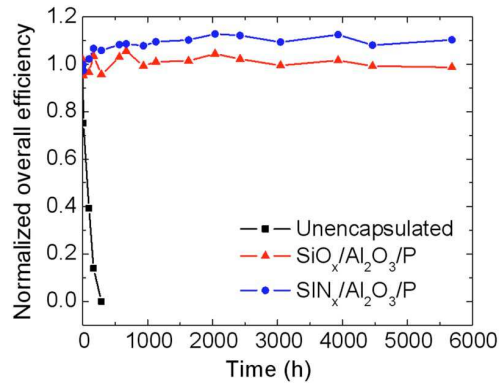


Fig.1.12. Normalised power conversion efficiency as a function of irradiation time of encapsulated and non-encapsulated pentacene/C₆₀ solar cells. Irradiation source: xenon lamp ^[106].

Polymer/clay

Priolo et al. ^[107] proposed a different approach of barrier improvement introducing a layer of nanoparticles into encapsulation. The encapsulation based on quadlayer of superposed polyethyleneimine (PEI), poly(acrylic acid) (PAA), PEI and montmorillonite clay have been obtained by layer-by-layer (LBL) deposition of aqueous ionic mixtures (Fig.1.13.). The inorganic particles of montmorillonite were placed in between the layers of polymers. The obtained multilayer coatings contains 26.2 wt % (for 5 quadlayers) of particles which is nearly one order greater than most conventional bulk composites. The optimal composition of four quadlayers deposited on silicon substrate with a total thickness of 51 nm displayed oxygen permeability $<5 \times 10^{-2} \text{ cm}^3 \text{ cm cm}^{-2} \text{ s}^{-1} \text{ Pa}^{-1}$, which is at least 2 orders of magnitude below that reported for completely inorganic SiO_x barrier thin films and 4 orders of magnitude lower than a 25 μm EVOH copolymer film.

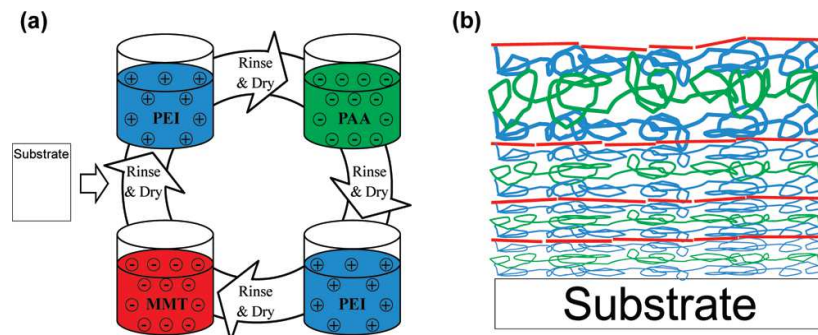


Fig.1.13. (a) Scheme illustration of layer-by-layer deposition and (b) the nanobrick wall structure resulting from the alternate adsorption of PEI (blue), PAA (green), PEI, and MMT (red) onto a substrate [107].

Polymer/nanoparticles

Another approach is to use a layer of nanoparticles encapsulated by a polymer in a multilayer system as it has been developed by Tera-Barrier Films (TBF) Pte Ltd, [108]. This layer on 95 wt % consist of nanoparticles which are encapsulated into a polymer matrix (5 wt %) where polymer covers the particles on 80-100 % of their surface and plays basically fixing function. These sealing layer exhibits high packing density of particles and strong bonding between them. It is placed between aluminium foil and transparent oxide film (barrier layer) and plays the role of gap for permeants (Fig.1.14.). The nanoparticles (Al or Zn oxide based) coated by a polymer through crosslinking /curing, absorbs and reacts with water and oxygen molecules to trap them, thus further lowering the amount of moisture and air passing through the film. The particles may also penetrate effectively into the pores or the defects of barrier oxide and plug the defects. An amphiphilic cross-linkable multi-unsaturated fatty acid based polymers or their derivatives were used as polymers for particles coating, and a 60-70 nm thick Al_2O_3 or SiO_x layer as a barrier.

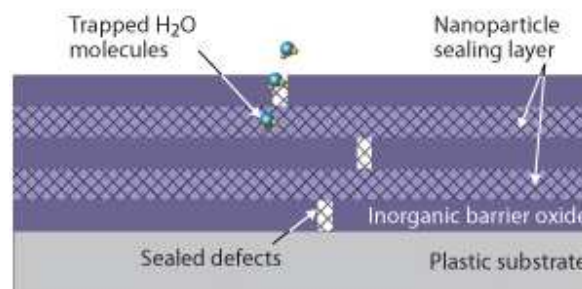


Fig.1.14. Schematic block mechanism of permeants diffusion by nanoparticle sealing layer [109].

One of the investigated structures made of two dyads multistack of Al₂O₃ layer (sputtering manufacturing process)/ encapsulated Al₂O₃ nanoparticles on PET substrate exhibits $1 \times 10^{-4} \text{ g m}^{-2} \text{ day}^{-1}$ WVTR at 60 °C and 90 % RH. The layer showed good transparency (85 % of transmittance). It was claimed that foils produced with using such a sealing layer can reach WVTR more than $1 \times 10^{-6} \text{ g m}^{-2} \text{ day}^{-1}$ [110].

2.2.2.3. Polymer/nanocomposites

One of the strategies to increase the barrier properties is to incorporate nanofillers capable of interacting with moisture and/or oxygen to retard the penetration of the moisture and/or oxygen. In order to keep the transparency of the coating the particles size must be typically 1/2 and preferably 1/5 of the solar light wavelength. Typically, these ratios correspond to particles size less than 200 nm and preferably less than 100 nm.

Another approach to improve the gas barrier properties is to include inorganic nanofillers into the polymer, which gives nanocomposites. Compared to the previously described example, nanocomposites have low inorganic loadings $\leq 5 \text{ wt } \%$ [111]. It has been shown that inclusion of inorganic nanoparticles at a small amount results in enhancement of different properties, such as heat resistance [112-114], thermal stability [114], mechanical [115], electrical [116] and other properties. Another very significant feature, especially for nanolamellar structured particles, is their ability to enhance the barrier properties [94], which can be explained by the creation of tortuous diffusion pathways in the nanocomposite layer.

PVA/Na-MMT

The optimisation of sodium-montmorillonite clay (Na-MMT) loading into poly(vinyl alcohol) (PVA) matrix in order to obtain suitable material for OSC encapsulation have been performed by *Gaume et al.* [117]. The nanocomposite layers were processed by solution casting of aqueous solutions. Further, the cells were coated by PVA or its nanocomposite deposited onto PET substrate. Fig.1.15. demonstrates that in the case of PET encapsulation, PCE of organic solar cells decreased by 80 % within less than 70 h of exposure in sun simulator. Whereas, in the case of a PET film with a PVA nanocomposite coating encapsulation, PCE remained about 40 % of its initial value after the same exposure time.

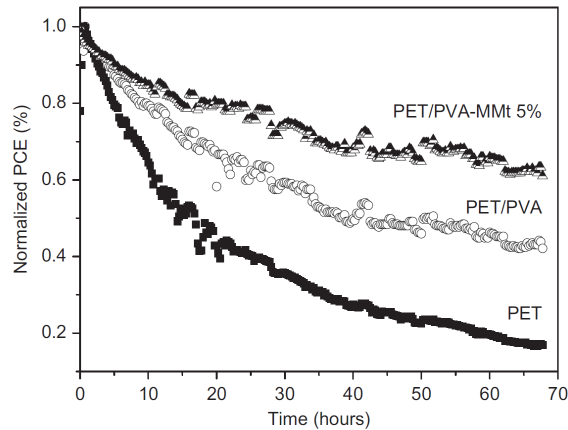


Fig.1.15. Normalised power conversion efficiency (PCE) of organic solar cells encapsulated in a PET film, a PET/PVA (1 μm) and a PET/PVA-MMt (5 wt %) (1 μm) ^[117].

Another nanocomposite based on poly (ethylene-co-vinyl alcohol) (EVOH) and MMT filler have been proposed by *Seethamraju et al.* ^[118]. As determined from the Ca test, the WVTR of the nanocomposite with 5 wt % MMT loading was lower by more than one order than that of the neat polymer. The EVOH/MMT composite films exhibited WVTR in the order of $10^{-3} \text{ g m}^{-2} \text{ day}^{-1}$ (Fig.1.16).

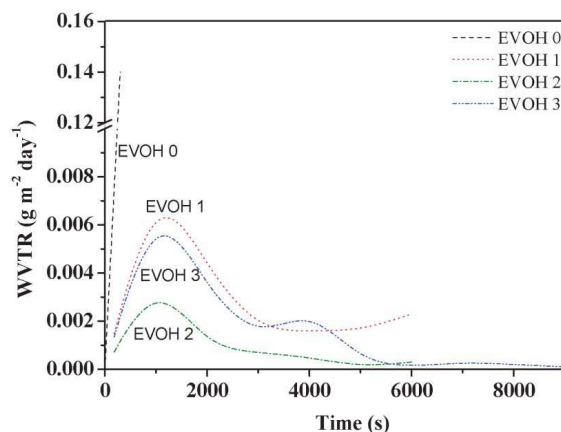


Fig.1.16. Influence of MMT loading into EVOH matrix on WVTR linked to time of Ca-corrosion test: neat polymer (EVOH 0) and composites (EVOH 1, 2, 3 compositions represent 1, 2, and 5 wt% of MMT in EVOH, respectively) films ^[118].

2.3. Conclusions

Different materials and strategies have been proposed for the encapsulation of OSCs. The inorganic layers were used in majority of analysed published papers to provide good barrier

performance. However, such materials endanger the device to fail due to the cracking risk and the defects growth under bending working conditions. Moreover, single-thin film layers are limited in performance due to defects and pinholes, hence, they cannot reach the permeability levels more than three orders lower than those exhibited by bare polymer substrates^[58]. At last, common fabrication methods like PECVD and ALD require expensive and complicated vacuum deposition systems.

Alternating organic-inorganic multilayer system was demonstrated to be an effective solution to achieve coating with improved flexibility, surface smoothing, thermal and barrier properties. These encapsulants can already reach WVTR required for OSCs. Nevertheless, these coatings have restrictions due to high-cost fabrication processes and the issues of production in large-scale. In general, the majority of barriers were initially developed for OLED protection, which is extremely moisture sensitive. Unfortunately, the stability under sunlight, which is an important issue for OPV devices, has not been taken into account. Hence, commonly these materials exhibit limited durability under sunlight exposure ($\lambda > 300$ nm) in the presence of air and humidity.

Mixing of inorganic particles with polymer has been shown to be an effective solution for polymers to enhance the material properties desired for coating applications. Nanocomposites exhibit improved barrier properties, thermal stability, mechanical reinforcement, and etc. In addition, the possibility to apply simple and low-cost processing method for their fabrication opens scalability for roll processing in comparison to deposition techniques applied for inorganic layers. Through, the single nanocomposite layer cannot reach the requirements to barrier levels for OSC. But, it can be used to improve the barrier properties within a multistack, and therefore, brings more potential to replace the organic layer. It may significantly reduce the difficulties with encapsulation production, and thus, decrease the price of end-product.

3. NANOFILLERS

The purpose of this work was to develop a new nanocomposite in order to improve the initial properties of commercially available, cheap, and widely used polymer into packaging, for its further integration into organic multilayer encapsulation for OPV. Regarding to the aggressive environment of OSC operation, particular attention has to be paid on nanocomposite durability under light exposure and damp heat conditions.

Polymer nanocomposites are particle-filled polymers for which at least one dimension of the dispersed particles is in the nanometer range (1-100 nm) ^[112, 119]. Nanoscale particles can be classified in three groups depending on their geometry: nanoparticles, nanotube, and lamellar nanofillers (Fig.1.17.).

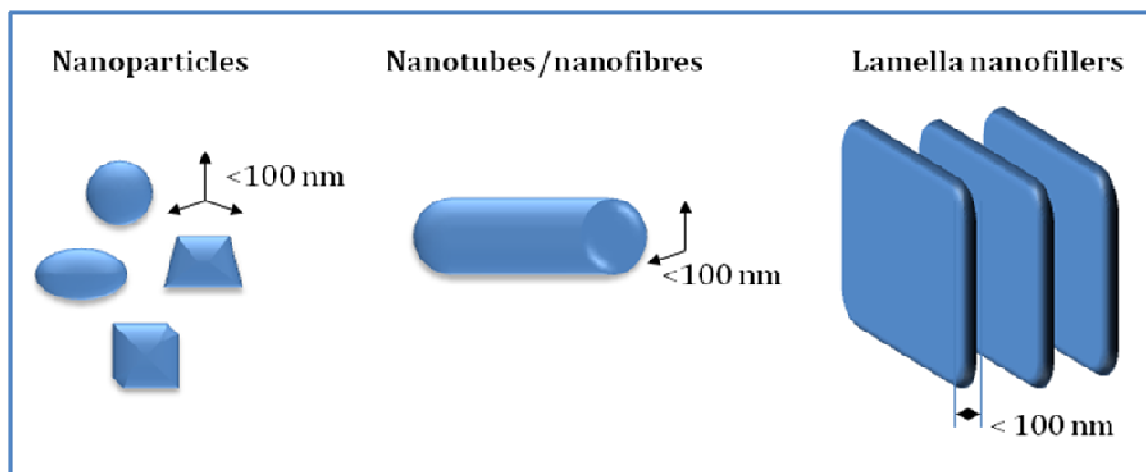


Fig.1.17. Types of nanofiller reinforcements/geometries.

When all the three dimensions are in the order of nanometres, and the aspect ratio (the highest dimension divided by the lowest) is around 1, they are referred as nanoparticles such as silica nanoparticles. Usually, these fillers are used due to their specific optical, electrical or magnetic properties.

Particles characterised by two dimensions in the nanometer scale, and the larger third forming an elongated structure, are generally called “nanotubes” or nanofibers/whiskers/nanorods. The most interesting are carbon nanotubes (CNTs) and cellulose whiskers, which are extensively studied as reinforcing nanofillers yielding materials with exceptional properties.

The third type of fillers, distinguished by only one dimension in the nanometre range, is related to nanolayers/nanosheets and is usually called lamella nanofillers. They consist of

layers with an aspect ratio of at least 25. In this case the filler is present in the form of sheets of one to few nanometres thick and hundreds to thousands nanometres long. For such materials, clays (layered silicates) and layered double hydroxides (LDHs) are the most studied.

The most commonly used nanofillers for the development of polymer nanocomposites are clays (phyllosilicates, natural cationic clays like montmorillonite, and synthetic anionic clays such as layered double hydroxides) and carbon nanotubes.

a. Phyllosilicates, also called layered silicates, are constituted by a stack of layers of tetrahedral (T) and octahedral (O) structure formed from oxygen on the sides and the central ion (Si or Al). A central octahedral sheet of alumina is fused to two external silica tetrahedrons by the tip, so that the oxygen atoms of the octahedral sheet also share the tetrahedral sheets, as it is shown in Fig.1.18.

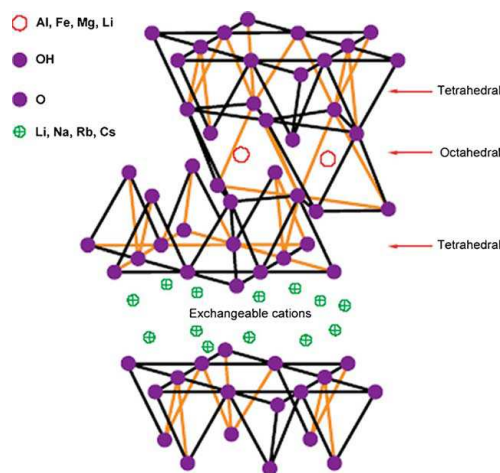


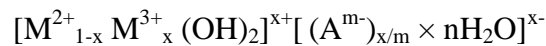
Fig.1.18. Structure of a phyllosilicate ^[120].

Montmorillonite (MMT) is one of the most studied members of phyllosilicates. Its layered structure results from partially substituting the three-valent Al-cation in the octahedral sheet by the divalent Mg-cation. The negative charge of the layer is balanced by Na and Ca ions located in the interlayer space. Due to weak forces, which keep layers together, polar molecules can penetrate in the interlayer gap, thus swelling all molecules (for dehydrated MMT the interlayer distance is about 1 nm).

Besides MMT, hectorite and saponite have a great interest in the field of electrical insulating material manufacturing owing to their high aspect ratio (up to 1000) and peculiar

intercalation/exfoliation capability, which can be exploited to improve polymer electrical, thermal and mechanical properties.

Layered double hydroxides (LDHs), also known as hydrotalcite-like materials, are a class of synthetic two-dimensional nanostructured anionic clays which structure can be described as brucite-like layers, where a fraction of the divalent cations coordinated octahedrally by hydroxyl groups have been replaced isomorphously by trivalent cations, giving positively charged layers with charge-balancing anions between them. Chemical composition of LDH (Fig.1.19.) is generally expressed as following:



where, M^{2+} and M^{3+} are divalent and trivalent cations, A is an interlayer anion, m is the charge of interlayer ion.

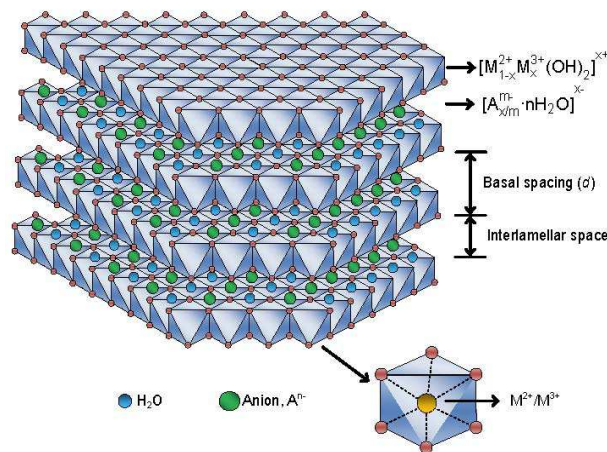


Fig.1.19. Chemical structure of Layered Double Hydroxide (LDH) [121].

Different metal ions can be used to form positively charged layers, divalent such as Zn^{2+} , Ni^{2+} , Cu^{2+} , Co^{2+} , Fe^{2+} , and trivalent, like Cr^{3+} , Al^{3+} , Fe^{3+} , Mn^{3+} , Ga^{3+} . Regarding the interlayer space, LDH can be characterised by their anion exchange capacity, where anions can be inorganic, complex, organic or polymeric anions. A wide range of chemical combinations of metal oxide layers and negative interlayers allows engineering a hybrid LDH that may be compatible with polymer matrices.

b. Carbon nanotubes are long cylinders of covalently bonded carbon atoms [122, 123]. Two basic types of CNTs exist: single-wall carbon nanotubes (SWCNTs), which have the fundamental cylindrical structure, and multi-wall carbon nanotubes (MWCNTs), which are made of coaxial cylinders (Fig.1.20.), having interlayer spacing close to that of the interlayer distance in graphite (0.34 nm). These cylindrical structures are only few nanometres in

diameter, but the cylinder can be tens of microns long, with most end-capped with half of a fullerene molecule.

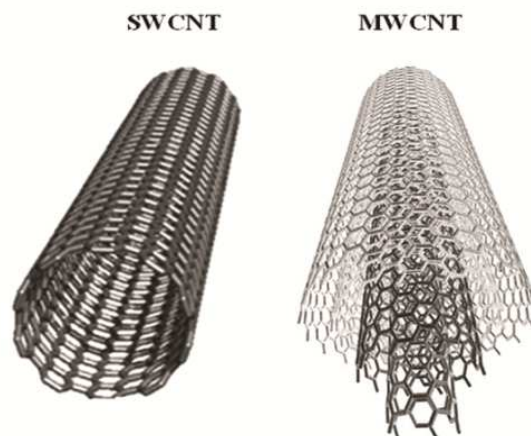
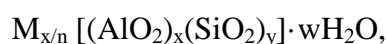


Fig.1.20. Schematic diagrams of single-wall carbon nanotube (SWCNT) and multi-wall carbon nanotube (MWCNT) [122].

CNTs have exceptional mechanical and thermal properties. Moreover, they can be electrically conductors, semiconductors or insulators depending on their chirality. The most common problem is their poor dispersion in the polymer matrix. Hence, chemical functionalisation treatment of CNTs is a common procedure, which includes functionalisation of defect groups, covalent functionalisation of sidewalls, non-covalent functionalisation, e.g., formation of supramolecular adducts with surfactants or polymers [122].

c. Nanoparticles. There are many types of nanoparticles. In this paragraph, we focus on zeolites, which were used in the present study for their water barrier properties. Zeolites, materials with ordered porous structure, can be synthesised in the nanometre range and are classified as nanoparticles in terms of geometry.

Zeolites are a class of crystalline aluminosilicate materials built from an infinitely extending three dimensional network of $[\text{SiO}_4]^{4-}$ and $[\text{AlO}_4]^{5-}$ tetrahedrals connecting to each other by the sharing of oxygen atoms [124, 125]. The structure formula of zeolite is based on the crystallographic unit cell [126]:



where M is an alkali or alkaline earth cation, n is the valence of the cation, w is the number of water molecules per unit cell, x and y are the total number of tetrahedra per unit cell, and

the ratio y/x usually has values from 1 to 5, though for the silica zeolite, y/x can be ranging from 10 to 100.

Zeolite is an open-structure framework that consists of many channels and/or interconnected voids of discrete size (in the range 0.3-20 Å). Each AlO_4 tetrahedron in the framework bears a net negative charge that is balanced by a cation. Typically, these counter ions are elements from the IA and IIA groups of the periodic table. Some zeolite structures are shown in Fig.1.21.

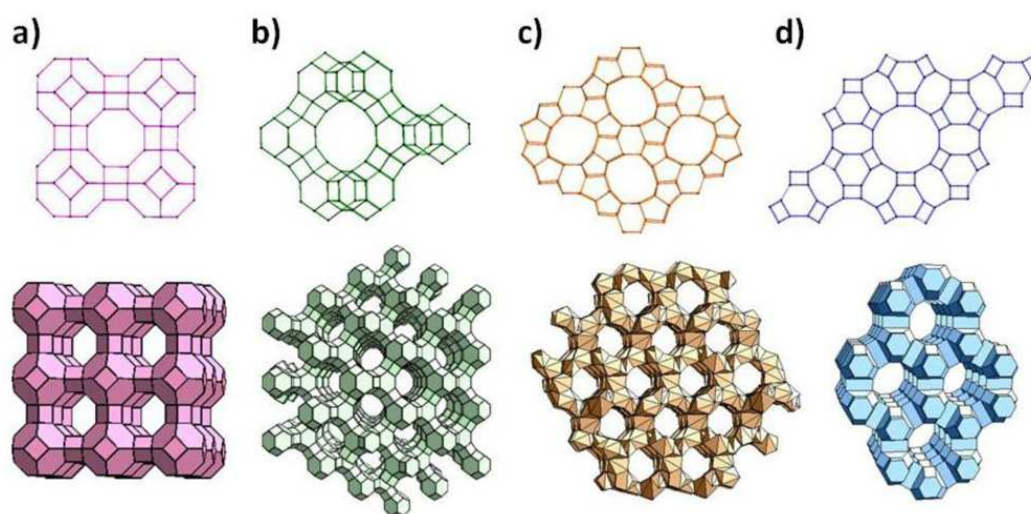


Fig.1.21. Representative zeolite frameworks (with pore openings): (a) zeolite A (3D, 4.2 Å); (b) zeolite Y (3D, 7.4 Å); (c) zeolite L (1D, 7.1 Å); (d) ZSM-5 (silicalite) (2D, $5.3 \times 5.6 \text{ Å}, 5.1 \times 5.5 \text{ Å}$)^[127].

Numerous types of synthetic zeolites with variable framework type structures with one-, two- and three-dimensional pore systems can be synthesised. Table 1.2. gathers the typical oxide formula of some synthetic zeolites.

Table 1.2. Typical oxide formula of some synthetic zeolites

Zeolites	Typical oxide formula
Zeolite A	$\text{Na}_2\text{O}\cdot\text{Al}_2\text{O}_3\cdot 2\text{SiO}_2\cdot 4.5\text{H}_2\text{O}$
Zeolite N-A	$(\text{Na},\text{TMA})_2\text{O}\cdot\text{Al}_2\text{O}_3\cdot 4.8\text{SiO}_2\cdot 7\text{H}_2\text{O}$
Zeolite H	$\text{K}_2\text{O}\cdot\text{Al}_2\text{O}_3\cdot 2\text{SiO}_2\cdot 4\text{H}_2\text{O}$
Zeolite L	$(\text{K}_2\text{Na}_2)\text{O}\cdot\text{Al}_2\text{O}_3\cdot 6\text{SiO}_2\cdot 5\text{H}_2\text{O}$
Zeolite X	$\text{Na}_2\text{O}\cdot\text{Al}_2\text{O}_3\cdot 2.5\text{SiO}_2\cdot 6\text{H}_2\text{O}$
Zeolite Y	$\text{Na}_2\text{O}\cdot\text{Al}_2\text{O}_3\cdot 4.8\text{SiO}_2\cdot 8.9\text{H}_2\text{O}$
Zeolite P	$\text{Na}_2\text{O}\cdot\text{Al}_2\text{O}_3\cdot 2\text{-}5\text{SiO}_2\cdot 5\text{H}_2\text{O}$
Zeolite O	$(\text{K}_2\text{Na}_2,\text{TMA}_2)\text{O}\cdot\text{Al}_2\text{O}_3\cdot 7\text{SiO}_2\cdot 3.5\text{H}_2\text{O}$
Zeolite Ω	$(\text{Na},\text{TMA})_2\text{O}\cdot\text{Al}_2\text{O}_3\cdot 7\text{SiO}_2\cdot 5\text{H}_2\text{O};$
Zeolite ZK-4	$0.85\text{Na}_2\text{O}\cdot 0.15(\text{TMA})_2\text{O}\cdot\text{Al}_2\text{O}_3\cdot 3.3\text{SiO}_2\cdot 6\text{H}_2\text{O}$
Zeolite ZK-5	$(\text{R},\text{Na}_2)\text{O}\cdot\text{Al}_2\text{O}_3\cdot 4\text{-}6\text{SiO}_2\cdot 6\text{H}_2\text{O}$

Zeolites are classified in four groups based on their pore size: ultra-large (more than 14-membered ring), large (12-membered ring), medium (10-membered ring) and small (eight-membered ring) pore molecular sieves. In general, zeolites with medium and large pores are mostly used in catalysis in order to ensure the easy diffusion of the molecules to the catalytic active sites in the zeolite pores. On the other hand, those with high concentration of cation exchange sites and small pores are suitable for sorption processes due to the molecular sieving effect.

In addition to the classical applications in ion-exchange, separation and catalysis, zeolites are attractive for novel technologies including highly selective membranes, host-guest chemistry, chemical sensors, etc. About 170 types of zeolites exist ^[128], and among them 40 types are natural. Most of the zeolites are micro-sized, but they can also exist in a nanometric range.

Zeolites are highly hydrophilic sorbents due to their electrostatic charged framework and the abundance of extra-framework cations. Almost all of the zeolites show type I water sorption isotherm, which indicates a high affinity to water at low partial pressure. The water sorption capacity is generally proportional to the size of the pores, therefore large pore aluminosilicate zeolites with 12-membered ring have the highest capacity for water. Higher water capacity is served for aluminium rich zeolites due to their high concentration of hydrophilic active sites. These zeolites are usually used as desiccants ^[125].

3.1. Processing of nanocomposites with clays

Polymer nanocomposites with clays are synthesised via various methods that can be categorised into four major routes ^[123, 129] :

1. *Solvent method (exfoliation adsorption)* also called polymer or pre-polymer intercalation from solution, is based on a solvent in which the polymer or pre-polymer is soluble. Thus, a solvent system consists of swollen particles and solubilised polymer or pre-polymer. When the polymer and layered silicate solutions are mixed, the polymer chains intercalate and displace the solvent within the interlayer of the silicate. Upon solvent removal or precipitation in non-solvent media, the intercalated structure remains, resulting in polymer/layered silicate nanocomposite. This method is good for the intercalation of polymers with little or no polarity into layered structures and facilitates production of thin films with polymer-oriented clay intercalated layers.

2. *In situ polymerisation.* Using this technique, polymer formation can occur between the intercalated sheets of layered silicates. *In situ* polymerisation is based on the prior swelling of the layered particles within a liquid monomer or a monomer solution and further polymerisation. The polymerisation reaction is initiated between the intercalated sheets by radiation, heat, the diffusion of a suitable initiator, or by catalyst fixed through cationic exchange inside the interlayer before the swelling ^[112, 130]. At first, this approach was applied in manufacturing of nylon–montmorillonite nanocomposite (Fig.1.22.) ^[131].

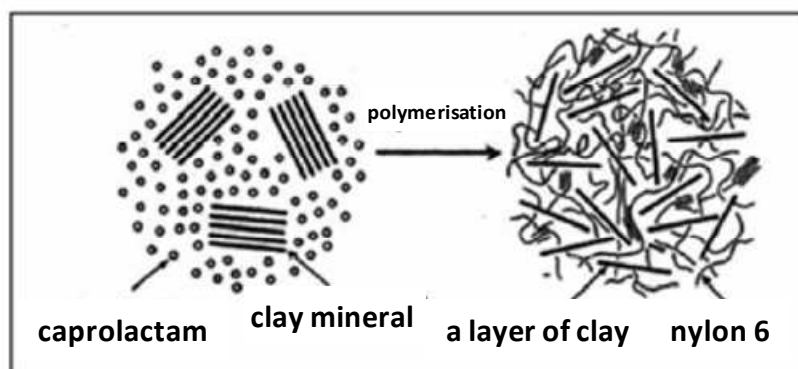


Fig.1.22. Illustration for synthesis of Nylon-6/clay nanocomposites ^[131].

This method can be used for both, thermoplastic ^[132] and thermosetting ^[133] polymers with different nanofillers, e.g., metallic oxides or layered silicate.

3. *Sol–gel method (or template synthesis).* This approach involves the formation of the inorganic filler in an aqueous solution or gel containing the polymer and the filler building

blocks. It consists of hydrolysis of the constituent molecular precursors and subsequent polycondensation to glass-like form. Different additives can be easily introduced into the glassy network at room temperature during processing. During the process, the polymer contributes to the nucleation and growth of crystals, which are entrapped in the matrix. This method can disperse fillers in a polymer in a single step.

4. Melt blending. Solvent free and thus, environmentally friendly, this technique involves annealing the polymer matrix at high temperatures, adding the filler, and finally kneading the composite to achieve uniform distribution. Melt intercalation is the typical standard approach for synthesising thermoplastic polymer nanocomposites. It is also considered compatible with industrial processes such as injection moulding and extrusion, which makes it more convenient to use. However, the high temperatures used in the process can damage the surface modification of the filler. Therefore, optimisation of the processing conditions is a very important factor that plays a big role in achieving good dispersion and exfoliation. Weak electrostatic forces among the filler interlayers and compatibility with the polymer matrix allow the polymer to crawl into the interlayers forming intercalated or exfoliated nanocomposites.

The *in-situ* polymerisation and the melt blending methods are the most commonly used techniques for manufacturing thermosetting and thermoplastic nanocomposites, respectively.

3.2. Properties of polymer/nanocomposites

Since Toyota group has developed nylon/MMt nanocomposite ^[134], the tremendous research interest for nanocomposite materials demonstrated the improvement of the material properties ^[112, 135-137]: mechanical ^[115, 138-140], thermal ^[114, 141], optical ^[142], electrical ^[116, 143], barrier ^[115, 138, 144]. Table 1.3. displays different examples of incorporated into polymer matrix nanofillers and their reinforcement effect on material properties.

Table 1.3. Examples of nanoscale fillers incorporated in polymer composites for other property enhancement than reinforcement ^[137]

Nanofiller	Property enhancement(s)	Application/utility
Exfoliated clay	Flame resistance, barrier, compatibilizer polymer blends	
SWCNT; MWCNT	Electrical conductivity, charge transport,	Electrical/electronics/optoelectronics
Nanosilver	Antimicrobial	
ZnO	UV adsorption	UV screens
Silica	Viscosity modification	Paint, adhesives
CdSe, CdTe	Charge transport	Photovoltaic cells
Graphene	Electrical conductivity, barrier, charge transport	Electrical/electronic
POSS	Improved stability, flammability resistance	Sensors, LEDs
Zeolites	Improved permselectivity, dessicant properties, ion exchange	Membranes, absorbents

Changes in *mechanical properties* can be related to the fact that with nanoparticle incorporation, nucleation with crystallisation can occur. Nucleation effect resulted in increased onset temperature and a decreased half-time of crystallisation has been observed in different nanocomposites ^[145-147]. However, at higher levels of nanoparticle addition, a delay for crystallisation was noticed. This delay was present even in the systems where nucleation was observed at low content of nanoparticles and was mentioned to occur due to diffusion constraints ^[147-149].

Another “nano-effect” reported in the literature is the change in the T_g of polymer matrix in the presence of nanoparticles. Both, an increase or a decrease in the T_g value have been reported depending upon the interactions between the particles and the matrix ^[137]. Nevertheless, modest changes of T_g (<10 °C) are observed.

Common reason for adding nanofillers to polymers is to increase strength, modulus or stiffness via reinforcement mechanism of well dispersed particles ^[150]. However, an opposite effects can occur in case of poor adhesion of the filler to the matrix.

It was shown that fillers such as magnesium hydroxide, organically modified MMT, polyhedral oligomeric silsesquioxane (POSS), LDH with good dispersion can successfully serve as *flame retardant*, improved properties for targeted high-temperature applications ^[151].

The **barrier properties** of polymers can be efficiently improved by adding particles with sufficient aspect ratio to alter the diffusion path of permeant molecules as illustrated in Fig.1.23.

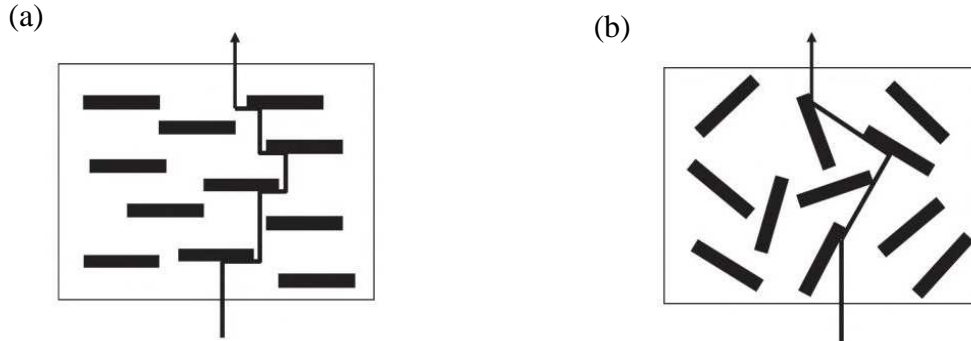


Fig.1.23. Representation of (a) path of permeant molecule in composite with completely aligned platelets; (b) misaligned platelets ^[152].

- Permeability

Different theories are developed for the prediction of the barrier properties through nanocomposites. For example, Nielsen theory is based on the reduction in the permeation through the composite (P_c) as a function of filler volume fraction φ_f and filler aspect ratio α described as follows:

$$\frac{P_c}{P_m} = \frac{\varphi_m}{1 + \frac{\alpha \cdot \varphi_f}{2}} \quad (\text{Eq.1.1})$$

Where P_m and φ_m are the permeation through polymer matrix and polymer volume fraction respectively. Other modified finite elements models predicting the permeation reduction exist, such as the Cussler-Aris model, the Fredricson-Bicerano model, the Lusti-Gusev model, and etc. From all of them it can be based on the shape (aspect ratio) of the nanoparticles and hence, their dispersion degree and just secondary, on their size. The difference in the orientation of particles was taken into account by Bharadwaj ^[153] who introduced the variable of orientation (S) into Nielsen equation:

$$\frac{P_{nano}}{P_{poly}} = \frac{1 - \varphi}{1 + \frac{\alpha}{3\varphi \left(S + \frac{1}{2}\right)}} \quad \text{where } S = \frac{1}{2}(3 \cos^2 \theta - 1) \quad (\text{Eq.1.2})$$

- **Sorption**

The introduction of selective zeolite, which acts as molecular sieves, in a polymer film generally enhance the permselectivity properties of membrane separation ^[154]. Nevertheless, due to well-known high sorption capacity of zeolites, their nanocomposites exhibit high water uptake, which has been used to develop the functional food packaging for humidity control ^[155, 156]. It was find that zeolite at 5 wt % loading can also enhance water-retention properties of the filled materials ^[157].

3.3. EVOH copolymers and nanocomposites

Ethylene-vinyl alcohol copolymer (EVOH) relates to semi-crystalline random copolymers of vinyl alcohol and ethylene units (Fig.1.24.).

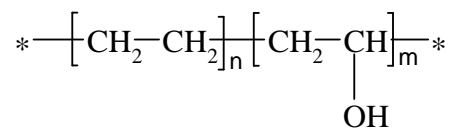


Fig.1.24. Chemical structure of EVOH.

In order to indicate the ratio of vinyl alcohol and ethylene in the copolymer, the following abbreviation is usually used: EVOH X, where X is the concentration (mole %) of ethylene part.

The polar nature (presence of –OH groups in polymer structure) and excellent self-organisation offer high barrier properties to oxygen with an OTR around $10^{-3} \text{ cm}^3 \text{ m}^{-2} \text{ day}^{-1} \text{ atm}^{-1}$ for the lower content in ethylene (Table 1.4.). EVOH integrates the good processability of PE with the high oxygen barrier property of PVA. The excellent barrier performance in combination with good transparency, crack resistance, considerable chemical resistance, lead to a wide use of these copolymers as oxygen barriers for improved food and pharmaceutical packaging shelf life and as hydrocarbon barriers for fuel tanks.

With an increase of ethylene content in the copolymer, the moisture barrier properties improve and the gas barrier properties decrease (Table 1.5) ^[158].

Table 1.4. Barrier properties of EVOH (film thickness 25,4 μm)^[159].

EVOH (mol% Ethylene)	Gases ^a				Moisture ^b
	O ₂	CO ₂	N ₂	He	
27	0.01	0.04		7.7	6.8
32	0.02	0.05	0.002	15.5	3.8
38	0.03	0.10	0.003	25.5	2.1
44	0.07	0.20	0.005	40.0	1.4
48	0.11	.032	0.007	52.0	1.4

^a in cubic centimeter-mils per 100 in². 24 hours per atm at 20 °C at 65 % RH.

^b in gram-mils per 100 in². 24 hours per atm at 40 °C at 90 % RH.

This trend gives an opportunity to tune the chemical composition of the copolymer depending on the assigned task. Anyway, to keep good barrier properties, a composition in the range of 25-45 mole % of ethylene is required^[160]. The barrier properties to oxygen are extremely sensitive to moisture due to interaction of H₂O molecules and hydroxyl groups of the polymer chain. Hence, EVOH layer is designed to be sandwiched between highly hydrophobic materials, usually polyolefins. Different EVOH-based multilayer structure combinations such as PP/EVOH/PP^[161], PE/EVOH/PE^[66], PE/EVOH/EVA^[162] have been developed for packaging applications.

In order to bring better performance to EVOH based materials, different nanofillers can be introduced into this matrix:

- lamellar nanofillers: organoclays (bentonite^[163], kaolin^[164], kaolinite^[84], cloisite^[165-167], MMT^[118, 166, 168, 169]), LDH^[170], thermal reduced graphene^[171];
- Nanotubes: carbon nanotubes^[172], cellulose nanowhiskers^[173];
- Nanoparticles: mesoporous silica^[174], carbon black and graphite^[175].

Due to the good chemical resistance of EVOH, its nanocomposites can be processed by melt-mixing technique^[176] or solution mixing^[118, 166, 169] or precipitation^[166, 167] using solvents such as dimethylsulfoxide (DMSO)^[118, 172], dimethylformamide (DMF)^[171], toluene, and water/1-propanol^[163].

Most of the EVOH nanocomposites have been developed using montmorillonite and cloisite (organically modified montmorillonite) as fillers. Interestingly, EVOH polar nature allows for improved dispersion and incorporation of nanoparticles without using a compatibiliser.

EVOH/kaolin

Nanocomposite based on EVOH with 27 mole % of ethylene (EVOH27) and kaolin ($\text{Al}_2\text{Si}_2\text{O}_5(\text{OH})_4$) nanofillers was used as a core layer in 5-layers films structure ^[164]. The multilayer films consisted of polypropylene skin layers and maleic anhydride modified polypropylene tie layers were processed by co-extrusion. The reinforcement of mechanical as well as barrier properties was observed for multistack with integrated nanocomposite layer in comparison to unfilled barrier. The WVTR for EVOH/kaolin with 5 wt % of nanofiller content was $0.61 \text{ g m}^{-2} \text{ day}^{-1}$, which is two times lower than the WVTR of pristine EVOH.

EVOH/kaolinite

Another type of clays such as kaolinite was used as nanofiller in order to improve barrier properties of EVOH ^[84]. Kaolinite clay is a very cheap raw material of the tile industry that needed to be refined and chemically modified prior to melt intercalation. To improve the morphology of nanocomposite, a treatment with dimethylsulfoxide, methanol and octadecylamine was carried out. Consequently, the basal plane distance of the original clay increased by three times. Transmission electron microscopy (TEM) images showed a strong adhesion between EVOH (containing 32 mole % of ethylene) and the clay (Fig.1.25.) and intercalation (but not total exfoliation) was observed, respectively, which were correlated with 3 °C to 6 °C higher T_g values for the nanocomposites and, thus, higher rigidity. The nucleation effect of kaolinite particles resulted in increased crystallinity. This resulted in enhanced barrier properties of the nanocomposite. The measured OTR for 110 μm thick films of the pristine polymer was found to be $0.35 \text{ cm}^3 \text{ m}^{-2} \text{ day}^{-1}$ what is 4 times lower than permeability rate reported in Table 1.4. ($0.02 \text{ cm}^3 \text{ mil day}^{-1} 100 \text{ in}^{-2}$ after recalculation for the same units and film thickness gives value of $1.39 \text{ cm}^3 \text{ m}^{-2} \text{ day}^{-1}$).

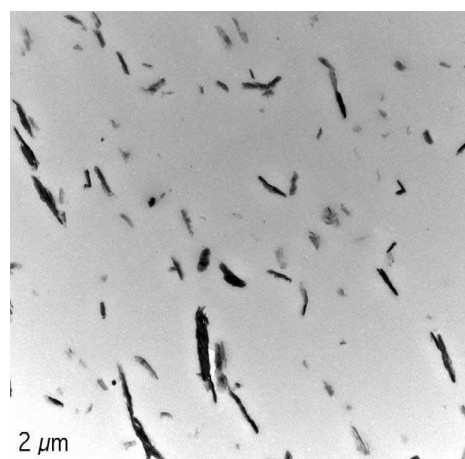


Fig.1.25. TEM image of EVOH/nanocomposites containing 2% of modified kaolinite clay ^[84].

EVOH/MMT

Attention was also focused on the incorporation of montmorillonite into EVOH contained 44 mole % of ethylene units. Enhancement of barrier properties was offered by lamellar shape of the particles. It has been reported OTR value of $5 \times 10^{-2} \text{ cm}^3 \text{ m}^{-2} \text{ day}^{-1}$ ^[168]. Calcium degradation test showed a gradual reduction of WVTR from $\sim 10^{-1} \text{ g m}^{-2} \text{ day}^{-1}$ to $10^{-4} \text{ g m}^{-2} \text{ day}^{-1}$ with an increase of MMt loading in the nanocomposite ^[118].

Thermal analysis of EVOH/MMt nanocomposites showed a sharp decrease of heat of fusion, melting and crystallisation temperatures with clay ^[177, 178]. As compatibiliser of EVOH with clay, maleic anhydride grafted ethylene vinyl acetate (EVA-g-MA) or maleic anhydride grafted linear low-density polyethylene (LLDPE-g-MA) were used. The addition of compatibilisers enhances the intercalation levels of EVOH into clay galleries. Depending on blending conditions and clay content, the obtained morphology was intercalation, delamination or complete exfoliation (Fig.1.26.).

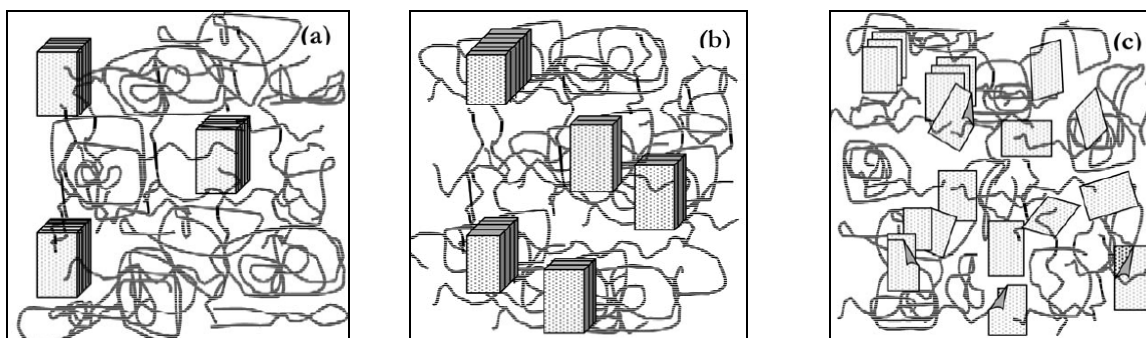


Fig.1.26. Schematic description of clay fracturing and an onion like delamination process, where thin platelets peel off and blend into the matrix: (a) before intercalation and/or delamination process, (b) intercalation and clay fracturing, (c) advanced delamination process ^[177].

Nanocomposites with only 0.5 % surface-modified MMt loading obtained by extrusion at 200 °C and 40 rpm presented an exfoliated structure and, regardless of the clay content, the tensile modulus and strength were observed to increase up to 40 % and 30 % respectively relative to the neat EVOH, highlighting the high level of intercalation of the filler with the EVOH matrix ^[177].

EVOH/LDH

Carbonate and stearate intercalated LDHs were used as fillers in EVOH-nanocomposites preparation ^[170]. Hydrotalcite (LDH-CO₃), having sheets with exposed hydroxyl groups, allows strong hydrogen bonding with the alcohol functional groups present in the polymer. Differential scanning calorimetry (DSC) showed that the presence of the fillers interfered with the polymer crystallisation processes (Fig.1.27.). Both fillers acted as nucleating agents in EVOH. The fillers had a reinforcing effect and the impact strength of EVOH increased significantly (from 4.9 kJ m⁻² to 9.7 kJ m⁻²) when 10 wt % LDH-stearate was added.

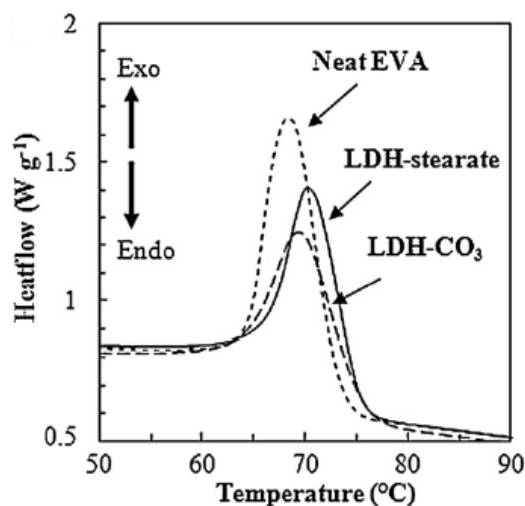


Fig.1.27. DSC cooling traces for EVOH polymer composite systems^[170].

Other EVOH/nanocomposites

Another family of particles, which are used as fillers for EVOH/nanocomposite, is carbon nanotubes (CNTs)^[171, 179]. EVOH/multiwall nanotube (MWNT) nanocomposites were prepared by the incorporation of electron beam irradiated MWNTs in EVA/toluene solution and saponification in an ethanol/KOH, where hydrolysis of EVA took place. Scanning electron microscopy (SEM) indicates that the nanocomposite particles had a highly porous, sponge-like structure of connected matrix polymers and MWNTs^[179]. With the incorporation of 10 wt % pristine MWNTs, it was found that the thermal stability improved significantly and the maximum of degradation temperature shifted from 450 °C to 500 °C. The increase in the degradation temperature of the polymer matrix by addition of CNTs has also been reported^[180].

An effective strategy was reported to fabricate EVOH nanocomposite with well dispersed thermally reduced graphene (TRG) sheets in the polymer matrix via solution mixing method using DMF^[171]. The resulting material EVOH/TRG showed increased mechanical properties (tensile strength and elongation at break and noticeably improved barrier properties (permeability coefficient decreasing from 3.9×10^{-11} down to $8.5 \times 10^{-15} \text{ cm}^3 \text{ cm cm}^{-2} \text{ s}^{-1} \text{ Pa}^{-1}$) (Fig.1.28.).

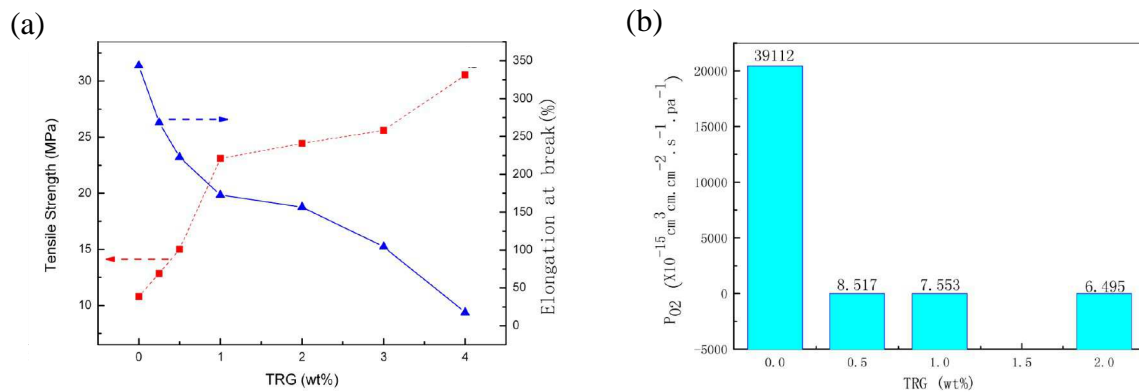


Fig.1.28. (a) Tensile strength and elongation at break versus TRG loadings; (b) Permeability coefficients (P_{O_2}) of O_2 for TRG/EVOH nanocomposite films as a function of TRG loading ^[171].

Summarising studies dealing with development and characterisation of EVOH/nanocomposites, major part of research has been concentrated on clays such as montmorillonite and cloisite. Regarding to the particles dispersion and enhancement of barrier, thermal and mechanical properties, 5 wt % particles loading is considered to be the optimal filler content. Little attention was paid on the nanocomposite stability, in particular to the temperature, and no information about photostability of EVOH nanocomposites was found.

3.4. Photodegradation of nanocomposites

Stability of nanocomposites determines their usefulness and the lifetime of the related end-product. Thus, the study of degradation and stabilisation of polymer nanocomposites should be a compulsory issue for industrial and scientific sectors. Understanding the degradation mechanisms gives an opportunity to predict the stability of potential candidates and to successfully engineer the materials with assigned lifetime. Depending on the use environment, different ingress factors (temperature, chemical and biochemical environment, mechanical stresses, UV-irradiation, and etc.) should be taken into account during durability estimation. This paragraph describes the influence of different nanofillers on photodegradation and photostability of polymer nanocomposites.

3.4.1. Nanocomposites based on nanolayers

Most of the publications dealing with nanocomposite photodegradation are devoted to polyolefin nanocomposites due to their key applications such as packaging in medical and food industry, electronic appliances, automotive and household products. Most of the attention has been focused on polypropylene (PP), polyethylene (PE), ethylene propylene diene monomer (EPDM) and polystyrene (PS).

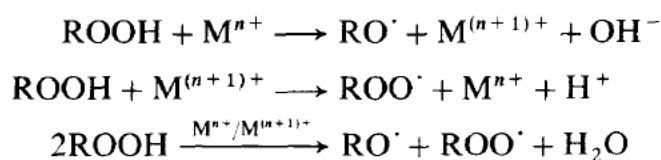
Polymer/MMT

The photooxidation studies of montmorillonite based nanocomposites of PP^[176, 181, 182], PE^[183], and EPDM^[184-186], polyamide-6 (PA-6)^[187], polycarbonate (PC)^[188], epoxy resins^[189, 190] and PVA^[191] showed that incorporation of nanofillers has a pro-degrading effect, what results in faster degradation of nanocomposites in comparison to unfilled polymer. In addition, it was shown that the presence of organo-MMt decreased the efficiency of conventional stabilisers such as phenolic antioxidant or hindered amines.

Several causes for the higher level of photooxidation of nanocomposites were proposed:

- interactions between clays and stabilisers;

The catalytic effect of the metal ion impurities, such as iron, which are present in naturally occurring clays^[181, 192]. This effect is based on decomposition of primary hydroxides formed upon polymer photooxidation (Scheme 1.1.).



Scheme 1.1. Catalytic decomposition of hydroperoxides by metal ions^[193].

- photodegradation of alkylammonium surfactant (the organic part of the organo-MMt)^[181, 192].
- thermal degradation products of alkylammonium^[194, 195].

To overcome the prodegradant effect of clays, additives such as anti-UV^[185], a metal deactivator^[183, 196] and phenolic antioxidant^[186] addition has been studied.

In order to stabilise EPDM/MMt nanocomposite, an UV absorber (Tinuvin P) and an antioxidant (2-mercaptobenzimidazole) have been used^[185]. It was shown that the addition of either Tinuvin P or 2-mercaptobenzimidazole inhibits prodegradant effect of MMt. This effect

might result from the combination of ZnO and 2-mercaptobenzimidazole, where 2-mercaptobenzimidazole acts as a peroxide decomposer as well as antioxidant by donating hydrogen. ZnO acts as a vulcanisation accelerator and may also form a complex with mercaptobenzimidazole [Zn-coordinate complex], which acts as an antioxidant and a peroxide decomposer.

The introduction of metal deactivator into PE/MMt displayed good success for the stabilisation strategy [183, 196]. Fig.1.29. shows that metal deactivator totally cancelled the pro-degrading effect in comparison to UV stabilisers. The use of metal deactivator highlighted the significance of impurities such as metals and brings a new knowledge to the development of efficient stabilisation approaches.

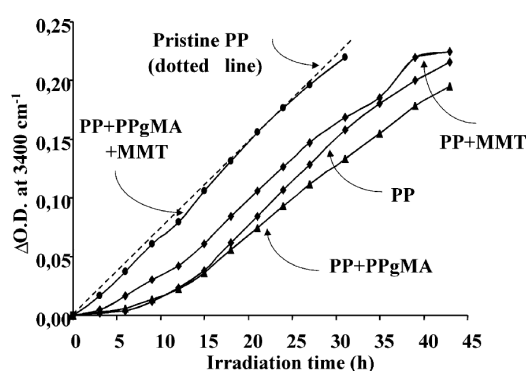


Fig.1.29. Increase of hydroxyl group absorbance as a function of irradiation time [176].

Lonkar *et al.* [186] showed more efficient stabilising effect of phenolic antioxidant for EPDM/MMt nanocomposite prepared via extrusion by the introduction of antioxidant into the polymer before mixing with the particles. It might be explained by avoiding adsorption of antioxidant along with clay during processing. In this way, interactions with metallic impurities present in clay powder and antioxidant were reduced, hence, antioxidant stabilising efficiency was enhanced.

Polymer/LDH

Very few papers have reported on the photooxidative behavior of nanocomposites with synthetic LDHs [197-199] or hydrotalcite [200]. The photooxidative behaviour of the PP/LDH nanocomposites showed that the presence of LDH can modify the chemical structure of the photoproducts accumulating in the matrix [200]. The rates of oxidation were influenced by the nanofiller, depending on the divalent cations of the LDH layers. LDH phases containing Mg^{2+}

have a prodegradant effect on the polymer, whereas LDH based on Zn^{2+} divalent cations has no influence on the rate of oxidation of the polymer ^[198]. LDHs containing Mn or Co as divalent cations were reported to have a prodegradant effect on PE oxidation, even in very low amount ^[201].

3.4.2. Nanocomposites based on nanotubes

A lot of attention has been focused on processing CNTs nanocomposites of polymers (polyolefins, polyacrylates, polyenes, polyamides, polyurethanes, etc.) due to enhanced flame retardancy and the improvement of mechanical and electrical properties. The influence of the nanotubes on both the photooxidation mechanism and the rates of oxidation of the matrix was characterised for EVA/CNT nanocomposites ^[202]. On one hand, it was shown that the carbon nanotubes act as inner filters and antioxidants, which contribute to the reduction of the photooxidation rate of the polymeric matrix. On the other hand, it was observed that light absorption could provoke an increase of the local temperature and then induce the photooxidation of the polymer. The competition between these effects determines the global rate of photooxidation of the polymeric matrix. The stabilising effect of CNTs was also present for PP in condition of photo- and thermal oxidation ^[203]. Besides antioxidant nature of CNTs, it was concluded that these particles might absorb oxygen molecules. Such a mechanism could be responsible for abstracting oxygen molecules from the polymer chains and leads to a decrease of the rate of photooxidative reactions inside the amorphous phase in the first stages of photooxidative process.

Enhanced photostability was displayed for bisphenol A epoxy resin ^[204] and PMMA ^[205]. In the case of PMMA ^[205], an efficient light scattering by particles was proposed to be one of the explanation of increased durability.

3.4.3. Nanocomposites based on nanoparticles

Various nanoparticles such as silica ^[182], carbon black (CB) ^[206], metals (Cu ^[207]), metal oxides (ZnO ^[182], titanium dioxide (TiO₂) ^[208, 209]), calcium carbonate CaCO₃ ^[210, 211]) and etc. have been used as fillers for polymers in order to reinforce targeted functional properties for assigned applications. All nanoparticle fillers can be divided into two groups: photochemically inert and photocatalytic nanoparticles ^[119].

Photochemically inert nanoparticles

Calcium carbonate (CaCO_3) and silica (SiO_2) are considered to be photochemically inert. The introduction of CaCO_3 into HDPE was reported to result in changes of polymer photodegradation mechanism^[210]. Contradictory explanations of particles effect were based on an acceleration of chain scission reactions and on a protective barrier effect for UV light penetration in HDPE. Moreover, addition of nano CaCO_3 leads even to more fast photodegradation of PP in comparison to micro sized particles^[211]. This effect was explained by the presence of Si, Mg and Al impurities as well as the formation of defects at the interface between matrix and filler particles.

Li et al.^[212] reported that CaCO_3 and SiO_2 increase the degree of chain scissions in PP under natural degradation. The influence of the nanosized SiO_2 particles on PP photooxidation^[213] has been related to O_2 permeability or the spherulites size of the nanocomposites, the smaller spherulites leading to higher stability of the nanocomposites. Nevertheless, another work showed contradictory results where SiO_2 accelerates HDPE photooxidation^[214].

It brings to the conclusion that the influence of “photochemically inert nanoparticles” on photooxidation of polymer nanocomposites is not fully understood.

Photocatalytic nanoparticles

ZnO and TiO_2 are well known broad band-gap semi-conducting oxides exhibiting a photocatalytic activity. It has been demonstrated that the photocatalytic effect of semiconductors such as ZnO, mainly results in the formation of radicals that are able to degrade the polymer matrix^[215]. The photocatalytic effect of ZnO and TiO_2 is however counterbalanced by the UV inner filter played by these fillers, which absorb in the UV range.

At the same time, the stabilisation effect of ZnO nanoparticles on the photooxidation of LLDPE was found to be better than that of Al_2O_3 or SiO_2 nanoparticles^[216].

The photostability of PMMA/ TiO_2 nanocomposite films with different kinds of TiO_2 nanoparticles was studied under accelerated artificial ageing^[217]. The photocatalytic oxidation of the polymer by TiO_2 provokes the formation of cavities and free volume (voids) between polymer chains and the nanofiller.

The photochemical behaviour of PLA/ TiO_2 and PLA/ZnO nanocomposites has been studied^[218-220]. Two opposite effects of UV-screening and photocatalysis of these two nanofillers showed that, the influence of these metal oxides on polymer lifetime cannot be

confidently predicted. Photodegradation of PLA/TiO₂ nanocomposite films showed a decrease of photostability [218].

Carbon black

Carbon black (CB) was reported to have a stabilising effect on epoxy resin [206], PE [221] and PP [222]. CB can act as an UV absorber, a free radical scavenger, and as a filler of micropores and microcracks of the polymer matrix maintaining the barrier properties of the coatings during degradation [206]. Schematic influence of CB on epoxy resin coatings showed in Fig.1.30. The physical nature of carbon black mainly accounts for its UV stabilising activity due to its UV absorption ability that decreases the UV dose received by the polymer. In addition, the termination reactions of free radicals generated during photooxidation may also contribute to the UV stability brought by carbon black. This phenomenon retards the degradation of the coatings. Besides, CB nanoparticles act as obstacles for propagation of microcracks. It was also approved that CB nanoparticles can fill micropores in the coating and limit penetration of water into the coating [206].

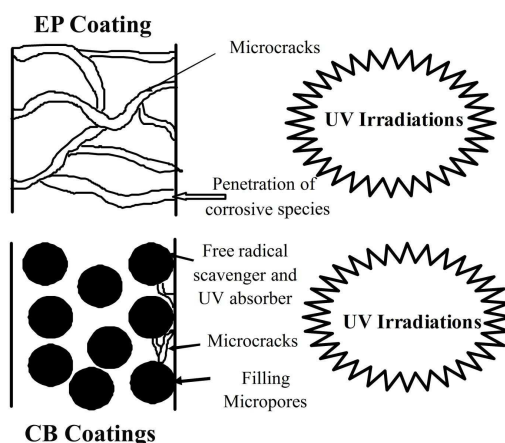


Fig.1.30. Schematic illustration of the CB nanoparticles mechanism for preventing UV degradation of coatings [206].

Conclusions

The influence of nanofillers on polymer photodegradation depends on various factors. Montmorillonite provokes a faster photooxidation of the polymeric matrix whereas the effect of LDH or carbon nanotubes can be tuned. Stabilisation effect can be obtained by adding a metal deactivator to nanocomposites with naturally occurring clays (montmorillonite), or by

using suitable divalent cations into LDH nanocomposites. In the case of CNTs, photostabilisation can be achieved by adding suitable type and amount of nanotubes. The competition between the two antagonistic effects of ZnO and TiO₂ leads either to stabilising or prodegradant effects, with heterogeneous degradation resulting from oxidation profiles.

As a conclusion, one can say that there are no general rules for stabilisation of polymer nanocomposites. The resulting effect strongly depends on the studied system: nanofiller, polymer, and additives.

3.5. Polymer/zeolite nanocomposites

Researchers have widely investigated zeolite thin films within the last 15 years, most of these studies were motivated by the potential application of these materials as separation membranes and membrane reactors.

Nowadays, zeolite based nanocomposites are used in sensors, cathodes of the cells, anticorrosive, selective membranes, gas separation^[223], fuel cell applications^[224], catalysts, and selective removal of heavy metal ions^[225] and other pollutants^[226] from sea water and industrial waste water.

Several aspects are responsible for the unique properties of zeolite nanocomposites and their industrial success^[227]: (i) very high and adjustable adsorption capacity, (ii) catalytic sites of different strengths can be generated in the frameworks, (iii) the size of their channels and cavities is in the range of many molecules of interest, and (iv) excellent ion exchange capacities.

Nevertheless, up to now the application of zeolite-based nanocomposites does not cover the packaging and coating sectors.

Unlike traditional fillers, conditions of zeolite synthesis can be well-matched, and this provides a broad range of potential properties (antibacterial properties, selective gases/liquids adsorption and catalytic properties) and the ability to tailor the functions of composite materials.

Taking into account the high sorption capacity of zeolites, these fillers were proposed as desiccants for electronics in order to protect moisture sensitive devices (like OLEDs)^[228]. Since 1990, zeolite-resin composite based desiccants have appeared in electronics^[229-231]. Traditionally, a relatively high quantity of desiccant has been used in the non-transparent bottom side of electronic devices. However, the transparency or the flexibility of the desiccant

(usually up to 40 wt %) was never an issue until the development of top emitting OLEDs, and further, semitransparent OPVs. To solve this problem and keep good moisture getter properties, *Wu et al.* ^[232] processed transparent composite moisture getter layer to encapsulate top emitting OLEDs. Acrylic resin with 10 wt % of Beta zeolite nanoparticles was tested as a moisture getter encapsulation film deposited on the top of OLED module. Nanocomposites exhibited WVTR less than $10^{-3} \text{ g m}^{-2} \text{ day}^{-1}$ and water absorption capacity of 3.6 g m^{-2} (highly dependent of the conditions of previous zeolite activation). The resulted material does not achieve requirements for OLED encapsulation, but such a film could match the demands of less sensitive OPV ^[66].

Beta zeolite nanocrystals were also tested in another material as native starch. They addition resulted in changed tensile and water barrier properties of the film ^[233]. Water vapour permeability of films was shown to be slightly decreased (by 6-20 %). At the same time, Beta zeolite based nanocomposites exhibited decreased tensile strength and increased elongation at break. The results showed that zeolite dispersion is a critical point for obtaining reinforcement effect.

Zeolite based nanocomposites has a great potential application in the development of transparent and flexible encapsulations, in terms of reinforcement effect and of great sorption capacity.

CONCLUSIONS

The review of the current literature dedicated to OSCs degradation and encapsulation, and the role of nanocomposites, highlights the following key findings:

- The degradation of OSCs is mainly caused by the combined action of light, oxygen, water and temperature. Degradation involves every part of the cell, as well inorganic (electrodes) and organic components (PAL, PEDOT: PSS), as interfaces. Ageing processes lead to a loss in cell efficiency due to a worsen light absorption, a drop in charge carrier transport, morphology changes and delamination. A good barrier encapsulation is a solution to protect the cell from external ingress of oxygen and water, which would allow for an increase the device lifetime.
- Different strategies and approaches to reach strong barrier properties for efficient encapsulation have been proposed. The most common systems currently used are based on alternating multilayer stack, which can achieve the permeation level required for OSCs. However, the drawbacks of high-cost deposition methods and limitation in large-scale fabrication hinder OSCs competitiveness in the market.
- Summarising the research done in the OPV encapsulation, one can say that it is mostly focussed on the operation performance of the cell, but it neglects the issue of encapsulation stability, which is however essentialal to obtain stable device over lifetime.
- Introduction of the nanofillers into a polymer matrix can enhance different material properties, in particular, barrier to oxygen and/or water. The introduction of such nanocomposite into multilayer encapsulation may increase the efficiency of barrier properties, and hence, increases OSC lifetime. Nevertheless, depending on the studied materials, the presence of nanofiller can increase or reduce the photochemical stability of nanocomposites, highlighting the need to study the photostability of each new nanocomposite material.
- Zeolites are shown to be potential materials to be used as nanofillers for polymers in order to improve desiccant properties of the polymer layer and decrease the ingress of moisture into OSCs by an efficient trapping of water molecules. Nevertheless, to the best of our knowledge, no studies of zeolite polymer photostability have been done so far.

On the basis of the knowledge from literature data, we have chosen to elaborate and characterise new polymer nanocomposites based on EVOH copolymers as an organic matrix and on zeolites nanofiller as fillers for their water getter properties. Considering the various issues described above, we will focus on the properties of the nanocomposites, optical properties for transparency of the encapsulation coating, mechanical properties for the flexibility of the OSC, water barrier properties for the protection of the OSC against water ingress. We also take into account what we consider as major issue, which the durability of these properties under the stresses of the device environment.

CHAPTER II:

EXPERIMENTAL METHODS

INTRODUCTION

This chapter concerns the experimental part of the manuscript. The materials and processing methods are described, the setup and accelerated ageing conditions are given, and the methods and characterisation techniques for polymer and polymer nanocomposites are represented.

1. MATERIALS AND SAMPLE PREPARATION

1.1. Materials

Polymer

Commercial ethylene vinyl alcohol copolymers with 27 and 44 mole percentages of ethylene in the copolymer composition (named EVOH 27 and EVOH 44 respectively) were supplied by Scientific Polymer Products, Inc. Polymer specifications are described in the following table:

Table 2.1. EVOH copolymer characteristics (provided by supplier)

	Density	T _m	T _g
EVOH27	1.20	191	72
EVOH44	1.14	165	55

Solvents

Dimethylsulfoxide (DMSO) of 99.9 % purity was purchased from Sigma Aldrich Ltd (St. Louis, MO) and used without further purification. 2-propanol, *o*-xylene (98% grade) supplied, respectively, by Alfa Aesar and BHD from VWR International, were used for preparation of zinc oxide (ZnO) and active layer solutions.

Organic solar cells (OSCs)

Poly(3-hexylthiophene-2,5-diyl) (P3HT) and [6,6]-phenyl-C61-butyric acid methyl ester (PC60BM) were supplied by Merck Chemicals and Solen Inc. respectively, and were used as active layer in organic solar cells.

Poly(3,4-ethylenedioxythiophene)-poly(styrenesulfonate) (PEDOT:PSS) from Heraeus Precious Metals GmbH & Co. KG was used as hole transport layer in OSCs fabrication.

Metallic calcium from pellets of ≥ 99.5 % purity from Carl Roth GmbH & Co. were used for calcium corrosion test.

Silver from pellets supplied by Kurt. J. Lesker were used for electrodes vacuum evaporation.

Two adhesive bonds have been used in this work. The first, an UV-curing based on modified epoxy resin glue LP655 from DELO Industrial Adhesives, selected as an adhesive bond, has a WVTR of $6.1 \text{ g m}^{-2}\text{day}^{-1}$ at $60 \text{ }^\circ\text{C}/90 \text{ \% RH}$ for the layer thickness of 1 mm. The

second, Dymax 3030 acrylic UV-curable adhesive from Dymax Edge with a water absorption of 1.6 % (25 °C / 24 h).

Ultra-barrier solar film from 3M (WVTR of 5×10^{-4} g m⁻²day⁻¹ at 23 °C / 85 % RH) was used as a flexible substrate for calcium sensors.

Zeolites

Synthetic zeolites were supplied by Clariant Produkte GmbH with the trade names Lucidot NZL 40 LP3533 and Lucidot DISC, abbreviated NZL and DISC respectively. Particle specifications provided by supplier are reported in Table 2.2.

Table 2.2. Specification of the zeolite particles (provided by supplier)

Specification	NZL	DISC
Size of primary particles	15-60 nm	0.5-2 μm
X-ray diffractometry (XRD)	LTL standard, additional characteristic properties of nanoscale particles	LTL standard
Water content, wt%	10-13	7-8
Specific surface area (BET) of the hydrated material, m ² /g	150-170	50-55

Both zeolites are related to L-type particles, LTL standard (Fig.2.1.), with shapes of tube (NZL) or disc (DISC).

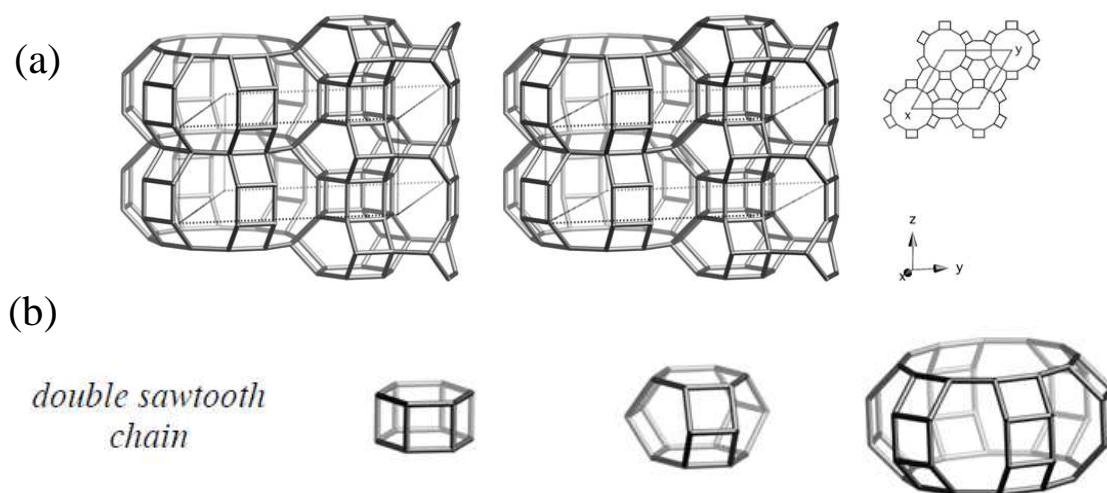


Fig.2.1. (a) LTL framework type viewed normal (upper right: projection down); (b) Composite building units ^[234].

1.2. Sample preparation

Processing of polymer/nanocomposite films

Nanocomposites were processed by two different methods: solution mixing (method A) or melt-mixing using a twin-screw extruder (method B).

Method A. The polymer was dissolved in DMSO at 190 g/l. At the same time, a solution of zeolite particles with concentration of 95 g/l was placed in an ultrasonic bath for 30 min and then treated by an ultrasonic processor (a Vibra-Cell VCX 130 PB) for 5 min at a frequency of 20 KHz and amplitude 75 %, immediately preceding the mixing with polymer solution. After sonication, aliquots of zeolite suspension were added to achieve nanocomposites with 5-30 wt % of particles to the fixed volume of EVOH solution. The nanocomposite solutions were sonicated for 5 min using the ultrasonic processor with the same conditions as for the zeolite suspension.

Films of pristine EVOH and EVOH/zeolite nanocomposites were obtained with an Erichsen Coatmaster 809 MC film applicator by depositing the solutions onto glass sheets and their drying at 40 °C overnight. After solvent evaporation, films with thickness between 15 and 40 μm were obtained and then placed in an oven at 60 °C under vacuum for one week to remove solvent trace. Any residual presence of the solvent was verified by IR spectroscopy with the IR characteristic bands of DMSO at 950 cm^{-1} and 1020 cm^{-1} . A descriptive scheme of the deposition process is shown in the following Fig.2.2.:

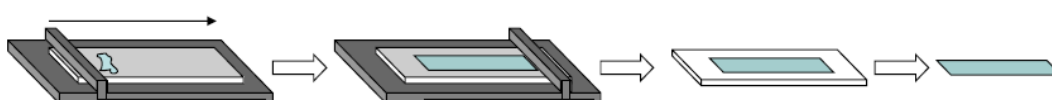


Fig.2.2. Principe of film processing using a bar coat.

Method B. A melt-mixing intercalation process was also used for nanocomposite preparation. Polymer and zeolite powders were melt-mixed in a twin-screw extruder (Thermo MiniLab Haake Rheomex CTW5, Germany) for 15 min at 210 °C and a screw speed of 40 rpm. Films were then obtained from solid polymer/zeolite nanocomposite pellets using a hydraulic press with 2 heated plates at a working temperature of 200 °C and the pressure 200 bar for 1.5 min. Films with thickness between 70 and 120 μm were obtained.

Fabrication of solar cells

Devices with the inverted architecture (see Ch.I Fig.1.4.) based on sequential superposition of ITO/ZnO/P3HT:PCBM/PEDOT:PSS/Ag on glass/flexible PET substrate, as it is shown in Fig.2.3., were fabricated by the following procedure. First, ITO coated substrates were cleaned by consequent sonication in acetone (5 min) and isopropanol (15 min). ZnO-ethanol suspension with 2.5 wt % of nanoparticles was deposited directly onto ITO by doctor blade at 65 °C and then, thermally annealed at 140 °C for 10 min in air. The P3HT:PCBM (1:0.8 by weight) solution in *o*-xylene with 5 wt % of 1-meta naphthalene additive was stirred 1 hour at 80 °C and deposited by doctor blade. The initial absorbance of the active layer at 510 nm was in a range of $1 \pm 0,1$ a.u. Then, PEDOT:PSS, diluted in isopropanol at 80 °C, was deposited on the top of the active layer. Devices were completed with the thermal evaporation of 150 nm of silver to form the top electrode, carried out in Univex 350G vacuum chamber from Leybold Vacuum GmbH. The active areas of obtained solar cells were about 27 mm². Current voltage measurements were performed using a Keithley 2400 source meter and a Xenon lamp with an intensity of approximately 100 nWcm⁻². Prior to testing, devices were annealed at 120 °C for 5 min. The devices were encapsulated by mono-, bi- or three-layer encapsulation foils consisted of EVOH polymer or nanocomposite layer with the thickness about 80-100 μm and/or 125 μm thick PET using epoxy- or acrylic-based adhesive glue. Thus, different combinations of encapsulation layers were used: EVOH monolayer, EVOH/PET bi-layer, and PET/EVOH/PET three-layer. All PET and EVOH layers were corona treated and then joined with the cell using adhesive glue, laminated and placed into an UVACure 100 curing chamber (Tangent Industries, Inc) for 20 min. P3HT:PC60BM based flexible devices were encapsulated in the glove box.

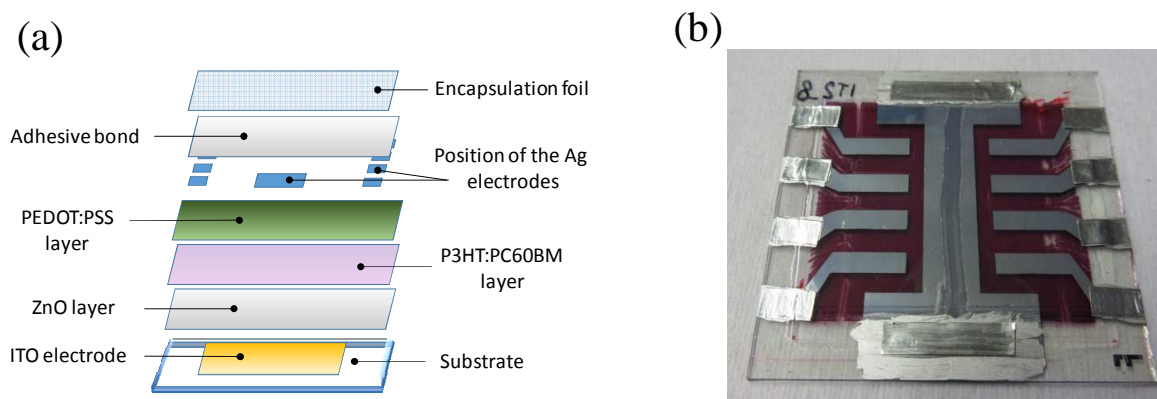


Fig.2.3. (a) Layers structure of the inverted P3HT:PCBM solar cell; (b) A photo of a studied device.

Fabrication of calcium sensors

Calcium sensors were fabricated to study orthogonal and lateral water diffusion through EVOH and EVOH nanocomposite films.

Sensors to study orthogonal diffusion. The permeation sensors were prepared as following: $3 \times 3 \text{ cm}^2$ square of 500 nm thick layer of calcium was deposited onto $5 \times 5 \text{ cm}^2$ glass/PET substrate by evaporation technique described above. Next, 250 nm thick silver contact pads were deposited to contact calcium with test board to measure the conductivity changes. The fabricated calcium sensor is shown in Fig.2.4.

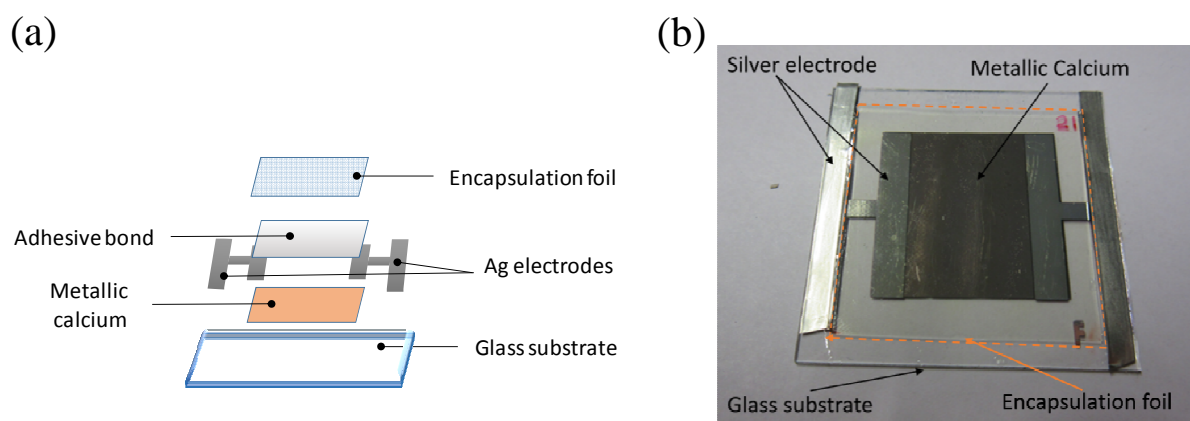


Fig.2.4. (a) Layers structure of calcium sensor to study orthogonal water diffusion; (b) A photo of calcium permeation sensor encapsulated by polymer foil.

Finally, the sensors were encapsulated with the materials of interest (neat EVOH or the nanocomposites) with the area of $4 \times 4 \text{ cm}^2$ fully covering the area of calcium film. The sensors were encapsulated by EVOH and its composite films using the epoxy glue and then, cured during 10 min in the UV chamber.

Sensors to study lateral diffusion. To study lateral water diffusion through the materials, a glass plate ($3,5 \times 3,5 \text{ cm}^2$) was deposited on a top of calcium sensor already sealed with EVOH based film ($3,5 \times 3,5 \text{ cm}^2$) (Fig.2.5.). The sealing was performed using the same epoxy-based adhesive. As a reference, a sensor with the same structure but without polymer encapsulation layer was used. As a substrate, a glass plate was used in this experiment.

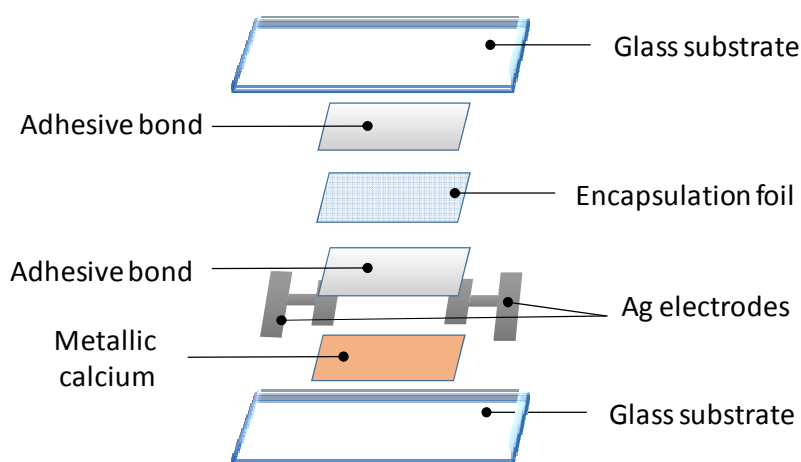


Fig.2.5. Layers structure of calcium sensor to study lateral water diffusion.

All processing steps, including the encapsulation, were performed in a glovebox system.

2. ACCELERATED AGEING

2.1. Accelerated photoageing

Samples were submitted to UV-Visible irradiation ($\lambda > 300$ nm) in a SEPAP 12/24 unit from Atlas^[235] at 60 °C in the presence (photooxidation) or absence (photolysis) of oxygen. This apparatus is equipped by four medium-pressure mercury lamps (a Novalamp RVC 400W) disposed vertically at each corner of a square chamber. Wavelengths below 300 nm are filtered by the borosilicate glass envelope of the lamps. The emission spectrum of the lamps is represented in Fig.2.6. The carousel has a capacity of 24 samples, placed at a 20 cm distance from the lamps axis, turning 4 times per minute. The chamber temperature is maintained at 60 °C during all experiments; this is controlled by a platinum probe in contact with a polyethylene film placed on the carousel.

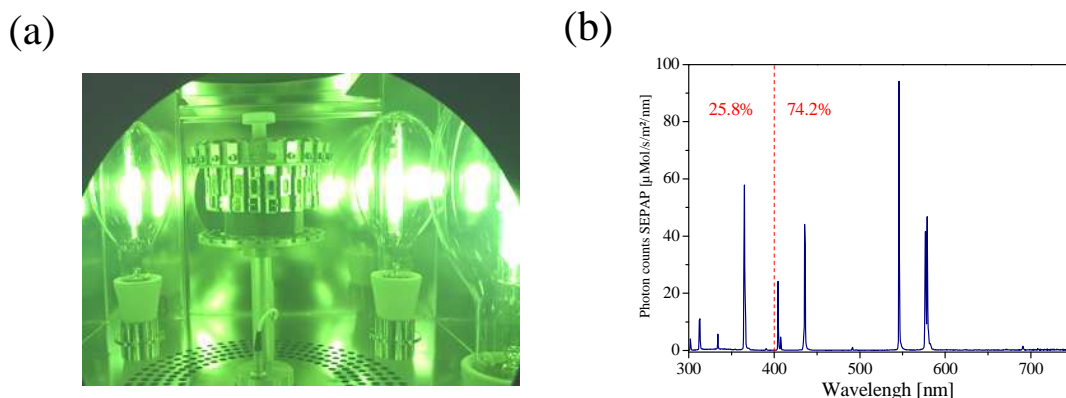


Fig.2.6. (a) The irradiation chamber of SEPAP 12/24 and (b) emission spectrum of Novalamp RVC 400W lamps measured by radiometer.

Two types of photoaging experiments were performed:

- photooxidation experiment, where samples were irradiated in ambient air conditions, and therefore in presence of oxygen;
- photolysis, where samples were irradiated in the absence of oxygen, film sample was introduced inside a tube made of borosilicate glass, where first, a primary vacuum ($P \approx 1$ Pa) was applied, and then followed by a secondary vacuum ($P < 10^{-4}$ Pa). The tube was then sealed and exposed to irradiation in the pertinent device.

2.2. Damp heat experiment

A damp heat test is the most common and crucial test for PV module qualification testing. The high temperature accelerates the degradation of polymeric and metallic compounds, inducing discoloration, delamination or corrosion, and especially the water vapour permeation into the module with the subsequent degradation reactions^[236].

In this work, the thermal degradation in controlled humid atmosphere was applied to the complete solar cells and calcium sensors encapsulated by pristine EVOH or the nanocomposites. The experiments were carried out in a Horstman climatic cabinet (HS 200 K 46 L) in the presence of air in the dark. For the complete photovoltaic device approval the conditions were fixed at 65 °C and 85 RH %.

3. CHARACTERISATION TECHNIQUES

3.1. Spectroscopy

UV-Visible absorption spectra were monitored between 200 and 800 nm using a Shimadzu UV-2600 spectrophotometer with an integration sphere for analysing the total light transmission (direct + diffuse).

Infrared spectra were recorded with a Nicolet 760 (Thermo Scientific) spectrophotometer working in a transmission mode and purged with dry air. The spectra were recorded with 32 acquisitions and 4 cm^{-1} resolution. Prior IR analysis, the samples were dried during 3 h in an oven at $60\text{ }^{\circ}\text{C}$ under vacuum.

Spectra treatment. The photooxidation kinetics of the polymer and the nanocomposites were followed by IR spectroscopy in the carbonyl domain (1730 cm^{-1}) and the region of C-H vibration (2852 cm^{-1}) by plotting the absorbance variation from initial spectrum ($A^t - A^{t_0}$) at 1730 cm^{-1} and 2852 cm^{-1} as a function of irradiation time. The absorption band at 1460 cm^{-1} is a characteristic band of the polymer, which was used to compare the same polymer amount. All spectra at $t=0\text{ h}$ were normalised for the same absorbance at 1460 cm^{-1} , and normalisation coefficients were applied to corresponding spectra during photooxidation. The values were taken as an average of three samples irradiated in parallel. It is worth noting that this allows for comparison of the degradation rates of the polymer with and without nanoparticles and does not correspond to the degradation of the nanocomposite material.

3.2. Chemical derivatisation treatments

Chemical derivatisation treatment is based on a treatment of aged sample with reagents capable to selectively react with degradation products. These reactions lead to the formation of new products with IR characteristic bands that are different from the initial ones^[237]. In these studies, 2,4-dinitrophenylhydrazine (2,4-DNPH), and ammonia (NH_3) have been used as reagents. In order to distinguish the reaction related to photoproducts to those of initial polymer chemical composition, samples of “non aged” films were used as references.

3.2.1. NH_3 treatment

NH_3 reacts with carboxylic acids to form ammonia salts, and with esters and anhydrides to form amides^[237] (Fig.2.7.-Fig.2.8.):

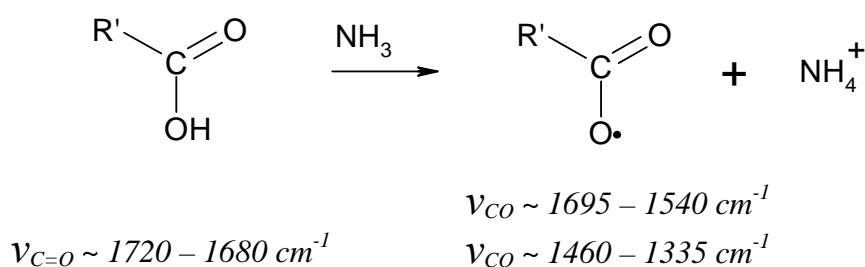


Fig.2.7. Reaction of carboxylic acids with ammonia forming carboxylate ions.

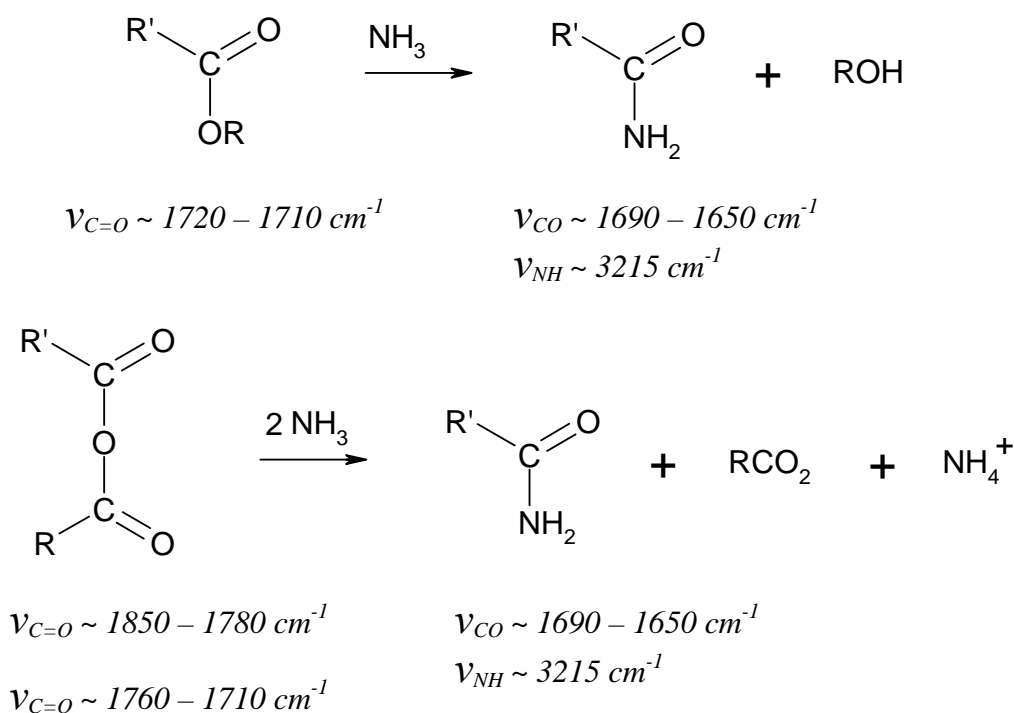


Fig.2.8. Reaction of esters and anhydrides with ammonia forming primary amides.

Experiment was performed on reference and aged polymer films placed in a teflon reactor. First, the reactor was purged with argon during 5 min to avoid side reaction of the samples with atmospheric environment. Then, NH_3 flow was injected into the reactor, firstly at high speed during 1 min, and then, at small for 30 min. After treatment, the reactor was again purged with a flow of argon for 5 min. The treated samples were analysed by IR before and immediately after the treatment.

3.2.2. 2,4-DNPH treatment

2,4-DNPH is known to react with aldehyde and ketone forming corresponding derivatives of 2,4-dinitrophenylhydrazone. This method is based on the following reaction (Fig.2.9):

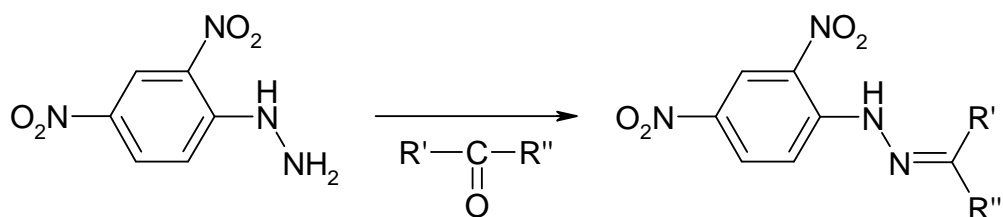


Fig.2.9. Reaction of aldehyde/ ketone with 2,4-DNPH.

Formed derivatives have two absorption bands in IR spectra: 1618 cm^{-1} (stretching vibration of C=N hydrazones ^[62]) and 1592 cm^{-1} (stretching vibration of C=C aromatic ring ^[238]). These products have also a strong UV absorption with a maximum at 365 nm.

Treatment with 2,4-DNPH was performed in a liquid phase (methanol) what implies a possible migration of low-molecular-weight products present in the oxidised polymer into the solvent. Therefore, low-molecular-weight products were removed by first soaking the aged sample. An aged sample and a virgin sample (as reference) were placed for 18 h in methanol in order to extract low-molecular-weight products, prior to be analysed by UV-Visible and IR spectroscopies (after drying in an oven). Then, the samples were placed in a saturated solution of 2,4-DNPH in methanol for 2 hours. The samples were then washed with methanol, dried in oven and then, re-analysed by UV-Visible and IR spectroscopies.

3.3. Chromatographic analysis

3.3.1. Solid phase micro extraction gas chromatography coupled with mass spectrometry detection

This technique, abbreviated SPME-GC-MS, was used to collect and to analyse the volatile compounds formed upon polymer oxidation. The basic principle of Solid Phase Micro Extraction (SPME) is the adsorption of chemical compounds in a polymeric phase supported on a silicon fibre. In this case, the analytes are adsorbed in the fibre from the gas phase over, meaning that it is employed a Head Space (HS) configuration. Once concentrated in the fibre, the chemical compounds are thermally desorbed in the Gas Chromatograph (GC) injector. Then, the mixture is transported through the column by a carrier gas, where the different molecules of the mixture are separated on the basis of their affinity for the stationary phase

and the oven temperature. At the column exit, molecules are analysed by a Mass Spectrometer (MS) detector.

Experimental conditions

The particular procedure applied to make this analysis is described below. A polymer film was introduced into a 20 ml flask sealed with a silicon septum, and then submitted to the ageing (photooxidation in the SEPAP 12/24). Prior to chromatographic determination, the flask was kept for 1 hour at 60 °C to ensure a good desorption of the photoproducts coming from the film matrix. Then, the fibre was introduced into the flask and kept there for 2 min to adsorb the volatile compounds. The fibre was then transferred manually to the chromatographic injector where the analyte molecules were desorbed at 280 °C during 2 seconds interval prior to the GC-MS analysis. The described steps are represented in Fig.2.10.

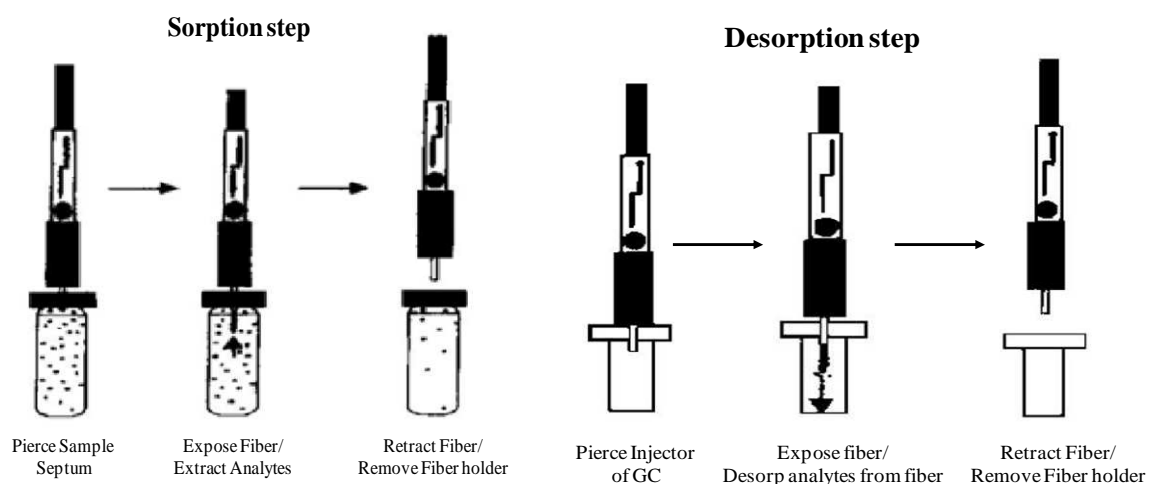


Fig.2.10. Description of adsorption-desorption procedures used in SPME.

The used SPME fibre is a 75 mm fibre made of carboxen-polydimethylsiloxane provided by Supelco (Bellefonte, PA, USA), and it was conditioned at 280 °C prior to every use. GC-MS equipment consists of a gas phase chromatograph Network System 6890N, from Agilent Technologies, coupled with a mass spectrometer Network Mass Selective Detector MSD 5973. The fused silica capillary column has a Carbowax 20 M (Supelco, Belle Fonte, PA, USA) stationary phase and dimensions of 30 m×0.25 mm. A carrier gas was helium with a constant pressure of 38 kPa and 50 ml/min flow. The column temperature was kept at 60 °C during the first 5 min, and then, increased up to 200 °C at a rate of 10 °C/min, and the final temperature was maintained for 15 min. The temperature of the transfer line was kept at

280 °C, and the ions source temperature was fixed at 230 °C. The ionisation was produced by electronic impact with 70 eV energy. The mass spectra as well as the reconstructed chromatograms were obtained by a mass scanning in the interval m/z 20-400.

3.3.2. Ionic chromatography

Ionic Chromatography (IC) was carried out at Service Central d'Analyse of the CNRS at Vernaison in order to detect molecular carboxylic acids formed and trapped in a polymer matrix during polymer ageing^[239]. EVOH films (100 mg), photooxidised during 1000 hours in SEPAP 12/24 were soaked for 24 hours in 11 ml of ultrapure water in order to extract the low-molecular-weight compounds soluble in water.

IC run conditions were next:

- Guard column: Dionex AG11 HC (50 mm×4 mm);
- Analytical column: Dionex AS11 HC (250 mm×4 mm);
- Eluent: gradient of NaOH from 0.5 mmol/l to 25 mmol/l;
- Flow rate: 1.5 ml/min;
- Injection volume: 100 µl;
- Detection: a conductivity detector Dionex ED 40;
- Column temperature: 30 °C;
- Suppressor: Dionex ASRS 300-4 mm;

The machine consists of a pump Dionex GP 50, an automatic injector Dionex AS 50, and a conductimeter ED 40 controlled by the acquisition software.

Calibration. The stock solutions of organic acids were prepared in the ultrapure water with concentration 1000 mg/l. From these solutions, five daughter solutions were prepared, and then injected in the IC upon analytical conditions described above.

3.4. Microscopic analysis

3.4.1. Transmission electron microscopy

Transmission Electron Microscopy (TEM) images were obtained with a Hitachi H7650 microscope equipped by a TN camera Hamamatsu with working voltage 80 kV. The observations were carried out at Centre Imagerie Cellulaire Santé, University of Auvergne.

The analysis of zeolite particles was carried out on a DMSO-zeolite suspensions (previously treated by the ultrasonic processor in conditions used for nanocomposite process) and were placed over a grid substrate with an ultrathin membrane.

TEM imaging of solid films was carried out on polymer or nanocomposite films included in an epoxy resin. The samples were then cut using a microtome in the direction perpendicular to the film surface to obtain film cross-sections that were deposited over a copper mesh.

3.4.2. Scanning electron microscopy

Scanning Electron Microscopy (SEM) images were recorded by a LEO 1550 scanning electron microscope with the energy of electron beam of 5 keV using an in-lens detector. Prior observation, films of polymer and nanocomposites were coated with a carbon layer. SEM experiment was performed at International Laser Centre in Bratislava.

3.4.3. Atomic force microscopy

Theory. The working principle of Atomic Force Microscopy (AFM) based on the measurement of interaction force between the probe tip and the sample surface. The probes consist of an elastic cantilever with a sharp tip on the end. The force applied to the tip by the surface, results in bending of the cantilever. Where the tip–surface interactive force can be evaluated by the measurement of a cantilever deflection. A basic set-up of an AFM is described in the following figure:

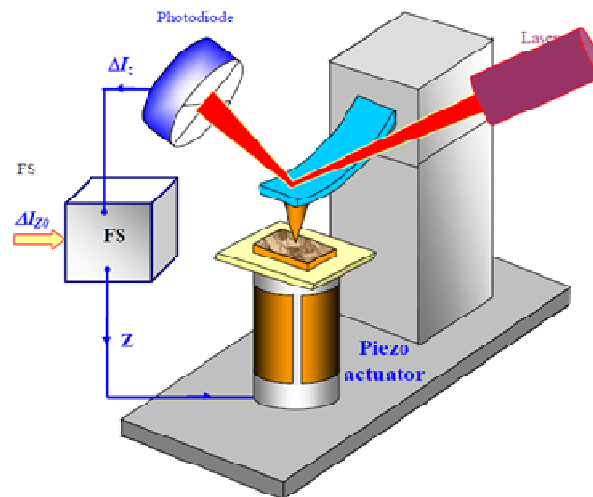


Fig.2.11. AFM setup with four-segment photodiode for detection of the laser beam deflection due to the bending and twisting of the cantilever ^[240].

AFM operation can be performed in one of three different mode types, according to the nature of the tip motion:

- **contact mode**, also called static mode. The tip is attached to the end of a cantilever with a low spring constant lower than the effective spring constant of the force holding the

atoms of most solids together. As the scanner gently traces the tip across the sample (or the sample under the tip), the contact force causes the cantilever to bend to accommodate changes in topography;

- ***semi-contact or tapping mode***. This mode maps topography by lightly tapping the surface with an oscillating probe tip. The cantilever's oscillation amplitude changes with sample surface topography. The topography image is obtained by monitoring these changes and closing the Z feedback loop to minimise them. Tapping mode is adapted to the analysis of soft samples such as polymers and thin films;

- ***non-contact mode***, there is no direct contact between the surface and the tip. The control system vibrates a stiff cantilever near its resonant frequency (typically 100–400 kHz) with amplitude of a few tens to hundreds of Angstroms. The topography is analysed only through interactions distances between the tip and the sample type of attraction-repulsion, which results in the change of resonance frequency. Non-contact mode is another useful mode for imaging soft surfaces, but its sensitivity to external vibrations and the inherent water layer on samples in ambient conditions often causes problems in the engagement and retraction of the tip.

One of the imaging modes used in this work is ***PeakForce Tapping***TM. This imaging technique is operated with the cantilever oscillated well below resonance. This results in a continuous series of force-distance curves. By the force control to keep the peak force constant, a multitude of material properties can be extracted and quantified from the force-distance curve at each pixel within an image, such as modulus, adhesion force, and etc. (Fig.2.12.). This analysis is automatically performed by the software to obtain corresponded feedback images.

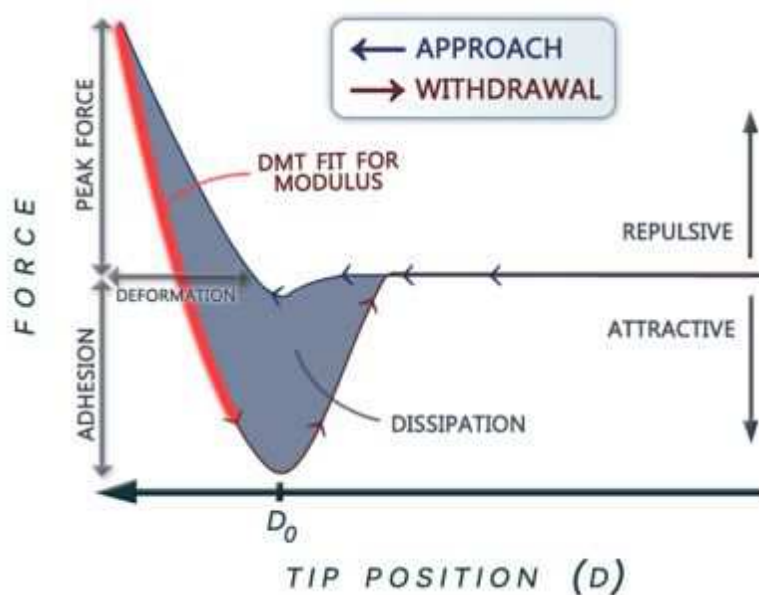


Fig.2.12. Schematic force distance curve derived during mechanical mapping in peak force tapping AFM mode with derivation of different mechanical parameters^[241].

Experimental conditions. In this study, a classical tapping mode (carried out at International Laser Centre in Bratislava) and Peak Force Quantitative Nanomechanics (QNM) tapping mode (performed at Institute of Chemistry of Clermont Ferrand) were used to analyse the samples surface.

To study the changes in the sample roughness a scanning probe microscope (SolverP47H-PRO) was operated in tapping mode. Images were recorded with a scan range $10 \times 10 \mu\text{m}^2$ and 512×512 points using a phosphorous-doped silicon tip with a resonance frequency around 280 kHz. AFM measurements were collected from three different areas of the samples for statistical evaluation. From the measured AFM data, roughness (R_a) values were calculated as the average of the individual values obtained for three $10 \times 10 \mu\text{m}^2$ height images, recorded at different points of the sample surface. SPIP 6.4.2. and Gwyddion 2.40 softwares were used for the image processing and roughness calculations.

To study the surface morphology of polymer and nanocomposite films and the particles distribution, an Atomic Force/Scanning Probe Microscope (AFM/SPM) Multimode from Bruker operated in PeakForce Quantitative Nanomechanics (QNM) Tapping was used. The phosphorus doped silicon AFM probe (TAP-150A from Veeco) with a resonant frequency in the range of 130-180 kHz was used. Areas of $5 \times 5 \mu\text{m}$ were scanned. The topography images were processed using 7.20 Nanoscope software. The probe was not calibrated in this

experiment which did not allow us to extract any quantitative information of material properties such as modulus and adhesion, but it permits the relative comparison (contrast of colour mapping) of data collected for each individual tap of a recorded image.

The films of EVOH and EVOH/nanocomposite, used for AFM analysis, were obtained by deposition of polymer solution or polymer-particle suspension in DMSO (obtained as it is described in §1.2. method A) onto a glass substrate and then, dried in air at 40 °C to obtain solvent-free films.

3.5. Dynamic mechanical thermal analysis ^[242, 243]

Theory. Dynamic Mechanical Thermal Analysis (DMTA) is a technique where an oscillating force is applied to a sample in a cyclic manner and the material response to the deformation is monitored as a function of temperature or time (Fig.2.13.). This allows the material response to stress, temperature, frequency and other values to be studied. The deformation can be applied sinusoidally, in a constant (or step) fashion, or under a fixed rate.

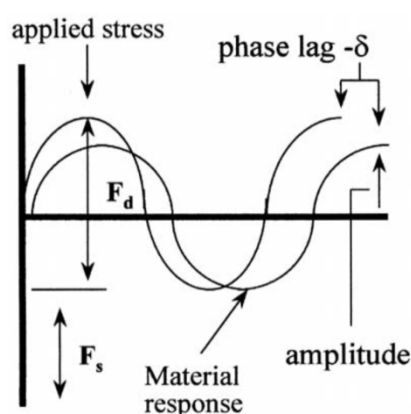


Fig.2.13. Basic principle of DMTA ^[243].

DMTA provides a direct link between a material's chemical makeup and its mechanical behaviour. The material is characterised in terms of its viscoelastic modulus, elasticity, viscosity, damping behaviour, and transition temperatures, and the changes of these with strain, strain rate, temperature, and oscillatory frequency.

Viscoelastic parameters. The elastic and viscous stresses are related to material properties through the ratio of stress to strain. A ratio of the elastic stress σ' to strain ϵ is the elastic (or storage) modulus E' (Eq.2.1.). A ratio of the viscous stress σ'' to strain is the viscous (or loss) modulus E'' (Eq.2.2.). The sum of viscous and elastic moduli is called Young's or complex modulus (E^*), which shows mechanical overall resistance to deformation (Eq.2.3.).

$$E' = \sigma' / \varepsilon = E^* \cdot \cos \delta \quad (\text{Eq.2.1.})$$

$$E'' = \sigma'' / \varepsilon = E^* \cdot \sin \delta \quad (\text{Eq.2.2.})$$

$$E^* = \sigma^* / \varepsilon = E' + E'' \quad (\text{Eq.2.3.})$$

The ratio of the loss to storage modulus, called tan delta, is the tangent of the phase angle σ , or phase shift between applied deformation and measured response.

$$\tan \delta = E'' / E' \quad (\text{Eq.2.4.})$$

In the case of purely elastic materials (Hookean solid) $\sigma=0^\circ$. Contrary, for purely viscous materials (Newtonian liquid) $\sigma=90^\circ$.

Loss and storage modulus curves (Fig.2.14.) give an information about the glass transition temperature (T_g or T_α) which corresponds to partial chain motions in the polymer. Except of the glass transition, it is possible to scan also transitions at lower temperatures. β -transition (T_β) is accredited to other changes in molecular motions. β -transition is often connected with side chains or correlated to the motions of separate groups. γ - and δ -transitions (T_γ and T_δ) are related to stretch/bend and local motions respectively. Considering the rubbery plateau, α' transition or the liquid-liquid transitions can appear in semi-crystalline or amorphous polymers. Idealised temperature dependence of storage and loss moduli and the effect of different molecular relaxation are shown in Fig.2.14.

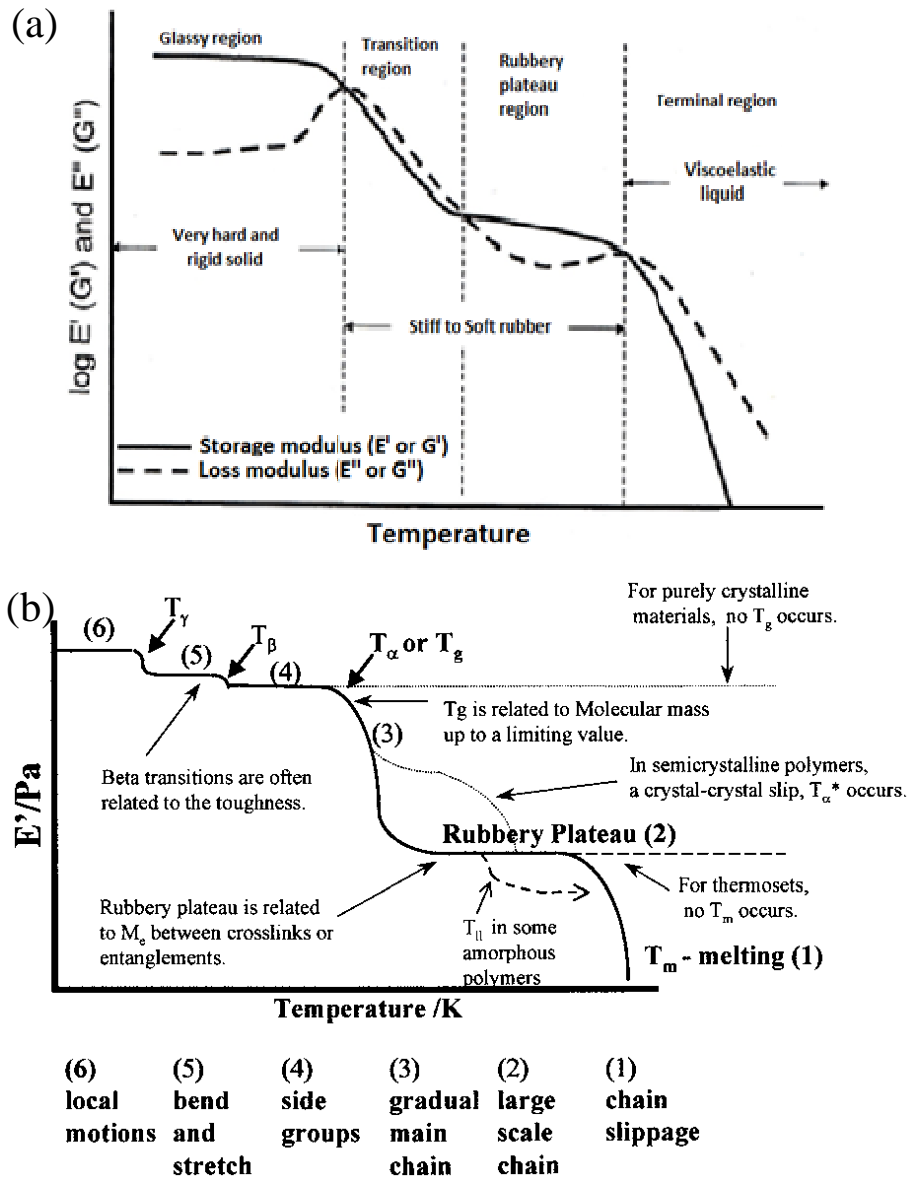


Fig.2.14. An idealised DMTA scan: (a) temperature dependence of the loss and storage moduli ^[244]; (b) effect of various molecular relaxations on the storage modulus ^[243].

Experimental conditions. In these studies, DMTA measurements were performed in a tensile mode using a DMTA Q800 from TA Instruments (New Castle, USA). The polymer films with dimensions 10 mm × 7 mm × 0.09 mm were analysed in a temperature range from -50 to 195 °C with a ramp 1.5 °C/min, at a frequency 1 Hz, and a strain 0.06 %. The chosen frequency and temperature ramp of experiment allow comparing the glass transition temperatures obtained from DMTA experiment with those obtained by differential scanning calorimetry (DSC).

For all experiments, in order to prevent sample buckling during heating, the ‘force track’ option was activated and set at 125 % with an initial pre-load force 0.5 N and a Poisson's ratio 0.44. Prior experiment, all samples were dried in oven at 60 °C under vacuum during 3h.

3.6. Differential scanning calorimetry

Differential Scanning Calorimetry (DSC) measures the difference in heat flow between a sample and a reference in a controlled atmosphere in order to determine various thermal changes in a sample. These changes include melting, glass transition, evaporation and chemical reactions that can be either exothermic or endothermic in nature. For example, DSC detects exothermic (crystallisation) or endothermic (melting) processes of a polymer. All these phenomena are presented in Fig.2.15.

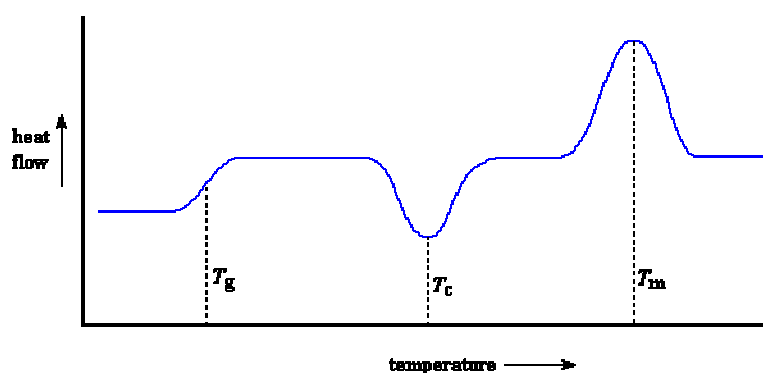


Fig.2.15. Transitions of a polymer determined by DSC: glass transition temperature (T_g), crystallisation temperature (T_c), melting temperature (T_m).

Experimental conditions. DSC analyses were performed on a Mettler Toledo DSC 822 under an ambient airflow. The thermal characteristics of the films were determined from the first scan using a heating rate 10 °C/min from 25 °C to 225 °C.

Approximately 10 mg of the polymer film was placed in an aluminium crucible with volume of 100 μ l. A degree of crystallinity of the samples was calculated by the ratio between the enthalpy of melting of the analysed sample (ΔH_m) and the enthalpy of melting of a 100 % crystalline poly(vinyl alcohol) ($\Delta H_m^\circ = 157.8 \text{ Jg}^{-1}$ [245, 246]).

3.7. Water permeability ^[247, 248]

Theory of permeability. Generally, the transportation of gas, water and volatile compounds through a polymer (non-porous) system can be characterised by three phases:

- dissolution and sorption in the membrane from the side corresponding to the higher partial pressure of the gas in question (upstream face) sorption;
- diffusion through the membrane under the influence of concentration gradient (chemical potential);
- evaporation in the gaseous state on the downstream face: desorption.

The general phenomenon of permeation results of these three stages is presented in Fig.2.16.

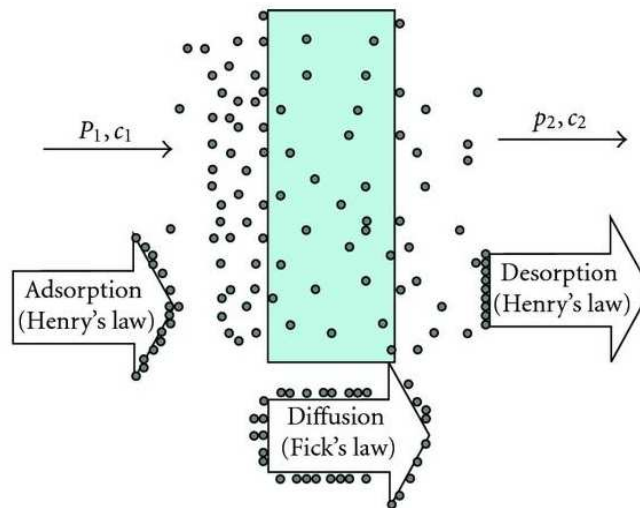


Fig.2.16. General mechanism of gas or vapour permeation through a polymer film ^[248].

Diffusion is the process by which a small molecule is transferred into a system due to random molecular motion. This is a term expressing the kinetic mobility of permeant. These phenomena are described through the laws of ordinary diffusion established by Fick. The first Fick's law establishes a proportional relationship between the amount of permeant diffusing through the membrane per unit area J and the concentration gradient in conditions of steady state ($\Delta C = \text{constant}$).

According to the first Fick's law, the diffusion flux of permeant (gas or vapour), indicated by J , is described by the following equation:

$$J = D \times \frac{(c_1 - c_2)}{l} \quad (\text{Eq.2.5.})$$

where l is a thickness of the polymer film, C_1 and C_2 are the permeant concentrations linked to permeant respective partial pressures p_1 and p_2 in the Henry's Law equation described below:

$$C_n = P_n \times S \quad (\text{Eq.2.6.})$$

where S is the solubility coefficient of the substance in material.

The permeability coefficient P is the product of a kinetic parameter, the diffusion coefficient D (m^2s^{-1}), and a thermodynamic parameter, solubility S ($\text{m}^3_{\text{permeant}} \times \text{m}^2_{\text{membrane}} \times \text{p}^{-1}_{\text{amount}}$) and is described by equation below:

$$P = D \times S \quad (\text{Eq.2.7.})$$

Table 2.1. reports the various units of the permeability, which are commonly used.

Tab.2.1. Different units of permeability

	Dimension	Units
OTR	$\frac{[Quantity_{\text{permeant}}]}{[Time]}$	$\frac{cm^3}{m^2 \cdot day}$
WVTR	$\frac{[Quantity_{\text{permeant}}]}{[Surface_{\text{membrane}}] \cdot [Time]}$	$\frac{g}{m^2 \cdot day}$
Permeability coefficient, P	$\frac{[Quantity_{\text{permeant}}] \cdot Thickness_{\text{membrane}}}{[Surface_{\text{membrane}}] \cdot [Time] \cdot [Pressure_{\text{amount}}]}$	$\frac{g(\text{or } cm^3) \cdot cm}{cm^2 \cdot sec \cdot Pa}$

For practical reasons, one often uses the transmission rates, oxygen transmission rate and water vapour transmission rates (OTR and WVTR respectively). They are often normalised by the surface and are directly linked to the encapsulation device. Other quantities, such as permeability coefficient (P), normalise the flow relative to the thickness of the encapsulation as well as the partial pressure upstream.

Water absorption models.

The cases when diffusion causes the concentration to change with time can be modelled by the second Fick's law:

$$\frac{\partial c(x, t)}{\partial t} = - \frac{\partial J}{\partial x} = D \cdot \frac{\partial^2 c}{\partial x^2} \quad (\text{Eq.2.8.})$$

Sorption measurements

The sorption by polymeric membrane derived from the second Fick's law for the conditions of infinite slab which permit the weight variations M_t to be measured as a function of time, and according to the literature described by (Eq.2.9.)^[249].

$$\frac{M}{M_{eq}} = 1 - \frac{8}{\pi^2} \sum_{n=0}^{\infty} \frac{1}{(2n+1)^2} \exp \left[-\frac{D(2n+1)^2 \pi^2 t}{l^2} \right] \quad (\text{Eq.2.9.})$$

where l is the thickness of the polymer film sample or the length of the diffusion path, D is the effective diffusion coefficient and t is the time; M_{eq} is defined as the weight at equilibrium state. In this equation, M is calculated by Eq.2.10., with M_0 being the initial weight of the sample before moisture absorption.

$$M = M_t - M_0 \quad (\text{Eq.2.10.})$$

At the short time, it can be simplified to described below:

$$\frac{M}{M_{eq}} = \frac{4}{l} \sqrt{\frac{Dt}{\pi}} \quad (\text{Eq.2.11.})$$

By constructing a sorption curve (M/M_{∞} versus \sqrt{t}), the effective diffusion coefficient for the short-time sorption can be calculated from the initial slope b , and the final equilibrium state of the curve using the following equations:

$$b = \frac{4}{l\sqrt{\pi}} \sqrt{D} \quad (\text{Eq.2.12.})$$

$$D = \pi \frac{l^2}{16} b^2 \quad (\text{Eq.2.13.})$$

Regarding Eq.2.7. and Eq.2.13., the permeability for Fickian behaviour case can be calculated as follows:

$$P = \frac{\pi(M_{eq} - M_0)}{M_0} \frac{\rho}{\Delta P} \frac{l^2}{16} b^2 \quad (\text{Eq.2.14.})$$

Where solubility is described by the following equation:

$$S = \frac{(M_{eq} - M_0)}{\frac{M_0}{\rho}} \frac{1}{\Delta P} \quad (\text{Eq.2.15.})$$

In this equation, M_0 and M_{eq} are defined as the relative weights at the beginning of sorption and equilibrium state, ΔP is the pressure difference and ρ is the density of polymer.

However, the diffusion process does not always follow Fick's laws. Different models were developed to describe non-Fickian behaviour of polymer and composite materials. One of the most common models, proposed by the Carter and Kibler^{[250] [251]} was used to describe moisture uptake within composites^[251-253]. These models assume the existence of "mobile", free to diffuse, and "bound" diffusant molecules. In this model, the solution for moisture uptake can be approximated as:

$$\frac{M_t}{M_\infty} = \left| \frac{\beta}{\beta+\gamma} e^{-\gamma t} \left[1 - \frac{8}{\pi^2} \sum_{n=0}^{\infty} \frac{e^{-k(2n+1)^2 t}}{(2n+1)^2} \right] + \frac{\beta}{\beta+\gamma} (e^{-\beta t} - e^{-\gamma t}) + (1 - e^{-\beta t}) \right| \quad (\text{Eq.2.16.})$$

Where n represents the number of mobile molecules (per unit of time) with a probability γ (s^{-1}) to become bound β (s^{-1}) is the probability that bound molecules become mobile to become mobile. k is related to the diffusion coefficient described by Eq.2.17.

$$k = \pi^2 \frac{D}{l^2} \quad (\text{Eq.2.17.})$$

For the cases when the sorption time is short and $kt < 0.7$, Eq.2.17. yields the approximation:

$$\frac{M_t}{M_\infty} = \frac{4}{\pi^{1/2}} \left(\frac{\beta}{\beta + \gamma} \right) \frac{\sqrt{Dt}}{l} \quad (\text{Eq.2.18.})$$

The diffusion thus behaves as a Fickian process with an apparent D_{app} ^[254] such as:

$$D_{app} = D \left(\frac{\beta}{\gamma + \beta} \right)^2 \quad (\text{Eq.2.19.})$$

In the case of long-time exposure when kt is large compare to unity ($kt \gg 1$), the following approximation holds:

$$\frac{M_t}{M_\infty} = 1 - \left(\frac{\gamma}{\beta + \gamma} \right) e^{-\beta t} \quad (\text{Eq.2.20.})$$

3.7.1. Gravimetric immersion water uptake (IWU)

Experiment description. Water uptake experiments were performed to investigate the water sorption capability of polymer and nanocomposite materials. Films of pristine EVOH and EVOH/zeolite nanocomposites (with the samples weight of around 80 mg) were soaked in

distilled water at ambient temperature under shaking with an orbital shaker Biosan OS-10 in 30 ml of distilled water. The water sorption capacity was monitored by a difference of weight of sample after soaking in water up to an equilibrium state with a constant weight and weight of a moisture-free film (virgin film after drying 2 h at 120 °C under vacuum) and the same film.

Films of EVOH polymer and nanocomposites were prepared by melt-mixing in extruder.

3.7.2. Dynamic vapour sorption

Dynamic Vapour Sorption, also known as DVS, permits the amount and rate of absorption of a solvent by a sample to be measured. This gravimetric technique measures the change in mass of the sample. The sorption isotherms are then treated to obtain the diffusion and permeability characteristic of the samples.

Experiment description. Sorption isotherms were obtained using a benchtop dynamic vapour sorption analyser (IGAsorp, HidenIsochema, Warrington, UK) with ultrasensitive balance (resolution of 0.1 µg) measuring the mass of the sample as a function of time at fixed relative humidity and temperature. Controlled humidity was maintained using a laminar flow with wet–dry vapour mixing.

The polymer and nanocomposite films with thickness range of 70-80 µm were prepared by method B, and then cut to obtain a mass around 60-100 mg. Samples, were initially held at 0 % RH at the temperature 40 °C until the mass of sample is stable over the time (72 hours). This mass was used as a reference mass (M_0) for the mass uptake calculations. After, the RH was increased up to 85 % at 38 °C. The mass was then recorded as a function of time.

The isotherms were treated according the procedure described for second Fick's law in paragraph 3.7. Diffusion coefficient, was calculated using Eq.2.13.

3.7.3. Calcium test

Theory. Calcium test is today the most commonly used to characterise flexible substrates for encapsulation purposes [255, 256]. This test relies on the chemical conversion of calcium to calcium hydroxide or calcium oxide in the presence of water or oxygen. Accompanying this chemical change is a change of the metal properties, since calcium is conductive and opaque and calcium oxide and hydroxide are nonconductive and transparent. Therefore, the permeation rate can be calculated from the change of electrical and optical properties of a

calcium layer, which is deposited on the test sample and encapsulated hermetically on the backside.

The Ca-test can be used in different geometries (see example in Fig.2.17.). The calcium film can be applied directly onto a barrier (left) to be tested and sealed or it can be fabricated on a separate carrier that is then joined with the barrier (centre figure).

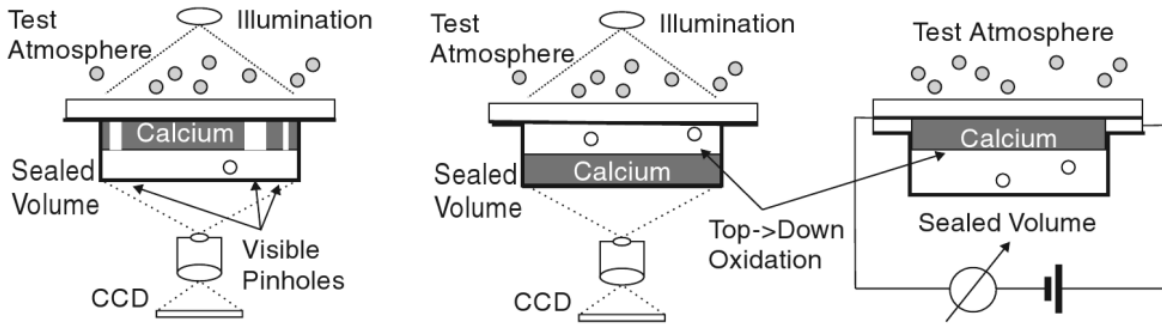


Fig.2.17. Different Ca-test setups where the conversion of Ca can be monitored by optical transmission (left and centre) or by electrical resistance measurements (right) ^[255].

In the current work, calcium corrosion has been detected by change of the calcium conductivity.

Assuming homogeneous corrosion of the calcium layer from the substrate surface, the resistance R is inversely proportional to the height h of the remaining metallic calcium (the oxidised Ca salts are insulators)^[256] as it is described in following equation:

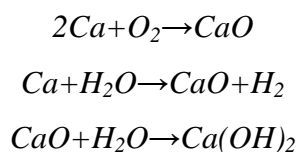
$$R = \frac{\rho \cdot l}{b \cdot h} \quad (\text{Eq.2.21.})$$

where ρ denotes the Ca resistivity, l is the length and b is the width of the Ca layer. The permeation rate P through the foil is then proportional to the slope of the conductance curve $1/R$, plotted versus measured time t (Eq.2.22.)

$$P = -n \frac{M_{(reagent)}}{M_{(Ca)}} \delta p \frac{l}{b} \frac{d(1/R)}{dt} \quad (\text{Eq.2.22.})$$

where n is the molar equivalent of the degradation reaction (see below), $M_{(reagent)}$ and $M_{(Ca)}$ are the molar masses of the permeating reagent and Ca, respectively, and d is the density of Ca. The degradation reactions in humid air closely resemble the ageing mechanisms of the

cathode in a device. The important chemical reactions of calcium with air are assumed to be the following:



Therefore, each calcium atom can react with a half of oxygen molecule ($n=0.5$) or up to two water molecules ($n=2$).

Experimental conditions. The Ca-test experiment was performed at Belectric OPV in Nuremberg. Lateral and vertical water vapour diffusion rates were determined by Ca-test carried out in a Horstman climatic cabinet (HS 200 K 46 L) via controlled environmental conditions (65 °C / 85 % RH). The Ca sensors (see the samples fabrication in Ch. II § 1.2.) were connected to a Keithley 2750 multimeter by four-point-probe technique to monitor their resistance under damp heat conditions. The permeation rates were calculated according to Eq.2.22.

3.8. Time-of-flight secondary ion mass spectrometry

Time-of-Flight Secondary Ion Mass Spectrometry (ToF-SIMS) is a surface analytical technique that focuses a pulsed beam of primary ions onto a sample surface, in result of a sputtering process, the secondary ions and neutral species are formed (Fig.2.18.). These species are then accelerated into a "flight tube" and their mass is determined by measuring the exact time at which they reach the detector (i.e. time-of-flight).

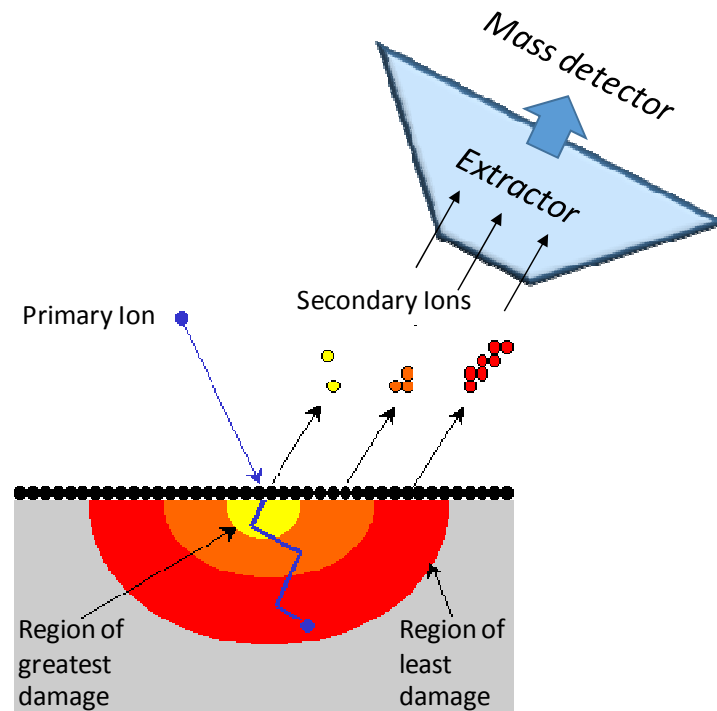


Fig.2.18. Working principle of ToF- SIMS. Adapted from ^[257].

SIMS process requires a vacuum environment. As primary ions for the secondary emission, a pulsed ion source is necessary. This ions source can work on the base of liquid metal ion gun (LMIG) principle using different elements species (usually atomic, small cluster or polyatomic).

Due to the mechanisms of the secondary ions formation, the positive and negative ions are mostly singly charged. Positive ions spectra are dominated by electropositive species and negative ions spectra by electronegative species but metal clusters and fragment ions can appear in both polarities with different intensities relatives according to their oxidation degree. Therefore, many factors may influence the obtaining of a high intensity of the emitted secondary ions as shown by the following equation ^[258]:

$$I_m = I_p \cdot Y_m \cdot \alpha^+ \cdot \theta_m \cdot \eta \quad (\text{Eq.2.23.})$$

where I_m is the secondary ion current of element m , I_p is the primary particle flux, Y_m is the sputter yield, α^+ is the ionisation probability to positive ions, θ_m is the fractional concentration of the chemical fragment m in the surface layer and η is the transmission of the analysis system.

ToF-SIMS has a capability to provide high molecular specificity, high spatial resolution and high sensitivity to surface (<0.5 nm). The secondary ions analysis gives the information about molecular and elemental species present at the surface. In case of polymer analysis following information can be extracted: molecule structure (branching), saturation or unsaturation, conformation of chain, functions of groups, molecular weight distribution, ends groups etc. [259].

Three operational modes are available using ToF-SIMS:

1-study of surface morphology by mass spectra allows determination of the elemental and molecular species at surface with a high mass resolution >10 000;

2- Surface imaging forward information to visualise the distribution of individual species present in the surface (XY) with a lateral resolution <500 nm;

3- Depth profiling which is used to determine the distribution of different chemical species as a function of depth (Z) from the surface. The depth resolution is inferior to 1 nm and very thin layer ranging from 1 nm up to 10 μm can be analysed.

Analysis conditions. ToF-SIMS experiment was performed at International Laser Centre in Bratislava. ToF-SIMS analysis was conducted using Ion-ToF (GmbH) (SIMS IV) in dual beam mode. A Bi^{3+} liquid metal ion gun operated at 25 keV was used as an analyser gun and Cs^+ at 2 keV as a sputtering gun for the depth profile acquisition. To minimise charge build-up at the surface the flood gun was used. The extractor was operated in both, negative and positive ion mode, regarding the specific conditions. The schematic view of used experimental setup is shown in Fig.2.19.

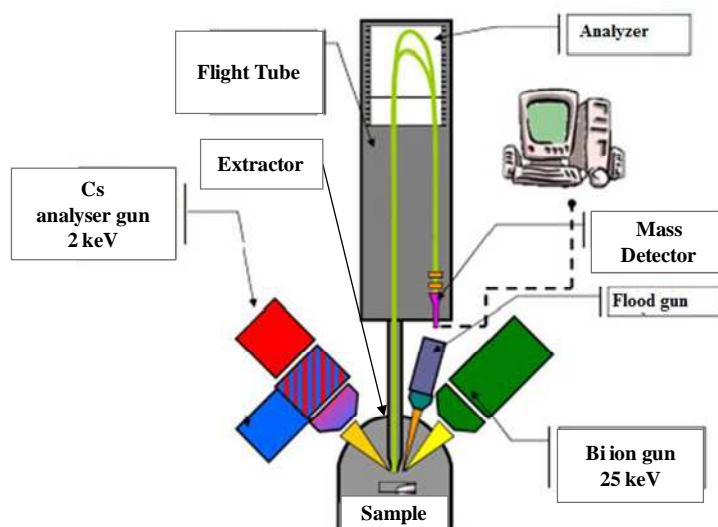


Fig.2.19. Experimental setup for ToF-SIMS measurements.

To analyse the composition of EVOH44 and EVOH44/NZL, the mass spectra of the film surfaces were analysed in both, positive and negative ion fields. The positive mass spectra of samples were recorded in interlaced mode and one shot/pixel randomly rastered with resolution of 128×128 pixels during 1147 s.

To study EVOH44 and EVOH44/NZL-20 film photooxidation, the negative ion field was analysed. $150 \times 150 \mu\text{m}^2$ scan area of sample surface was bombarded by primary ions for 1574 s. All images were obtained in interlaced mode with randomly rastered shots and resolution of 512×512 pixels where 3 shorts per spot were applied.

For quantitative analysis of ions areas, each signal was normalised against total ion intensity (counts) to avoid any possible instrument effects. In order to compare relative composition between samples after the appropriate calibration process, a common peak list was applied to each analysis. Then, the average of data obtained from two analysed areas was calculated. SurfaceLab 6 software package from Ion TOF was used for the processing of obtained mass spectra.

Samples

All the analysed samples were processed by melt-mixing in twin-screw extruder in order to avoid the additional fragmentation of the solvent. Prior the ToF-SIMS analyses of photooxidised film, the samples were exposed during different times to light irradiation in air in SEPAP 12/24.

CHAPTER III:
INITIAL CHARACTERISATION OF
EVOH/COMPOSITES

INTRODUCTION

The aim of this work is to achieve stable materials with durable properties, which could be applied for encapsulation coatings of organic solar cells. Before studying the behaviour of the materials under the various stresses that are likely to provoke their degradation (UV light, oxygen, water, temperature), the characterisation of their initial properties has to be performed. This is the aim of this third chapter, which is devoted to the characterisation of the initial properties of EVOH copolymers and their nanocomposites with up to 20 wt % of zeolite nanoparticles or microparticles. These properties concern as well the chemical structure of the materials, as the morphology, the physico-chemical properties, with the optical, thermal, mechanical and water sorption properties.

Two EVOH copolymers with 27 and 44 mole % of ethylene part were used as polymer matrix, with two different kinds of zeolite particles: micro- and nanosized particles (respectively DISC and NZL zeolites). The (nano)composites were elaborated by two different methods: solution mixing (method A) or melt-mixing in extruder (method B). The dispersion of the nanofillers was characterised by different microscopic analysis: SEM, TEM AFM. The influence of zeolite on the transparency was monitored by UV-Visible absorption spectroscopy, the mechanical and thermal properties by DMTA and DSC, the surface properties by AFM and ToF-SIMS and finally the water sorption properties by gravimetry and DVS.

The final goal of this chapter was to determine which material would be the “best” candidate for encapsulation of organic solar cells in term of the required properties, e.g. transparency, flexibility, surface roughness, and in particular, water permeability/sorption properties.

1. CHARACTERISATION OF ZEOLITE PARTICLES

Firstly, the zeolite particles that we used as fillers were characterised. The morphology and chemical structure of zeolites named NZL (nanosized) and DISC (microsized) are presented in this paragraph.

1.1.Morphology

In order to determine the particles morphology in DMSO solution used for nanocomposite processing, TEM observations were carried out on NZL and DISC particle suspensions (Fig.3.1.).

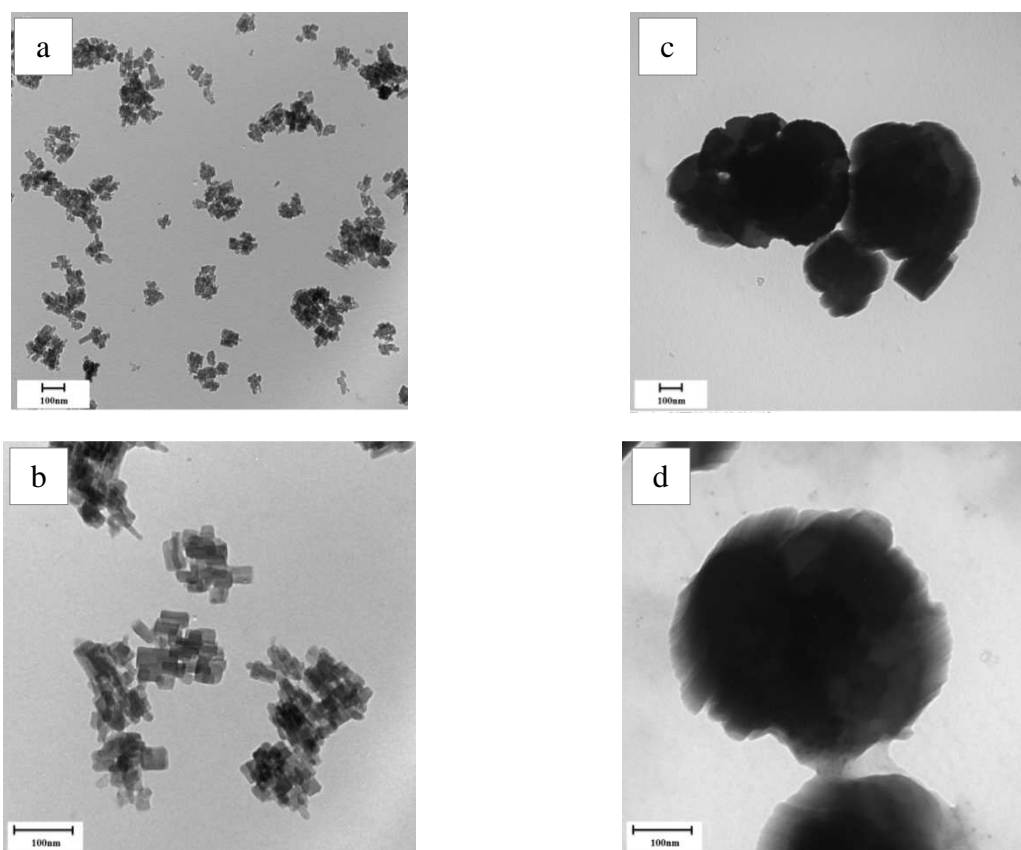


Fig.3.1. TEM images of zeolite particles dispersed in DMSO (95 g/l): (a-b) NZL and (c-d) DISC.

The images show the specific morphology of the particles related to zeolites of LTL-type^[260]. NZL particles display nanoscale dimensions in the range of 30-55 nm in length and 15-20 nm in diameter (Fig.3.1.a-b). In contrast, disc shape particles, abbreviated DISC, have micrometric size in the range of 0.3-1.3 μm in diameter and 0.2-0.3 μm in thickness

(Fig.3.1.c-d). One observes that both zeolite particles form aggregates in the solvent in the size range of 70-200 nm and 2-20 μm for NZL and DISC respectively.

The results obtained from TEM images of the particles are consistent with the specifications given by the supplier (see Ch.II Table 2.2.).

1.2. Chemical structure

1.2.1. Elemental composition

The chemical composition of zeolite particles (NZL and DISC) was determined by elemental analysis (Service Central d'Analyse of the CNRS at Vernaison) (Table 3.1.). According to the analysis, the zeolites have the following formula: $[\text{K}_9(\text{H}_2\text{O})_{16}] [\text{Si}_{27}\text{Al}_9\text{O}_{72}]$ with Si/Al ratio close to 3, which is typical for L-type zeolites. The results indicated the presence of iron impurities in both samples, and other elements were detected in trace amounts (≥ 20 ppm).

Table 3.1. Elemental analysis of zeolites

Chemical element										
	H	Si	Al	K	Fe	Zn	Cu	Co	Mn	Na
	(%)	(%)	(%)	(%)	(ppm)	(ppm)	(ppm)	(ppm)	(ppm)	(ppm)
NZL	1.20	24.75	9.07	13.31	63	<20	<20	<20	<20	≤ 20
DISC	1.33	28.87	8.80	12.00	610	≤ 20	≤ 20	≤ 20	≤ 20	39

1.2.2. IR analysis

FTIR spectra of NZL and DISC zeolite powders into KBr pellets are shown in Fig.3.2.

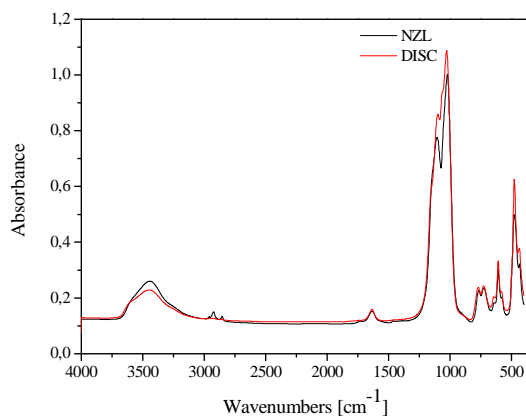


Fig.3.2. FTIR spectra of NZL and DISC zeolite nanoparticles (in KBr pellets).

This figure shows that the spectra of both zeolites are similar, which was expected considering their similar chemical compositions (Table 3.1.) and structures (LTL-type). IR spectra display absorption bands in $900\text{--}1200\text{ cm}^{-1}$, $550\text{--}800\text{ cm}^{-1}$, $540\text{--}640\text{ cm}^{-1}$, and $400\text{--}500\text{ cm}^{-1}$ regions, which are characteristic for aluminosilicate materials ^[261-263].

The most intense bands at 1033 cm^{-1} and 1093 cm^{-1} are assigned to asymmetrical stretching vibrations of Si-O bond. The $540\text{--}650\text{ cm}^{-1}$ frequency domain is called the region of "chainlet" vibrations and it corresponds to the chainlets of tetrahedrons in the mixed silicon-aluminium-oxygen skeleton. The absorption band with a maximum around 478 cm^{-1} corresponds to T-O bending mode, and the shoulder band around 435 cm^{-1} is characteristic of the pore opening of external linkages ^[264].

2. EVOH/ZEOLITE NANOCOMPOSITES CHARACTERISATION

The initial properties of EVOH/zeolite nanocomposites were characterised and compared to those of the neat polymer. Different methods and techniques were used to characterise the morphology of the nanocomposite and to determine their optical, mechanical, thermal and sorption properties. Their chemical composition was studied by ToF-SIMS.

2.1. Spectroscopy analysis

2.1.1. IR analysis

Fig.3.3.a shows the IR spectra of the pristine EVOH copolymers, EVOH27 and EVOH44 (respectively with 27 and 44 mole % of ethylene units). Fig.3.3.b shows the spectrum of the

NZL zeolite nanoparticles, and the spectrum of the nanocomposite of EVOH44 with 20 wt % of NZL loading (EVOH44/NZL-20) films. The spectrum of the pristine EVOH44 is also reported on this figure. The characteristic IR bands assigned to EVOH ^[265-269] and to zeolite L-type particles ^[261-263] have been previously described and are summarised in Table 3.2.

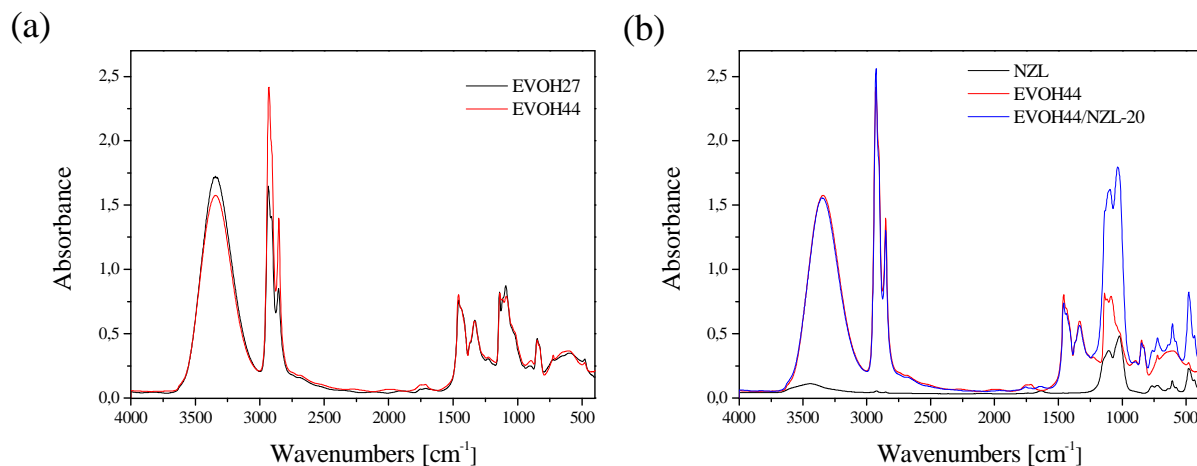


Fig.3.3. FTIR spectra of (a) EVOH44 and EVOH27 films, and (b) NZL, EVOH44 and EVOH44/NZL-20 nanocomposite films.

Table 3.2. Assignments of IR bands of EVOH/L-zeolite nanocomposites

Wavenumber [cm ⁻¹]	Attribution	Origin
3350	$\nu(\text{OH})$ stretching	Polymer
2930	$\nu_{\text{as}}(\text{CH}_2)$ stretching	
2852	$\nu_{\text{sym}}(\text{CH}_2)$ stretching	
1460	$\nu(\text{OH})$ skeleton vibrations	
1715	$\nu(\text{C}=\text{O})$	
1120	$\nu(\text{C}-\text{C})$ stretching	
1093	$\nu_{\text{as}}(\text{Si}-\text{O})$ stretching	Zeolite
1033		
845	$\nu(\text{CH}_2)$ rocking	Polymer
827		
763	Symmetric stretch of internal tetrahedra as well as for external linkages	Zeolite
723		Polymer + Zeolite
643	Vibration of tetrahedral structure	Zeolite
609		
575		
478	T-O bending vibrations	Zeolite
435	Pore opening of external linkages	Zeolite

EVOH copolymers

The prominent IR bands of both EVOH copolymers (Fig.3.3.a) are those of hydrogen-bonded O-H stretching (3350 cm^{-1}), asymmetric (2930 cm^{-1}) and symmetric (2852 cm^{-1}) CH_2 stretching, the C-O and C-C stretching (1715 cm^{-1} and 1120 cm^{-1} respectively). The synthesis of EVOH being based on the hydrolysis of ethylene vinyl acetate, the presence of acetate groups with a low intensity band at 1715 cm^{-1} can be noted in the IR spectra.

Comparison of EVOH with 27 and 44 mole % of ethylene units indicates differences in the relative intensities of the absorption bands (Fig.3.3.a). The (OH)/(C-H) ratio is higher in the case of EVOH27 than for EVOH44, which was not unexpected if one considers the relative amounts of vinyl alcohol and ethylene groups of both copolymers.

Nanocomposites

The IR spectrum of EVOH44/NZL-20 nanocomposite film was presented above in Fig.3.3.b, and the corresponding IR band assignments are described in Table 3.2. It shows the expected contributions of the IR absorption bands that are related to the polymer ($2850\text{-}3350\text{ cm}^{-1}$) and to the zeolite structure ($430\text{-}650\text{ cm}^{-1}$, $1000\text{-}1200\text{ cm}^{-1}$).

Fig.3.4.a shows the IR spectra of EVOH44/NZL nanocomposites with different NZL loadings. The absorbances of the IR bands at 478 , 1033 and 1093 cm^{-1} increases with the zeolite content (Fig.3.4.b). and can be used to quantify the amount of zeolite (see insert). As expected, the intensities of those bands in the case of EVOH27/NZL nanocomposites (see appendix Fig.A.1.) follow the same trends as for EVOH44.

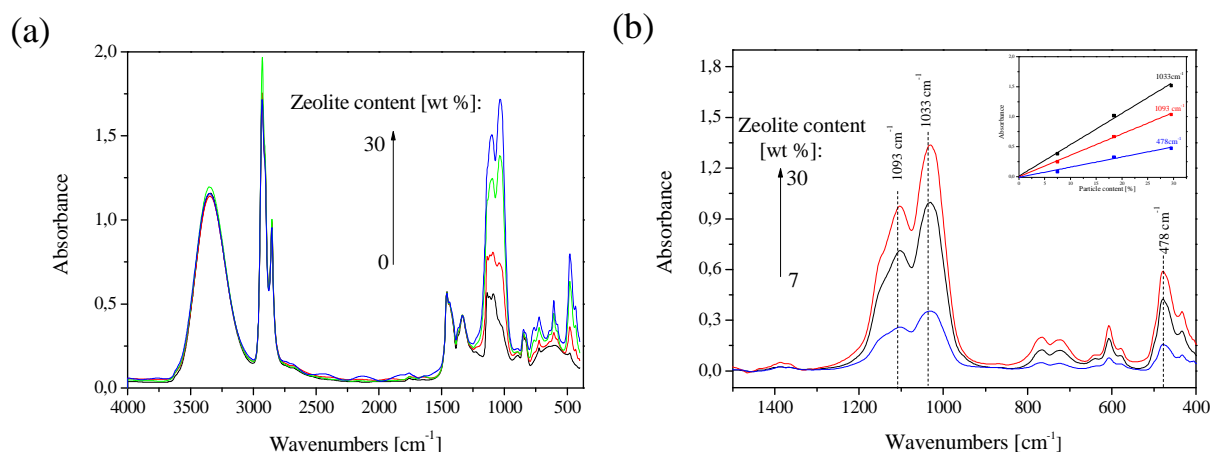


Fig.3.4. (a) FTIR spectra of pristine EVOH44 and EVOH44/NZL nanocomposite films with different particles content (7-30 wt %); (b) Subtracted IR spectra in the 400-1500 cm^{-1} region. Inset: absorbance at 1033 cm^{-1} , 1093 cm^{-1} , and 476 cm^{-1} as a function of particle content in EVOH44/NZL nanocomposites.

2.1.2. UV-Visible analysis

The optical properties of both pristine EVOH films were characterised by UV-Visible spectroscopy (Fig.3.5.a). The influence of NZL nanoparticles on the EVOH/NZL nanocomposite films transparency was also evaluated by UV-Visible spectroscopy for nanocomposites with increasing amount of zeolite nanoparticles (Fig.3.5.b).

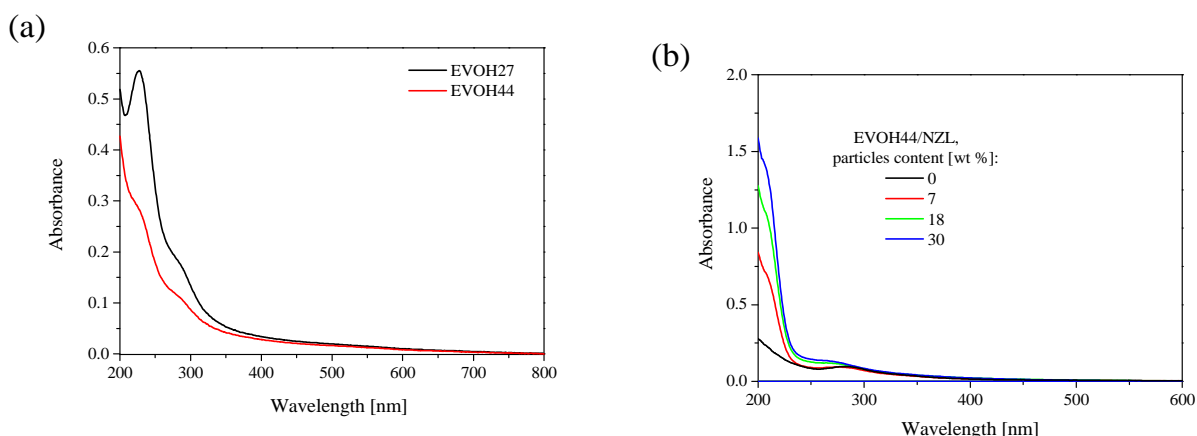


Fig.3.5. UV-Visible spectra of: (a) EVOH44 and EVOH27 films; (b) EVOH44/NZL nanocomposite films with different zeolite contents.

The UV-Visible spectra of EVOH44 and EVOH27 films (Fig.3.5.a) show little absorption in the visible domain (400-800 nm), which confirms the transparency of the films. The

maximum at 230 nm, which is more intense in case of EVOH27, and the shoulder at 285 nm, could result from residual processing additive.

Due to the nanometric size of the NZL particles, the EVOH/NZL nanocomposite films maintain good transparency even with 30 wt % particle loading (Fig.3.5.b). This may bring the opportunity to include relatively high amount of particles into the polymer matrix and, hence, this allows the water scavenger properties of the material to be increased while maintaining the optical properties required for OSCs encapsulation.

2.2. Morphology characterisation

2.2.1. Surface morphology

SEM images were recorded with the aim to study the influence of the zeolite particles on the EVOH surface morphology. SEM images of the surface of pristine EVOH44 film and the nanocomposite films with NZL and DISC particles prepared by DMSO solution mixing (method A) are shown in Fig.3.6.

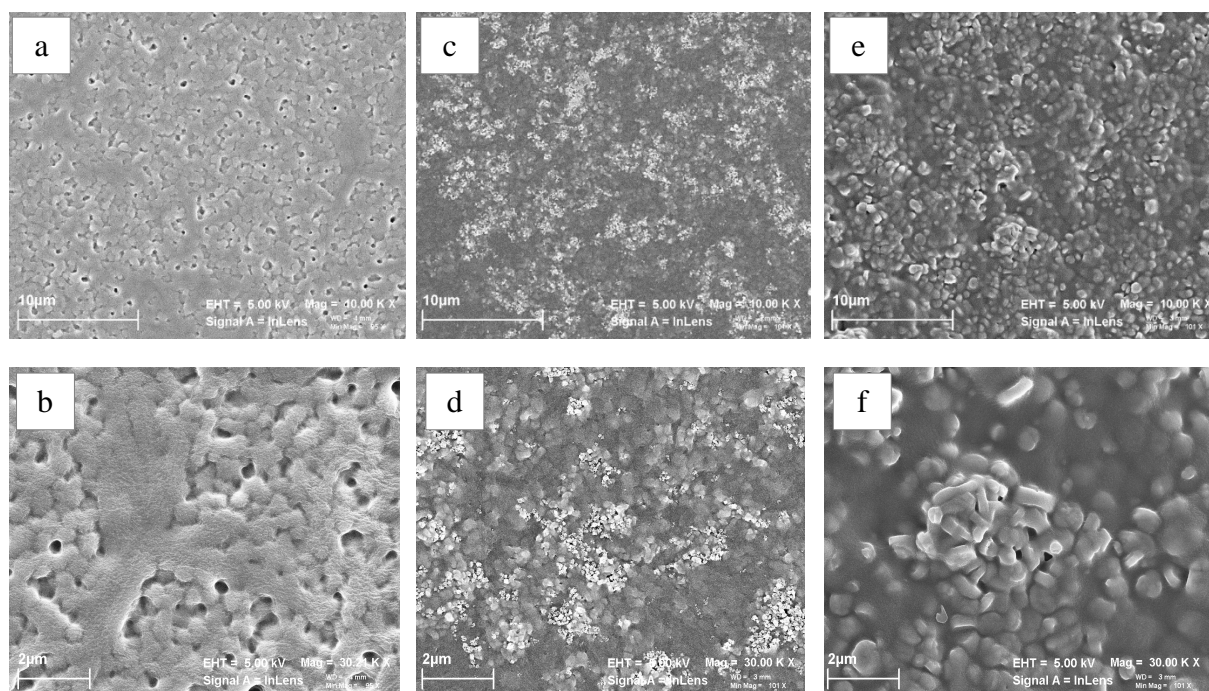


Fig.3.6. SEM images of film surfaces of (a-b) EVOH44(A), (c-d) EVOH44/NZL-20(A), and (e-f) EVOH44/DISC-20(A).

Both the nano- and micro-composites exhibit a regular distribution of zeolite filler at the film surfaces. At the same time, the polymer films without particles displays voids and

irregularities, which could result from solvent evaporation (Fig.3.6.a-b). Additionally, the morphology at the surface of the composites is affected by the particles. It depends on the shapes and size of NZL and DISC where the larger size of DISC microparticles leads to more irregular surfaces (Fig.3.6.e-f)

SEM images of the surface of EVOH44/NZL nanocomposite films with 5 and 20 wt % zeolite loading (Fig.3.7.) show that with an increase of NZL content, the particles concentration at the surface also increases.

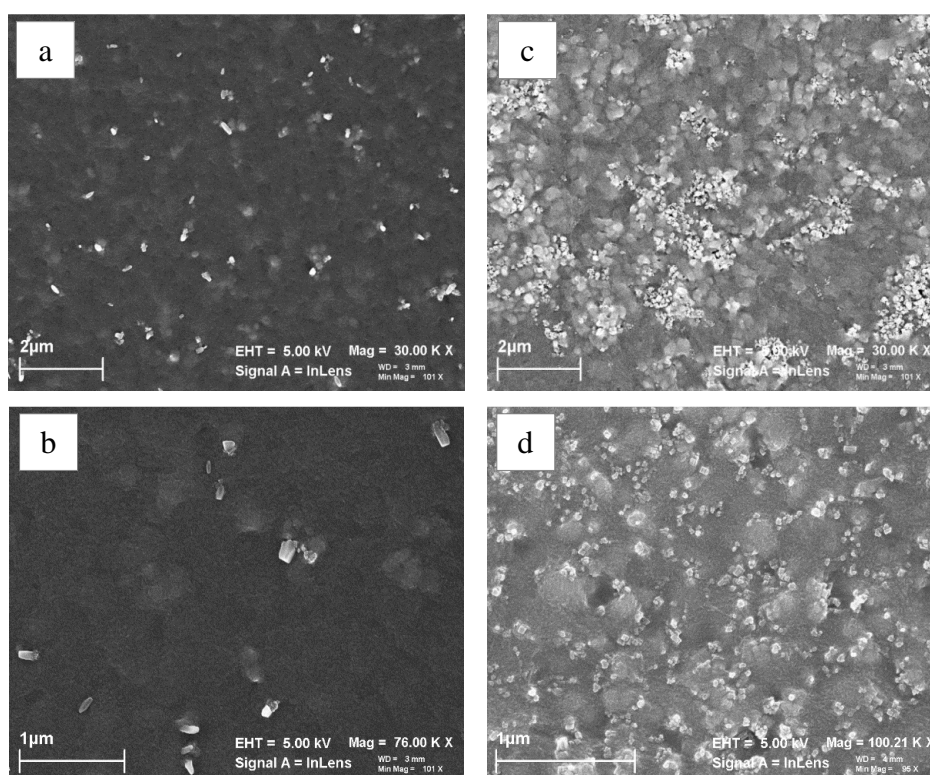


Fig.3.7. SEM images of EVOH44/NZL nanocomposite film with different zeolite loading: (a) 5 wt % and (b) 20 wt %.

Further scaling at the EVOH nanocomposite film surfaces with 20 wt % of NZL and DISC particles is shown in Fig.3.8.

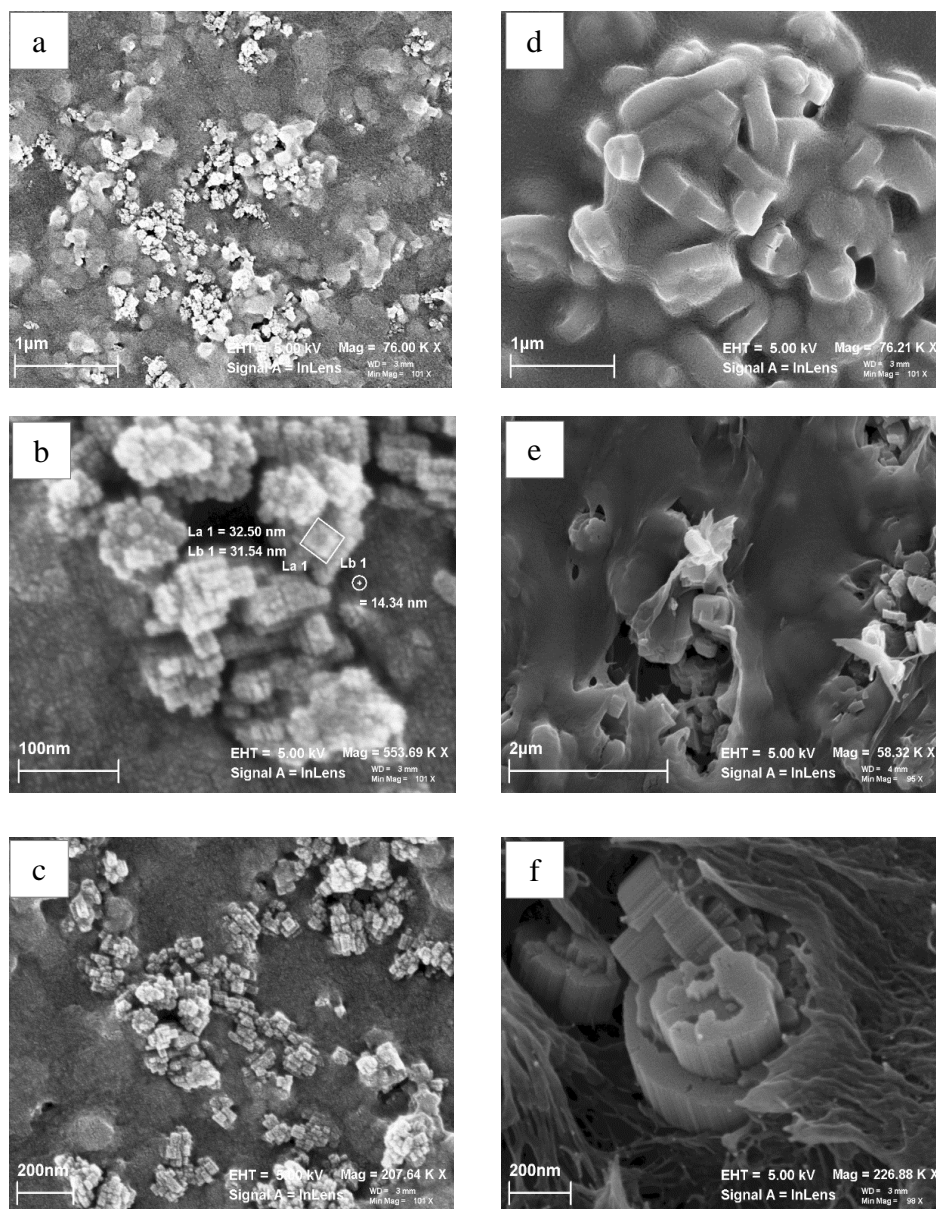


Fig.3.8. SEM images of EVOH44 nanocomposites surface morphology with 20 wt % of (a-c) NZL, and (d-f) DISC particles.

The SEM images in Fig.3.8. indicate that particles, NZL and DISC, are present at the surface either covered or uncovered by the polymer matrix.

2.2.2. Particles dispersion and distribution in film thickness

TEM was used to determine the particles dispersion and distribution in the bulk of EVOH/zeolite nanocomposites and also in the cross-section of films. The aim was to choose the best nanocomposite composition (zeolite loading and processing method).

Influence of processing method

TEM images of EVOH44/NZL-20 of cross-sectioned films processed by melt-mixing (method B)(a-c) and solution mixing (method A)(d-f) are shown in Fig.3.9.

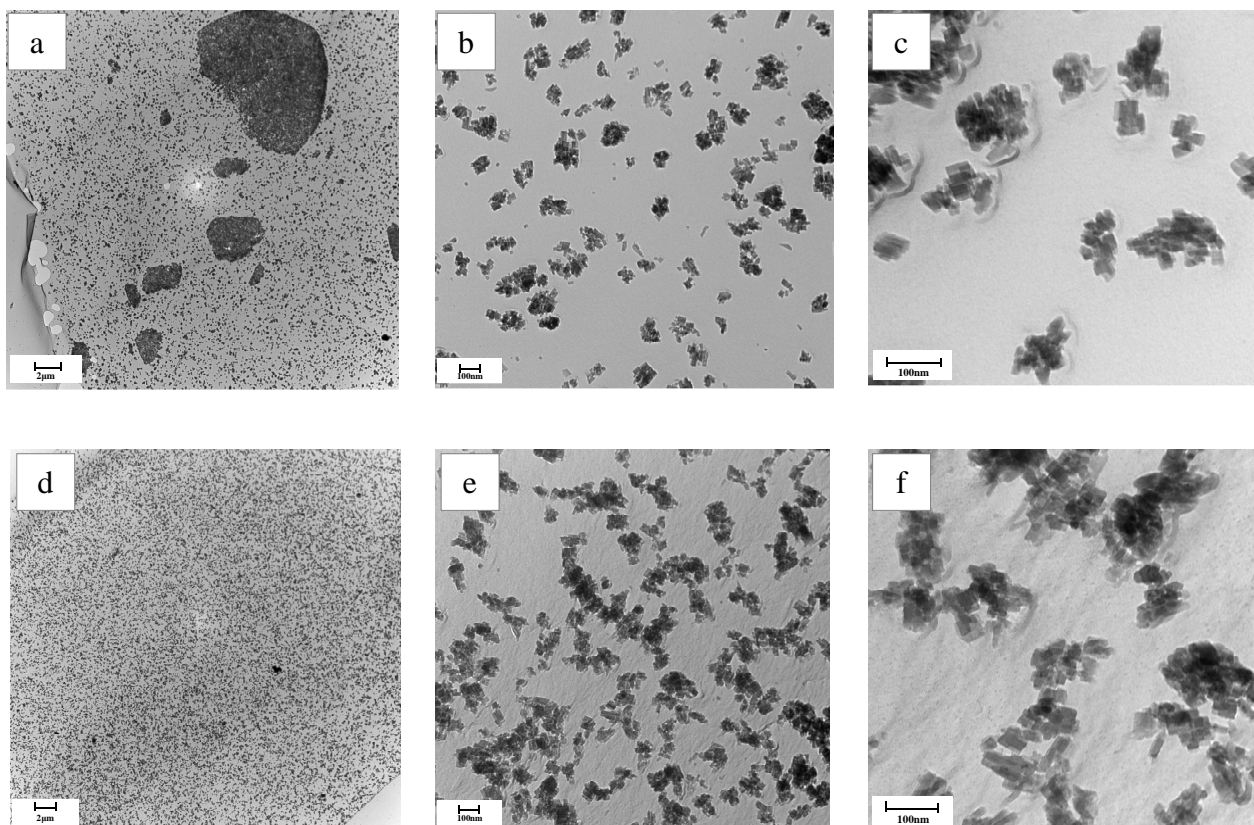


Fig.3.9. TEM images of cross-sections of EVOH44/NZL-20 nanocomposite films processed by (a-c) melt-mixing (B) and (d-f) solution mixing (A).

TEM images (Fig.3.9.c,f) show that with NZL zeolite particles, the specific nanoparticle morphology was maintained within the EVOH matrix with a nanometric size of the primary particles connected to each other to form aggregates. These aggregates are in the same size range (70-200 nm) as those observed for NZL particles in DMSO suspension (Fig.3.1.), which indicates that no aggregation occurs after mixing the zeolite suspension and the polymer solution in DMSO (method A).

The nanocomposites obtained by melt-mixing in a twin-screw extruder (Fig.3.9.a-c) leads to the formation of areas with high particles concentration with a 5 – 20 µm diameter.

At the same time, the nanocomposites obtained by DMSO solution mixing (Fig.3.9.d-f) exhibit good particles dispersion and homogeneous distribution in the whole film thickness. The same observations and then the same conclusions can be made for nanocomposites with

EVOH44 and EVOH27 with the various NZL contents considered in this work (5-20 wt %) (see appendix Fig.A.2.-Fig.A.3). The best particles dispersion and distribution is then achieved by solution mixing (method A).

Influence of zeolite particle size

In order to compare if solution mixing with micrometric DISC particles is as efficient as it is with NZL nanoparticles, TEM images of EVOH44 with 20 wt % loading of NZL and DISC were compared (Fig.3.10.).

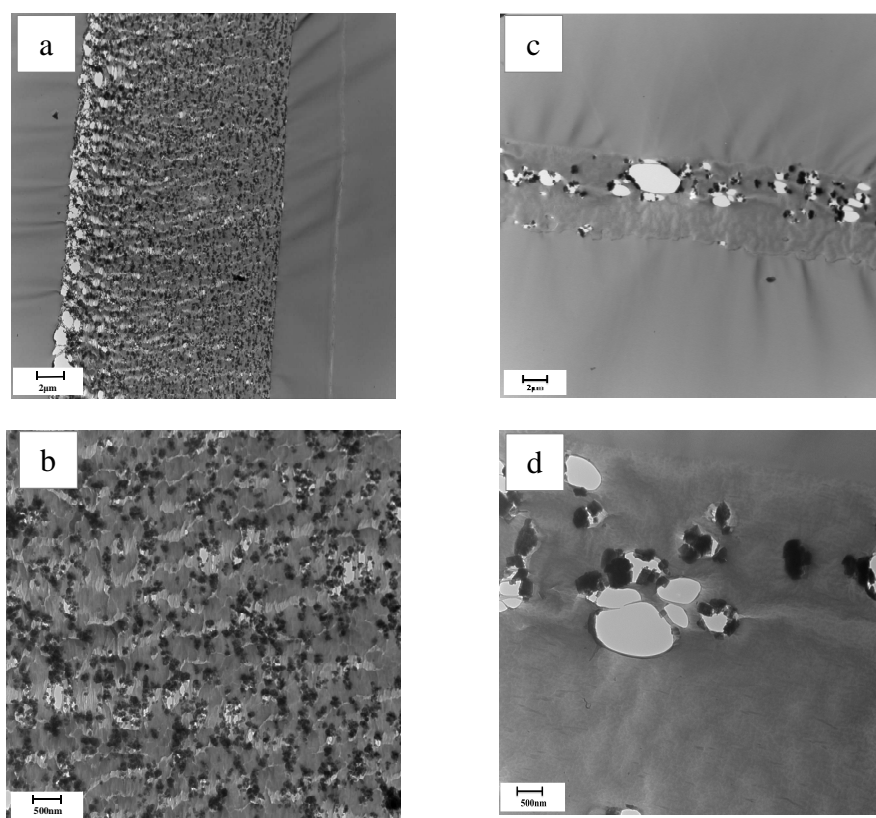


Fig.3.10. TEM images of film cross-sections of (a-b) EVOH44/NZL–20 nanocomposite and (c-d) EVOH44/DISC–20 composite obtained by solution mixing (method A).

The images indicate that sedimentation occurs during the drying step of EVOH44/DISC films (Fig.3.10.c-d). This decreases the dispersion of particles, and as a result, this may worsen the desired composite performance. The same observations can be noticed for TEM cross-section images of EVOH27/DISC shown in Fig.3.11.

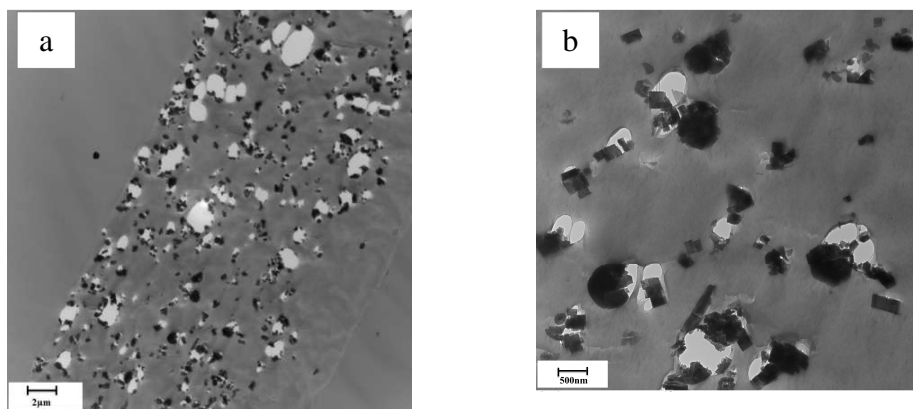


Fig.3.11. TEM images of film cross-sections of EVOH27/DISC-20 composite processed by solution mixing (A).

In contrast, a good distribution of NZL particles in EVOH/NZL nanocomposites is observed for all the NZL loadings considered here (5-20 wt %) (Fig.3.12.).

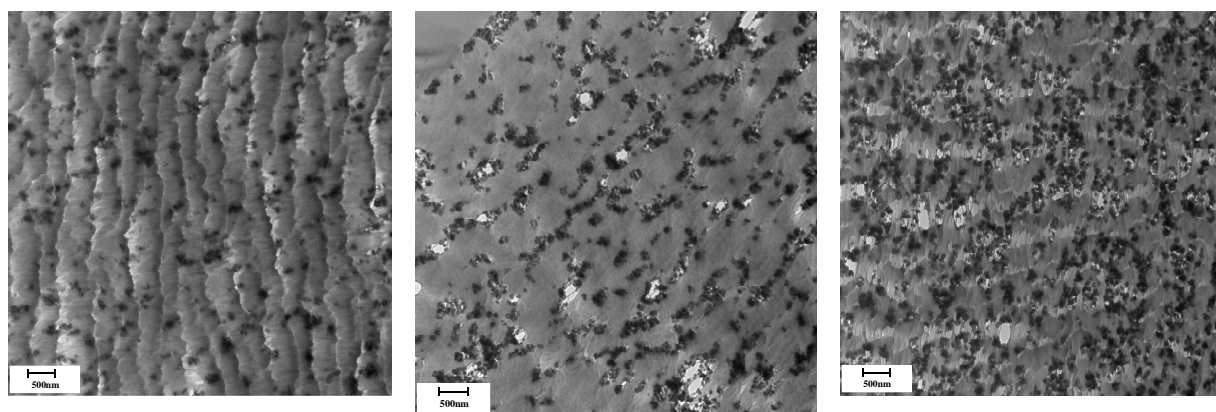


Fig.3.12. TEM images of film cross-sections of EVOH44/NZL nanocomposite processed by solution mixing (A) with different zeolite loading: (a) 5 wt %, (b) 15 wt %, (c) 20 wt %.

Influence of ethylene content in EVOH copolymer

To study the effect of the ethylene amount in the copolymer on the particles distribution, TEM images of EVOH44/NZL and EVOH27/NZL nanocomposites were analysed. Fig.3.13. shows cross-sectioned EVOH27/NZL-20 nanocomposite films.

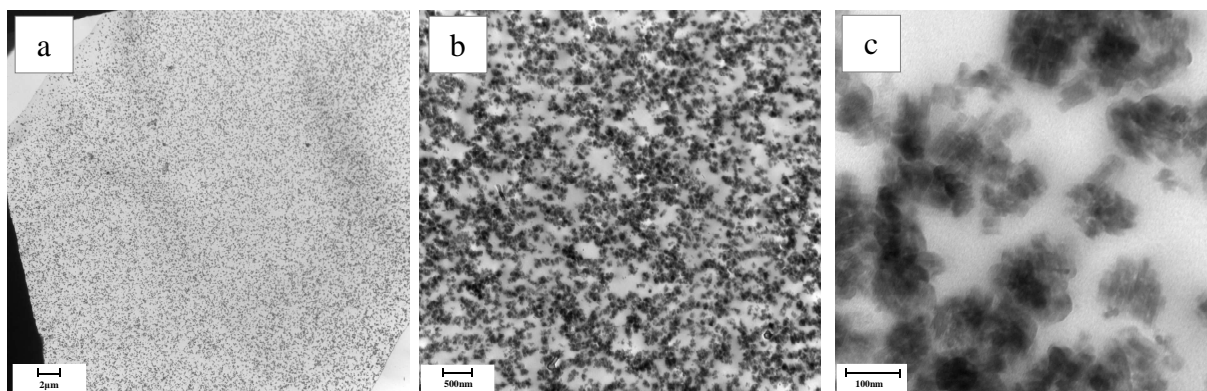


Fig.3.13. TEM images of film cross-sections of EVOH27/NZL-20 processed by solution mixing (A).

Comparing the TEM images of cross-sectioned films of EVOH27/NZL-20 (A) nanocomposite (Fig.3.13.) and EVOH44/NZL-20 (A) (Fig.3.9.d-f.) with the same particles content (20 wt %), it can be concluded that the NZL distribution and dispersion are similar with both EVOH copolymers. Both EVOH44/NZL and EVOH27/NZL nanocomposites exhibit good dispersion and distribution in the whole film thickness when prepared by solution mixing in DMSO.

Surface roughness

The film surface was characterised by AFM analysis. The surface roughness has been extracted from the AFM images. Two different setups were used. The first one was carried out in a tapping mode to determine the effect of particles on the surface roughness by analysing height images. The second one, performed in peak force tapping mode, helped us to distinguish the particles and the polymer at the surface as a consequence of their different interactions with the tip.

Fig.3.14. shows the height images obtained by AFM in classical tapping mode at the surface of EVOH44 and EVOH27 films and the corresponding EVOH/NZL nanocomposites films with different NZL loadings.

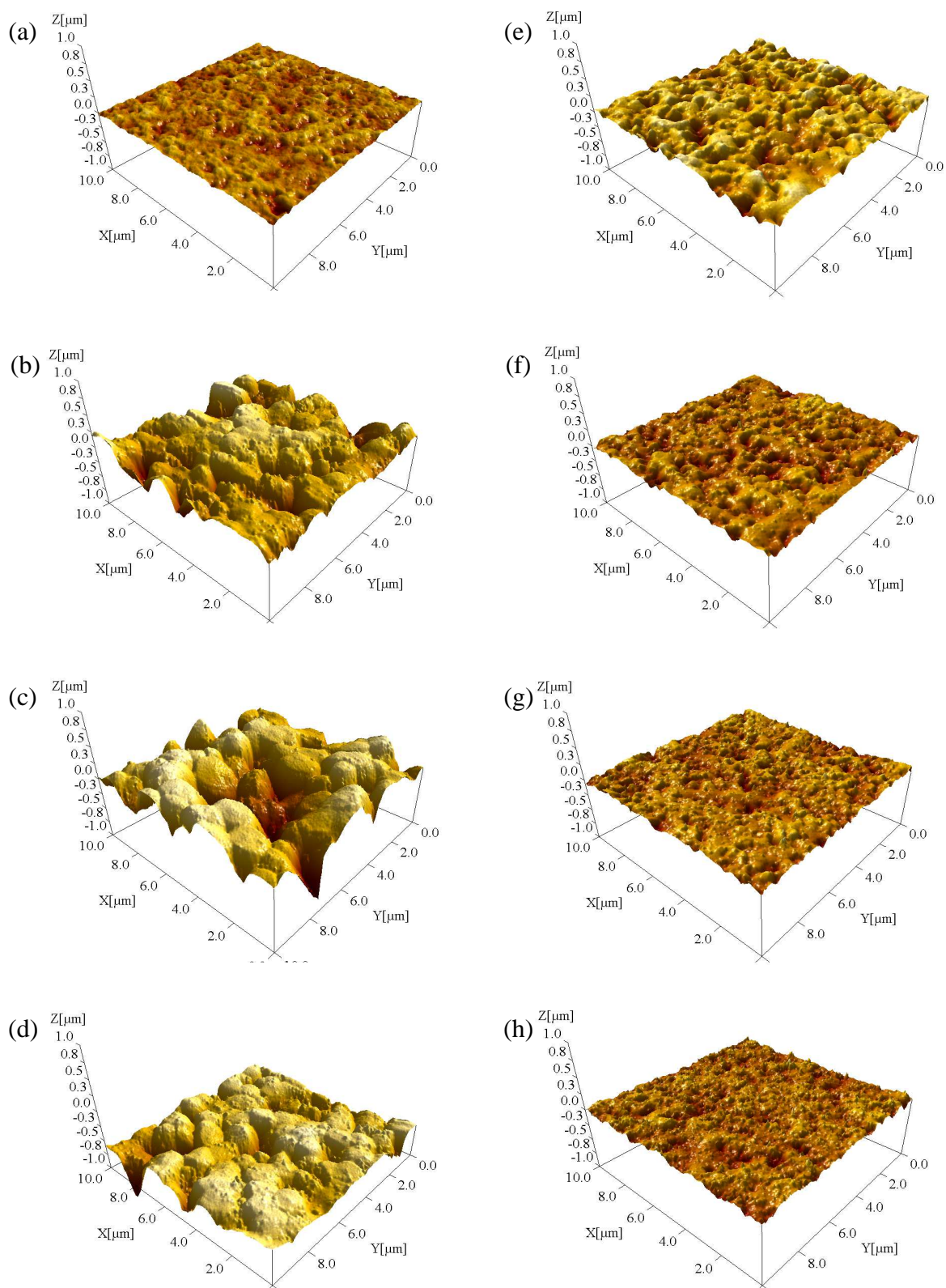


Fig.3.14. AFM 3D height images of (a-d) EVOH44 and (e-h) EVOH27 with different particles content, wt %: (a,e) 0; (b,f) 5; (c,g) 10; (d,h) 20.

The images corresponding to EVOH44 and EVOH27 film surface (Fig.3.14.a,e) show quite rough surface, which can be attributed due to solvent evaporation. Addition of NZL nanoparticles increases the roughness, which is even more significant in the case of EVOH44.

In order to highlight the presence of NZL nanoparticles at the surface of nanocomposite films, 2D height images of EVOH44 or EVOH27 with 20 wt % of NZL nanoparticles are shown in Fig.3.15. White small spots that exhibited higher value of height indicate the presence of nanoparticles (shown in black circles).

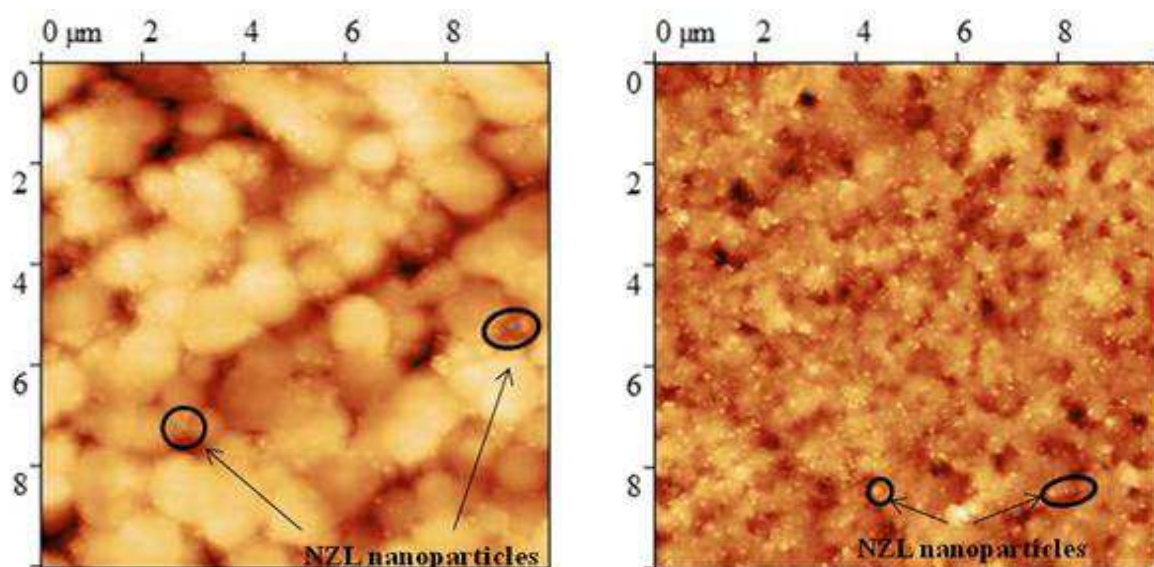


Fig.3.15. AFM 2D height images of (a) EVOH44/NZL-20 nanocomposite and (b) EVOH27/NZL-20 nanocomposite.

The effect of nanoparticle loading on the EVOH surface roughness is plotted in Fig.3.16. for both EVOH copolymers.

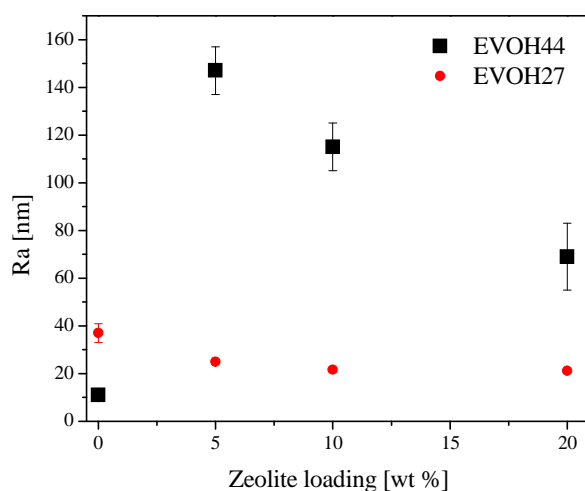


Fig.3.16. Evolution of surface roughness with increasing NZL loading for EVOH44/NZL and EVOH27/NZL nanocomposite films.

This figure shows that, in the case of the pristine materials, the roughness of EVOH27 is slightly higher than the roughness of EVOH44, which reflects the AFM images displayed in Fig.3.14.a,e.

Fig.3.16. shows that adding NZL particles to EVOH44 leads to a significant increase of the roughness at the surface. At opposite, NZL zeolite addition (5-20 wt %) has no effect on the film surface for EVOH27 based nanocomposites (Fig.3.14.e-h). The highest roughness is observed in the case of the EVOH44/NZL with 5 wt % loading ($R_a = 150$ nm) but, further, the roughness decreases with increasing zeolite content (Fig.3.14.c-d).

Particles distribution

In order to distinguish the particles and the polymer at the surface, AFM images of films of EVOH without and with NZL particles were performed in peak force tapping mode (Fig.3.17.).

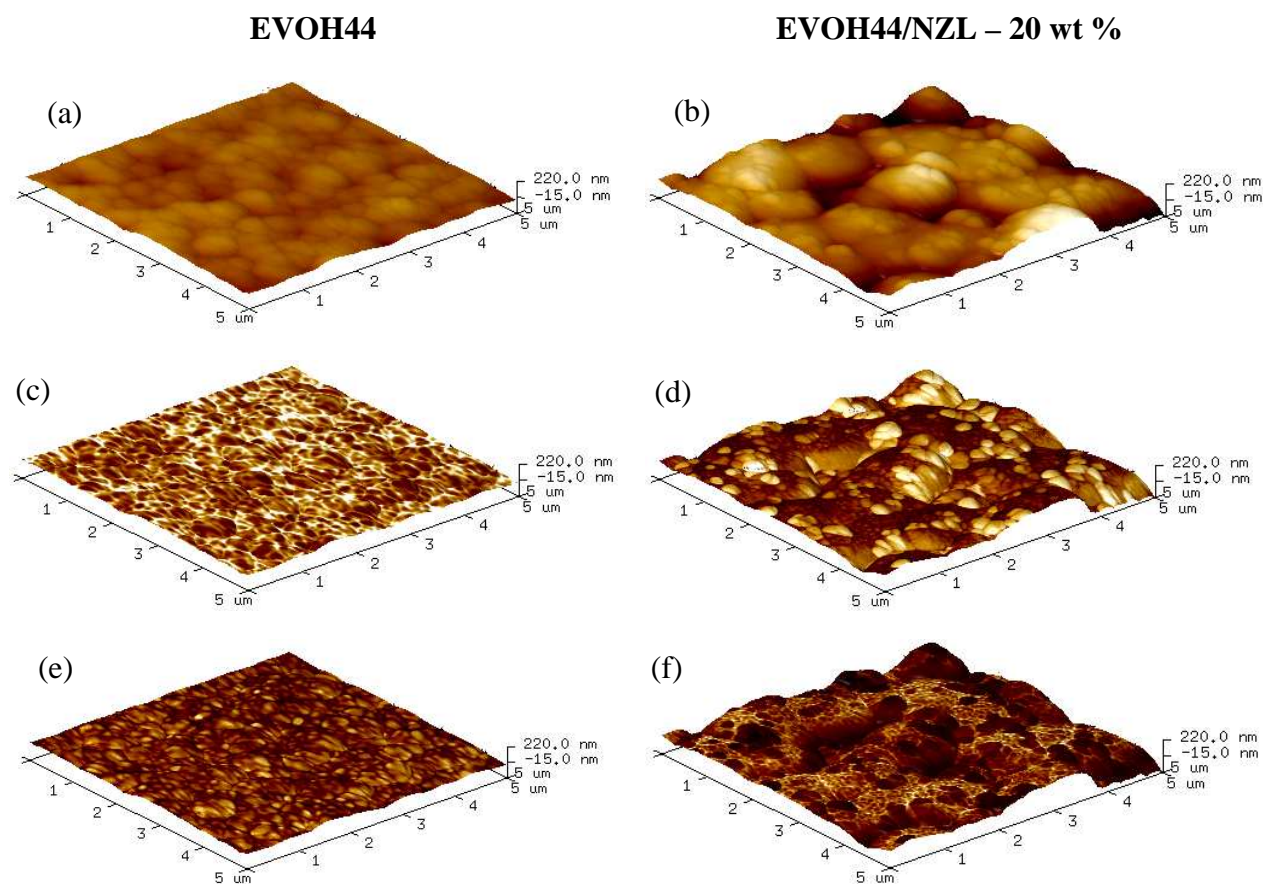


Fig.3.17. AFM 3D images of EVOH44(A) and EVOH44/NZL-20(A). Plot type: (a-b) height, (c-d) height mixed with modulus, (e-f) height mixed with adhesion.

The height images obtained in the case of an EVOH44 film and an EVOH44/NZL-20 nanocomposite film confirm the results of AFM experiments shown above (Fig.3.16.) with an increase of roughness.

Further, to observe the contrast between the particles and the polymer, the elastic modulus at the film surface was characterised in qualitative mode of AFM scanning. The colour contrast in this mode corresponds to the difference of values of the elastic modulus (in white, high modulus and in black, low modulus). The same colour code is also used for adhesion.

The 3D images mixing height and modulus (Fig.3.17.c-d) allow us to distinguish zeolite particles and polymer matrix at the surface of nanocomposite film. Fig.3.17.c,e (pristine EVOH44) displays very low contrast, whereas for the EVOH44/NZL nanocomposite, Fig.3.17.d-f shows an important contrast (it is recalled that the white spots correspond to the zeolite and high modulus regions, and dark areas are related to the polymer).

Fig.3.17.e,f shows 3D images of height mixed with adhesion. The same explanation can be given concerning the height-adhesion images, but with opposite colours.

In order to show the differences between the polymer and the zeolite nanoparticles 2D height-modulus image of an EVOH44/NZL-20 nanocomposite film is presented in Fig.3.18.

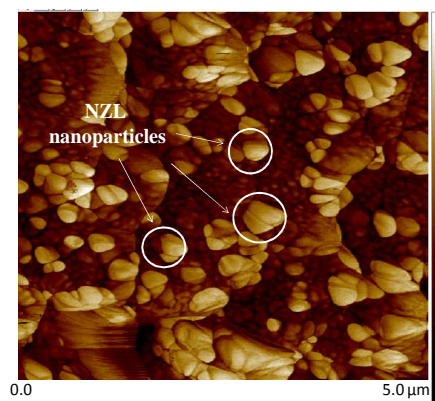


Fig.3.18. AFM 2D image of EVOH44/NZL-20 nanocomposite film. Height mixed with modulus (white circles indicate particles).

Particles with high modulus appear in white contrarily to the polymer matrix that appears in black.

These results confirm that nanoparticles are well distributed in the polymer nanocomposites.

2.3. ToF-SIMS surface characterisation

Time-of-Flight Secondary Ion Mass Spectrometry (ToF-SIMS) analysis was performed at the surfaces of EVOH44 and EVOH44/NZL-20 films in order to determine chemical composition and both, positive and negative secondary ions were acquired. This experiment was carried out at International Laser Centre.

Positive-ion characterisation

Positive-ion mass spectra of EVOH44 and EVOH44/NZL-20 film surfaces were recorded and are given in Fig.3.19.-Fig.3.20. For better observation, two mass windows are displayed, one below (Fig.3.19.) and one above 55 m/z (Fig.3.20.). Definitions of labelled peaks are also added at the right sides of the figures.

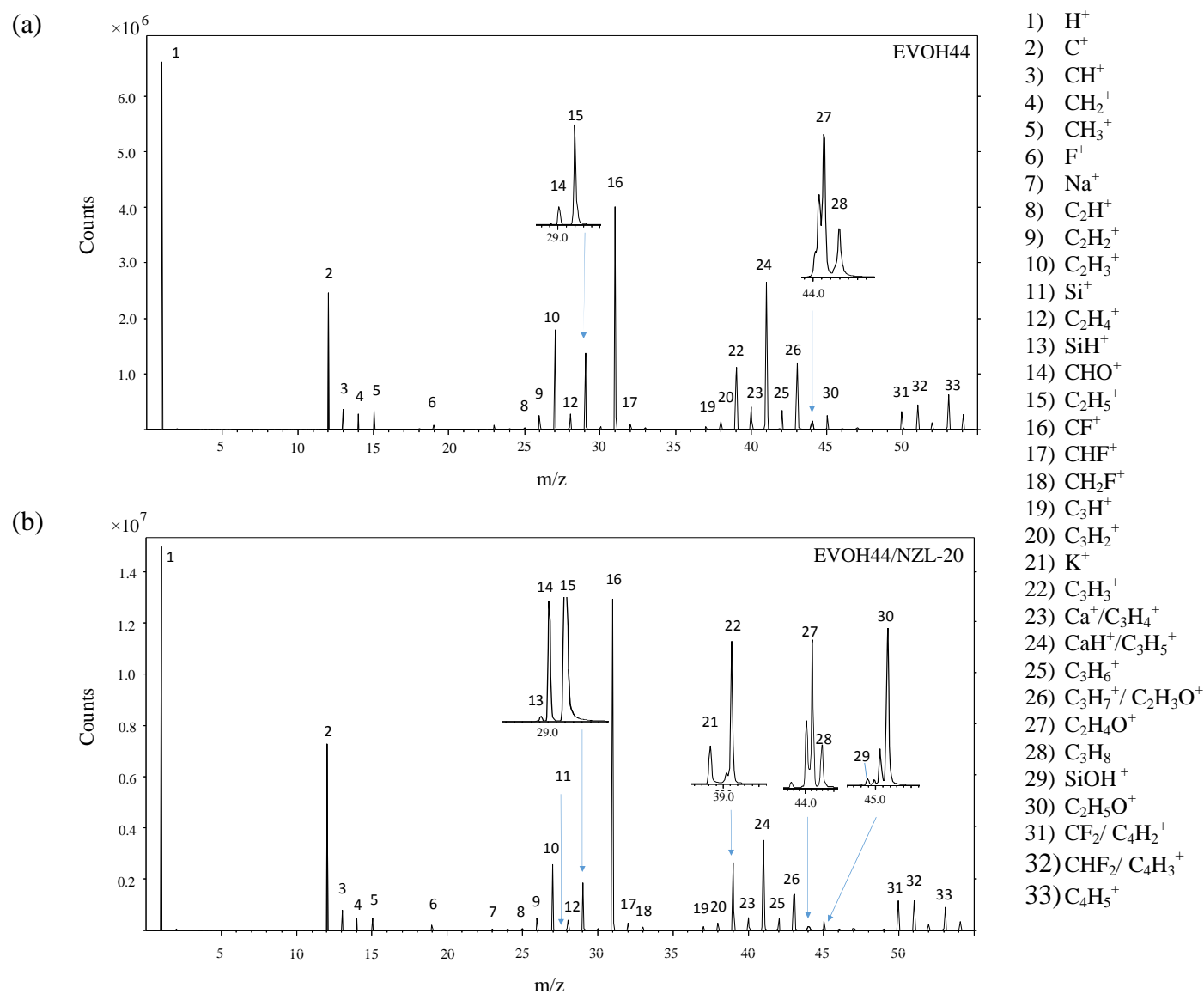


Fig.3.19. Positive-ion ToF-SIMS spectra of (a) EVOH44 and (b) EVOH44/NZL-20 processed by melt-mixing. Peak assignments are based on exact mass determination. Mass range 0-55 m/z.

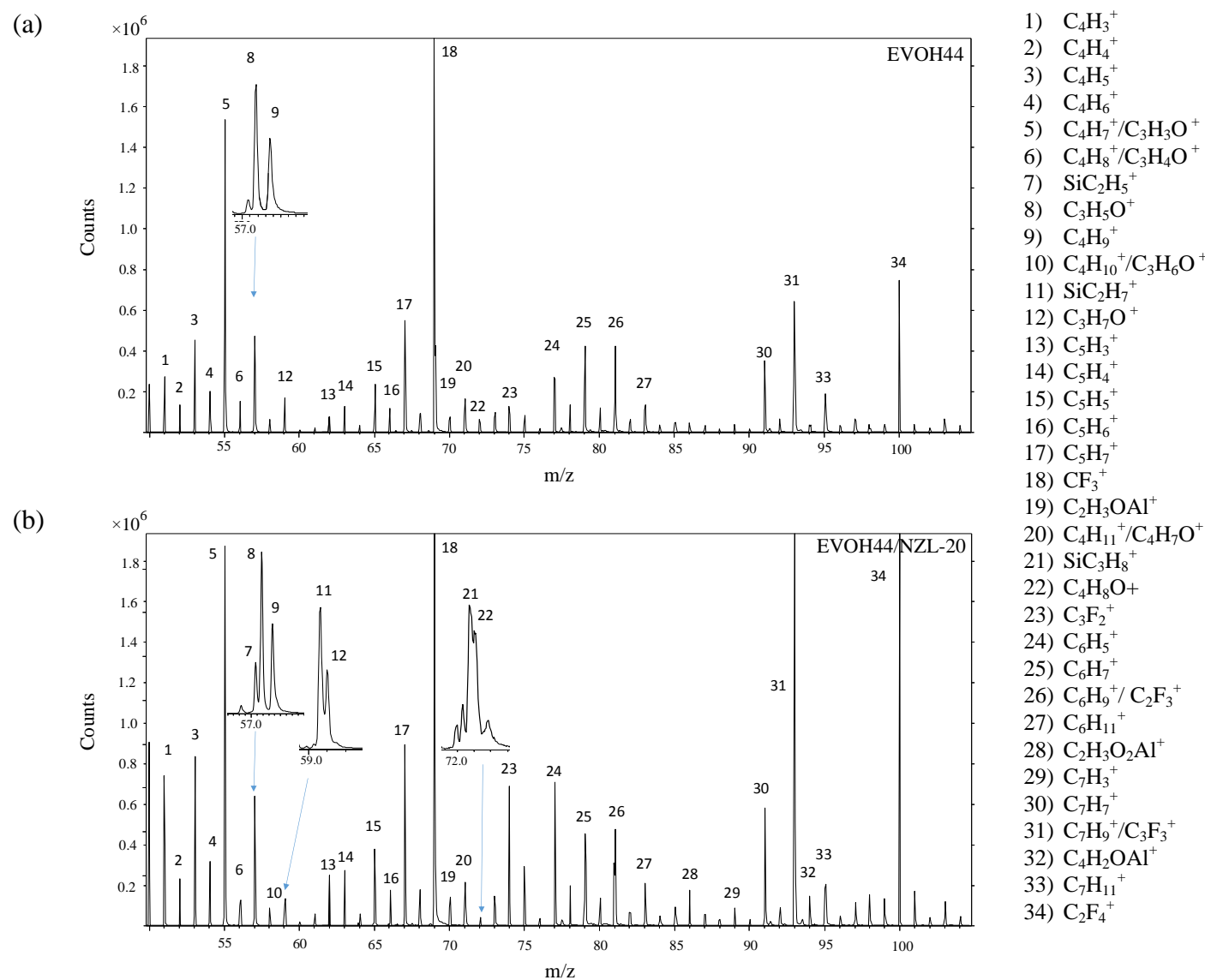


Fig.3.20. Positive-ion ToF-SIMS spectra of (a) EVOH44 and (b) EVOH44/NZL-20 processed by melt-mixing. Peak assignments are based on exact mass determination. Mass range 50-105 m/z.

The mass spectra of both, EVOH44 and EVOH44/NZL-20 exhibit the presence of fragment ions resulted from polymer chain fragmentation. These ions can be described by general formula $C_nH_y^+$ and $C_nH_yO_z^+$ where last mainly indicates fragments consist -OH groups, present in vinyl alcohol units of EVOH copolymer.

The presence of numerous F-contained ion fragments can be mentioned from the spectra. High peak intensities of these fragments can be explained by high relative sensitivity factor of fluorine detection. The formation of these ions might result from the fragmentation of additives, introduced into the polymer during the processing. It is known that fluoroelastomers or fluorothermoplastics based additives are commonly used for LDPE processing. One of commonly used chemicals is DynamarTM [270].

Thus, it can be considered that ions with formula $C_xF_y^+$ and $C_xH_yF_z^+$ are mainly related to present in EVOH polymer processing additives. This information has to be taken into account during the interpretation of degradation processes in EVOH and its nanocomposites. Comparing mass spectra, Si- and Al-contained positive ions were detected for EVOH/NZL nanocomposite, in contrast to EVOH44, where their intensity was comparable to the level of noise. K^+ , Na^+ and Ca^+ ions are also present in EVOH/NZL and were considered to come from the zeolite nanoparticles powder. Nevertheless, the ions related to zeolite fragmentation cannot be characterised like those of high intensity. In addition, the analysis in positive extractor mode does not detect the presence of any other metallic impurities like Cu, Zn, Co, Cd, Mn, Ni. This observation is in a good agreement with results of elemental analysis of zeolite powder given in Chapter III. § 1.2.

Negative-ion characterisation

Spectra recorded in negative polarity are more convenient to follow such elements as O, C, H and Si and thus, are more promising for the characterisation of EVOH composition and the presence of zeolite nanoparticles. Recorded negative-ion spectra of EVOH44 and EVOH44/NZL-20 are shown in Fig.3.21.-Fig.3.22. As in case of shown above positive-ion mass spectra, the obtained after surface bombarding negative ions are represented in two mass windows: 0-55 m/z (Fig.3.21.) and 55-105 m/z (Fig.3.22.). The high intensity ions and the ions of interest (ions related to zeolite nanoparticles) are labelled by numbers and described at the right sides of the figures.

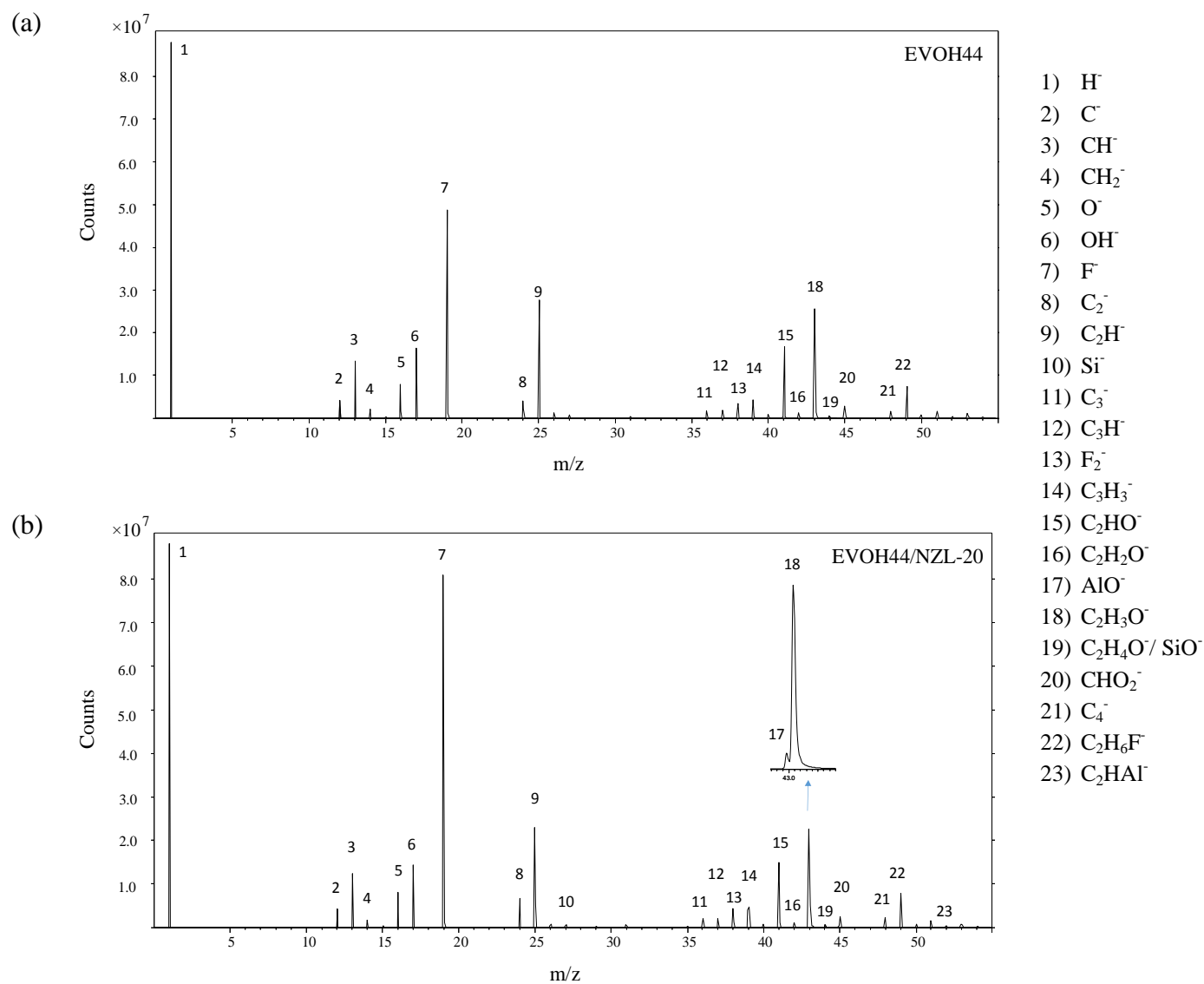


Fig.3.21. Negative-ion ToF-SIMS spectra of (a) EVOH44 and (b) EVOH44/NZL-20 processed by melt-mixing. Peak assignments are based on exact mass determination. Mass range 0-55 m/z.

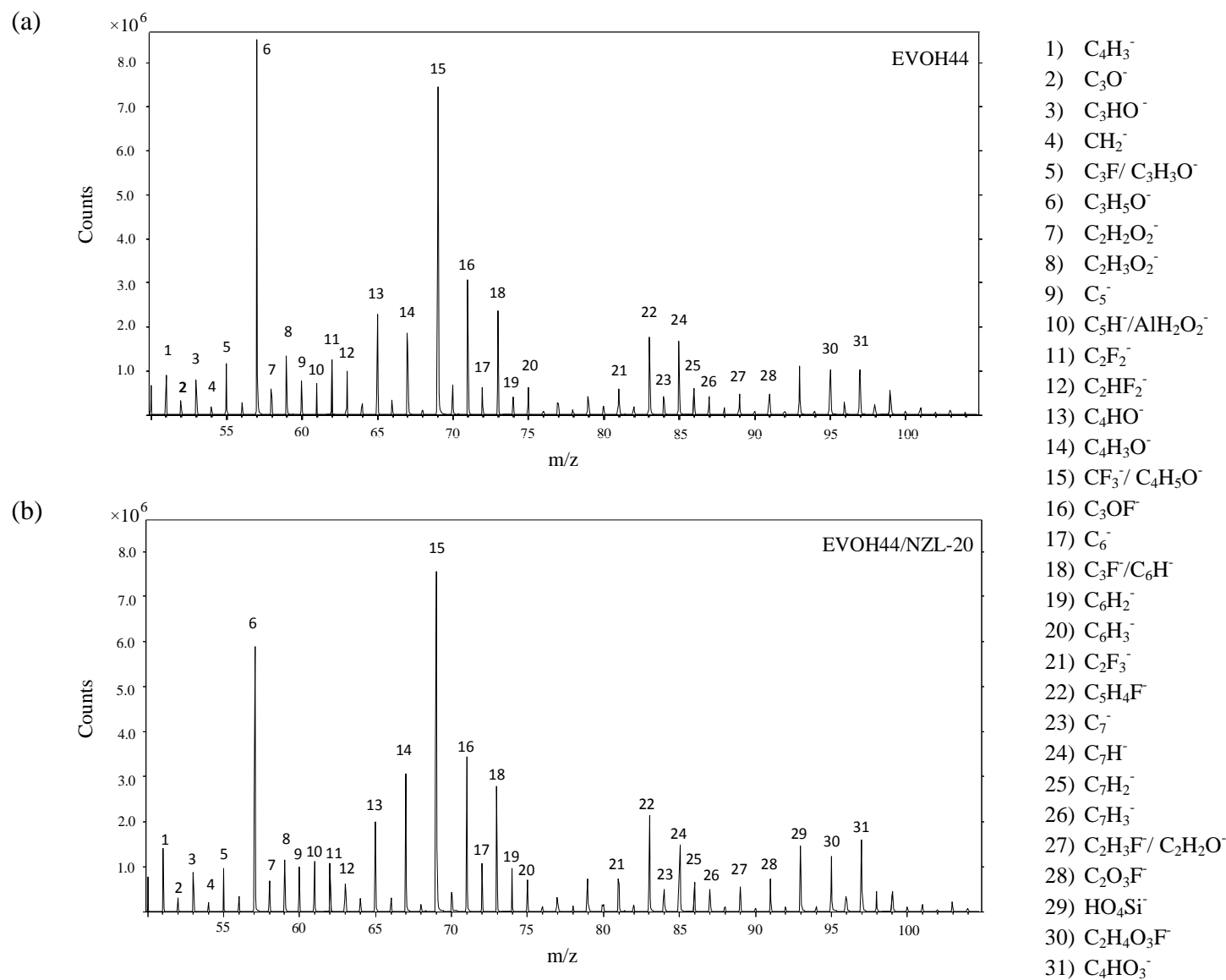


Fig.3. 22. Negative-ion ToF-SIMS spectra of (a) EVOH44 and (b) EVOH44/NZL-20 processed by melt-mixing. Peak assignments are based on exact mass determination. Mass range 50-105 m/z.

Mass spectra obtained in the negative field display similarities to those recorded in positive polarity. First, the presence of F-contained fragments ($C_xF_y^-$, $C_xH_yF_z^-$, $C_xH_yO_zF_t^-$) related to the introduced processing additives is observed. Second, $C_nH_y^-$ and $C_nH_yO_z^-$ ions indicate the fragmentation of the polymer chain. It can be mentioned that higher quantity of the oxygen contained ions ($C_nH_yO_z^-$) was detected in negative polarity in contrast to their appearance in positive field ($C_nH_yO_z^+$). Third, Si- and Al-contained ions indicate the zeolite particles in the EVOH/NZL.

Summarising both, negative and positive ion mass spectra, all detected patterns can be divided into 5 groups as it is described in Table 3.3.

Table 3.3. Ion groups determined during fragmentation of EVOH44 and EVOH44/NZL-20 nanocomposite in positive and negative polarity fields.

	Origin	Chemical compound(s)	Ion fragments
A	Small fragment ions resulted from sputtering		m/z <30 C,O,H,F or their combinations
B	Oxygen free EVOH chain fragments	* $-\left[CH_2-CH_2\right]_n-\left[CH_2-\underset{\substack{ \\ OH}}{CH}\right]_m^*$	C_xH_y x=2-7, y=1-11
C	Oxygen contained EVOH chain fragments		$C_xH_yO_z$
D	Fragments of processing additives	$C_xH_yF_z$ C_2H_4	F-contained ions C_xH_y x:(1-2)
E	Fragments of NZL zeolite nanoparticles	$[K_9(H_2O)_{16}][Si_{27}Al_9O_{72}]$	Na;K;Ca Si- and Al-contained ions

*determination of fragment for studied mass range (0-105 m/z).

First group (A) includes small fragment ions, originating from ToF-SIMS ionisation processes. It contains H, C, F, O, and their combinations of some (or all) of these elements. These elements are mostly located below m/z 40.

Second (B) and third (C) groups can be described by general formula C_nH_y and $C_nH_yO_z$ and are dominated by peaks originating from EVOH chain fragmentation. Ions from group B can be detected as well in positive as in negative detection mode, while group C is more visible in negative domain what can be explained by electronegativity of oxygen.

The last group E is resulted from the present zeolite nanoparticles and is detected just at EVOH/NZL film surfaces. The fragments of this group can be indicated by the presence of Si or Al in the detected pattern.

2.4. Viscoelastic properties

Viscoelastic behaviour of EVOH

The mechanical properties of both EVOH copolymers (EVOH27 and EVOH44) were studied by dynamic mechanical thermal analysis (DMTA). Taking into account the OSCs operation temperature that can rise up to 65 °C, a particular attention was paid to the behaviour of EVOH copolymers in the temperature range of 30 – 65 °C.

Fig.3.23. shows storage and loss moduli, and tan delta of both EVOH copolymers recorded in a tensile mode.

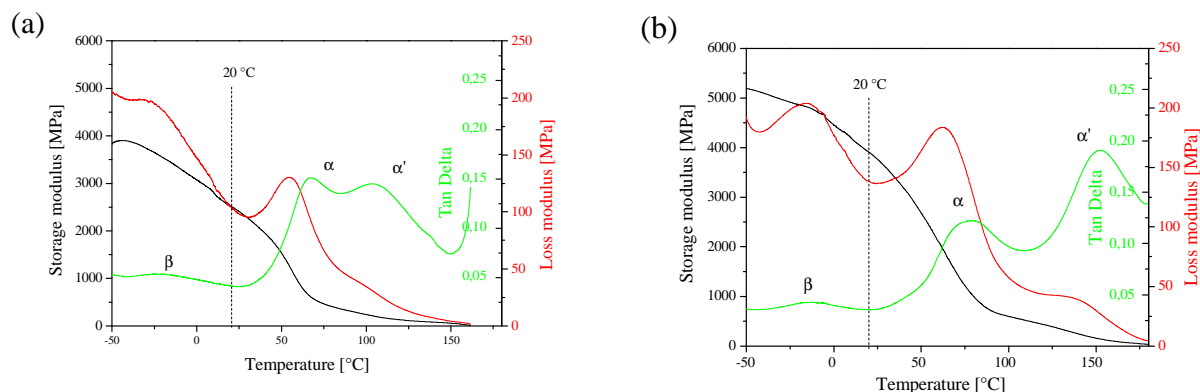


Fig.3.23. Temperature dependence of tan delta, storage and loss moduli in tensile mode for (a) EVOH44 and (b) EVOH27.

It is observed that the loss and storage moduli decrease with the temperature and reach a zero value, which corresponds to the behaviour of a liquid. On the loss modulus curves, we can observe three maxima, which are usually correlated to polymer transition phases. From tan delta curves it can be observed that both EVOH copolymers exhibit three transitions being named as β , α and α' for increasing temperatures ^[271, 272].

The β relaxation is usually related to the motions of pending groups. This relaxation, which has a relatively weak intensity, appears for EVOH copolymers at a temperature below 0 °C and characterises the behaviour of the polymer in the glassy state. The temperature location of the β peak observed for EVOH copolymers suggests a similar mechanism to that found in the

case of LDPE ^[273], the relaxation corresponds to motions of chain units in the interfacial region ^[274].

One of the main relaxations in EVOH, labelled α , is considered to be the glass transition temperature. As observed in Fig.3.23., the T_{α} increases for EVOH27, which is due to the higher amount of vinyl alcohol groups compared to EVOH44. This trend can be linked to the rigidity of vinyl alcohol groups and to the intermolecular hydrogen bonds ^[273].

The last relaxation observed at the highest temperature, called α' is usually related to the polymer melting. This relaxation is characteristic of crystalline and semi-crystalline polymers ^[244] and is associated with the slippage between crystallites. According to *Cerrada et al.* ^[273], α' -relaxation, which corresponds to motions within the crystalline phase of EVOH, is strongly related to the molecular orientation in the polymer, and is caused either by the relaxation of hydrogen bonds or by the movements close to the crystalline lamellar surface (translational, reorganisational and vibration motions within the crystals). Thus, it can be concluded that this transition can be strongly affected by the processing conditions and/or physical ageing. This transition temperature is higher for EVOH27 than for EVOH44. This can reflect the different size of crystallites.

The transition temperatures and values of viscoelastic moduli at 20 °C are presented in Table 3.4.

Table 3.4. Viscoelastic behaviour of EVOH copolymers: transition temperatures, storage, loss and Young's moduli.

	Transition Temperature[°C]			Viscoelastic moduli [MPa] at 20 °C		Young's modulus [MPa]
	β	α	α'	Storage	Loss	
EVOH44	-20	68	104	2495	100	2595
EVOH27	-14	76	152	3928	138	4066

Table 3.4. gives the values of the transition temperatures using tan delta curves. These results confirm the previous observations made from Fig.3.23. From the loss and storage moduli curves, the viscoelastic moduli at 20 °C have been obtained. From these values it is possible to calculate the Young's modulus of both EVOH copolymers. We can clearly see that EVOH27 presents a higher value of Young's modulus and this can be correlated to the higher concentration of vinyl alcohol groups and therefore hydrogen bonding.

Influence of water on the mechanical properties of EVOH

It is known that EVOH copolymers are sensitive to water molecules that act as plasticisation agent [275]. Water molecules, at high concentration, disrupt the existing hydrogen bounds, hence, decreasing inter- and intramolecular interactions in the polymer. As a result, understanding the moisture sorption effect on the mechanical performance of EVOH copolymers is of high interest to predict the polymer behaviour in service applications. The plasticisation effect is known to be higher for EVOH copolymers containing more vinyl alcohol in their composition [275]. Thus, the effect of ambient moisture has been investigated on EVOH27. Fig.3.24. shows the storage and loss moduli (Fig.3.24.a) and tan delta (Fig.3.24.b) for the EVOH27 films with different drying time (without drying corresponding to ambient moisture, 3 and 5 hours under vacuum at 60 °C).

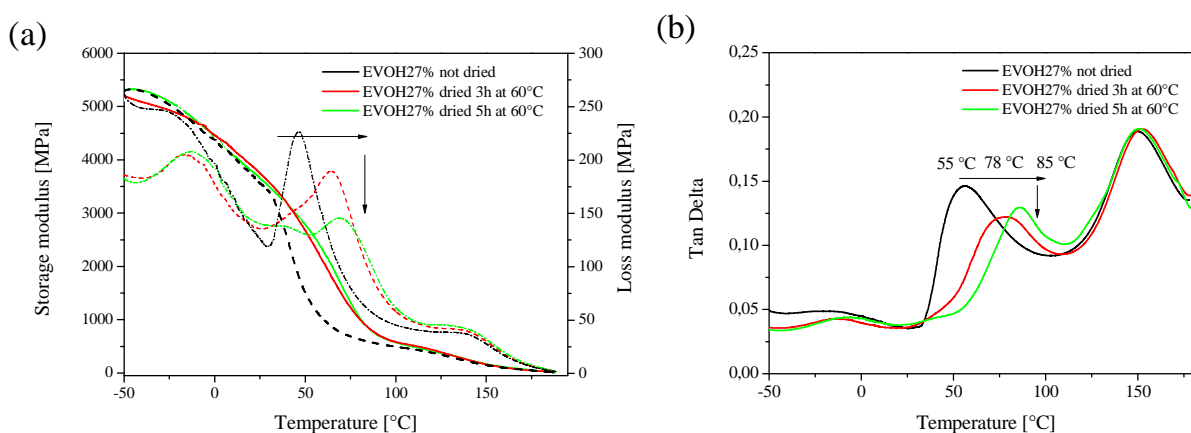


Fig.3.24. Dependence of viscoelastic properties of EVOH27 with different drying conditions: (a) storage (dash line) and loss (dotted line) moduli; (b) tan delta.

Fig.3.24.a shows that between 20 and 100 °C, an increase of the storage modulus is observed with drying time. Concerning the loss modulus, we can see a shift of the maxima to higher temperatures with increasing drying time. The shift of loss modulus peak is related to the shift of tan delta. In Fig.3.24.b, the maximum of tan delta peak is shifted from 55 to 85 °C upon drying. This maximum of tan delta corresponds to the glass transition temperature. As the glass transition temperature increases with drying, this indicates a plasticising effect of water in ambient conditions.

Influence of zeolite nanoparticles

One of the functions of encapsulation layers used for organic electronics is to provide support against the mechanical damage, but at the same time to keep the flexibility.

It is well known that nanoparticles can act as reinforcing agents for polymer materials, in particular enhancing/modifying the viscoelastic behaviour. The interaction of nanoparticles with a polymer can be repulsive, attractive, or neutral, and depending on these interactions, the T_g can decrease, increase, or remain constant.

DMTA was used as a tool to observe the changes in mechanical properties of EVOH with zeolite nanoparticles addition. Fig.3.25. compares the viscoelastic parameters of EVOH44 and EVOH44/NZL nanocomposites with 20 wt % of zeolite nanoparticles.

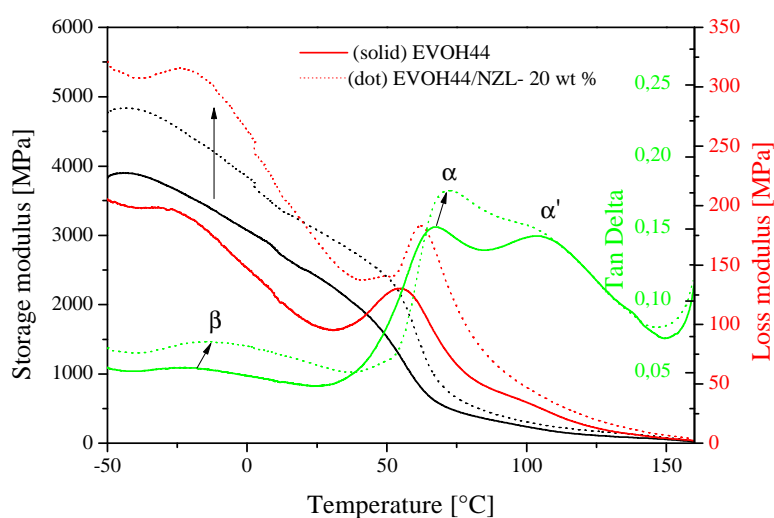


Fig.3.25. Temperature dependence of storage and loss moduli, and tan delta: comparison of viscoelastic behaviour of EVOH44 and EVOH44/NZL-20 nanocomposite.

As observed in Fig.3.25. nanocomposite films have higher storage and loss moduli than pristine EVOH44 films, which reflects the classical reinforcement effect of nanofillers.

The three main transition temperatures for EVOH44 and EVOH44/NZL-20 nanocomposite are given in Table 3.5. In order to compare the Young's modulus of pristine and filled EVOH at 20 °C, storage and loss moduli are also reported in Table 3.5.

Table 3.5. Viscoelastic behaviour of EVOH44 and EVOH44/NZL-20 nanocomposite: transition temperatures, storage, loss and Young's moduli.

Transition Temperature[°C]			Viscoelastic moduli [MPa] at 20 °C		Young's modulus [MPa]	
	β	α	α'	Storage		Loss
EVOH44	-20	68	104	2495	100	2595
EVOH44/NZL-20	-11	72	104	3550	240	3790

In table above, one can observe that the β and α transitions temperatures increase in presence of particles. This could be linked to the presence of interactions between NZL nanoparticles and the polymer. However, no change of $T_{\alpha'}$ is observed suggesting no influence of zeolite nanoparticles on the crystalline phase of EVOH.

In Table 3.5., the Young's moduli were calculated for EVOH44 and EVOH44/NZL-20 nanocomposite. We can see that the nanocomposite presents a higher value of Young's modulus and this can be correlated to the reinforcement effect of the filler.

2.5. Thermal properties

The effect of zeolite particles on EVOH thermal properties in nanocomposites was analysed by differential scanning calorimetry (DSC). The normalised DSC curves (corrected for a same polymer amount in each sample) obtained for first heating and cooling of EVOH44 and EVOH44/NZL (5-20 wt %) nanocomposites are shown in Fig.3.26.

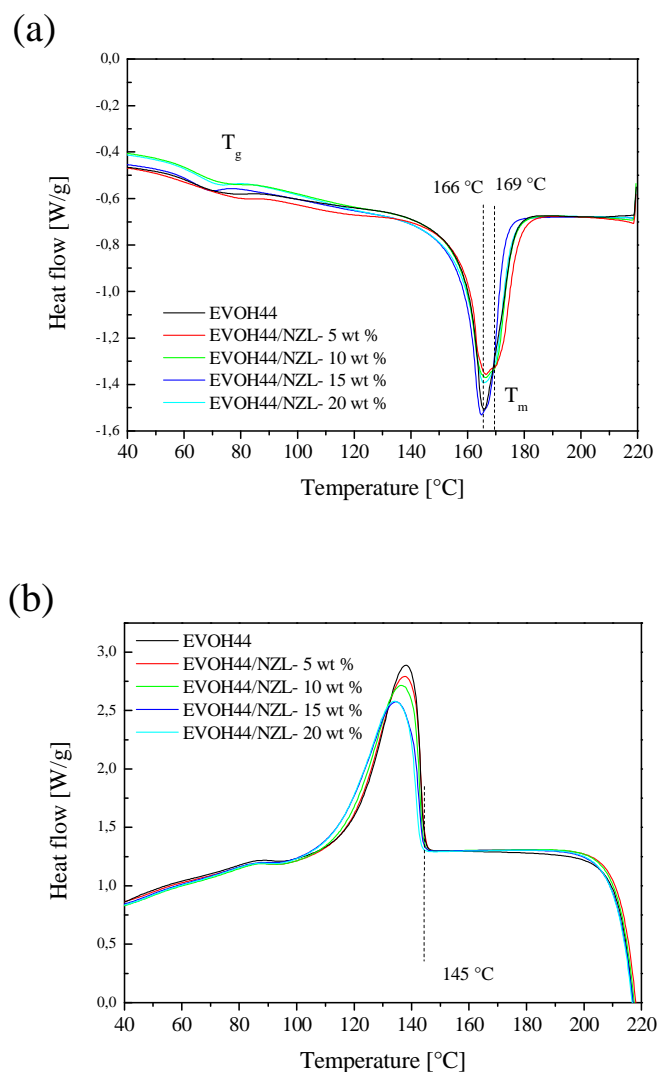


Fig.3.26. DSC curves for EVOH44 and EVOH44/NZL nanocomposites with different NZL loading (ramp 10 °C/min): (a) first heating; (b) cooling.

In the heating curves (Fig.3.26.a), an endothermic peak is observed. This peak with a maximum at 166 °C is related to the melting of the crystalline part of EVOH. Whatever the concentration of the filler is, the melting temperature does not change. However, the shape of the melting peak is modified in presence of zeolite nanoparticles. A shoulder appears around 169 °C. This can be correlated to the formation of different kind of crystals. From these curves the glass transition temperature (T_g) can also be observed. No evident modification of T_g is noticed in presence of zeolite nanofiller. In Fig.3.26.b, the curves corresponding to the cooling of the samples show that the presence of zeolite does not modify the onset temperature of the crystallisation peak but, it can be seen that the presence of particles decrease the enthalpy of crystallisation.

From the melting peak, the total crystallinity χ_c of EVOH in the presence or absence of filler can be obtained. The results are reported in Table 3.6.

Table 3.6. Thermal properties of EVOH44 and EVOH44/NZL nanocomposites during first heating run: temperatures of onset, endset and maximum of melting peak (T_m), crystallinity χ_c .

	$T_{g \text{ onset}} [^{\circ}\text{C}]$	$T_{m \text{ onset}} [^{\circ}\text{C}]$	$T_m [^{\circ}\text{C}]$	$T_{m \text{ endset}} [^{\circ}\text{C}]$	$\chi_c^{**} [\%]$
EVOH44	54±1	159±1	166±1	177±1	45±1
EVOH44/NZL-5 wt %	53±2	159±1	166±1	178±1	45±2
EVOH44/NZL-10 wt %	54±1	157±1	166±1	176±1	44±1
EVOH44/NZL-15 wt %	55±1	158±1	165±1	173±1	44±2
EVOH44/NZL-20 wt %	54±2	157±1	166±1	176±1	44±2

*each value is average of two measurements; calculated for the weight of EVOH in the sample

**using 100% pure crystalline PVA with $\Delta H_{m^{\circ}} = 157.8 \text{ J/g}^{[246]}$

In this table, it is shown that there is no evolution of both the crystallinity and the transition temperature. It can be concluded that the addition of the zeolite filler does not modify the thermal properties of the EVOH polymer matrix.

The results obtained for the cooling are presented in Table 3.7.

Table 3.7. Thermal properties of EVOH44 and EVOH44/NZL nanocomposites during cooling: temperatures of onset, endset and maximum of crystallisation peak (T_c), enthalpy of crystallisation (ΔH_c).

	$T_{\text{endset}} [^{\circ}\text{C}]$	$T_c [^{\circ}\text{C}]$	$T_{\text{onset}} [^{\circ}\text{C}]$	$\Delta H_c [\text{J/g}]$
EVOH44	145±1	138±1	119±1	70±1
EVOH44/NZL-5 wt %	145±1	137±1	118±1	70±1
EVOH44/NZL-10 wt %	144±1	135±1	114±2	70±1
EVOH44/NZL-15 wt %	144±1	134±1	112±1	67±1
EVOH44/NZL-20 wt %	144±1	133±1	111±1	65±2

*each value is average of two measurements; calculated for the weight of EVOH in the sample

Table 3.7. shows that the addition of particles has no effect on the endset temperature of crystallisation. However, the presence of zeolite nanoparticles results in a decrease of the

onset (T_{onset}) and maximum (T_c) temperatures of the peak. It can be explained by the different populations of crystals formed during cooling for EVOH44 and EVOH44/NZL nanocomposites.

It can also be noticed that the cooling peak for the nanocomposite samples does not have the second shoulder that had been observed during heating. Additionally, the presence of particles leads to a decrease of crystallisation enthalpy (ΔH_c).

2.6. Water sorption properties

Zeolites exhibit good water sorption characteristics displaying Langmuir sorption isotherm, and are commonly used as desiccant materials. The water sorption properties of the EVOH/zeolite nanocomposites were characterised by gravimetric immersion water uptake (IWU) and were compared to those of pristine EVOH.

2.6.1. Gravimetric immersion water uptake (IWU)

The influence of particle content in EVOH44/NZL nanocomposites on water sorption was studied by performing water uptake experiment by immersion of films into water at ambient temperature.

Water sorption of EVOH44

At first, we present the water sorption curve obtained in the case of an EVOH44 film with a thickness of 104 microns and a dry mass of 79.6 mg. The water sorption curve obtained from the gravimetric data of an EVOH44 film is presented in Fig.3.27. The water mass gain was obtained by dividing the measured mass gain by the dry mass of the sample before immersion and was plotted as a function of immersion time (Fig.3.27.a). The relative water sorption (M/M_{eq}) was obtained by dividing the water mass by the water uptake M_{eq} and was plotted as a function of the square root of time (Fig.3.27.b) to characterise the diffusion behaviour of water in this EVOH44 copolymer.

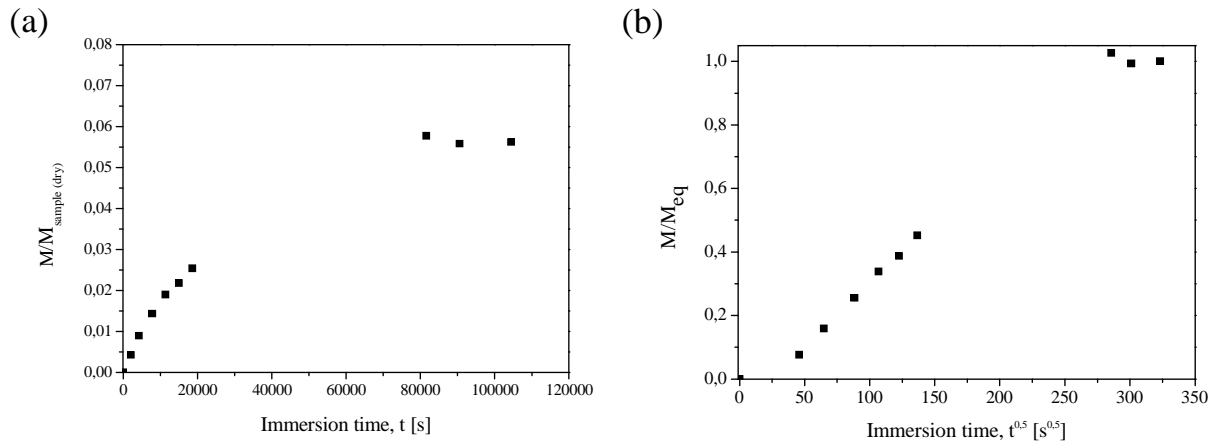


Fig.3.27. Water sorption curve of an EVOH44 film (weight 79.6 mg) in water at 25 °C: (a) water mass gain as a function of time; (b) normalised water sorption as a function of the square root of time.

As can be seen in the Fig.3.27.a, water mass gain starts to increase linearly with time. After this first initial stage, the rate of water uptake decreases gradually until it reaches the asymptotic constant equilibrium value (M_{eq}).

From Fig.3.27.a, the water uptake (%) of EVOH44 can be determined at the plateau, giving M_{eq} value of 5.7 %.

Fig.3.27.b shows that the curve presents a linear shape in a first phase. This reflects a Fickian behaviour, as reported in the literature^[249]. Assuming that classical Fickian diffusion takes place, water diffusion coefficient may be calculated from the initial linear part of the curve shown in Fig.3.27.b using Eq.2.13.

$$D = \pi \frac{l^2}{16} b^2 \quad (\text{Eq.2.13.})$$

where b is the slope of the linear portion of the curve at the beginning of the sorption phenomena. The measured slope was $4.1 \times 10^{-3} \text{ s}^{-0.5}$. Considering a sample thickness of 79.6 microns ($79.6 \times 10^{-4} \text{ cm}$), this gives a diffusion coefficient of $3.6 \times 10^{-10} \text{ cm}^2 \text{ s}^{-1}$.

Influence of zeolite loading on water sorption by EVOH44/NZL nanocomposites

The influence of zeolite loading on the water sorption properties of the nanocomposites was then studied in the case of EVOH44 copolymer with increasing NZL loadings ranging from 5 wt % to 20 wt %. The obtained data were processed following the same way as described just above and are plotted in Fig.3.28. The water mass gain as a function of time is given in

Fig.3.28.a and the relative water sorption as a function of the square root of time is given in Fig.3.28.b.

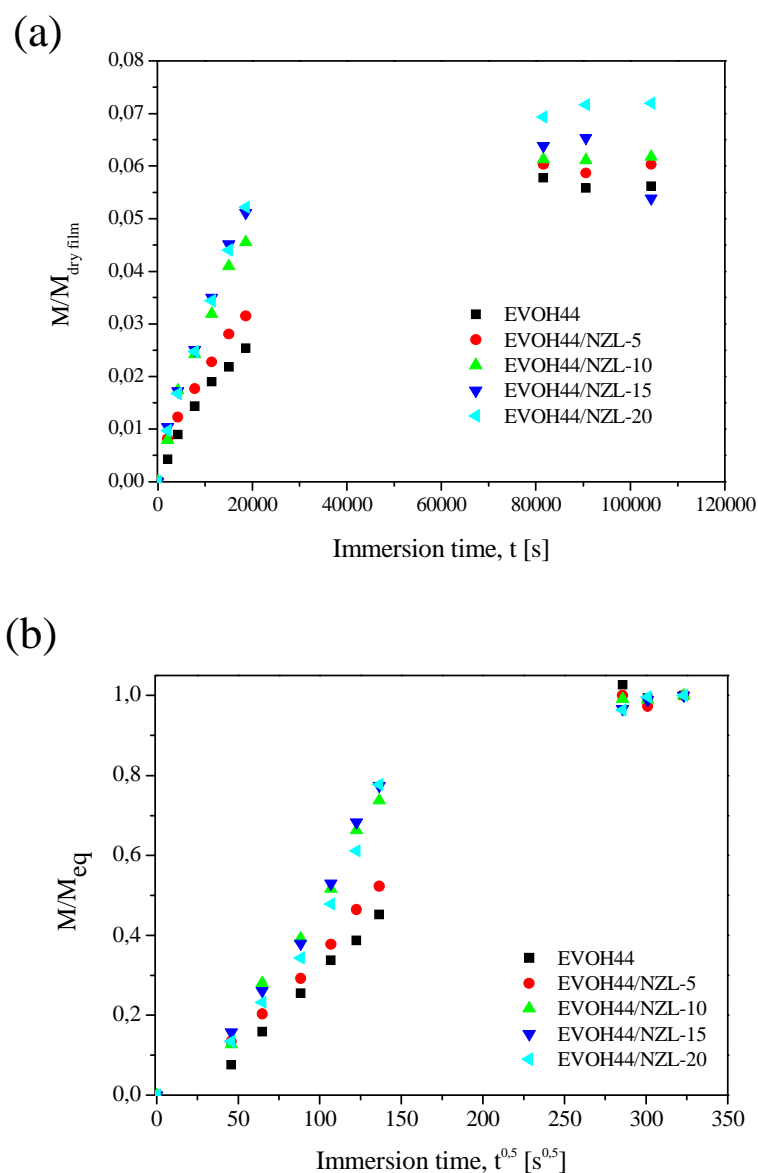


Fig.3.28. Water sorption curves of EVOH44/NZL nanocomposite films (with NZL loadings from 0 to 20 wt %) in water at 25 °C: (a) water mass gain as a function of time; (b) normalised water sorption as a function of the square root of time.

Adding zeolite nanoparticles to EVOH44 has an effect on the water uptake EVOH44/NZL nanocomposites (Fig.3.28.a). The water uptake progressively shifts from 5.7 % in the case of neat EVOH44 up to 7.3 % for 20 wt % NZL loading. The behaviour observed in the case of nanocomposites can be attributed to both the water uptake by the polymer and the water uptake by the zeolite water getter.

Fig.3.28.b shows a Fickian behaviour for all the analysed samples at least in the first period. One can then determine the diffusion coefficients for all the nanocomposites. The results are gathered in Table 3.8. This table also indicates the thickness of the samples and the sample dry mass (M), (in the case of the nanocomposites, this is the weighted mass of the sample).

For NZL loadings higher than 5 wt %, the relative water sorption curves show two different linear slopes, the one used to calculate D (short immersion times) and a higher slope for time $t^{0.5} > 100 \text{ s}^{0.5}$, which did not receive any explanation.

After prolonged exposure beyond the time for the equilibrium state, certain polymer systems are known to start losing mass due to chemical degradation. In such case, there is an additional stage in the curve which is for a lowering in M after “equilibrium”. This mass loss is mainly caused by decomposition of the low-molecular-weight constituents leading to leaching of species (ions) into the water medium.

Table 3.8. Water uptake and diffusion coefficient for EVOH44/NZL nanocomposites (25 °C, 100 % RH).

EVOH/NZL nanocomposites	l [μm]	M [mg]	Water uptake [%]	Slope, b [$10^{-3} \text{ s}^{-0.5}$]	D [$10^{-10} \text{ cm}^2\text{s}^{-1}$]
EVOH44	104	79.6	5.7	4.1	3.6
EVOH44/NZL-5	96	80.0	5.9	4.3	3.4
EVOH44/NZL-10	79	78.4	6.1	6.7	5.5
EVOH44/NZL-15	80	81.7	6.4	6.9	6.0
EVOH44/NZL-20	92	80.5	7.3	6.9	7.8

The results given in Table 3.8. indicate a weak increase of the water diffusion coefficient with NZL loading. At the same time the water uptake also increases with NZL loading, which reflects the water getter property of zeolites. This results from a faster trapping of water molecules in the case of nanocomposites. It has however to be mentioned that the results obtained in the case of the nanocomposites reflect the transport of water in both the polymer and the zeolite, which should be treated using different theoretical models. This needs further experimentations (determination of sorption isotherms) and complementary concepts.

2.6.2. Dynamic vapour sorption analysis (DVS)

The water sorption properties of EVOH44 and nanocomposites with 5 % and 20 % of NZL nanoparticles were also studied by dynamic vapour sorption analysis at 38 °C/85 RH %. The DVS analysis was very recently performed, because the DVS apparatus was set up at the end of this PhD work. The experiments were not repeated and should be considered as preliminary results and will not be discussed in this manuscript. Only the results obtained in the case of EVOH 44 will be presented in the manuscript and for seek of clarity, this issue will be presented in Chapter IV § 2.3, which deals with the influence of photooxidation on the water sorption properties and will not be discussed in this manuscript.

CONCLUSIONS

This chapter was devoted to the characterisation of the properties of EVOH/zeolite nanocomposites, based on two different copolymers (EVOH27 and EVOH44) with various amounts of zeolites nanoparticles (NZL) and microparticles (DISC).

The characterisation by UV-Visible absorption spectroscopy has shown that EVOH/NZL nanocomposites films remain transparent in the visible domain, which, considering the required optical properties, makes these materials suitable for encapsulation of OSCs.

SEM and TEM observations have shown that NZL nanoparticules are well dispersed and homogeneously distributed in the whole film thickness up to 20 wt % loading processed by DMSO solution mixing (method A). At opposite EVOH/DISC composites exhibit poor dispersion and sedimentation occurs with method A.

DSC analysis did not reveal any observable nucleation effect of the zeolite nanoparticles on the polymer matrix, but at the same time attractive interactions between particles and polymer can be observed by DMTA. Introduction of zeolite nanoparticles led to a reinforcement with an increase of the viscoelastic moduli, the reinforcement being an important parameter for maintaining structural support of OSCs encapsulation.

AFM analysis has shown that the presence of NZL has a strong influence on the surface properties of film, and in particular, by increasing the roughness.

Experiments described in this chapter show the plasticising effect of the water. Adding 20wt % of NZL particles in EVOH matrix results in increased water uptake and diffusion coefficient, which leads to a faster trapping of water molecules. These observations bring to the conclusion that EVOH/NZL nanocomposite can be a good material as a water getter for encapsulation coatings of water sensitive OPV.

To achieve an EVOH/zeolite nanocomposite with transparency, mechanical and water sorption properties, 20 wt% of NZL zeolite nanoparticules dispersed in EVOH44 through DMSO solution mixing (method A) gives nanocomposites films with the required properties, although EVOH27 would give smoother surfaces.

The next step is then to study the photochemical behaviour of EVOH and zeolite nanocomposites to determine the "best" nanocomposite composition and processing method

on the point of view of durability of the properties. The strong and the weak points of the materials and possible failure mechanisms will be studied in the next chapter.

CHAPTER IV:
PHOTOCHEMICAL BEHAVIOUR OF
EVOH AND NANOCOMPOSITES

INTRODUCTION

This chapter is devoted to the study of the photochemical behaviour of EVOH and EVOH/zeolites nanocomposites exposed to UV light in the presence of oxygen, in conditions of artificial accelerated weathering. It aims to understand the impact of the zeolite particles on the photochemical behaviour of the materials. From a general point of view, a drawback to the use of nanoparticles is their negative impact on the photostability of the polymer. The addition of particles to polymers has been indeed shown many times to affect the photostability of the nanocomposites. While inorganic particles rarely experience significant photodegradation under sunlight exposure, they can change the mechanisms and/or the rate of photooxidation of the polymer matrix and must therefore always be accounted for when determining the photostability of the nanocomposite.

In a first part, we will focus on the photooxidation of EVOH under UV-Visible light irradiation ($\lambda > 300$ nm). The main objective is to identify different products of oxidation, as well the macromolecular products as the molecular trapped in the solid polymer matrix or the volatiles migrating to the gas phase surrounding the material. For this purpose, measurements involving spectroscopic analysis (UV-visible and IR), SPME (solid phase microextraction) and ionic chromatography will be performed. Two copolymers were investigated, EVOH44 and EVOH27, which allowed us to highlight the influence of the ethylene content. On the basis of the identification of the photoproducts, we will propose a comprehensive mechanism accounting for the photochemical degradation of EVOH copolymers.

In a second part, the photochemical behaviour of new EVOH nanocomposites based on zeolite particles processed by solution or melt-mixing will be reported. The attention was mainly focused on composites with EVOH44. The influence of zeolite particles with different size (nano vs. macro) and loading increasing loading on the photooxidation of EVOH is studied, using the analytical techniques reported just above. This study was completed by the analysis of the consequences of ageing on the surface morphology of the materials, using SEM, AFM and ToF-SIMS. The modifications of thermo-mechanical, thermal and water barrier properties resulting from photoageing were also followed, using DMTA, DSC and DVS analysis.

The work reported in this chapter aims to propose nanocomposite coatings for flexible solar cells taking into account the photostability of the barriers used for encapsulation.

1. PHOTOCHEMICAL BEHAVIOUR OF EVOH

To study the photochemical behaviour of EVOH in the presence of oxygen and the influence of the ethylene content on the mechanism and rate of photooxidation, films of both EVOH (EVOH44 and EVOH27) with thickness of 20-60 μm (prepared by solution mixing (method A)) were irradiated under artificial accelerated photoageing conditions in presence of air (see Ch. II § 2.1.).

1.1. UV-Visible analysis

The UV-Visible spectra of EVOH44 and EVOH27 films show a shift in absorbance to longer wavelengths without any defined maximum (Fig.4.1.). The increase of absorbance is however limited below 400 nm, and even after 750 h of exposure, both EVOH films do not show any absorption above this wavelength, in other terms no yellowing is observed and the samples remain transparent in the visible domain.

One can notice that differences between the two materials in term of kinetic evolution, since the modification of the spectrum of EVOH44 occurs at a higher rate than for EVOH27.

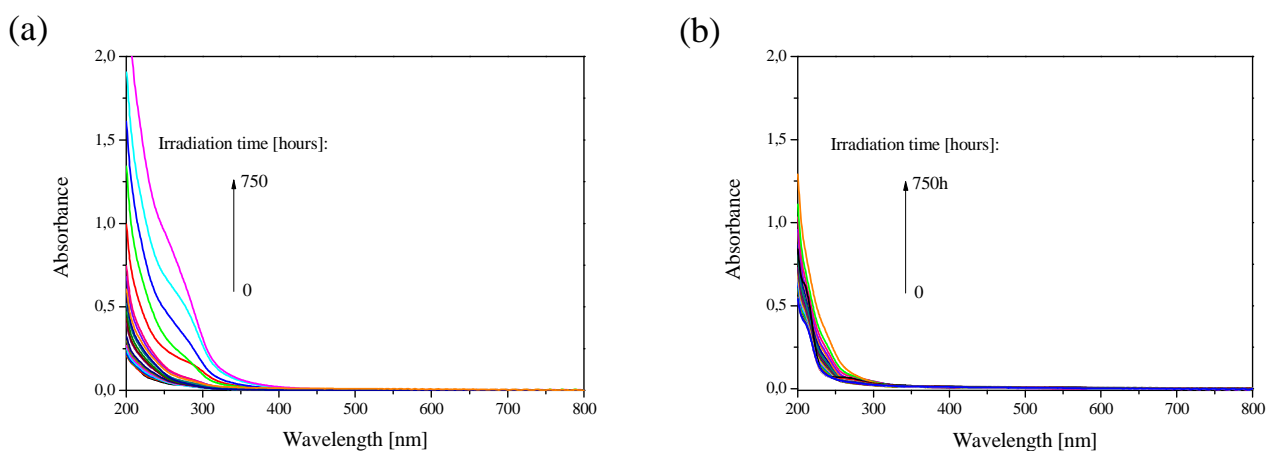


Fig.4.1. UV-Visible spectra of EVOH films during photooxidation: (a) EVOH44; (b) EVOH27.

1.2. IR analysis

The chemical changes resulting from irradiation of EVOH44 and EVOH27 were studied by infrared spectroscopy (IR). IR spectra during photooxidation for films of both samples are shown in Fig.4.2.

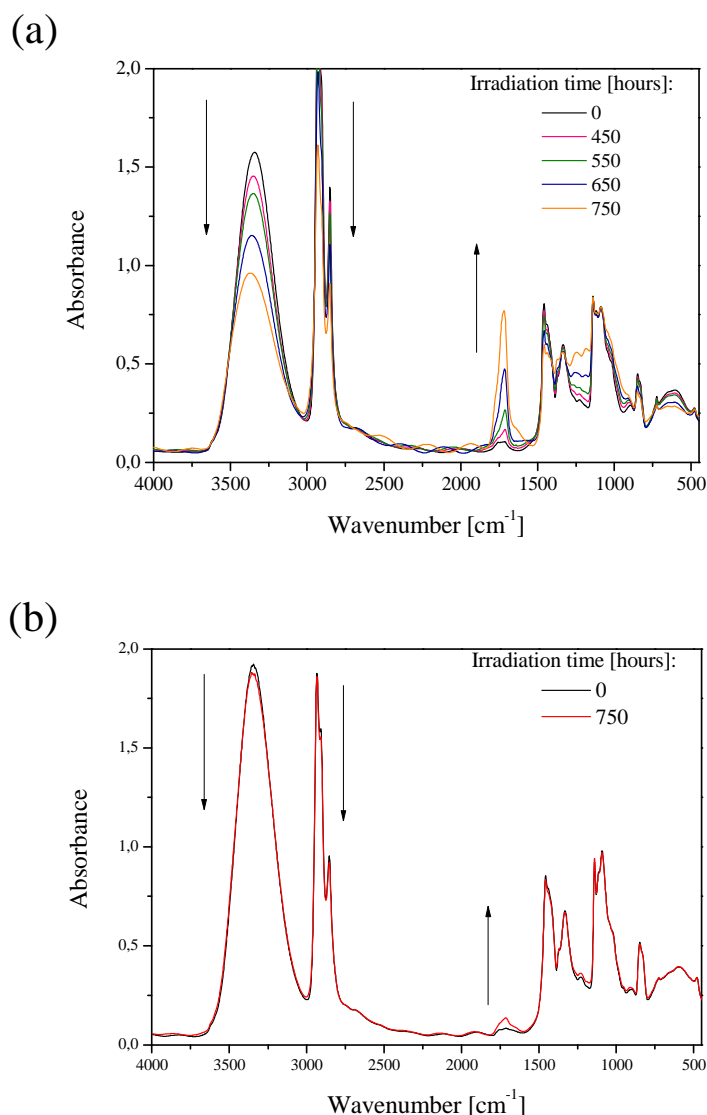


Fig.4.2. FTIR spectra of EVOH films during photooxidation: (a) EVOH44; (b) EVOH27.

Irradiation of EVOH44 in presence of air provokes dramatic modifications of the IR spectra, as shown in Fig.4.2.a after 750 h of exposure, whereas few changes appear in the spectra of EVOH27 (Fig.4.2.b) after the same irradiation time. The main modifications observed for EVOH44 are in the hydroxylated and the carbonylated domains, which reflects the oxidation of the polymeric matrix. Fig.4.2.b shows that the IR spectrum of EVOH27 is also modified in these domains, but at a lower extent. EVOH27 is less sensitive to photooxidation, which can be linked to the higher concentration of ethylene unit, “PE unit”, in EVOH44. It is known that PE degrades much more faster upon irradiation than PVA [276].

1.3. Identification of photooxidation products

In order to elucidate the photooxidation mechanism of EVOH copolymers, different methods and techniques were applied to EVOH44 films to identifying the photoproducts formed during exposure.

1.3.1. IR analysis

Fig.4.3. displays the subtracted IR spectra of EVOH44 photooxidation in the hydroxylated ($3650\text{-}2750\text{ cm}^{-1}$) and the carbonylated domain ($1850\text{-}1550\text{ cm}^{-1}$) after various irradiation times between 0 and 750 h. This facilitates observing the modifications of the spectra resulting from exposure.

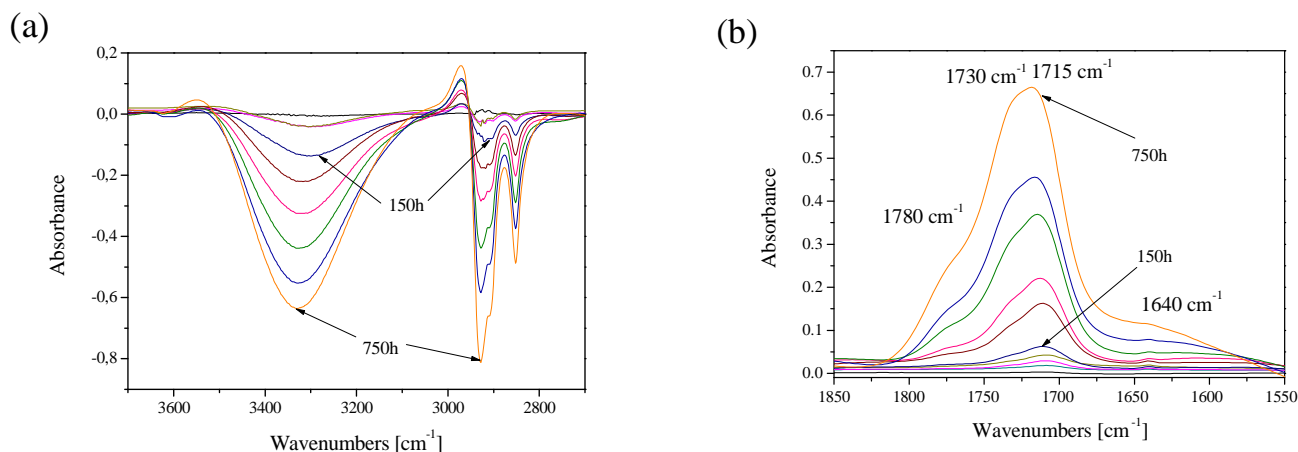


Fig.4.3. FTIR subtracted spectra of EVOH44 film during photooxidation:
(a) $3650\text{-}2750\text{ cm}^{-1}$; (b) $1850\text{-}1550\text{ cm}^{-1}$.

The main changes correspond to a decrease of R-OH (3350 cm^{-1}) and C-H (2930 , 2910 , 2852 cm^{-1}) vibration bands (Fig.4.3.a) and an increase in the carbonylated domain ($1600\text{-}1800\text{ cm}^{-1}$) (Fig.4.3.b) related to the formation of a broad band with a maximum at 1715 cm^{-1} and two shoulders with maxima around 1730 cm^{-1} and 1780 cm^{-1} .

These modifications of the infrared spectra fit quite well those reported in the case of polyethylene photooxidation ^[183, 277]. Formation of absorption bands at 1640 cm^{-1} and 910 cm^{-1} can also be noticed and can be attributed to double bonds, as also observed in the case of PE photooxidation ^[276]. These results indicate that the photooxidation of EVOH44 is similar to that of PE.

1.3.2. Chemical treatment

In order to identify the carbonylated photoproducts observed by IR analysis of the films, chemical derivatisation treatments by ammonia (NH_3) (Fig.4.4.) and 2,4-dinitrophenylhydrazine (2,4-DNPH) were performed (Fig.4.5. and Fig.4.6.) on photooxidised EVOH films. As described in the experimental part (Chapter II), NH_3 reacts with carboxylic acids and esters, and 2,4-DNPH reacts with aldehydes or ketones ^[237].

NH_3 treatment

The IR spectra recorded after treatment by NH_3 of a photooxidised EVOH44 film (after 155 h of exposure) are displayed in Fig.4.4.

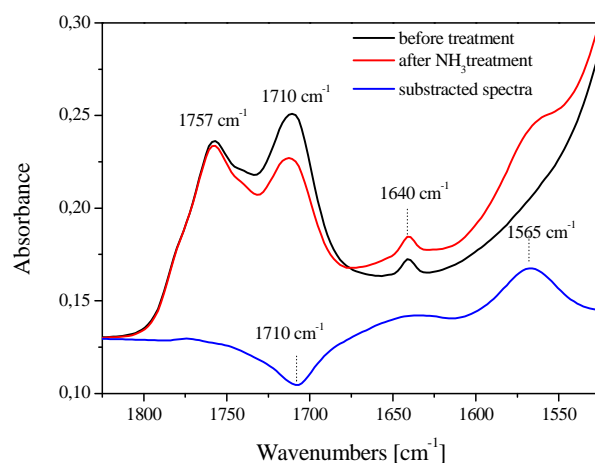


Fig.4.4. Derivatisation treatment with NH_3 of a photooxidised EVOH44 film (155 h of photooxidation). FTIR spectra before (black) and after 1h of NH_3 treatment (red), subtracted spectra after-before (blue).

A decrease of absorbance at 1710 cm^{-1} , associated with the appearance of an absorption band at approximately 1565 cm^{-1} is observed. On the basis of the numerous publications on NH_3 derivatisation treatments ^[278-280], these modifications reflect the reaction of carboxylic acids in the dimer form (observed at 1710 cm^{-1}) with NH_3 to form carboxylates (1565 cm^{-1}).

2,4-DNPH

Reactions with 2,4-DNPH of either aldehydes or ketones give derivatives of 2,4-dinitrophenylhydrazones ^[238]. The spectral modifications in IR and in UV-Visible domains after the treatments of photooxidised films of EVOH44 and EVOH27 can be observed respectively in Fig.4.5. and Fig.4.6.

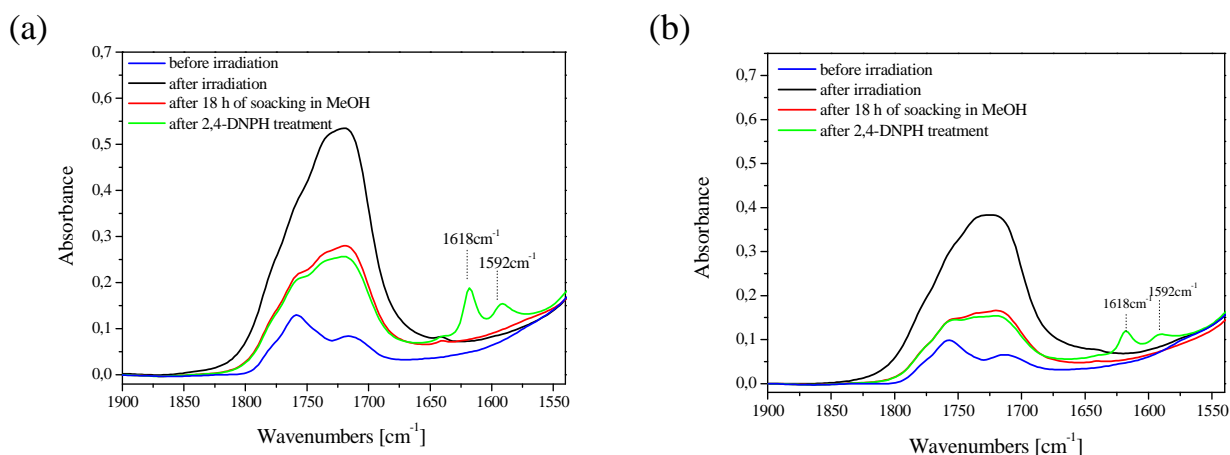


Fig.4.5. FTIR spectra of 2,4-DNPH treatment of (a) EVOH44 and (b) EVOH27 photooxidised 230 h and 380 h respectively. FTIR spectra before irradiation (blue), before treatment (black), after 18 h of soaking in MeOH (red) and after 2,4-DNPH treatment (green).

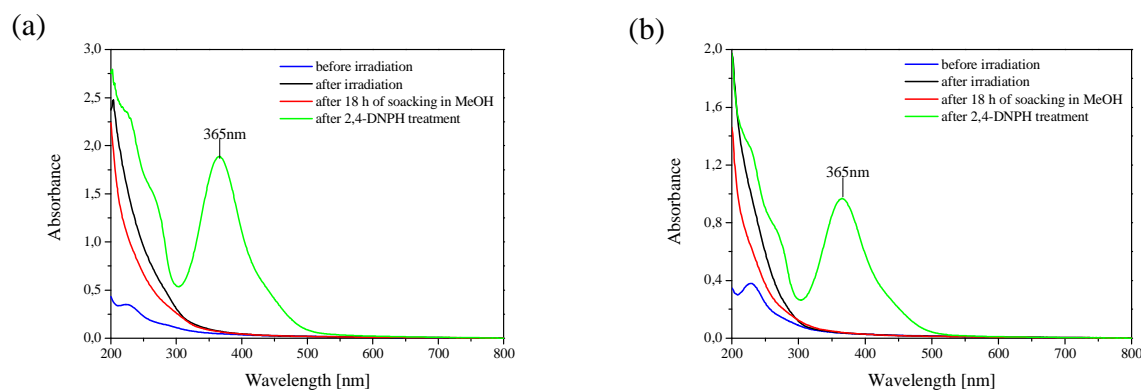


Fig.4.6. UV-Visible spectra of 2,4-DNPH treatment of (a) EVOH44 and (b) EVOH27 photooxidised 230 h and 380 h respectively: before irradiation (blue); before treatment (black), after 18 h of soaking in MeOH (red), after 2,4-DNPH treatment (green).

As explained in Ch. II, the DNPH treatment was performed following two successive phases: at first, an immersion in MeOH to extract the low-molecular-weight soluble products, trapped in the polymeric matrix, and then immersion in a methanolic solution of DNPH. The modifications of IR spectra observed in Fig.4.5. show a decrease of the whole carbonyl band, which indicates that some MeOH soluble products were removed. Then, a small decrease of the absorbance is observed with the simultaneous appearance of two absorption bands at 1618 cm^{-1} (C=N in hydrazone) and 1592 cm^{-1} ($\nu(\text{C}=\text{C})$ of aromatic ring), which reflects the reaction

of ketones and/or aldehydes. The observed decrease of the carbonyl absorbance resulting of the treatment by DNPH is rather weak and it corresponds to the decrease of the absorbance around 1717 cm^{-1} .

We verified in parallel that no modifications of the spectra were observed in the case of non-irradiated samples.

Fig.4.6. displays the UV-Visible spectra following the same procedure. In this case, MeOH soaking only gives a weak modification of the spectrum, whereas the reaction with DNPH gives the characteristic band at 365 nm indicating the reaction of ketones and/or aldehydes.

Based on the results obtained in this paragraph and the results previously described for PE photooxidation, the attribution of band maxima in carbonyl domain can be summarised in Table 4.1.

Table 4.1. Assignment of photooxidation products infrared bands of EVOH44 in the carbonyl domain

Wavenumber (cm^{-1})	Photooxidation products	Source
1710	Carboxylic acids	NH_3 treatment
$\cong 1717$	Ketones	2,4-DNPH treatment,
1730	Esters	[276, 281]
1780	Lactones/ anhydrides	[276, 281]

1.3.3. Analysis of volatile products by SPME-GC-MS

EVOH copolymers consist of ethylene and vinyl alcohol units. The IR analysis of EVOH44 film after 750 h of photooxidation reveals the oxidation of the PE units. However, previous studies on PVA photooxidation [282] have shown that a non negligible part of the PVA photoproducts are volatile and consequently cannot be detected by IR analysis of the photooxidised film, due to their migration out of the polymer matrix. Analysis of gas phase formed during EVOH photooxidation has then to be performed to detect any degradation products coming from the PVA units of EVOH. To determine the influence of the relative content of ethylene and vinyl alcohol groups on the quantities of detected products, SPME-GC-MS experiments were performed on EVOH44 and EVOH27. The composition of the gas phase of EVOH44 and EVOH27 photooxidised films is represented by the chromatograms in Fig.4.7.

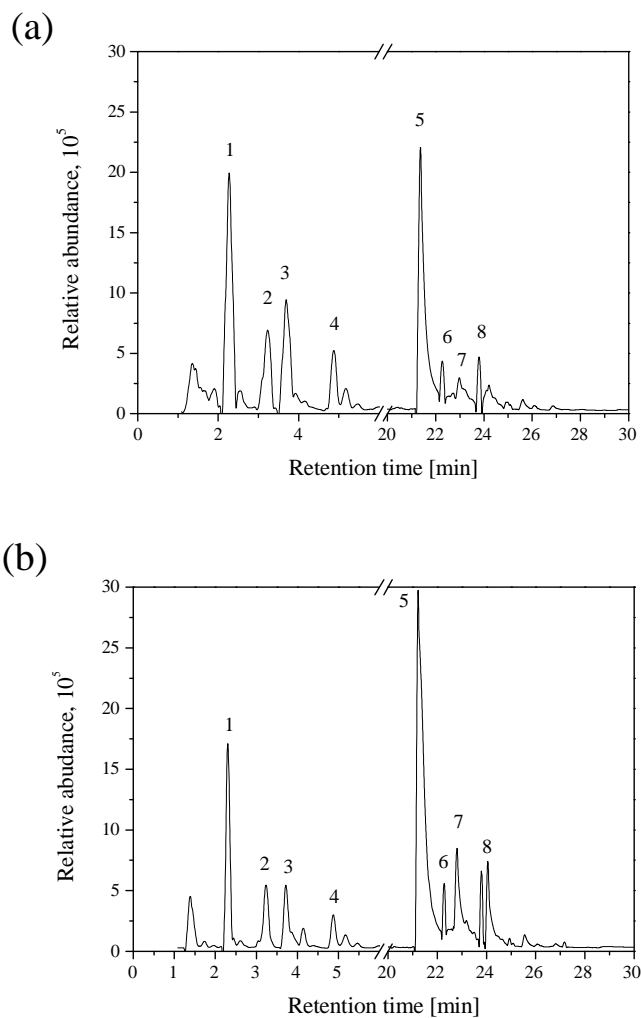


Fig.4.7. SPME-GC-MS chromatograms of gas phase of EVOH photooxidised films: (a) EVOH44 irradiated for 180 h and (b) EVOH27 irradiated for 280 h.

Several compounds were identified using this technique and are described in Table 4.2.

Table 4.2. Photoproducts of photooxidised EVOH films detected in gas phase by SPME-GC-MS

№	Retention time (min)	Compound	Area, Pct	
			EVOH44	EVOH27
1	2.3	Acetone	17.1	8.8
2	3.3	2-Butanone	5.8	3.5
3	3.7	2-Propanol	8.1	3.9
4	4.9	2-Pentanone	3.7	1.7
5	21.2-22.7	Acetic acid	31.5	51.1
6	22.3	2,5-hexanedione	2.2	2.5
7	22.8	Propionic acid	2.7	8.1
8	23.8-24.0	Gamma valerolactone	2.9	9.1

The results reported in Table 4.2. show that products such as γ -valerolactone, acetic and propionic acids were found in higher amounts in the case of EVOH27, whereas the quantities of acetone, 2-butanone, 2-propanol, and 2-pentanone were higher for EVOH44. Previous work carried out in our group ^[283] has shown that the same products as those observed in Table 4.2. were identified in the gas phase surrounding photooxidised PVA, except hexan-2,5-dione, propanol and pentanone. These three compounds are present in both EVOH copolymers, the last two being detected at higher concentrations in the case of EVOH44.

The presence of γ -valerolactone can be also detected in the solid phase of EVOH film by the absorbance at 1770 cm^{-1} where an IR absorption band developed upon photooxidation of EVOH film.

1.3.4. Ionic chromatography

To propose more comprehensive mechanism of photooxidation of EVOH, ionic chromatography (IC) was performed to analyse the low-molecular-weight photoproducts that were trapped in the film. A photooxidised film was soaked in water and the aqueous solution was analysed to identify the extracted molecular photoproducts. By comparing these products with standards, the primary released products were identified (Table 4.3.).

Table 4.3. Carboxylic acids extracted from irradiated EVOH and detected by ionic chromatography

Compound	Formula	C [mg/l]*		C [mg/g]**	
		EVOH44	EVOH27	EVOH44	EVOH27
Formic acid	H-COOH	14	14	1.3	1.1
Acetic acid	H ₃ C-COOH	48	38	4.5	3.0
Pentanoic acid	CH ₃ -(CH ₂) ₃ -COOH	8.4	3.9	0.8	0.3
Glutaric acid	HOOC-(CH ₂) ₃ -COOH	6.4	6	0.6	0.5
Malic acid	HOOC-CH ₂ -CHOH-COOH	10.8	10.4	1.0	0.8

* concentration detected in water extract

** recalculated concentration in polymer film

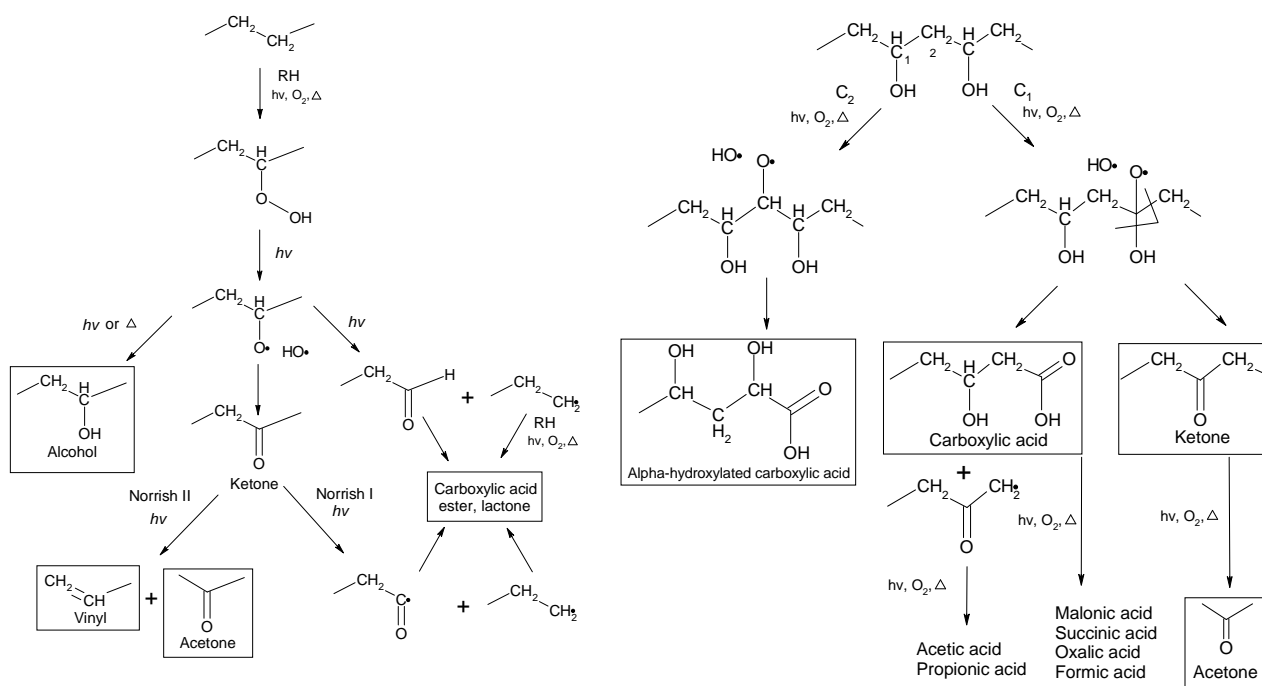
The presence of acetic acid, formic acid, malic acid, pentanoic acid and glutaric acid have been detected. Acetic and formic acids can be also detected in the case of PVA, pentanoic acid, glutaric acid and α -hydroxylated malic acid were only observed in the case of the EVOH copolymers. Their formation can be explained by a mechanism involving the oxidation of different vinyl alcohol and ethylene unit sequences (“PVA-PE-PE” or “PVA-PE-PVA”), which is detailed in the paragraph below.

1.4. Photooxidation mechanism of EVOH

The results obtained by analysis of the solid film (infrared spectroscopy), by analysis of the gas phase (SPME-GC-MS) and by analysis of extracts in solution (ionic chromatography) show that carboxylic acids are the main photoproducts formed by irradiation of EVOH in the presence of oxygen. Others classes of compounds, such as ketones and esters, have been also detected.

EVOH photooxidation mechanism involves the formation of photoproducts similar to those obtained in the case of PE and PVA (Scheme 4.1.), and also specific for EVOH photooxidation due to alternation of PE units and PVA units.

The photooxidation mechanisms of the PE and PVA homopolymers can be summarised on the basis of previous studies and published papers (Scheme 4.1.).



Scheme 4.1. Mechanisms of photooxidation of PE [281] and PVA [282].

The photooxidation of PE (Scheme 4.1. left) leads to the formation of hydroperoxides as primary photoproducts. Hydroperoxides decompose by scission of the O–O bond, which gives a macro-alkoxy and a hydroxyl radical HO•. The macro-alkoxy radical can react by several routes: β -scission with cleavage of the main chain to form aldehydes, abstraction of hydrogen without cleavage of the chain to form alcohols, cage reaction between the formed radicals, i.e. macro-alkoxy radical and hydroxyl radical HO•. The latter reaction produces chain ketones, which then photochemically react by Norrish type I or type II reactions. Photolysis of ketones by Norrish II processes results in the formation of vinyl-type unsaturated fragments, and produces a chain-end ketone, which also reacts by a Norrish II reaction and forms a vinyl unsaturation and acetone. The formation of carboxylic acids, esters and lactones comes from the various reactions involving both the aldehydes and the keto radicals formed by Norrish I reactions. The formation of vinylenes results from the mesomerism of allylic radicals [276].

Regarding the photooxidation of PVA (Scheme 4.1. right), the main photoproducts are carboxylic acids and ketones. Depending on the site of hydrogen abstraction (C₁ or C₂), α - or β -hydroxy carboxylic acids can be formed.

Two types of chain scissions may take place in the alkoxy radical obtained from the oxidation of C₁:

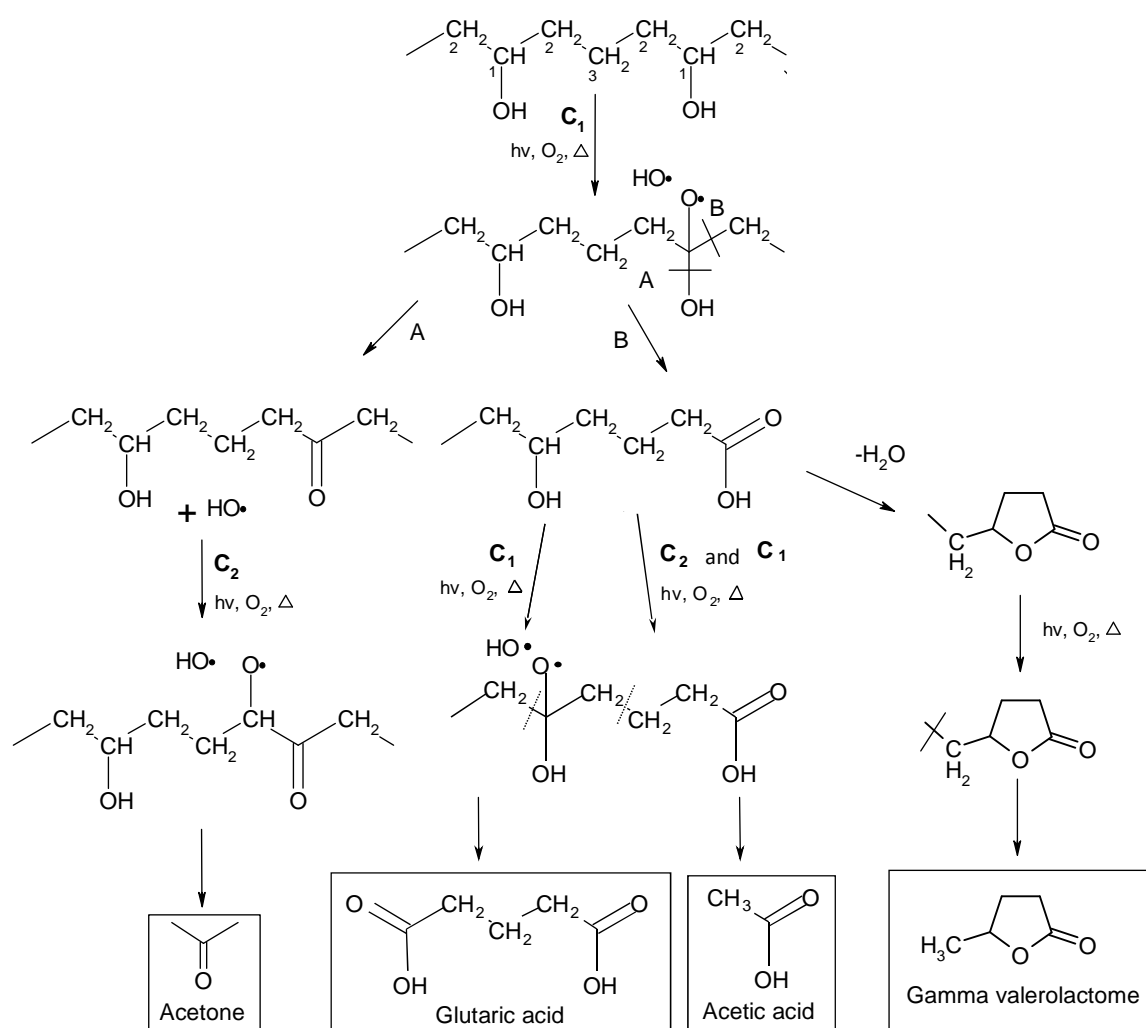
- cleavage of the C-O bond leading to the formation chain ketone and a hydroxyl radical;

-cleavage of the C-C bond causes the formation carboxylic acids and chain alkyl macroradical.

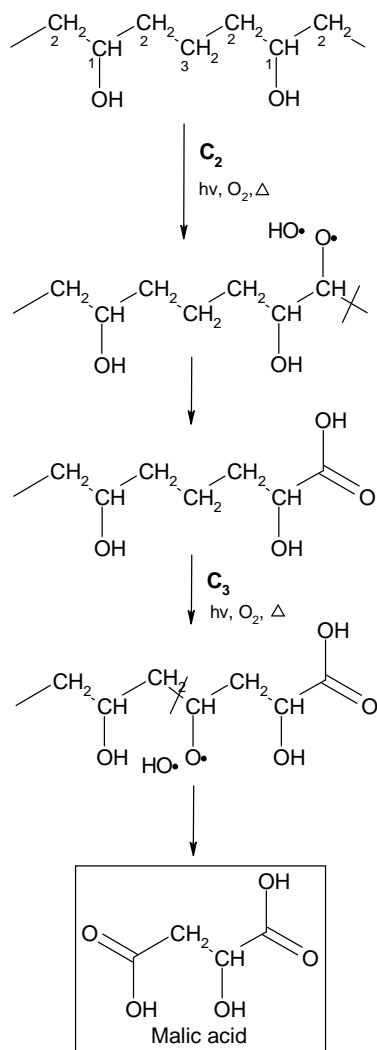
The alkoxy macroradical formed after reaction involving C₂ can lead to the formation of α -carboxylic acids as a result of subsequent β -scission.

EVOH photooxidation mechanism

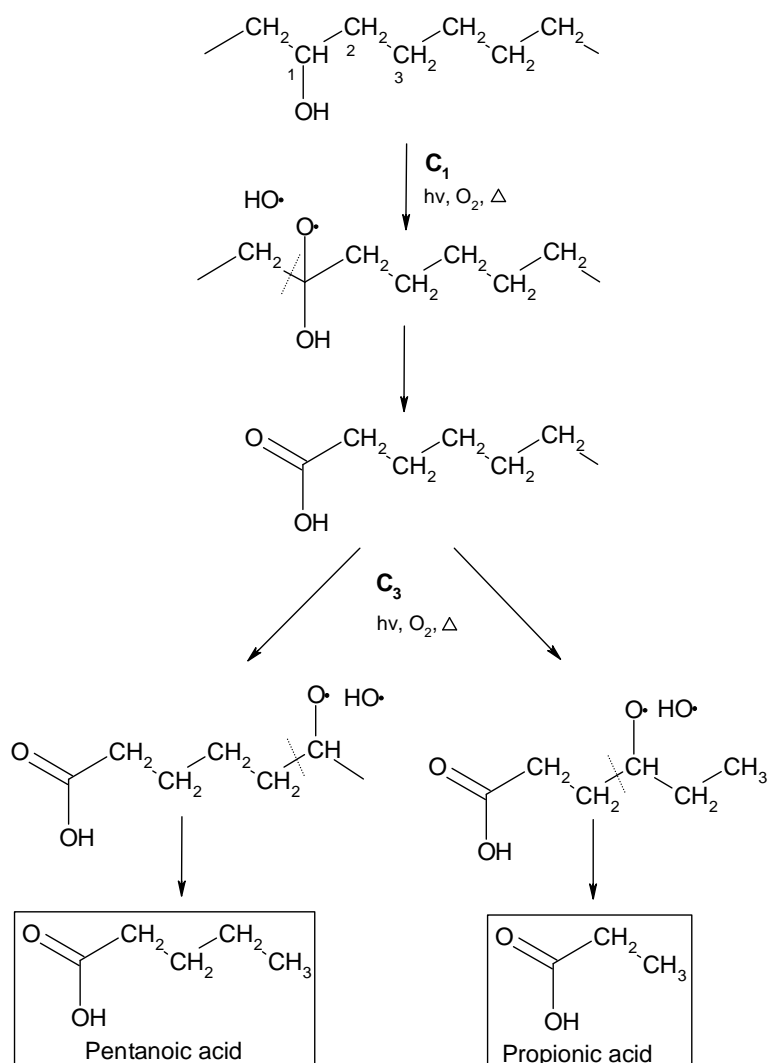
A comprehensive mechanism of EVOH photooxidation can be proposed on the basis of all the detected photoproducts and taking into account the photooxidation mechanisms of PE and PVA. This mechanism involves photoproducts formed as well in the case of the PE units as in the case of the PVA units, but also specific photoproducts that are only formed in the case of EVOH due to alternating sequences of PE units and PVA units. This mechanism is given in Scheme 4.2.-Scheme 4.4.



Scheme 4.2. Mechanism of photooxidation in PVA-PE-PVA unit involving oxidations at the tertiary (C₁) and the secondary (C₂) carbon atoms.



Scheme 4.3. Mechanism of formation of malic acid from PVA-PE-PVA unit photooxidation.



Scheme 4.4. Mechanism of photooxidation in PVA-PE-PE unit.

The identification of the various formed products gives evidences that the photochemically induced oxidation of EVOH involves the oxidation either on the tertiary (C₁) and/or on the secondary carbon (C₂ and C₃) in α - and β -positions to hydroxyl group (Scheme 4.2.- Scheme 4.4.) as well in the PE units, as in the PVA units, and that the PVA-PE-PVA and PVA-PE-PE sequences have also to be considered. The mechanisms are based on the classical sequences hydroperoxidation/decomposition of hydroperoxides/ β -scission of alkoxy radicals, which have been reported many times in the literature to explain the oxidation of organic polymers^[284]. The molecular carboxylic acids identified by ionic chromatography are formed by two oxidation steps. Glutaric acid is formed by oxidation on two tertiary carbon atoms C₁ on a PVA-PE-PVA segment unit (Scheme 4.2.). The secondary carbon noted C₂ reacts as in PVA photooxidation and leads to an α -hydroxylated acid, this reaction being followed by an

oxidation on a secondary carbon in β -position atom (C_3). This leads after chain scission to malic acid (Scheme 4.3.). Oxidation on a tertiary carbon atom C_1 in a PVA-PE-PE segment unit leads to a carboxylic function and an oxidation on a C_3 carbon atom can give after chain scission pentanoic acid or propanoic acid depending on which PE unit is oxidised (Scheme 4.4.).

Formation of photoproducts such as 2-pentanone requires the presence of sequence of three ethylene groups in EVOH, which is not the case in PVA. A higher relative amount of pentanoic acid is detected in the case of EVOH 44 compared to EVOH27, this is consistent with more PE-PE sequences in the case of 44 wt % of ethylene units.

To summarise, the mechanism of EVOH photooxidation involves oxidation on secondary and tertiary carbon atom, both in PE and PVA units, but also in specific alternating sequences of PVA-PE-PVA or PVA-PE-PE due to the chemical structure of EVOH copolymers.

2. INFLUENCE OF ZEOLITE NANOPARTICLES ON EVOH PHOTOOXIDATION

The behaviour of EVOH/NZL nanocomposites irradiated in presence of oxygen was studied in order to evaluate the influence of zeolite on the photochemical reactivity of the polymer. This study was carried out on nanocomposites based on EVOH44 (with 44 mol % of ethylene unit). To start with, EVOH/zeolite nanocomposites with 20 wt % of NZL nanoparticles were studied and then, the influence of both zeolite type (NZL or DISC) and the influence of the zeolite content (from 5 wt % to 20 wt %) was investigated. The influence of processing methods, solution mixing (method A) and melt-mixing (method B), on EVOH photooxidation rate was also studied.

2.1. Photooxidation of EVOH/NZL nanocomposites at $\lambda > 300$ nm

At first, the photochemical behaviour of EVOH44/NZL 20 wt % nanocomposite films processed by solution mixing (method A) was investigated.

2.1.1. UV-Visible analysis

The UV-Visible spectra of an EVOH/NZL-20 nanocomposite film during photooxidation are displayed in Fig.4.8.

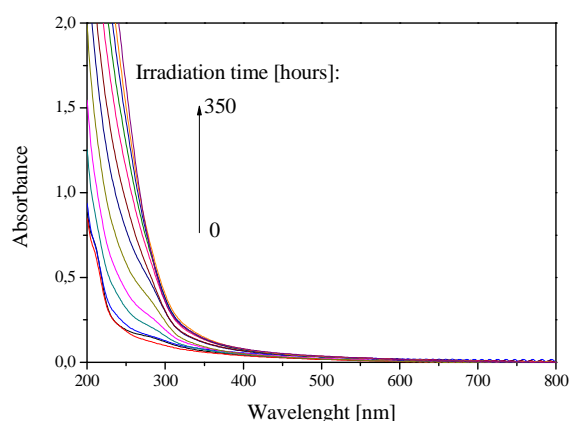


Fig.4.8. UV-Visible spectra of EVOH/NZL-20(A) nanocomposite film during photooxidation.

A shift of the absorption front towards the longer wavelengths is observed. As previously observed for pristine polymer, the absorption does not overlap the domain of the visible light. Thus, the nanocomposite film remains transparent and uncoloured. This is an important issue for encapsulation of electronic devices such as OSCs.

2.1.2. IR analysis

The modifications of the IR spectra during photooxidation of EVOH/NZL-20 nanocomposite film (Fig.4.9.) are similar to those of pristine EVOH (Fig.4.2.-Fig.4.3.) showing a decrease of band intensities in the hydroxyl domain corresponding to R-OH and C-H vibrations, and an increase in the carbonyl domain. This indicates that zeolite particles do not modify the photooxidation mechanism of the polymer. No changes of the IR bands that correspond to zeolite particles are observed, which suggests that the particles are photochemically stable.

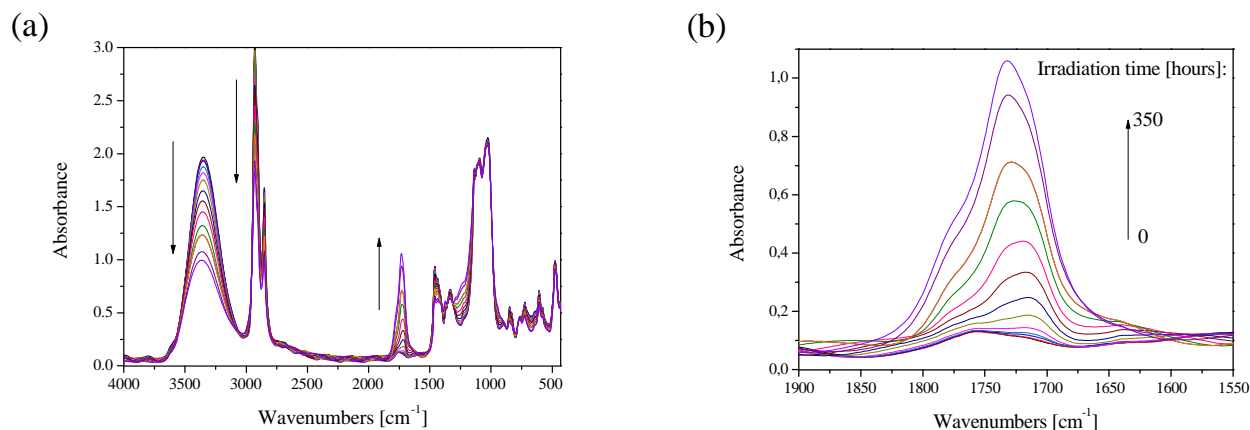


Fig.4.9. (a) FTIR spectra of EVOH/NZL-20(A) nanocomposite film during photooxidation, (b) in carbonyl region (1550-1900 cm^{-1}).

In order to look at the influence of the particle content, the changes in subtracted IR spectra in carbonyl domain for EVOH44/NZL nanocomposite with different zeolite content (0-20 wt %) are shown in Fig.4.10.

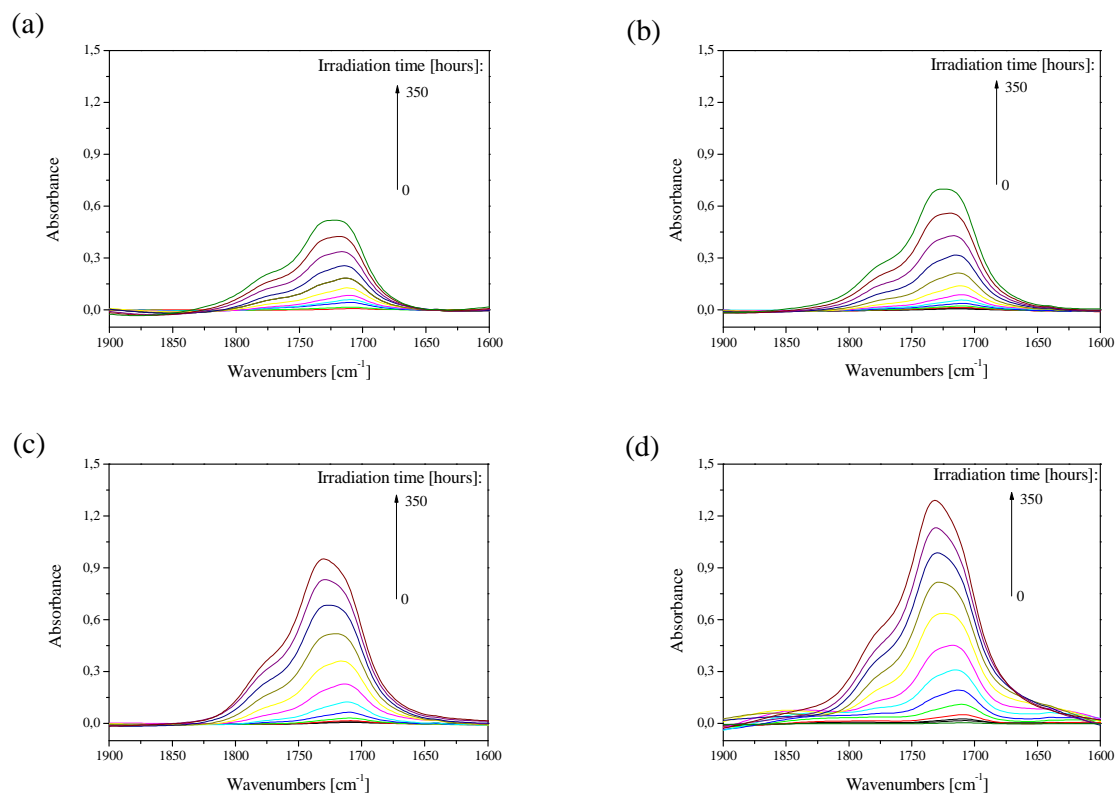


Fig.4.10. FTIR subtracted spectra of EVOH44/NZL film photooxidation in carbonyl domain with different NZL particle contents, wt %: (a) 5; (b) 10; (c) 15; (d) 20.

One can see an increase of a broad band with a maximum at 1715 cm^{-1} , which shifts to 1730 cm^{-1} at longer irradiation time, and a shoulder at 1780 cm^{-1} . This indicates that NZL particles do not modify the photooxidation mechanism of EVOH in the whole range of NZL content. However, these figures show that the concentration of oxidation photoproducts formed increases with the particle content, indicating a prodegrading effect of zeolite particles on EVOH44.

2.2. Influence of zeolite on photooxidation rate of EVOH

2.2.1. Influence of zeolite type

To investigate the effect of the morphology and the size of the zeolite particles on the polymer photostability, two types of zeolite particles (DISC and NZL, which are microsized and nanosized, respectively) were included into the polymer matrix (20 wt %) by method A. Fig.4.11. presents the oxidation kinetics evaluated by plotting the increase of absorbance at 1730 cm^{-1} and the decrease at 2852 cm^{-1} as a function of irradiation time, for pristine EVOH44 and EVOH44 loaded with 20 wt % NZL or DISC prepared by solution mixing.

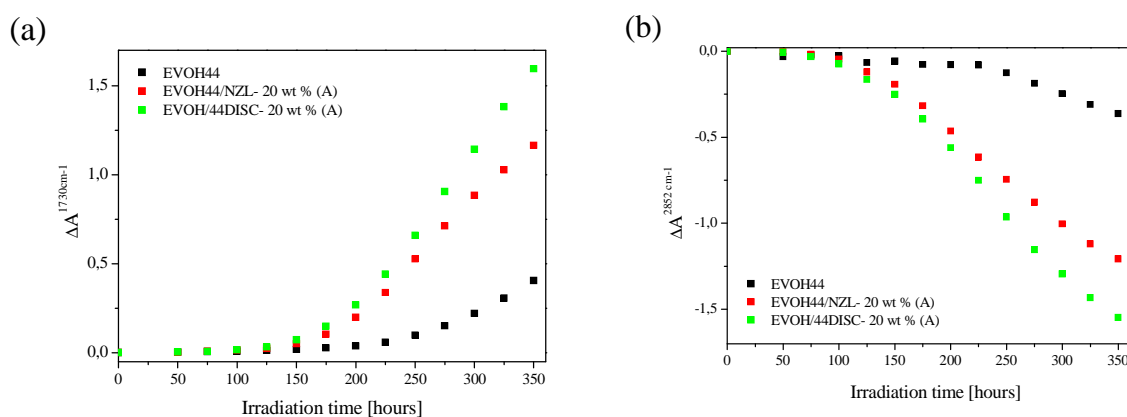


Fig.4.11. (a) Formation of carbonylated products and (b) a decrease of C-H bands intensity of EVOH44 and EVOH44/composite during photooxidation: pristine EVOH44(A) (black), EVOH44/NZL –20(A) (red), EVOH44/DISC –20(A) (green).

It is interesting to note that in presence of both zeolite particles, the induction period for oxidation is shortened (100 h vs 150 h) and the oxidation rate is higher than in the case of pristine EVOH. This result suggests that both zeolite particles have a prodegradant effect on EVOH. Regarding the composite stability in terms of particles type, DISC has a slightly

higher prodegrading effect than NZL, (Fig.4.11.a and Fig.4.11.b). One can also notice a slightly higher oxidation rate in the case of the micro-zeolite (DISC).

Such behaviour can be explained by the presence of iron impurities that are present in both zeolite particles, with an even higher amount in the case of DISC (10 times higher concentrations). Iron is known to induce the photodecomposition of hydroperoxides [193, 285, 286], producing radicals that can initiate oxidation of the polymer. This effect has been reported in the case of natural clays such as montmorillonite [176, 192, 219, 287-290]. The photoinducing effect of iron impurities is not proportional to the amount of iron, since it is expected that iron acts through a catalytic cycle. Another parameter that has to be taken into account is the specific surface of the particles, since nanoparticles (NZL) have a higher surface interaction than microparticles (DISC). Even if the amount of iron is lower in the case of the NZL nanoparticles, the observed effect on the polymer oxidation very certainly reflects the high specific surface of the zeolite nanoparticles.

2.2.2. Influence of zeolite loading

The influence of the zeolite loading on the photooxidation rate of EVOH was studied with increasing amount of NZL nanoparticles by plotting the increase of absorbance at 1730 cm^{-1} and the decrease at 2852 cm^{-1} as a function of irradiation time (as described in Ch.II § 2.1.) for EVOH44/NZL nanocomposites with particles from 5 up to 20 wt % (Fig.4.12.).

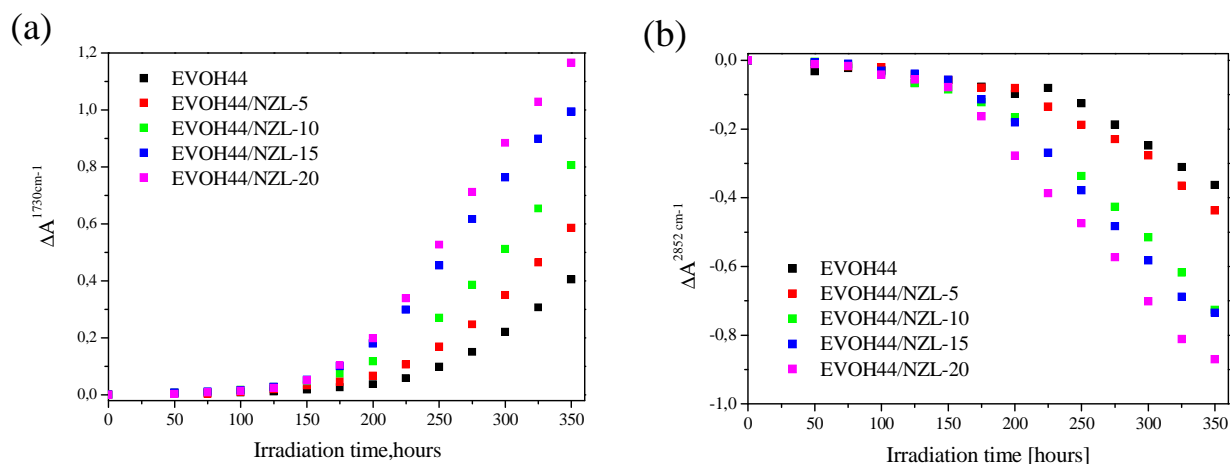


Fig.4.12. (a) Formation of carbonyl products and (b) a decrease of C-H bands absorbance for EVOH44(A) and EVOH44/NZL(A) nanocomposite films with different NZL particle contents (5; 10; 15; 20 wt %).

The kinetic curves clearly show that the prodegradant effect of NZL increases with the NZL particles content. Increasing the particle amount slightly decreases the induction period and increases the oxidation of the polymer.

2.2.3. Influence of processing method

To evaluate any effect of processing method on the photostability of the EVOH polymer matrix, we compared the formation of carbonyl photoproducts for pristine EVOH44 films obtained through evaporation of DMSO solution (A) or by press (B) (Fig.4.14.).

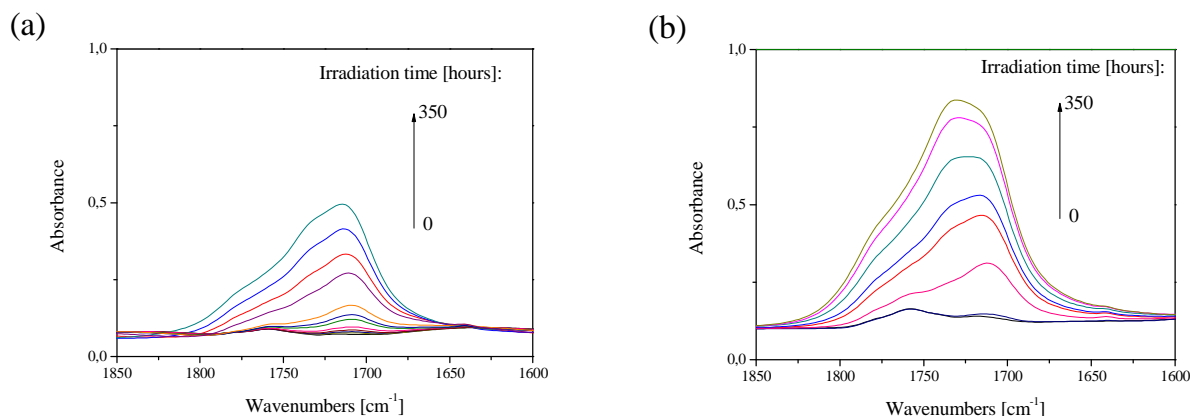


Fig.4.13. Formation of carbonyl products for (a) EVOH44(A) and (b)EVOH44(B). Film thickness: (a) 15 μm and (b) 52 μm .

Fig.4.13. shows differences in the band intensities of carbonylated photoproducts, which results from the different initial thickness of the films (the IR spectra were not corrected by sample thickness). The increase of the normalised absorbance at 1730 cm^{-1} (absorbance divided by the absorbance of an IR band of the polymer at 1460 cm^{-1}) is plotted for EVOH44 obtained by method A and B in Fig.4.14.

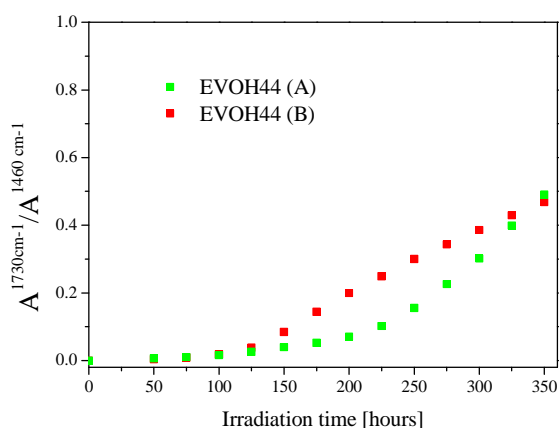


Fig.4.14. Formation of carbonyl products as a function of irradiation time: EVOH44 film processed by solution (green) and (b) by press (red).

The kinetic curves in Fig.4.14. show a higher oxidation rate in the case of the EVOH44 film prepared by press. This might be explained by small amount of chromophoric degradation products resulting from the extrusion at $210\text{ }^{\circ}\text{C}$ and hot pressed at $200\text{ }^{\circ}\text{C}$. However after 250 h of irradiation, the oxidation rate of the EVOH44 film prepared by press decreases,

which corresponds to the shift of the absorption maximum seen in Fig.4.13.b. This probably reflects the impact of the thickness on the oxidation, since film processed by method A was about 15 μm thick while film prepared by method B exhibited 3.5 times higher thickness (52 μm).

2.3. Surface morphology

The morphology changes of film surface for pristine EVOH polymer and the (nano)composites during photooxidation were followed by SEM and AFM analysis. All the studied films were processed by solution mixing (method A) (polymer-particle suspension in DMSO and solvent evaporation).

2.3.1. Scanning electron microscopy (SEM)

EVOH films

Fig.4.15. shows the SEM images obtained at the film surface of a neat EVOH44 film before and after ageing.

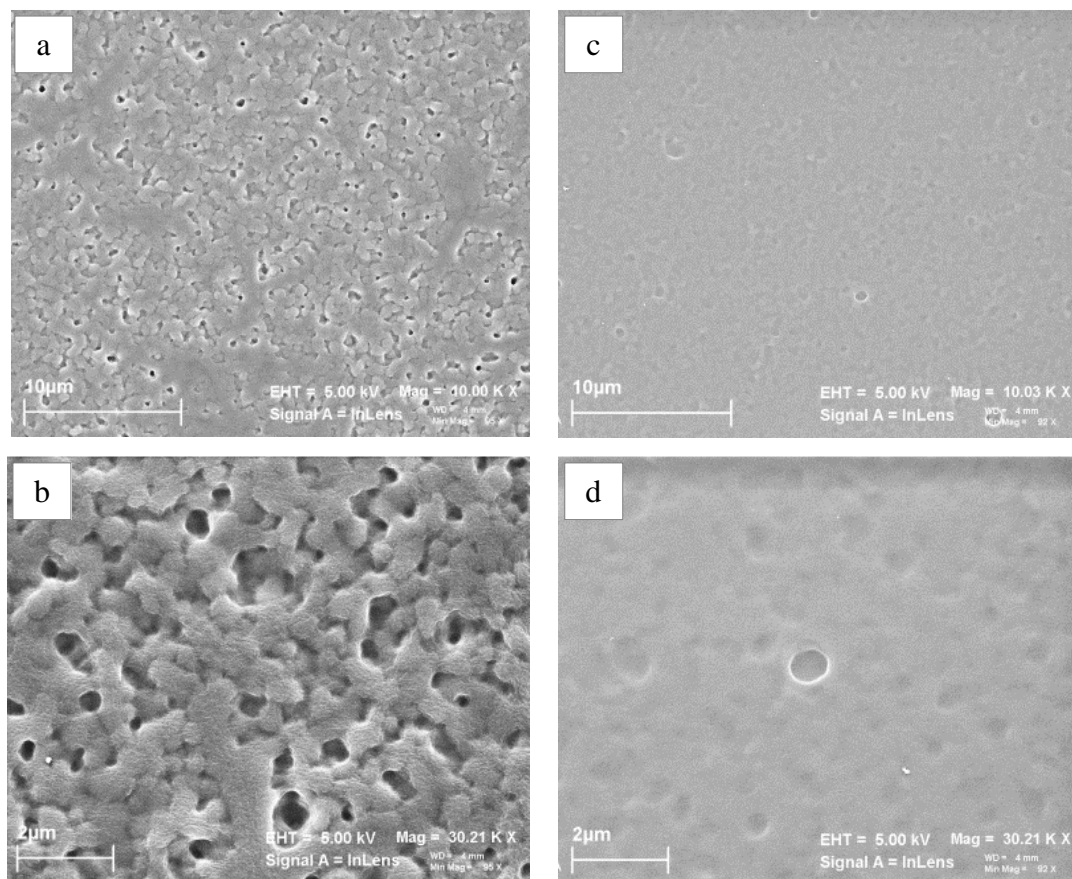


Fig.4.15. SEM surface images of EVOH44(A) films (a-b) before (0 h) and (c-d) after 1200 h of photooxidation.

One can observe that irregularities, voids and bulges that were formed during film drying became smaller and the surface became smoother after 1200 h of photooxidation. The formed holes almost disappeared after 1200 h of irradiation.

EVOH44/NZL nanocomposites

The influence of NZL nanoparticles on the surface morphology of nanocomposite film upon photooxidation can be evaluated from SEM images of EVOH44/NZL-20 nanocomposite film surfaces given in Fig.4.16.

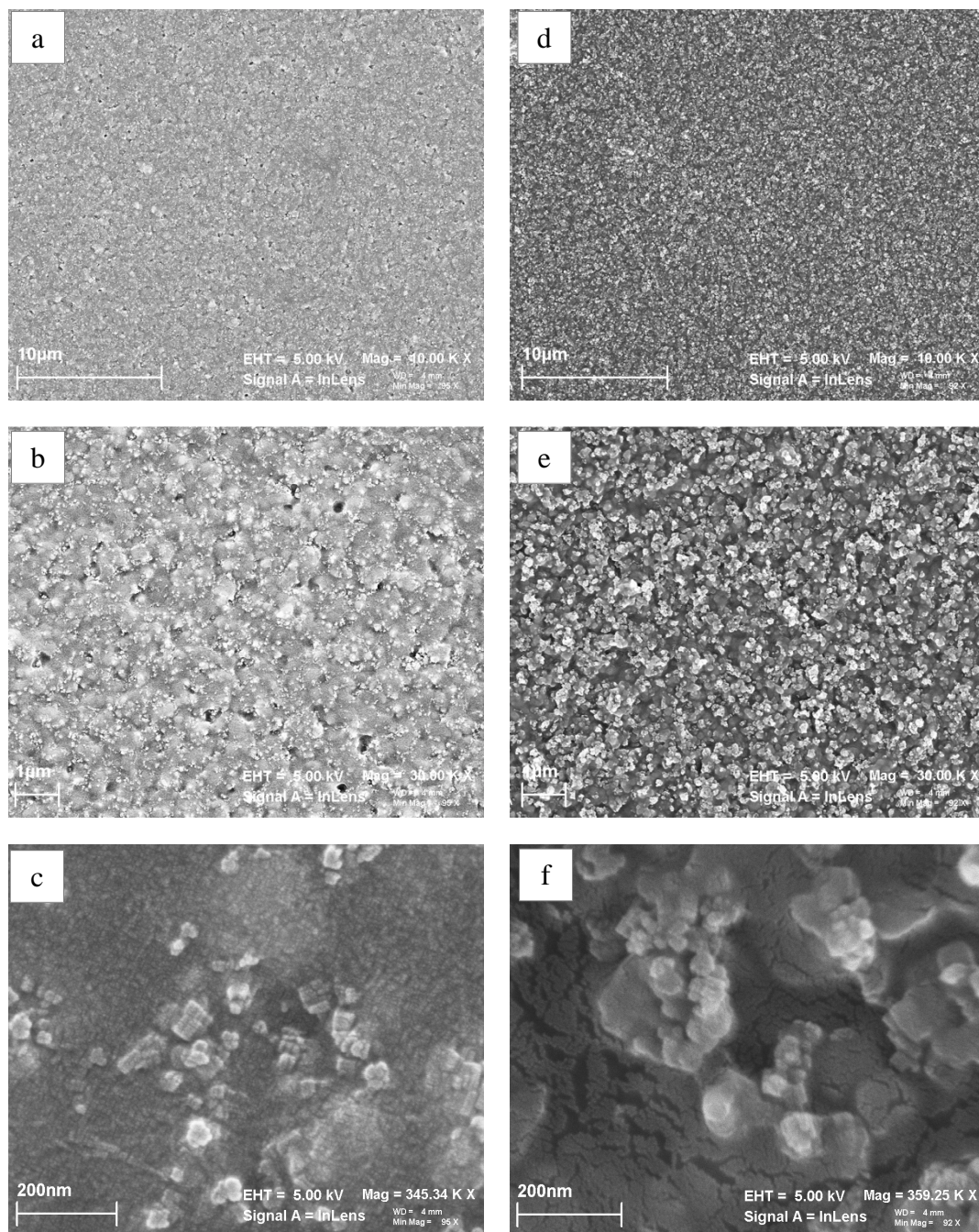


Fig.4.16. SEM surface images of EVOH44/NZL – 20 (A) films (a-c) before (0 h) and (d-f) after 1200 h of photooxidation.

Different trend is observed for nanocomposite film surface with 20 wt% of zeolite nanoparticles than thus for unfilled EVOH. It seems that after 1200 h of light exposure, particles remain at the surface meanwhile a loss of polymer from the surface is noticed. The loss of the EVOH polymer matrix can be explained by the photooxidation mechanism of EVOH involving chain scissions (as previously shown in the photooxidation mechanism in

Ch.IV §1.4.) and subsequent migration of low-molecular-weight products in the gas phase (as previously observed in the case of PVA degradation ^[191]). Consequently, zeolite agglomerates became more visible at the surface (Fig.4.16.f).

SEM images also indicate the formation of cracks and voids during photoageing at the surface of EVOH44/NZL-20 nanocomposite film (Fig.4.17).

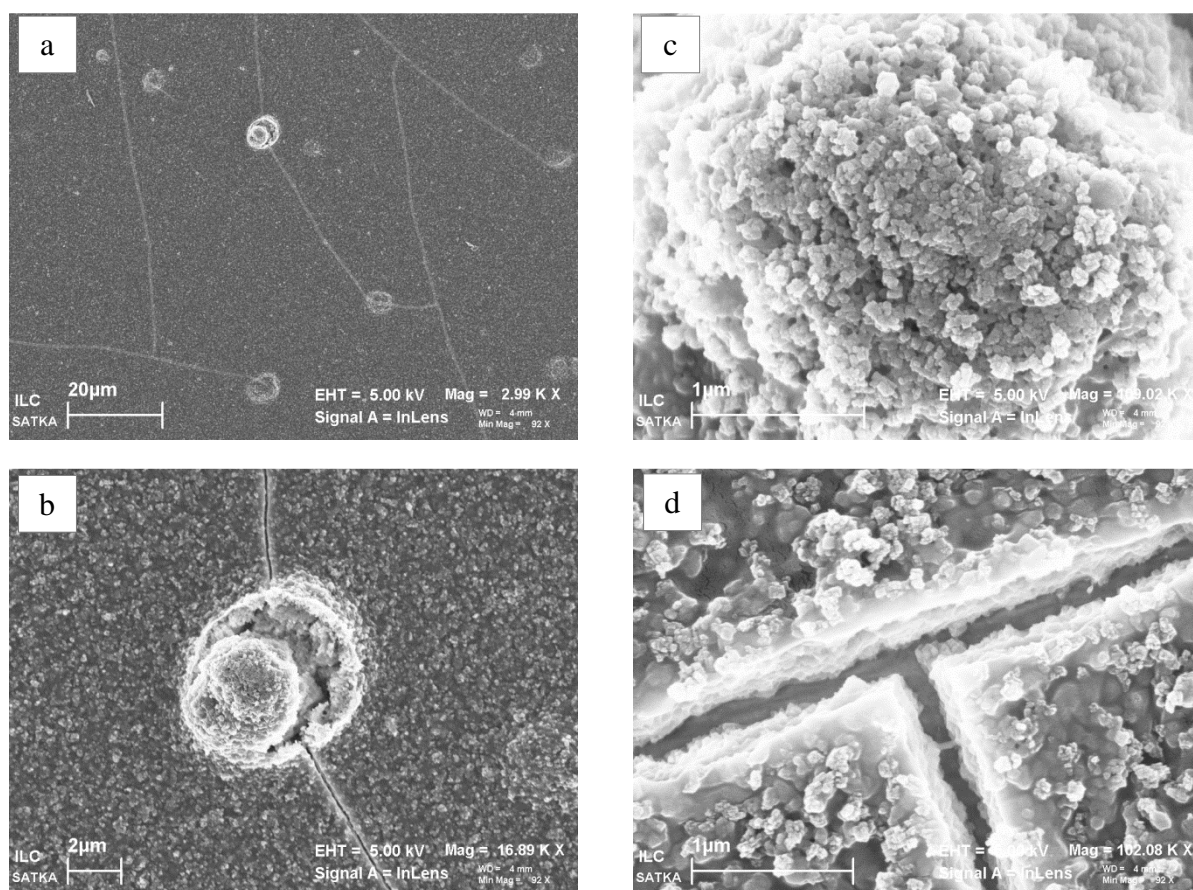


Fig.4.17. Formation of cracks and voids at the surface of EVOH44/NZL-20(A) film after 1200 h of photooxidation.

2.3.2. Atomic force microscopy (AFM)

The photooxidation of EVOH44 and EVOH27 films and the corresponding EVOH/NZL-20 nanocomposites obtained by solution mixing (method A) were also characterised by atomic force microscopy (AFM). AFM images obtained for EVOH44 and EVOH27 film surfaces during photooxidation are shown in Fig.4.18.

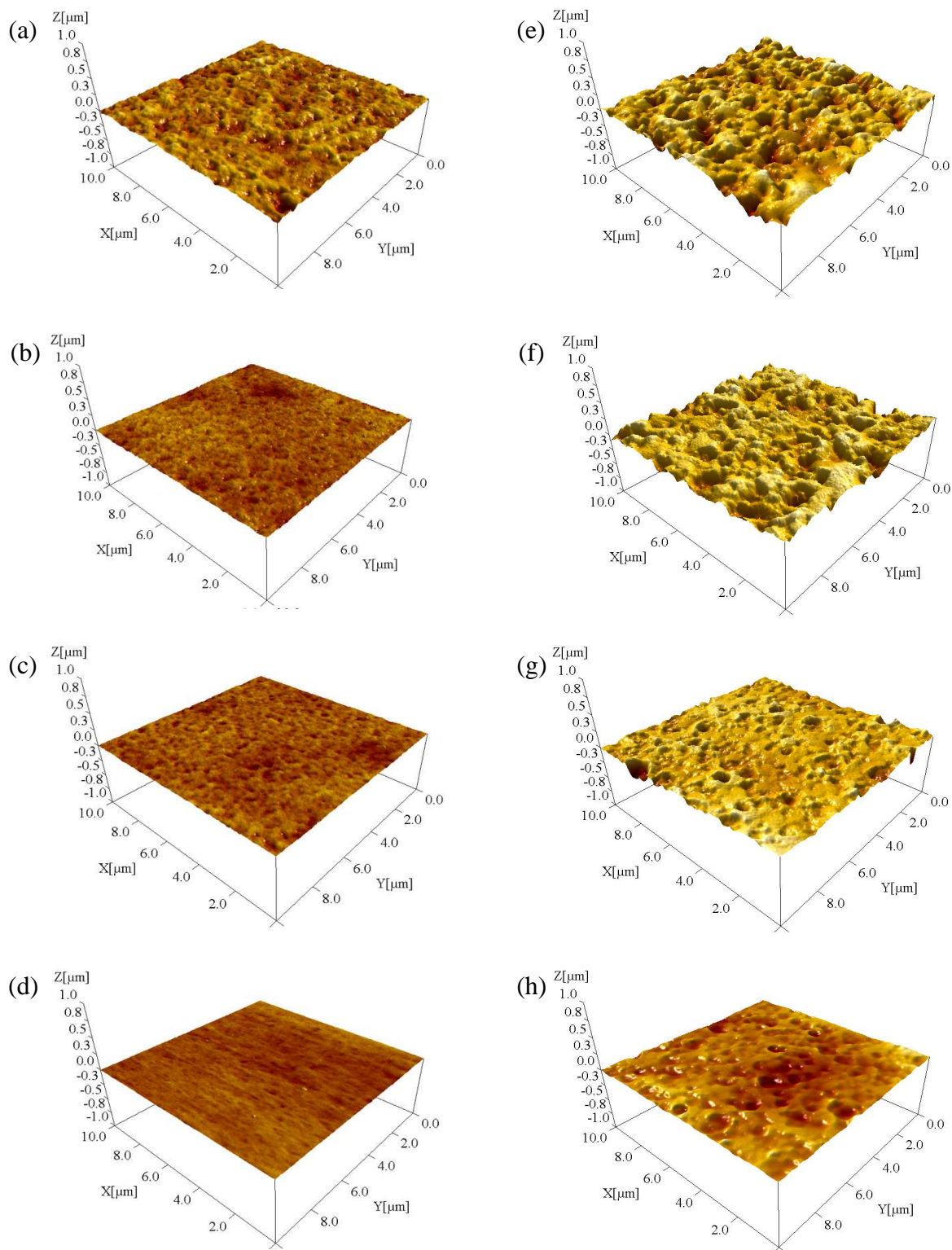


Fig.4.18. AFM 3D height images of (a-d) EVOH44(A) and (e-h) EVOH27(A) during photooxidation: (a,e) 0; (b,f) 300 h; (c,g) 500 h; (d,h) 1200 h.

Fig.4.18. shows that for both EVOH copolymers, EVOH44 and EVOH27, the film surfaces become smoother with the degradation time. This is consistent with observations made in SEM images (Fig.4.15.).

The AFM images of EVOH44/NZL-20 and EVOH27/NZL-20 nanocomposite films were recorded and are presented in Fig.4.19.

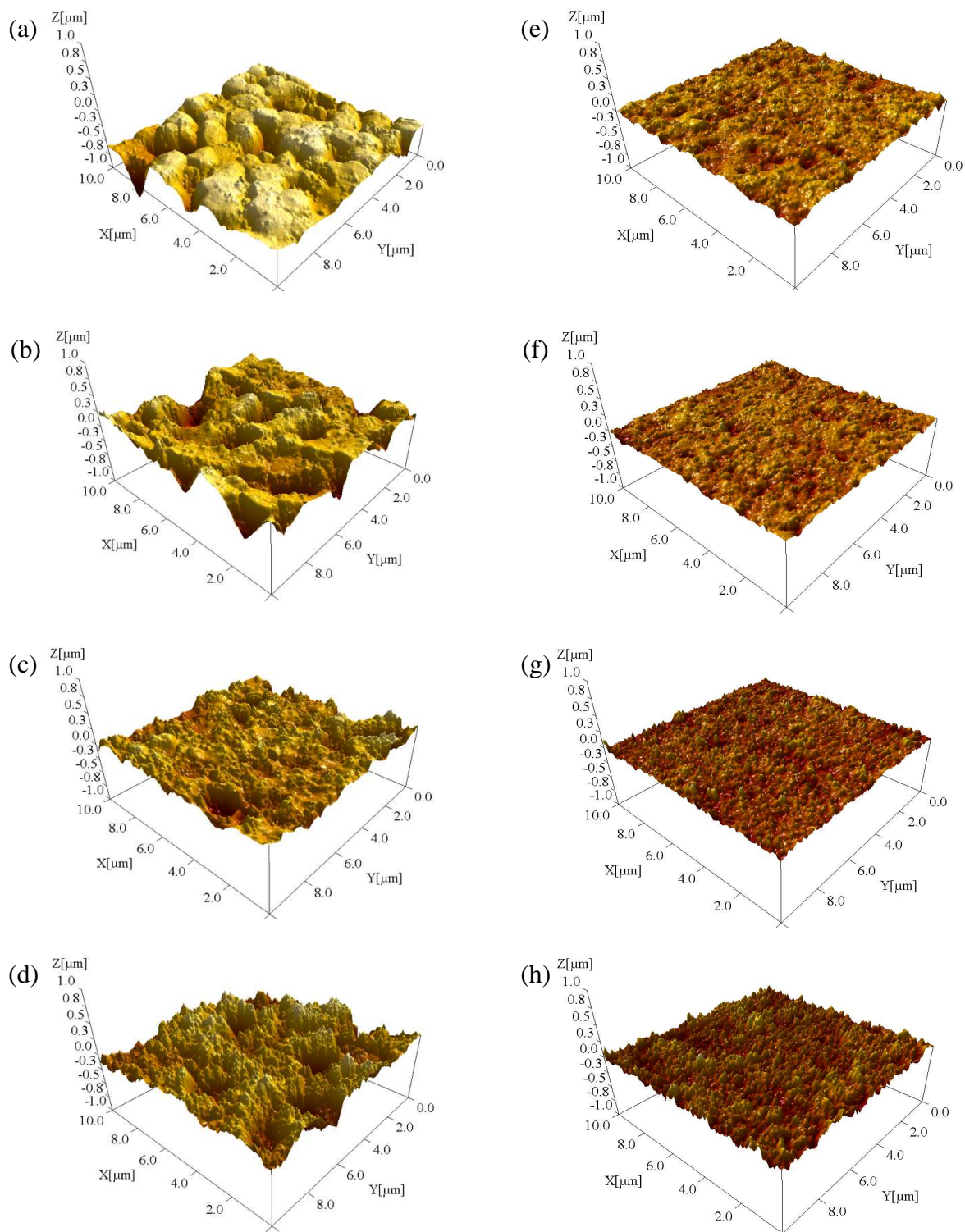


Fig.4.19. AFM 3D height images of (a-d) EVOH44/NZL-20(A) and (e-h) EVOH27/NZL-20(A) during photooxidation: (a,e) 0; (b,f) 300 h; (c,g) 500 h; (d,h) 1200 h.

Fig.4.19. shows that the morphology of EVOH44/NZL-20 and EVOH27/NZL-20 nanocomposite film surfaces changes during polymer oxidation, resulting in surface roughness changes, but different images are obtained for same irradiation time depending on the EVOH copolymer. AFM images of EVOH44/NZL-20 nanocomposite film (Fig.4.19.a-c) show that initial irregularities, introduced by solvent evaporation process disappeared with degradation time, leading the surface smoothing. However, at the same time, the presence of NZL nanoparticles leads to higher roughness for longer degradation times (Fig.4.19.d,h). This effect is less pronounced in the case of EVOH27/NZL-20 nanocomposite that is less oxidised for the same irradiation time compared to EVOH44 based nanocomposites (as observed from IR analysis on pristine EVOH copolymers). In order to better observe the effect of nanoparticles loading on photooxidation of copolymer surfaces, the surface roughness (R_a) of pristine EVOH44 and EVOH27 copolymers and their nanocomposites with 20 wt % of NZL nanoparticles are plotted versus degradation time in Fig.4.20.

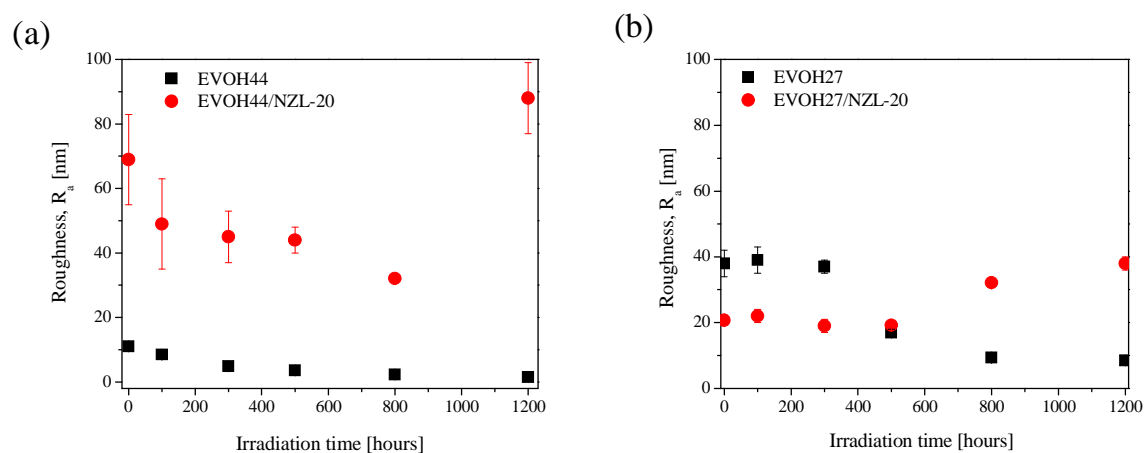


Fig.4.20. Evolution of surface roughness during photooxidation: (a) EVOH44(A) and EVOH44/NZL-20 (A); (b) EVOH27 and EVOH27/NZL-20(A).

As it is observed in Fig.4.20., the roughness of unfilled polymers (EVOH44 and EVOH27) shows a slight decrease with degradation time, which reflects the smoothing effect of photooxidation observed in AFM images (Fig.4.19.) and also in SEM images (Fig.4.15.).

At the same time, the R_a evolution is different for nanocomposites of EVOH44 and EVOH27. In the case of EVOH44/NZL-20 nanocomposite film, the roughness decreases up to 800 h of photooxidation, the last roughness value is probably an artefact as films present voids and cracks for such long irradiation time (as observed in SEM images Fig.4.17.). In the case of EVOH27/NZL-20 nanocomposites, the roughness values are lower than in the case of

the EVOH44 nanocomposites and display rather a small increase in roughness upon photooxidation in presence of zeolite, a different kinetic rate of polymer oxidation can lead to different morphology of particles agglomeration at the surface.

Particles distribution

AFM images of an EVOH44/NZL-20 film before and after 500 h of photoaging were also performed in peak force tapping mode (Fig.4.21.) in order to distinguish the presence of the particles and the modification of their distribution during photooxidation.

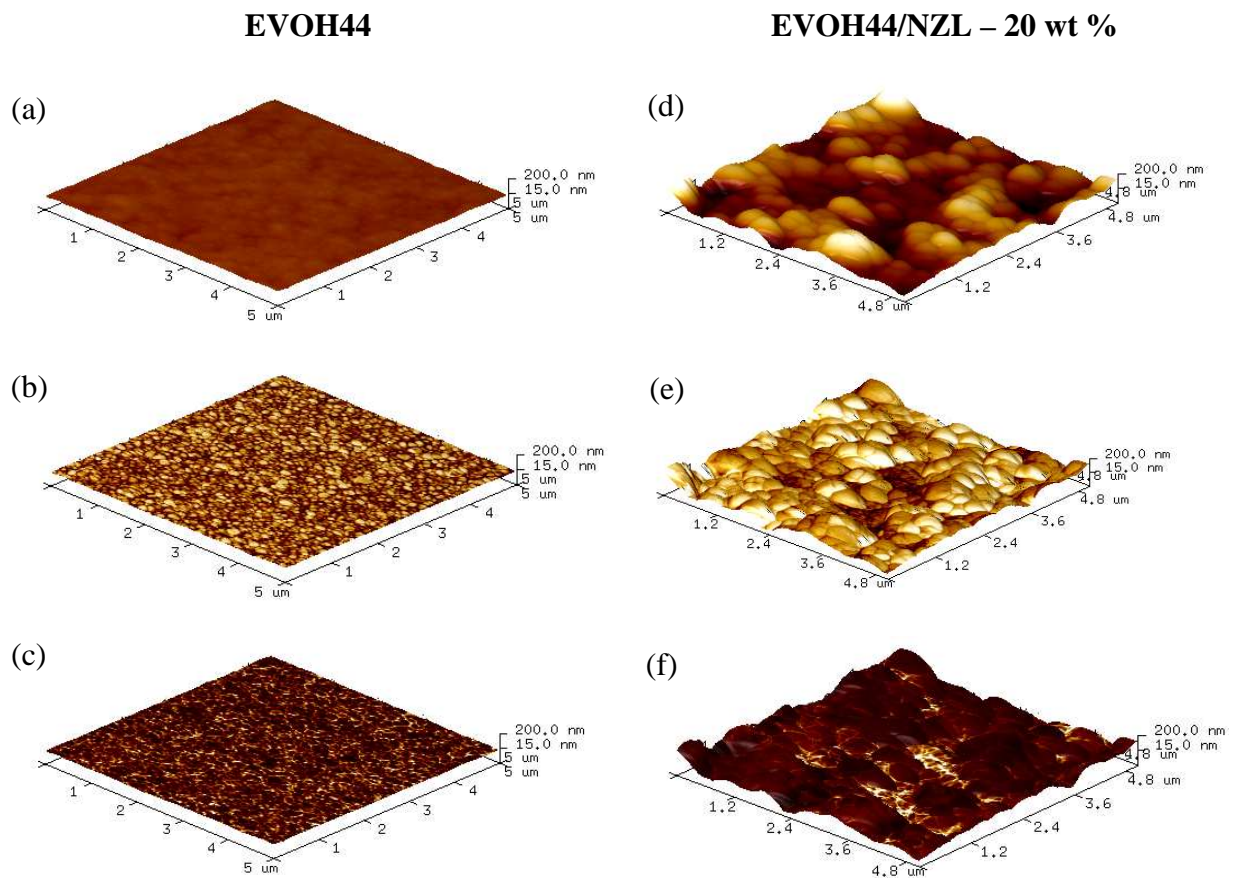


Fig.4.21. AFM 3D images of (a-c) EVOH44(A) and (d-f)EVOH44/NZL-20(A) after 500h of photooxidation. Plot type: (a,d) height, (b,e) height mixed with modulus, (c,f) height mixed with adhesion.

Fig.4.21. displays 3D height images (Fig.4.21.a,d), an height mixed with elastic modulus (Fig.4.21.b,e) and height mixed with adhesion (Fig.4.21.c,f). As it was previously explained in Ch.III § 2.2.2., the colour code in the mixed images (Fig.4.21.b-f) corresponds to the value

of the elastic modulus or adhesion (in white-high values and in black-low values for the modulus and opposite for adhesion).

The 3D height images of EVOH44 and EVOH44/NZL-20 nanocomposite after 500 h of light exposure show a higher surface roughness in the case of EVOH44/NZL-20 nanocomposite, as it was previously observed by AFM experiment (Fig.4.18.-Fig.4.19.).

The 3D images of height mixed with modulus (Fig.4.21.b,e) show that the image contrast is different for neat polymer and nanocomposite. The AFM image in Fig.4.21.e of EVOH44/NZL-20 nanocomposite shows clearly the presence of particles that exhibited high modulus (bright colours), which cover all the analysed nanocomposite surface. Based on the observations in Ch. III, Fig.3.18., where a clear contrast between zeolite (white spots) and polymer (dark areas), it suggests that in Fig.4.21.e. are mainly present NZL zeolite particles and only traces of remaining polymer. The same explanation can be given for height-adhesion images but with opposite colour (dark colours –particles; bright polymer) (Fig.4.21.c,f).

In order to better observe these differences, 2D mixed AFM images of EVOH44/NZL-20 film before and after 500 h of photodegradation are compared in Fig.4.22.

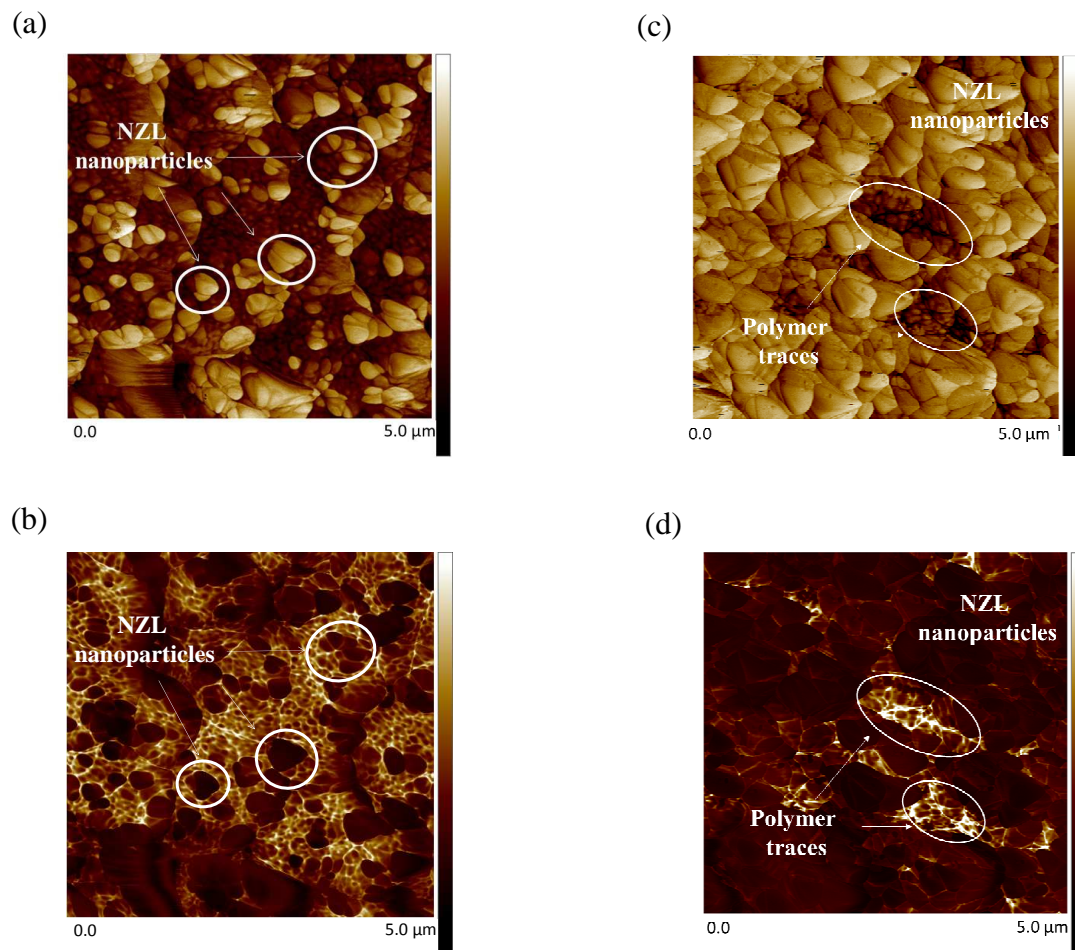


Fig.4.22. AFM 2D image of EVOH44/NZL-20 nanocomposite film(A) (a-b) before and (c-d) after 500h of photooxidation. (a,c) Height mixed with modulus; (b,d) height mixed with adhesion.

2D images confirm the decrease of polymer quantity at the film surface after photooxidation. AFM images of photooxidised EVOH44/NZL-20 nanocomposite (Fig.4.22.c-d) indicate polymer traces (in white circles).

2.4. ToF-SIMS surface analysis

The changes of chemical composition at the surfaces of EVOH polymer and EVOH/NZL nanocomposite were followed by time-of-flight secondary ion mass spectrometry (ToF-SIMS). This experiment was performed at International Laser Centre in Bratislava. This method allows the chemical analysis of material composition by the detection of secondary ions resulted from molecules fragmentation during surface bombarding by primary ions. The

evolutions of detected ions were achieved from an information of ion peak areas extracted from the mass spectra of films irradiated during 0, 500, 900, 1200 and 1500 h.

As it was mentioned in Ch.III, negative field of ion detection is more promising for analysis of samples contained O, C, H, Si in sample composition. This phenomenon is based on higher ionisation probabilities in the negative polarity of these elements. The evolutions of intensities of negative secondary ions during photooxidation are shown for EVOH44 and EVOH44/NZL-20 nanocomposite films in Fig.4.23. and Fig.4.25. respectively, where the mass spectra of samples degraded during 1200 h are displayed and the ion evolutions during photooxidation (an increase or a decrease), based on the calculated normalised ion peak areas, are indicated by arrows.

EVOH44

The negative-ion mass spectra of EVOH after 1200 h of photooxidation is given in Fig.4.23. The ions of interests are labelled by numbers placed next to corresponding peak of the spectrum. Peak descriptions are located at the right side of the figure. The arrows next to the ion peaks indicate the evolution of the peak area with the degradation time, where ↑ means an increase and ↓ indicates a decrease of ion peak area with photooxidation time. No arrow is shown for peaks without consequent increase/decrease evolution of peak area.

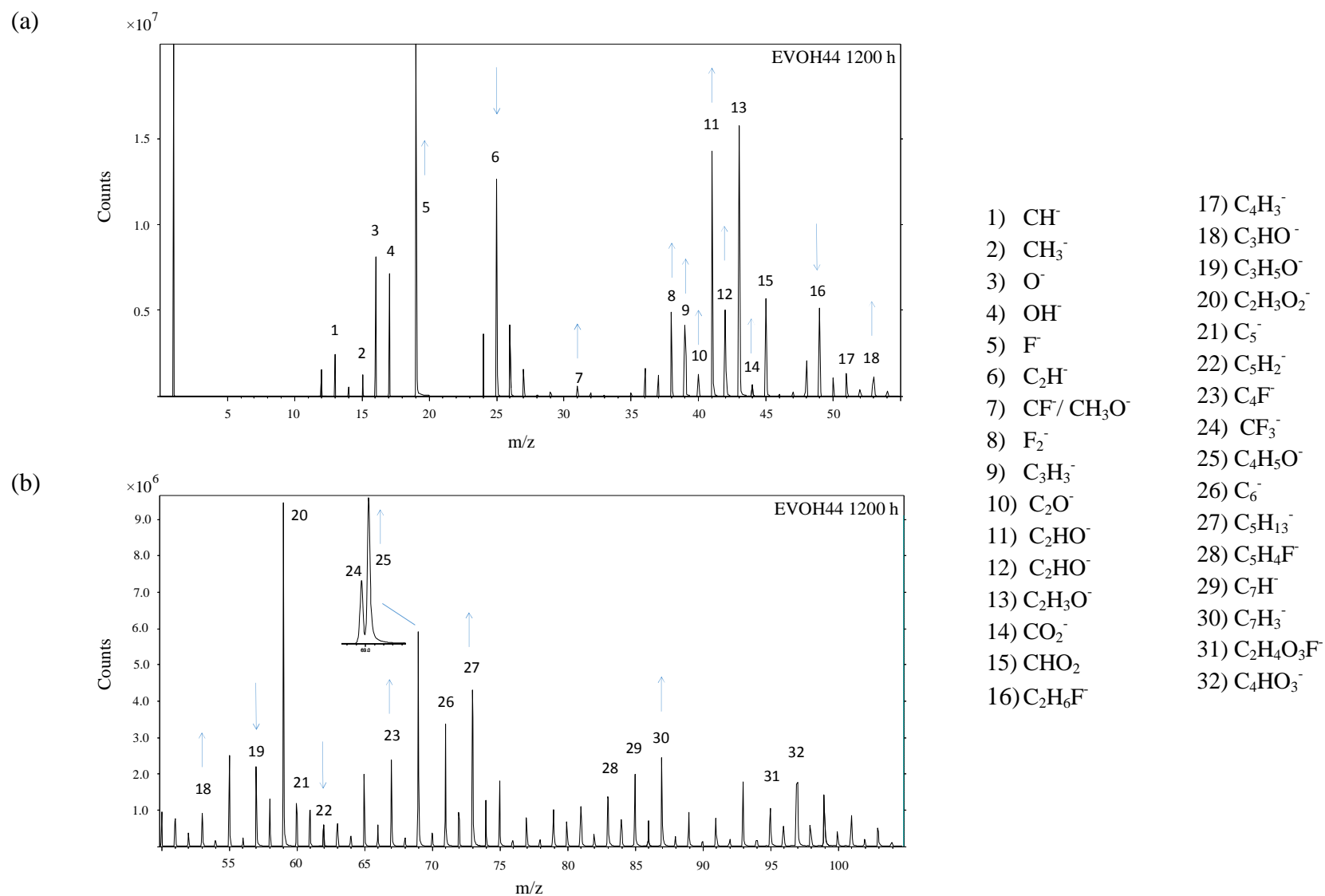


Fig.4.23. Negative-ion ToF-SIMS spectra of EVOH44 film surface after 1200 h of photooxidation.

Mass spectra represented in two different mass ranges: (a) 0-55 and (b) 55-105 m/z.

The fragments with different number of carbon atoms (from 1 to 7) are detected in the studied mass range (0-105 m/z). It suggests no specific chain length fragment is dominantly formed during bombarding. Observed high intensity of F-involved ions, considered to be related to processing additives, can be explained by high relative sensitivity of detector to this element. The evolutions of both, oxygen involved patterns ($C_xH_yO_z^-$) and those without oxygen ($C_xH_y^-$), are observed during photooxidation. In general, $C_xH_y^-$ ions are mainly related to non-oxidised carbon atoms of polymer molecule while $C_xH_yO_z^-$ corresponds as to oxidised fragments as to non-oxidised parts of polymer indicating vinyl alcohol group fragment(s). Basically, up to three oxygen atoms were detected to be included in $C_xH_yO_z^-$ fragment compositions. With an increase of number of oxygen atoms, the probability of this ion, related to the product of photooxidation, increases. Fig.4.24. show the normalised peak areas of the oxygen-contained ions plotted versus photooxidation time.

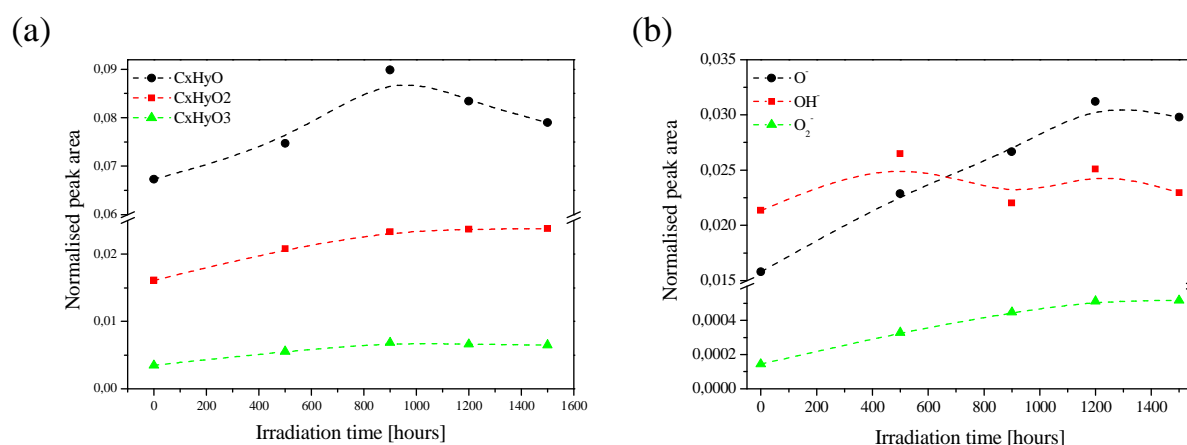


Fig.4.24. Negative ion normalised peak areas as a function of irradiation time.

From Fig.4.24.a, one can observe that the concentration of all displayed three types of ions ($C_xH_yO_z^-$, $z:[1-3]$) increases with degradation time but, $C_xH_yO^-$ concentration at 1500 h decreases while other ions concentrations remain at the same value range as those at 1200 h. It might be explained by higher order of polymer chain oxidation caused by long-term degradation what results in the reduced formation of the ions contained just one oxygen atom.

More general view on oxidation processes taking place in polymer chain can be represented by Fig.4.24.b. The evolutions of peak areas of O^- and O_2^- have similar trends and increase with degradation time up to 1200 h. It shows the evidence of present photooxidation processes. At the same time OH^- ion does not show clear evaluation trend.

Concluding, the concentration of numerous fragments, related to the polymer matrix fragmentation, increases with irradiation time up to 1200 h of exposure and then, either decreases or remains similar as this for 1200 h. It might be due to the high level of crosslinking in the polymer chain what hinders the ion formation.

EVOH/NZL analysis

In order to investigate the nanofiller effect, ToF-SIMS mass spectra of EVOH44/NZL nanocomposite, degraded in the same conditions as the pristine EVOH44 polymer, were recorded. The negative-ion mass spectra of EVOH44/NZL-20 after 1200 h of irradiation are shown in Fig.4.25.

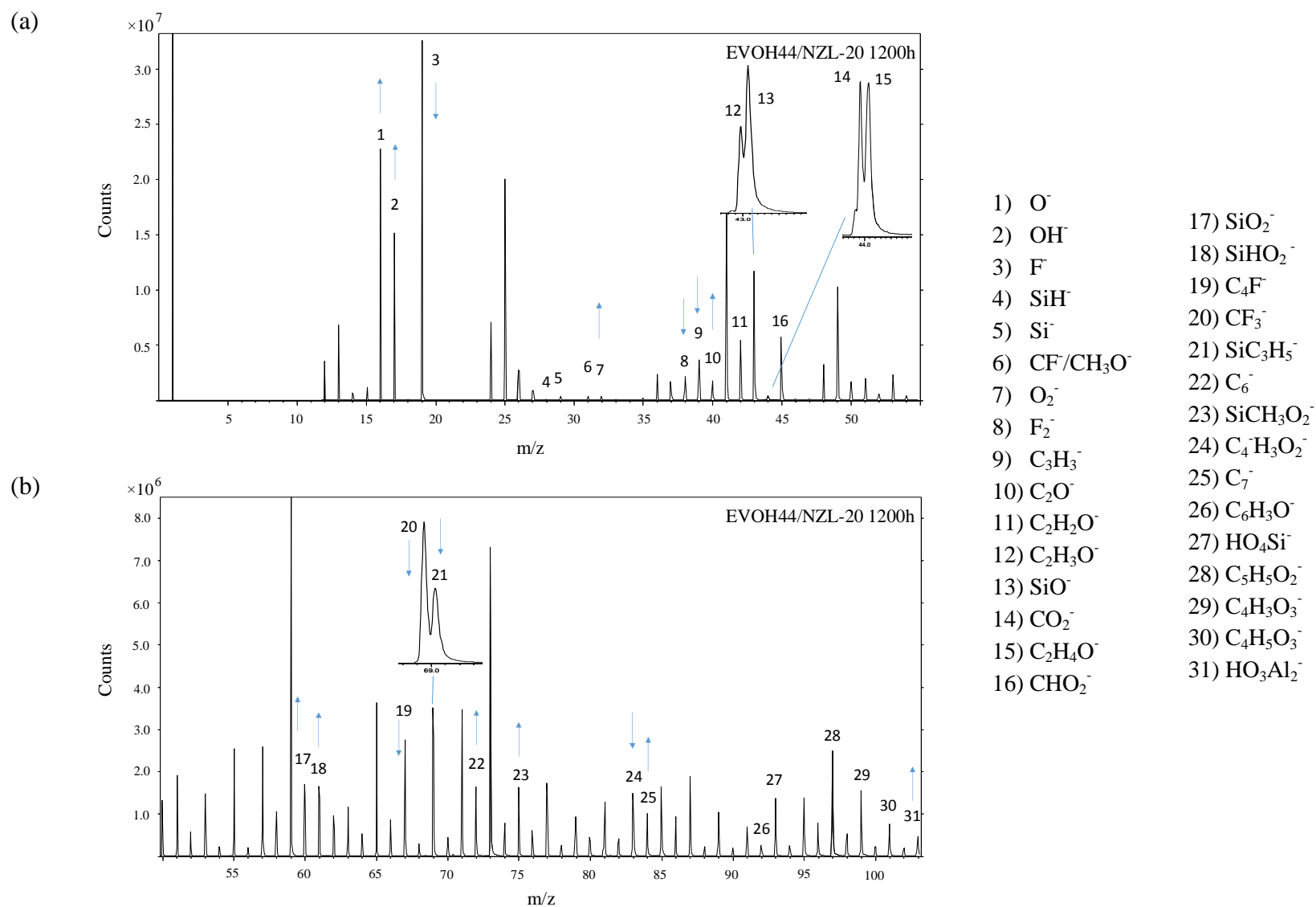


Fig.4.25. Negative-ion ToF-SIMS spectra of EVOH44/NZL-20 film surface after 1200 h of photooxidation. Mass spectra represented in two different mass ranges: (a) 0-55 and (b) 55-105 m/z.

Similarly to pristine polymer, the list of ions is given and their evolutions are displayed by arrows as in case of mass spectra of pristine EVOH44. The same groups of ions than those observed for pristine EVOH fragmentation are observed in EVOH/NZL spectra. The ions related to F-contained processing additives, similar to previously described in Ch.III DynamarTM additive [270], exhibit high intensity and are represented by labelled numbers 3,6,8,19,20.

As for EVOH44, $C_xH_yO_z^-$ fragments were evaluated for EVOH44/NZL nanocomposite as a function of the irradiation time. In order to compare the evolutions obtained for pristine polymer, the plot of $C_xH_yO_z^-$ ions with 1-3 oxygen atoms is shown in Fig.4.26.

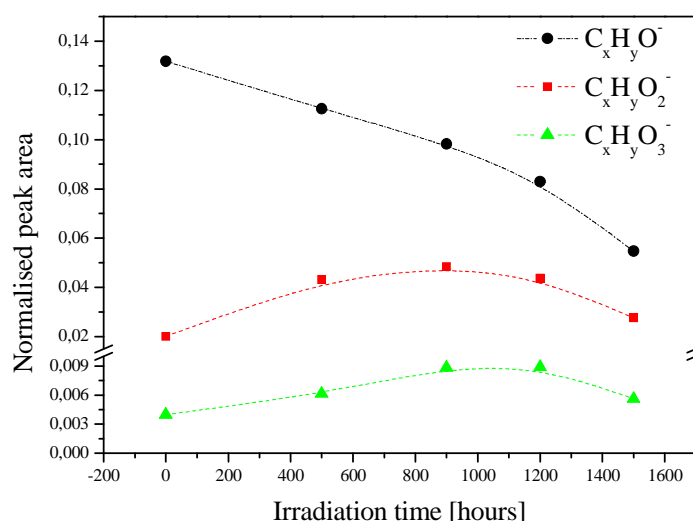


Fig.4.26. $C_xH_yO_z^-$ normalised ion peak areas as a function of irradiation time.

It is shown that the ions contained two and three oxygen atoms exhibit more or less the same evolution trends (an increase and then a decrease of the peak areas with the time) as those of pristine polymer. Nevertheless, $C_xH_yO^-$ decrease during all period of photoageing. As it was said before, this ion can be related to both, oxidised and non-oxidised fragments of EVOH. Suggesting that it basically characterises the initial state of the polymer, different evolutions of this ion for EVOH44 and EVOH44/NZL can be explained by the remaining of zeolite nanoparticles at the film surface during photoageing while the polymer is oxidising and consequently removed from the surface in the form of volatile photoproducts. Thus, less and less polymer matrix can be exposed by primary ions and lower quantity of the fragments related to polymer can be detected. This trend can be confirmed by Fig.4.27., which

represents the sum of peak areas of detected negative ions related to the polymer (C_x^- , $C_xH_y^-$ and $C_xH_yO_z^-$ where $x > 2$) as a function of irradiation time.

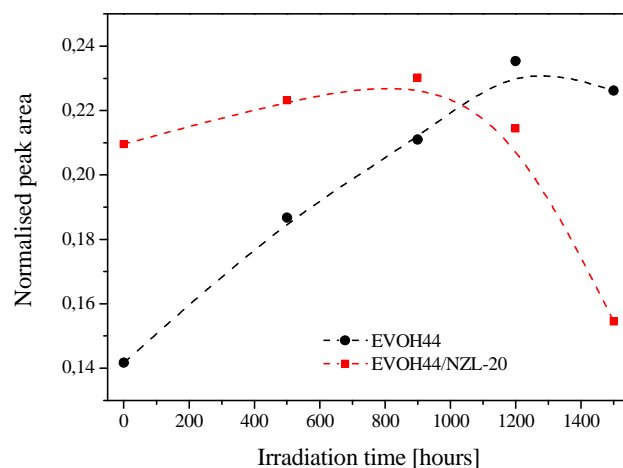


Fig.4.27. The total ion peak area of polymer related ions detected during EVOH44 and EVOH44/NZL surface sputtering as a function of irradiation time.

The figure above confirms differences caused by the particles presence. In case of pristine polymer the total ion area increases up to 1200 h and then slightly decrease due to fragmentation hindering. But, in case of nanocomposite, the areas drop is observed already after 900 h and is more significant. It can be explained by accelerated polymer degradation caused by zeolite nanoparticles as it was shown in Ch.IV §2.2.2. Nevertheless, based on the previous observations of AFM and SEM experiments the effect of particles remaining is more probable.

Moreover, an increase of O^- , OH^- and O_2^- ions can be observed from the mass spectra (Fig.4.25.). Better observation of ion area evolutions is shown on the plots presented in Fig.4.28.

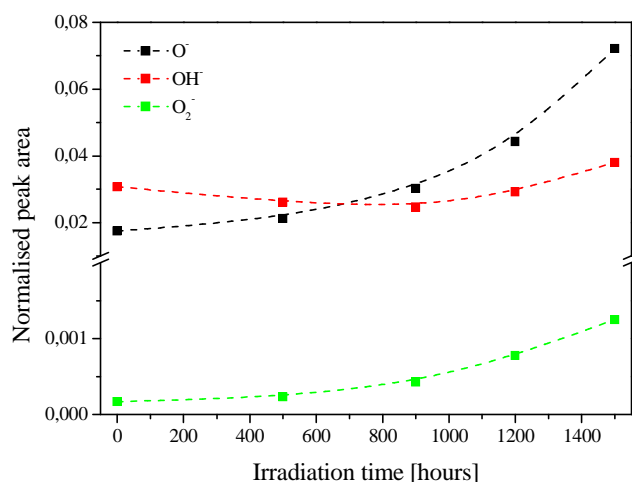


Fig.4.28. O^{\cdot} , OH^{\cdot} and $O_2^{\cdot-}$ normalised ion peak areas as a function of irradiation time.

Displayed in Fig.4.28. ions can be related to polymer as well as to zeolite fragmentation. It is observed that areas of OH^{\cdot} , O^{\cdot} and $O_2^{\cdot-}$ ions exponentially increase with the time. In the contrast to the ion peak area evaluations of these ions displayed by pristine polymer can be caused by the presence of zeolite particles, which concentration at the surface increases with the degradation time.

Next, it was interesting to compare O^{\cdot} and $O_2^{\cdot-}$ ions with carbon contained ions which were considered to be mainly formed from oxidation products. The evaluations of $CO_2^{\cdot-}$ and $CHO_2^{\cdot-}$ ions are shown in Fig.4.29.

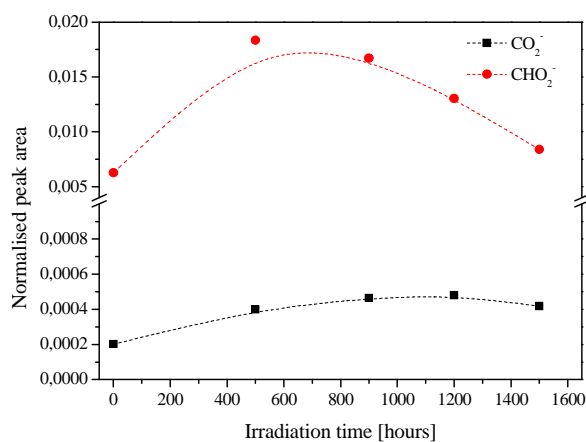


Fig.4.29. $CHO_2^{\cdot-}$ and $CO_2^{\cdot-}$ normalised ion peak areas as a function of irradiation time.

One can see that CO_2^- and CHO_2^- ions do not follow the same trends as O^- and O_2^- ions. A decrease of CO_2^- and CHO_2^- ion areas at high irradiation times indicates a decrease of polymer fragmentation mainly linked to a decrease of its concentration at the film surface.

Another ion group of interests of this study was a group related to the zeolite nanoparticles. It can be mentioned that more significant evolutions were observed for Si-contained ions while fragment ions with Al in general exhibited low relative peak areas. Thus, more attention was paid to ions contained Si. Fig.4.30.a. shows the evolution of Si-involved pattern. The ratio of total ion peak areas related to polymer and to particles is presented in Fig.4.30.b.

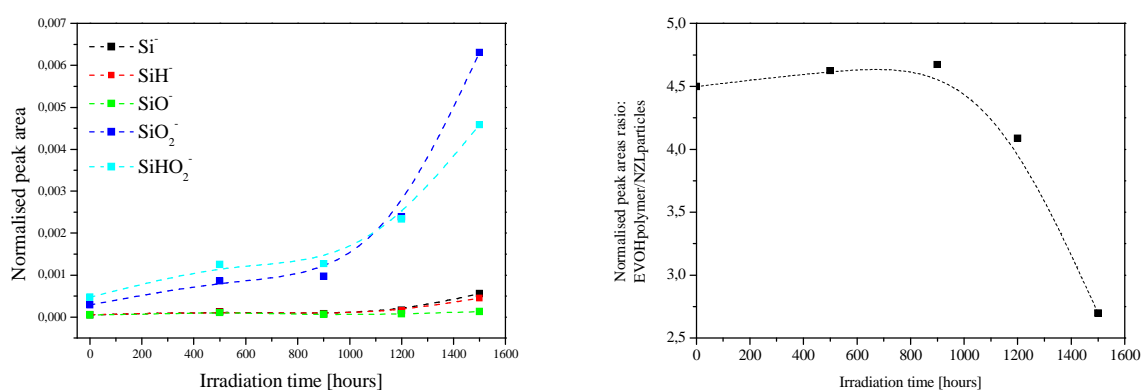


Fig.4.30. (a) Normalised peak areas of Si contained ions as a function of irradiation dose; (b) Ratio of total ion peak areas related to EVOH polymer and NZL particles.

It is observed that the formation of SiO_2^- and SiHO_2^- ions rise after 900 h of photooxidation and indicates an increase of particles concentration at the surface with irradiation time.

At the same time, Fig.4.30.b. shows that the ratio between polymer and nanocomposite particles remains constant up to 900 h and then was halved during 900-1500 h degradation time range.

Nevertheless, it is not possible, based on the data extracted from mass spectra, to conclude anything about the exact mechanism and the exact structure changes appeared upon photoageing.

Summarising, ToF-SIMS confirms the assumption of particles remaining at the composite surface during photoageing. Thus, it is hard to compare the ion peak areas of pristine EVOH44 and EVOH44/NZL-20 as the initial concentration of polymer matrix at the surface

is different and also evaluates differently during degradation due to present inorganic filler in nanocomposite composition.

2.5. Influence on viscoelastic properties

Ageing processes into polymers can impact their viscoelastic properties including flexibility, stiffness, and elongation at break. These properties are important for the assigned application as flexible encapsulation. Thus, the changes of mechanical properties were studied by dynamic mechanical thermal analysis (DMTA).

Degradation of neat EVOH44 copolymer

The changes of mechanical properties of EVOH44 caused by photooxidation can be observed in Fig.4.31. Fig.4.31.a represents the loss and storage moduli, and tan delta of an EVOH44 film before and after 900 h of photooxidation. Fig.4.31.b shows the evolution of tan delta curves with the degradation time.

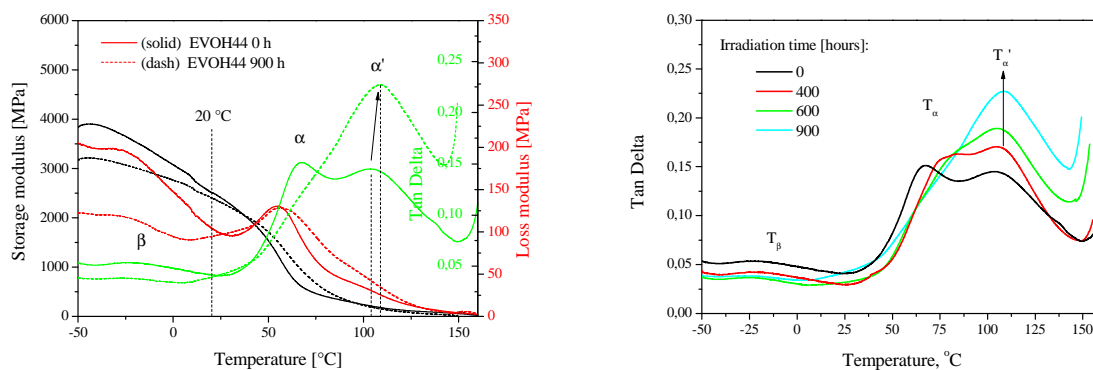


Fig.4.31. (a) Temperature dependence of tan delta, storage and loss moduli of EVOH44 before (solid) and after 900 h of photooxidation (dash); (b) Tan delta with exposure time.

Fig.4.31.a shows that 900 h of irradiation of EVOH44 leads to a decrease of storage and loss moduli in the domain below room temperature. Modification of tan delta curves is also observed. This is shown in Fig.4.31.b, which displays the curves at different irradiation times. The evolution of α -transition with degradation time, as shown in tan delta curves, (Fig.4.31.b) shows a progressive shift of the glass transition to higher temperatures with irradiation time. This transition is no more observed after 900 h of irradiation. At the same time, an increase of tan delta at the temperature of the α' -transition is observed as it was already noticed from

Fig.4.31.a. It seems that the whole area of tan delta remains more or less constant during irradiation.

The storage and loss moduli at 20 °C and the calculated Young's modulus are reported in Table 4.4.

Table 4.4. Viscoelastic behaviour of EVOH44: storage, loss and Young's moduli measured at 20 °C.

Irradiation time	Storage modulus* [MPa]	Loss modulus* [MPa]	Young's modulus [MPa]
0	2495±200	100±10	2595±210
300	2838±400	110±15	2948±415
500	3220±150	115±20	3335±170
900	2900±500	121±32	3021±532

**each value is an average of two measurements*

Table 4.4. shows that at room temperature, the storage and loss moduli values are nearly constant with irradiation time.

Degradation of EVOH44/NZL-20 nanocomposite

Fig.4.32. displays the viscoelastic behaviour of EVOH44/NZL-20 nanocomposite before and after photooxidation. Fig.4.32.a. displays the loss and storage moduli and tan delta of EVOH44/NZL-20 nanocomposite before and after 900 h of photoageing. And Fig.4.32.b is focused on the evolution of tan delta plots.

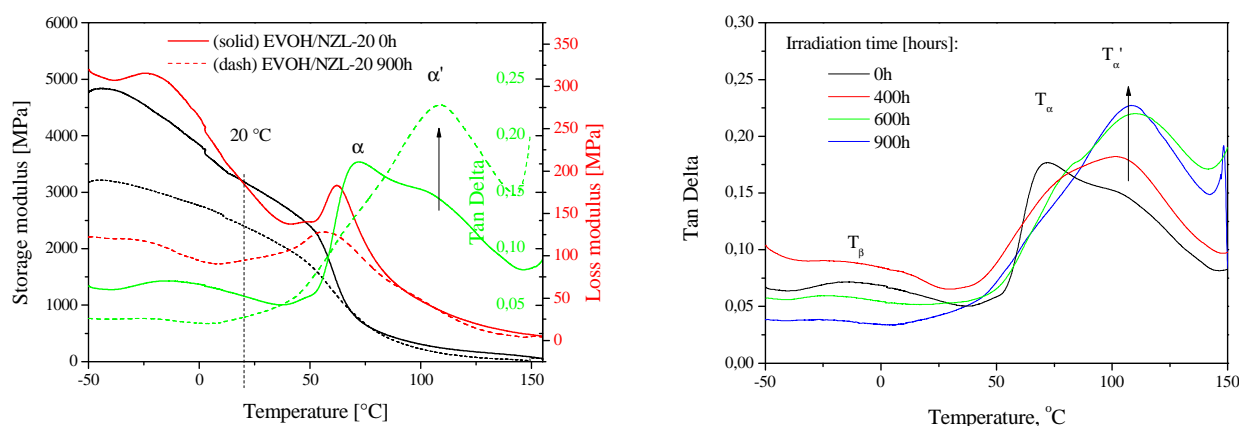


Fig.4.32. (a) Temperature dependence of storage and loss moduli, and tan delta of EVOH44/NZL-20 nanocomposite before (solid) and after 900 h of photooxidation (dash); (b) Tan delta with exposure time.

Comparison of Fig.4.31.-Fig.4.32. indicates similar behaviours for the EVOH44/NZL nanocomposites and the pristine polymer. The T_{α} progressively shifts to higher temperature and the corresponding peak is progressively hidden by the peak of the α' -transition (Fig.4.32.b). However, Fig.4.32.a shows a decrease of the storage and loss moduli at room temperature.

The storage, loss moduli and the calculated Young's modulus at room temperature (20 °C) are given in Table 4.5.

Table 4.5. Viscoelastic behaviour of EVOH44/NZL-20 nanocomposites: storage, loss and Young's moduli measured at 20 °C

Irradiation time	Storage modulus* [MPa]	Loss modulus* [MPa]	Young's modulus [MPa]
0	3550±300	240±50	3790±350
300	3480±200	200±70	3680±270
500	4010±270	190±40	4200±310
900	2820±600	186±30	3006±630

*each value is average of two measurements

These DMTA experiments reveal that the temperature of the α -transition progressively shifts to higher values, independently of the presence of NZL nanoparticles. After 900 h of

irradiation, the α -transition is no more observed, the tan delta peak being convoluted with the one of the α' -transition. The difference between the nanocomposite and the pristine EVOH44 deals with the storage and loss modulus at room temperature, which decrease in the case of the nanocomposite, whereas they remain constant in the case of the pristine polymer.

2.6. Thermal properties

Degradation of neat EVOH44 copolymer

The impact of photooxidation on the thermal properties of EVOH was also studied by DSC analysis of EVOH44 films at different photoageing times.

The results are shown in Fig.4.33., which displays the first heating and cooling curves.

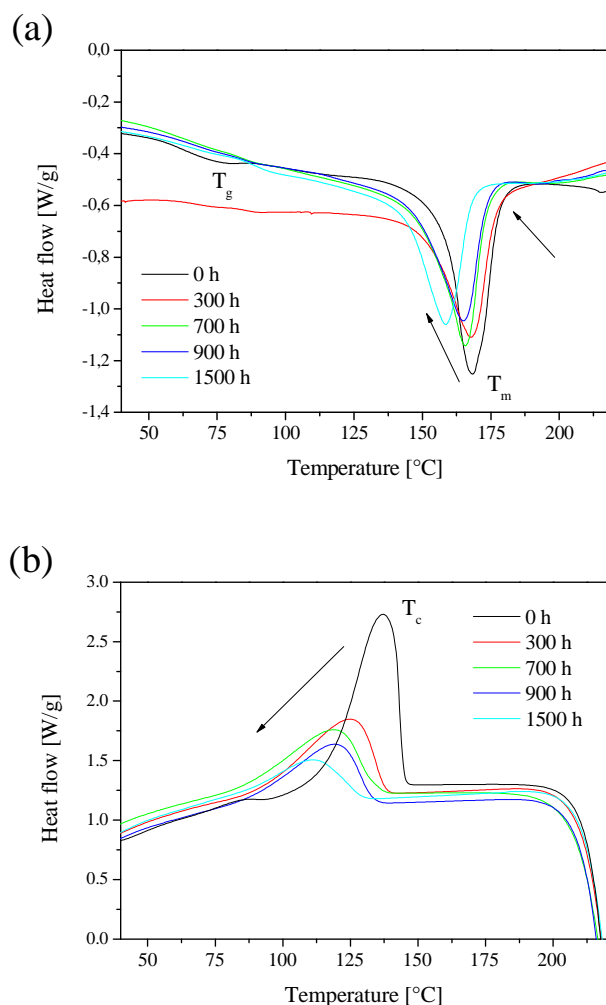


Fig.4.33. Normalised DSC curves of EVOH44 at different photooxidation time: (a) first heating; (b) cooling.

The first heating DSC curves show that the melting peak temperature as well as its intensity decreases. At the same time, the onset and onset temperatures of melting also decrease. All these observations suggest a decrease of polymer crystallinity and a decrease of the size of crystallites giving rise to a new crystal population that can be formed with ageing. By the cooling curves, it can be confirmed that the changes of crystallisation peak follow the same trends as those of melting.

Additionally, it seems that intensity of glass transition peak becomes weaker and glass transition cannot be anymore observed after 300 h of photoageing. This trend confirms the evolution of glass transition (α -transition) shown by DMTA experiment.

The values obtained for the melting and crystallisation temperatures, enthalpies and relative crystallinity of EVOH44 during photooxidation are reported in Table 4.6.

Table 4.6. Thermal properties of EVOH nanocomposite during first heating and cooling: onset, endset and temperatures of melting (T_m), crystallisation temperature (T_c), enthalpies of melting (ΔH_m) and crystallisation (ΔH_c), relative crystallinity χ_c

	T_g onset [°C]	T_m onset [°C]	T_m [°C]	T_m endset [°C]	T_c [°C]	ΔH_c [J/g]	χ_c^{**} [%]
EVOH44 – 0h	54±1	159±1	166±1	177±1	138±1	70±1	45±1
EVOH44 – 300h	60±2	150±1	167±1	177±1	125±1	44±1	42±1
EVOH44 – 700h	-	151±1	166±1	174±1	123±1	40±1	41±1
EVOH44 – 900h	-	146±1	166±1	173±1	119±1	36±1	42±1
EVOH44 – 1500h	-	141±1	158±1	168±1	112±1	18±2	36±1

*each value is average of two measurements

**calculated using 100% pure crystalline PVA with $\Delta H_m^\circ = 157.8 \text{ J/g}^{[246]}$

The values in Table 4.6. support the observations from Fig.4.33. T_m decreases from 166 to 158 °C after 1500 h of photoageing leading to the subsequent decrease of onset and endset temperatures by around 18 and 9 °C respectively. The relative crystallinity drops from 45 to 36 % after 1500 h.

Data from cooling run are in a good agreement with the first heating run, displaying a decrease of the cooling temperature from 138 to 112 °C and of the cooling enthalpy from 70 to 18 J/g.

Degradation of nanocomposite

The thermal analysis was also carried out on films of EVOH44/NZL-20 nanocomposites degraded in the same conditions as for pristine EVOH44 polymer in order to investigate the nanofiller effect. The obtained DSC curves are given in Fig.4.34.

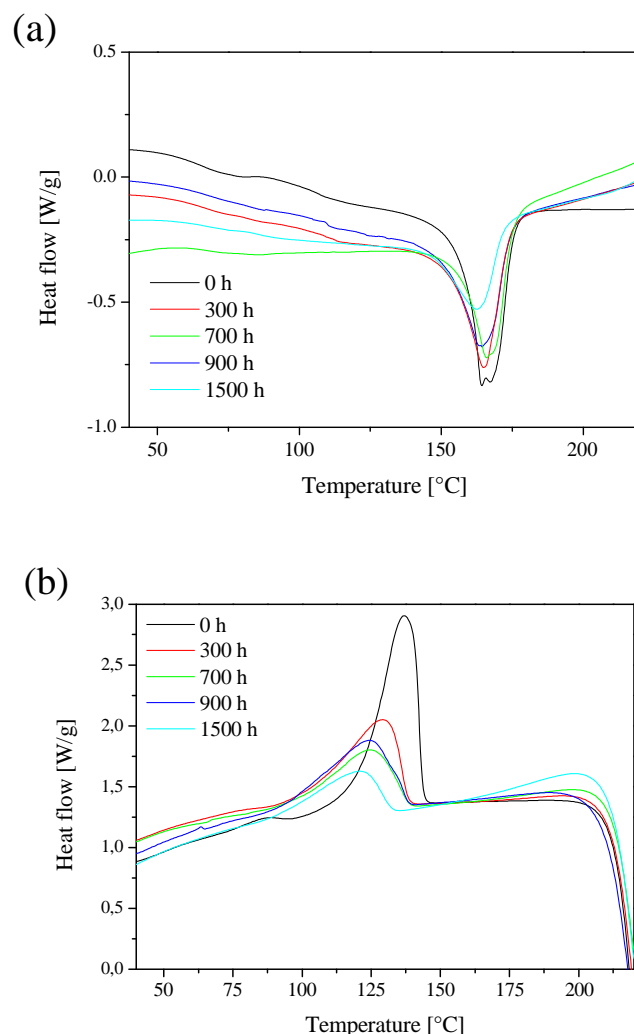


Fig.4.34. Normalised (to the amount of EVOH44 polymer in the sample) DSC curves of EVOH44/NZL-20 during photooxidation: (a) first heating; (b) cooling.

Similar evolution trends as those observed for neat EVOH are detected. All three values of temperatures of onset, endset and melting peak are decreasing during photooxidation indicating a decrease of crystal sizes. The shape of melting peak also changes. The second peak/shoulder at around 169 °C disappears after 300 h which can result from reorganisation in the polymer upon light exposure when the temperature is set up at 60 °C and polymer is close to its glass transition and therefore exhibits high mobility of the polymer chain. Cooling plots confirms the decrease of crystallinity and size of crystals. The data of thermal properties of EVOH44/NZL-20 nanocomposite are given in Table 4.7.

Table 4.7. Thermal properties of EVOH/NZL–20 nanocomposite during first heating and cooling: melting (T_m) and crystallisation (T_c) temperatures, enthalpies of melting (ΔH_m) and crystallisation (ΔH_c), relative crystallinity χ_c

	T_g onset [°C]	T_m onset [°C]	T_m [°C]	T_m endset [°C]	T_c [°C]	ΔH_m [J/g]	ΔH_c [J/g]	χ_c^{**} [%]
EVOH44/NZL - 0h	54±2	157±1	166±1	176±1	133±1	61±2	65±2	44±2
EVOH44/NZL - 300h	-	151±2	166±1	174±2	129±1	60±1	60±1	44±2
EVOH44/NZL - 700h	-	152±1	164±1	175±1	124±2	58±1	38±2	38±1
EVOH44/NZL - 900h	-	150±1	163±2	174±1	124±1	56±1	36±1	37±1
EVOH44/NZL - 1500h	-	143±2	163±1	172±1	120±1	50±1	29±1	35±1

*each value is average of two measurements

**calculated for the EVOH amount according to 100% pure crystalline PVA with $\Delta H_m^\circ = 157.8 \text{ J/g}^{[246]}$

Table 4.7. reflects the trends observed in the DSC curves (Fig.4.34.). The crystallinity of EVOH44 in the nanocomposite decreases during photooxidation, from 44 to 35 % after 1500 h of irradiation. Melting and crystallisation temperatures decrease from 166 to 163 °C and from 133 to 120 °C respectively.

Summarising, similar evaluations of thermal properties were observed for EVOH44 with and without particles addition. The germination process in the EVOH44 copolymer is becoming more and more impeded, the crystals are becoming smaller and are formed in smaller quantities. These phenomena have already been observed in the case of PVA photoageing^[283] and were attributed to chain scissions occurring during light exposure. It might be the case for EVOH where photooxidation mechanism involves many chain scissions (Ch. IV § 1.4.).

2.7. Influence on water sorption properties

The impact of photooxidation on the water sorption properties of EVOH44 was studied by DVS. The DVS analyses were very recently performed, because the DVS apparatus was set up at the end of this PhD work. The experiments should then be considered as preliminary results and only the results obtained in the case of the pristine material EVOH44 are reported in the manuscript. The experiments were performed before and after 200 h and 500 h of irradiation. The curves were treated as in Ch. III §2.6.1 using second Fick's law (described in Ch. II § 3.7).

The water sorption curve obtained from the DVS experiments of an EVOH44 film after different irradiation times is presented in Fig.4.35.a. The water mass gain was obtained by dividing the measured mass gain by the dry mass of the sample before immersion and was plotted as a function of immersion time. The relative water sorption ($M/M_{eq.}$) was obtained by dividing the water mass by the water uptake $M_{eq.}$ at the plateau and was plotted as a function of the square root of time to characterise the diffusion behaviour of water in this EVOH44 copolymer at the various irradiation times considered here.

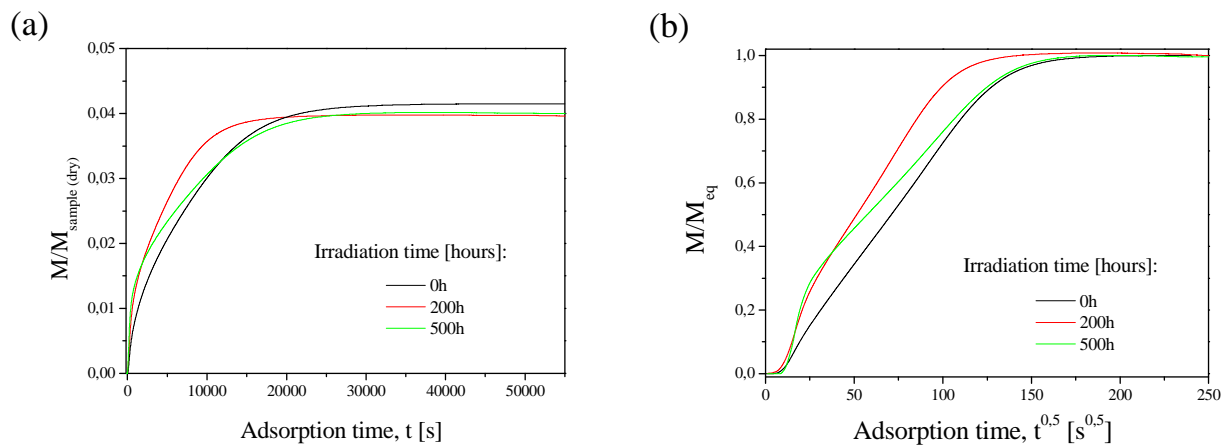


Fig.4.35. Water sorption curves of EVOH44 films obtained by DVS (85 % RH /38 °C) after different irradiation times: (a) water mass gain as a function of time; (b) normalised water sorption as a function of the square root of time.

Fig.4.35.b shows a Fickian behaviour for all the samples at least in the first period. One can then determine the diffusion coefficients. The results are gathered in Table 4.8. This table also indicates the thickness of the samples and the sample dry mass.

Table 4.8. Water uptake and diffusion coefficient for EVOH44 at different irradiation times (0, 200 and 500 h)

Irradiation time [hours]	l [μm]	$M_{\text{dry sample}}$ [mg]	M_{eq} [mg]	Water uptake [%]	Slope, b [$10^{-2} \text{ s}^{-0.5}$]	D [$10^{-9} \text{ cm}^2 \text{ s}^{-1}$]
0	83.6	58.7	61.2	4.2	1.0	1.4
200	71.2	63.4	65.9	4.0	1.7	2.9
500	92.8	54.7	56.9	4.0	2.4	9.7

The slopes of the curves (Fig.4.35.b.), which are linked to water diffusion rate, change with irradiation time and an increase can be noted. The changes of morphology reported above (crystallinity, presence of interfacial groups, segmental mobility, formation of cracks and voids) can explain the increase of the slope and then the increase of the diffusion coefficient.

CONCLUSIONS

In this chapter, we have studied the photooxidation of EVOH44 and EVOH27. The analysis performed by UV-Visible absorption spectrometry has shown that the polymers remained transparent under irradiation, which confirm their potentiality for applications as encapsulant coatings for OSCs.

The identification of the macromolecular and volatiles oxidation photoproducts revealed that the oxidation involves the oxidation either on the tertiary and/or on the secondary carbon in α - and β -positions to hydroxyl group as well in the PE units as in the PVA units and that, the sequences PVA-PE-PVA and PVA-PE-PE have also to be considered. On the basis of the identification of the products, a comprehensive mechanism accounting for the photooxidation of EVOH44 and EVOH27 was proposed.

Concerning the role played by zeolites on the photooxidation of EVOH44, we have shown that the nanocomposites remained transparent in the visible. The molecular analysis has shown that the photooxidation of EVOH mechanism remained unchanged in the presence of zeolites. However, our results indicate that the rate of oxidation of EVOH was modified in the presence of zeolites, which act as prodegradant and accelerate the photochemical oxidation of EVOH. This effect was mainly attributed to the iron impurities in the zeolite particles. This is a reasonable assumption, as iron ions are known to induce the photodecomposition of hydroperoxides, which in turn increases the rate of oxidation of the polymer. Moreover, as shown in the case of nanoparticles, this effect is proportional to the amount of zeolite in the composite (from 5 wt % to 20 wt %).

Photoageing was shown to slightly smooth the surface of the films, as well in the case of EVOH as for nanocomposites. The loss by evaporation of the low-molecular-weight photoproducts allowed for the observation of zeolites particles at the surface. This was confirmed by ToF-SIMS experiments.

The thermo-mechanical analysis that were performed in the case of EVOH44 and EVOH44/NZL nanocomposites indicate a shift around 40 °C of the α transition to higher temperatures, but did not evidence any modification of the Young's modulus at ambient temperature.

The preliminary experiments performed for measuring the water barrier properties indicate that the diffusion coefficient increases with photoageing, which confirms the necessity of a photostable polymer for developing encapsulation materials with durable barrier properties.

CHAPTER V:
MATERIALS TESTING IN DAMP HEAT
CONDITIONS

INTRODUCTION

This chapter is dedicated to the studies of barrier properties of the developed materials and their testing as encapsulant coating for organic solar cells. All the experiments reported in this chapter have been performed at Belectric OPV in Nuremberg, Germany

Three different kinds of experiments are described in this chapter:

- first, an electrical calcium test was carried out in order to determine the performance and applicability of EVOH and EVOH/NZL nanocomposites as barrier coatings.

- second, the films were used for encapsulation of OSC to test the device performance and lifetime in damp heat conditions.

- third, the experiment of different layer multistacks containing EVOH film and materials used for OSCs processing (substrate, glue, additional encapsulation layer(s)) was performed in damp heat conditions with the aim to model and understand the behaviour of EVOH films in conditions of OSCs device testing.

1. Calcium test

Electrical calcium test was used to determine water transmission rate of EVOH44 and EVOH27 and their nanocomposites. This experiment is based on the principle that water, permeating through a barrier film, reacts with metallic calcium layer converting it into transparent uncondusive calcium hydroxide. As a result of this reaction, the drop of conductivity can be detected and water permeation rate can be calculated from the slope of the conductance decrease $1/R$, plotted versus time t as it is described in Ch.II Eq.2.22.:

$$P = -n \frac{M_{(reagent)}}{M_{(Ca)}} \delta p \frac{l}{b} \frac{d(1/R)}{dt} \quad (\text{Eq.2.22.})$$

where $n=2$, $\delta(\text{Ca density})=1.54\text{g/cm}^3$, $\rho(\text{Ca resistivity})=4.09 \times 10^{-6} \Omega\text{cm}$ (at 75°C) [291] and $M_{\text{H}_2\text{O}}/M_{\text{Ca}}=0.4495$.

The descriptions of sample preparation and the calcium test are given in Ch.II § 1.2. and §3.7. respectively.

Orthogonal (perpendicular to film surface) and lateral water diffusion have been studied by Ca-test and are described below.

1.1. Orthogonal diffusion

The calcium sensors encapsulated by a single layer of EVOH or of EVOH/NZL nanocomposite were used to investigate the effect of zeolite content on the stability of the sensors. The conductance of the calcium film was monitored during all lifetime of sensors, which was indicated as the time when all the metallic calcium has reacted with permeant forming uncondusive product. Two types of substrates, flexible ultra-barrier (from 3M) and a glass plate, were used to investigate films barrier properties. As an adhesive, UV-curing based on modified epoxy resin glue was used.

a. Flexible substrate

The results of the calcium test performed on the samples with flexible substrate can be represented by plotting the normalised conductance as a function of damp heat exposure time, as shown in Fig.5.1.

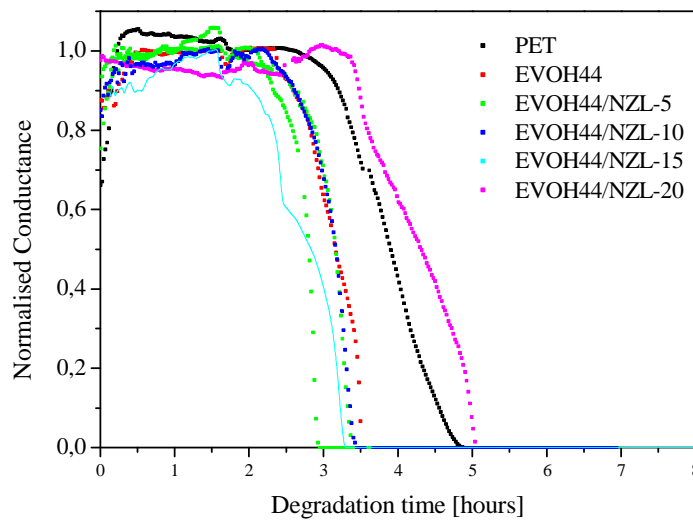


Fig.5.1. Normalised conductance of sensors on flexible substrate versus damp heat exposure time (65°C/85 % RH). Encapsulation foils: PET (e=125 µm), EVOH44 (e=82 µm) and EVOH/NZL nanocomposites with different particle content: 5 wt % (e=72 µm); 10 wt % (e=80 µm); 15 wt % (e=70 µm); 20 wt % (e=116 µm).

The conductance curves shown above exhibit characteristic shapes. The conductance versus damp heat exposure time shows no variation in the first hours, which is often interpreted as a “time lag” [292]. This time can be explained as a “reservoir effect” of the polymeric barrier [293], by a long tortuous path of H₂O molecules [137], or by high resistance of samples [294]. Next, the conductance rapidly drops within 1-2 hours of damp heat exposure and then reaches zero. This “fall off” region is mainly related to the interaction of diffused water with calcium film causing its transition into hydroxide. Time at zero conductance corresponds to sensor lifetime. Fig.5.1. shows that all the studied samples exhibit time lags between 2 and 3.5 hours. Unexpectedly, neat EVOH as well as EVOH/NZL nanocomposites show lower barrier performance than the PET film.

To better understand the mechanism of fast sensor failure, the photos of sensors taken during the damp heat experiment are shown and analysed below.

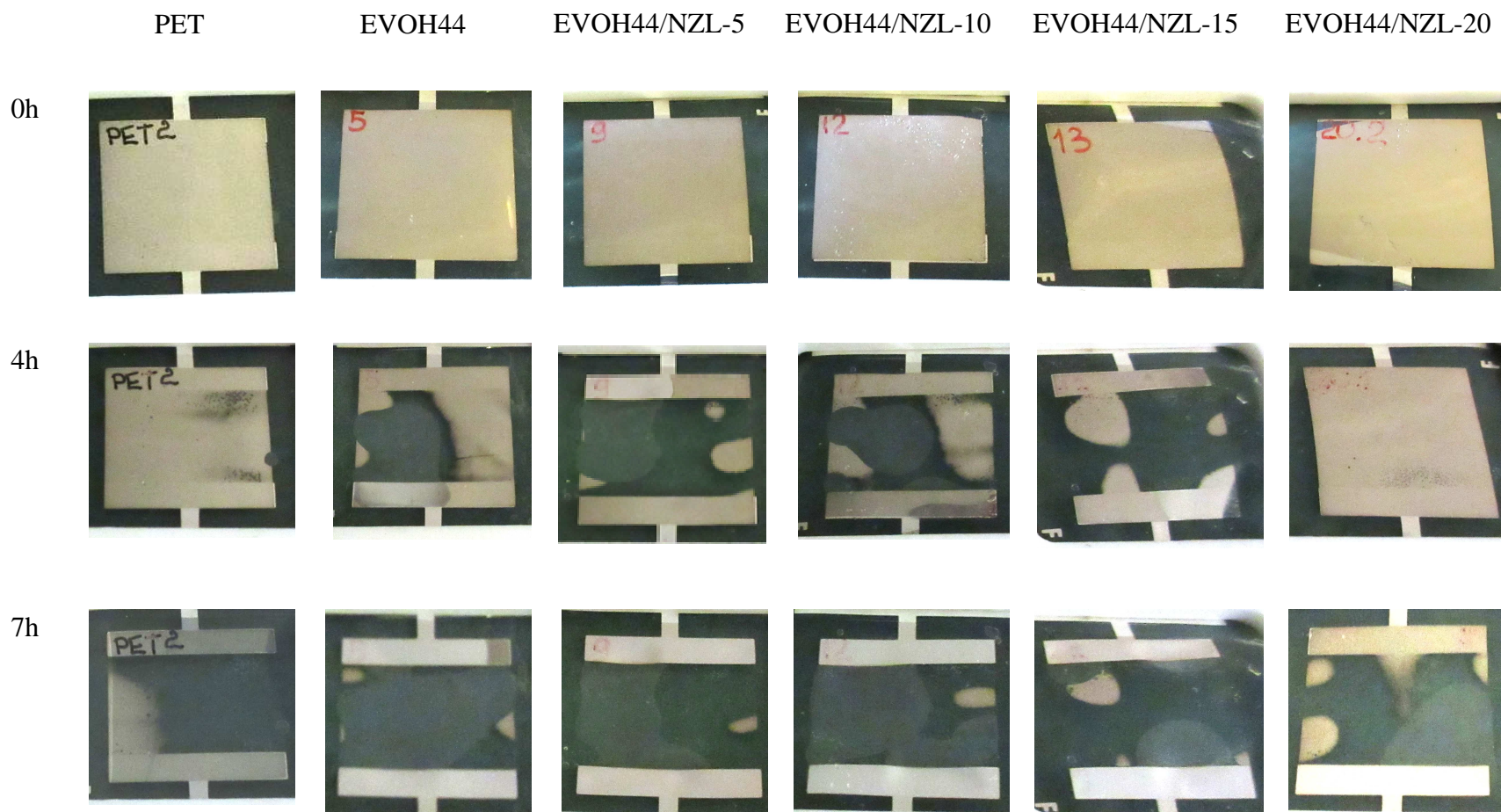


Fig.5.2. Pictures of calcium corrosion during electrical calcium test: PET, EVOH44 and EVOH/NZL before and after 4 and 7 h of damp heat exposure (65°C/85 % RH).

Firstly, it can be noticed from Fig.5.2. that the conductance drop is not related to the lateral water diffusion. In the sensors covered by EVOH based films, the calcium reaction with water randomly appears in the whole area of the metal layer, as well at the edges of the sensor as in the central area. After 4 hours of experiment, the calcium layer in all the samples, except for PET and EVOH44/NZL-20, was significantly oxidised exhibiting transparent areas of calcium film. At the same time the remaining opaque areas represent the metallic calcium. Nevertheless, the contact between electrodes and calcium has already been lost due to isolation of metallic areas by formed calcium hydroxide. This observation is in good agreement with the conductance plot, which shows that sensors covered by pristine EVOH44 and EVOH44 with 5, 10 and 15 wt % of NZL nanoparticles exhibit zero conductance after 4 hours. The better stability of sensors covered by PET and EVOH44/NZL-20 films can be explained by different reasons, one of the main reasons being the higher thickness of these two encapsulation layers in comparison to EVOH or the others nanocomposite films.

To better observe the changes on calcium sensors after damp heat exposure, Fig.5.3., given below, represents the pictures of calcium sensors after 7 h in damp heat experiment.

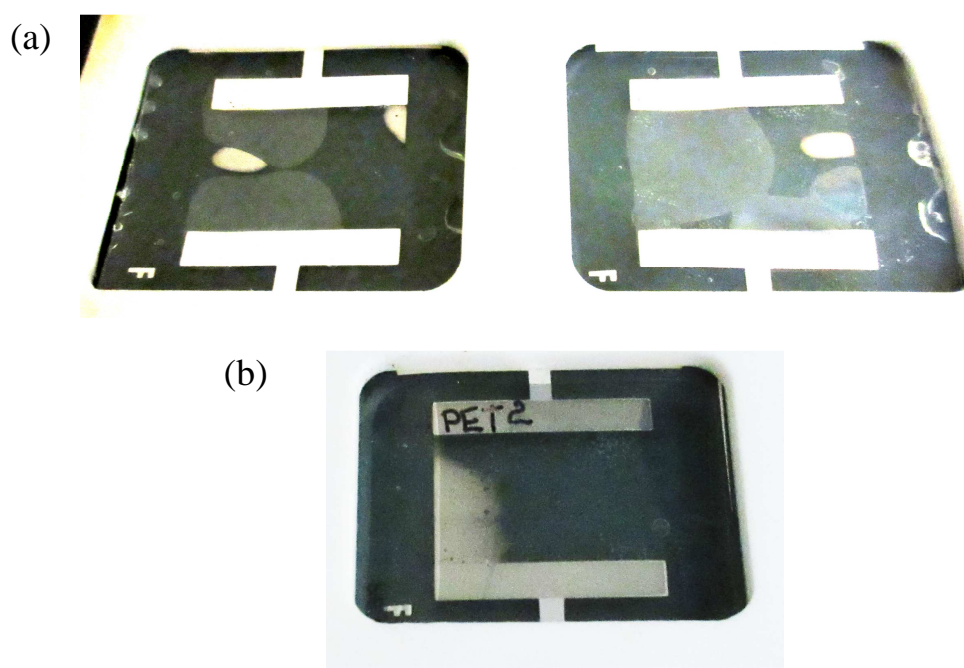


Fig.5.3. Calcium sensors after 7 h of damp heat experiment: bright areas on the sensor display the barrier-calcium films delamination. Samples encapsulated by (a) EVOH materials and (b) PET.

These pictures suggest that the drop of conductance in “fall off” region for sensors covered by EVOH and EVOH/NZL (Fig.5.3.a) is mainly caused by delamination processes appearing between the encapsulation film and calcium layer. Further, by visual analysis, it was found that delamination mainly takes place at epoxy glue-calcium interface.

Although not presented in this chapter, the electrical calcium studies on the sensors sealed with EVOH27 and EVOH27/NZL nanocomposites with 5-20 wt % of particles content were also performed. All the samples displayed the same delamination problems as those observed with EVOH44. Due to this reason, the extraction of the representative water barrier properties of those films was not done.

The observed phenomenon can be related to the water sorption property of EVOH and EVOH/NZL nanocomposites, which leads to important water uptake by the samples in damp heat conditions of experiment and thus, to an increase of their volume at the expense of the bending. To support this assumption, one can mention that the polymer exists in its rubbery state under experimental conditions ^[295, 296]. At the same time, no notable delamination was observed between calcium layer and PET (Fig.5.3.b), which is commonly used as a substrate.

b. Glass substrate

In order to improve the stability and to determine the impact of the substrate on the sensor behaviour, the flexible substrate was replaced by a glass plate. EVOH/NZL nanocomposite films with increasing amount of zeolite nanoparticles (from 0 up to 20 wt %) were used to encapsulate glass based sensors. As in the case of flexible sensors, a sensor encapsulated with PET was used as a reference. The corresponding conductance plots are displayed in Fig.5.4.

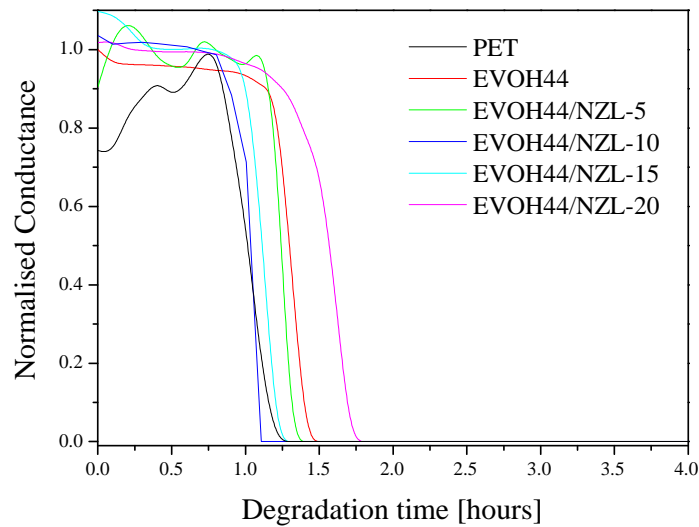
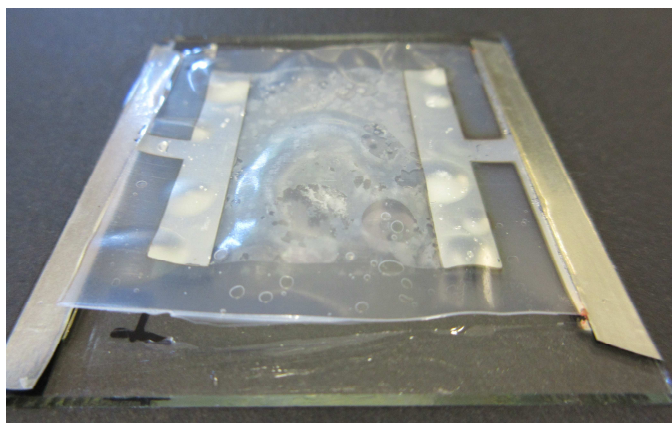


Fig.5.4. Normalised conductance of sensors on flexible substrate versus time.
Encapsulation foil: PET (e=125 μm), EVOH44 (e=80 μm) and EVOH/NZL
nanocomposites: 5 wt % (e=88 μm); 10 wt % (e=85 μm); 15 wt % (e=89 μm); 20 wt %
(e=89 μm).

Unfortunately, the obtained curves of normalised conductance show that the substrate replacement does not improve the stability of the sensors, as indicated by the sensor lifetimes detected in the range of 1-2 h (Fig.5.4.) which are even shorter than those observed for sensors on flexible substrates.

This fast failure of the sensors was also attributed to the delamination due to volume expansion as observed on the flexible substrate. This conclusion can be supported by an example comparing sensors covered by EVOH and PET after calcium test shown in Fig.5.5.

(a)



(b)

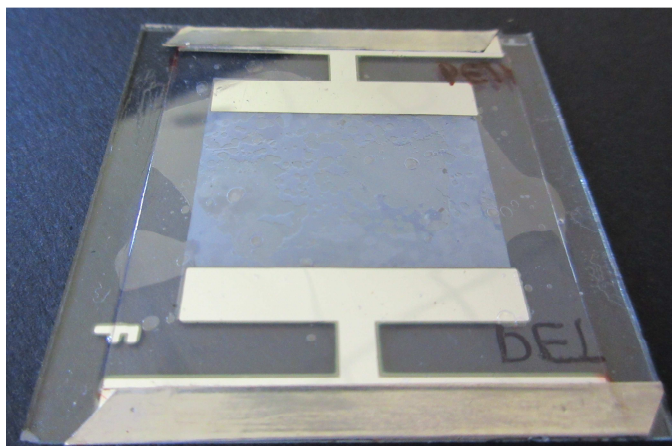


Fig.5.5. Calcium sensors after damp heat experiment: bright areas on the sensor display the delamination and bending of encapsulation layer. Samples encapsulated by (a) EVOH materials and (b) PET.

It can be mentioned that significant bending processes appeared for EVOH polymer while PET remains flat.

Summarising, the results obtained during calcium test do not represent the water barrier properties of the EVOH films, but reflect the delamination processes that appeared between the encapsulation and the calcium layers of the sensors. This experiment highlights the problem of dimensional stability of the polymer during ageing in damp heat conditions.

1.2. Lateral diffusion

In order to estimate the water diffusion through the EVOH films, an alternative approach was used and the lateral water diffusion into calcium sensors was studied. For this experiment, the sensors composed of substrate-calcium-electrodes-EVOH film were

additionally encapsulated by a glass plate on the top of EVOH layer using the same epoxy glue. It was expected that this top glass plate prevented the EVOH films from bending and delamination. A scheme giving the different layers of this “glass –Ca-sensor” has been shown in Ch.II § 1.2. Fig.2.5.

Assuming that water cannot come from front or rear sides of the sensor (protection by a glass plate), the decrease of calcium conductivity would be assumed to result from the water ingress through the lateral side. This lateral diffusion includes the impact of barrier properties of EVOH film and of the adhesive (epoxy glue) used to seal glass substrate-calcium-silver electrodes part of the sensor with EVOH film and then by top glass plate. As a reference sensor, a multilayer stack without internal EVOH layer was studied. In the case of reference, the lifetime of Ca sensor depends on the water permeation through the adhesive. This investigation will help to separate the contribution of the adhesive and EVOH to estimate the process of water diffusion through EVOH films, and its impact on the stability/degradation of the device with integrated encapsulation layer.

Photos obtained during the damp heat test (Fig.5.6.) display the different stability of all three types of sensors. While the reference does not display any corrosion of the calcium layer, sensors encapsulated either by the neat EVOH44 polymer or nanocomposite with 20 wt % zeolite nanoparticles indicate the reaction of metal with water.

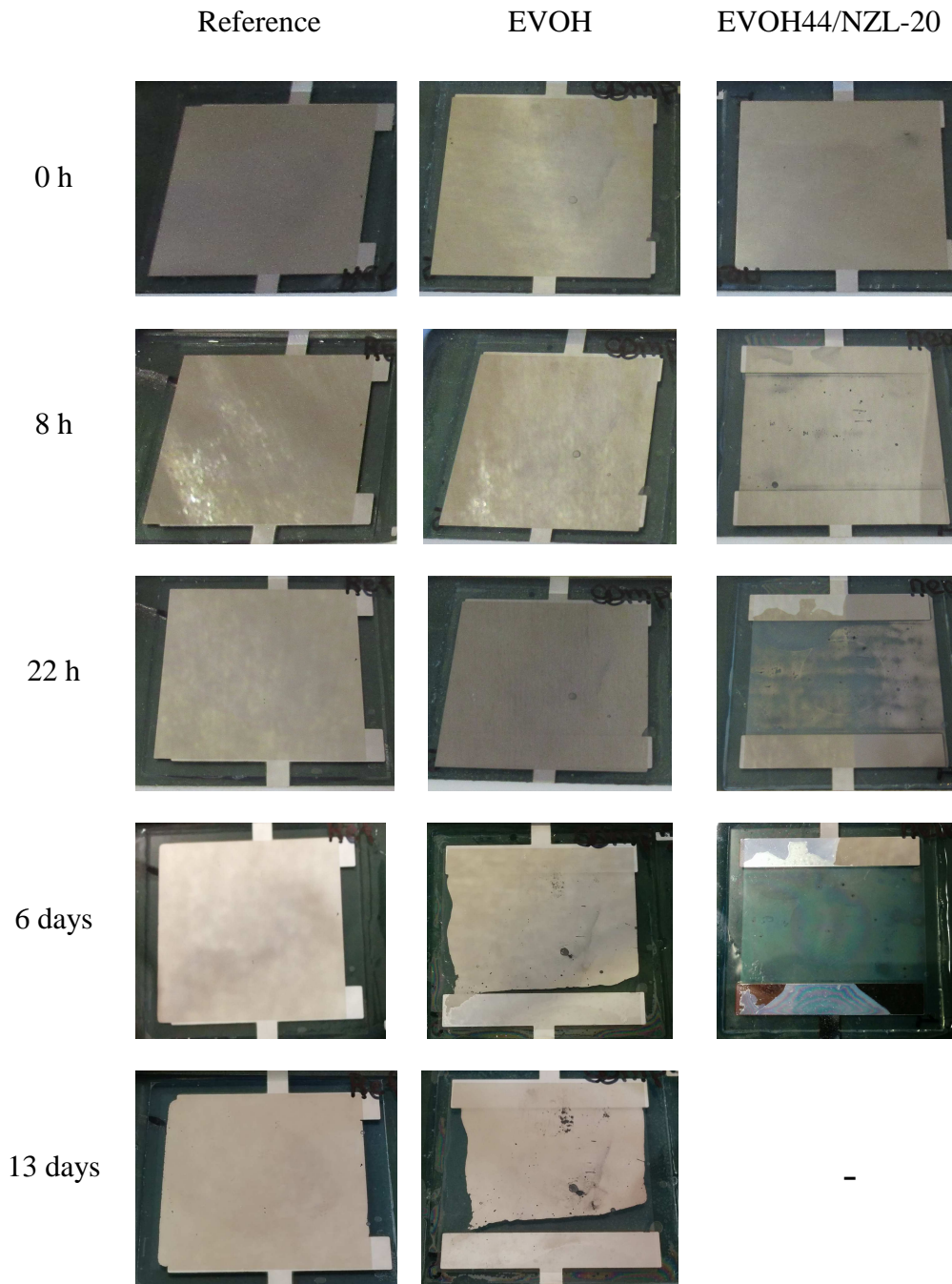


Fig.5.6. Pictures of calcium corrosion during lateral diffusion of water into the sensors studied by electrical calcium test.

In the case of EVOH44, the calcium corrosion takes place at the edges of Ca layer, while for EVOH44/NZL-20 the corrosion of entire layer area is observed. This difference is illustrated by the scheme given in Fig.5.7., which indicates the different water permeation rates through EVOH44, EVOH44/NZL, and epoxy glue, respectively abbreviated S^p_1 , S^{nc}_1

and S_2 . It is hard to compare S_1 and S_2 as the thickness of the glue layer is unknown. However, it can be postulated that $S_1^{nc} \gg S_1^p$.

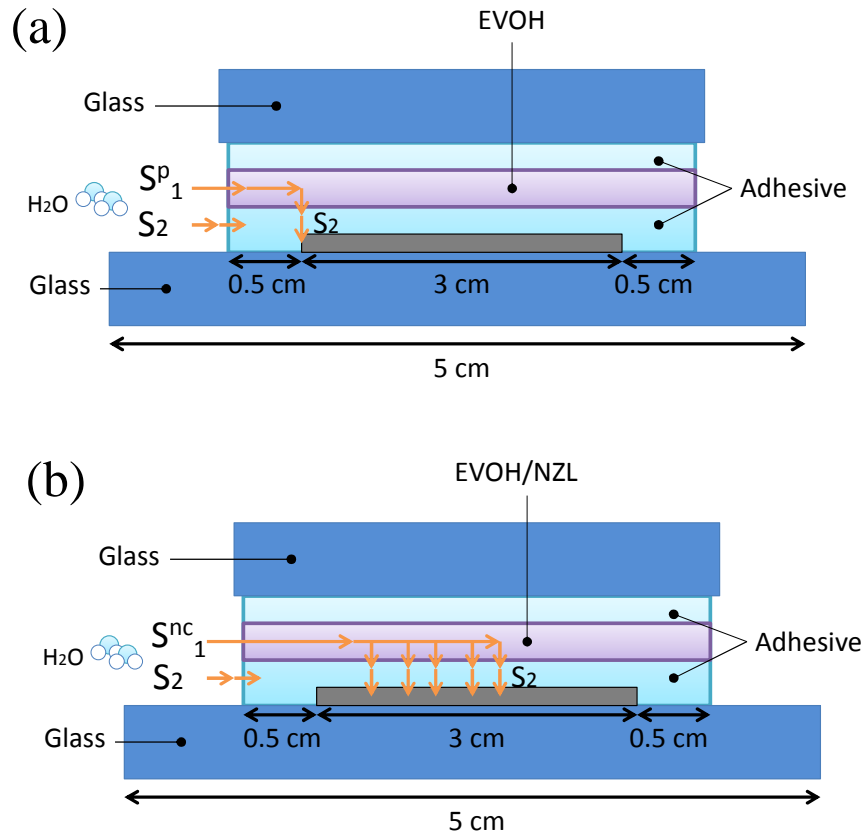


Fig.5.7. Schematic cross sectional view of water lateral diffusion into calcium sensor encapsulated by (a) EVOH and (b) EVOH/NZL-20 films. S_1 - water diffusion rate of EVOH or EVOH/NZL, S_2 - water diffusion rate of epoxy glue.

The normalised conductance as a function of time obtained for the calcium sensors sealed with EVOH44 and EVOH44/NZL-20 nanocomposite films is shown in Fig.5.8.

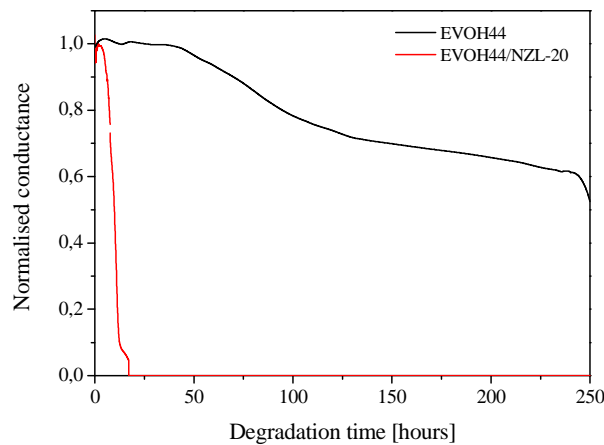


Fig.5.8. Normalised conductance versus degradation time of sensors encapsulated by EVOH44 or EVOH44/NZL-20 and a glass plate.

The characteristic values extracted from the curves given in Fig.5.8. are summarised in Table 5.1.

Table 5.1. Characteristics of calcium sensors under damp heat conditions. Lateral diffusion studies: time lag, sensor lifetime and water permeability rate

	Time lag [hours]	Lifetime [hours]	Permeability rate [$\text{g m}^{-2} \text{day}^{-1}$]
Reference	Stable up to 260 h of experiment		
EVOH44	41 ± 5	120 ± 10	0.0084 ± 0.002
EVOH44/NZL-20	8 ± 3	14 ± 2	0.28 ± 0.1

* values of two parallel measurements

The comparison of Fig.5.8. and Table 5.1. indicates that the calcium sensor encapsulated by the neat EVOH44 polymer has much longer time lag and lifetime than the sensor encapsulated with EVOH/NZL-20 nanocomposite. It can be noticed from the photos in Fig.5.6., the reference sensor with only the glue between top glass plate and calcium layer was stable during the whole time of measurements (260 h). The permeation rates, which were calculated from the slope of drop off conductance, show that the rate of water lateral diffusion significantly increases with the nanoparticles addition. This data is in a good agreement with the conclusions made on the basis of sensor photos shown above (Fig.5.6.).

2. Encapsulation of organic solar cells with nanocomposite layers

To investigate the efficiency of the EVOH based encapsulation layers, solution processed organic solar cells (OSCs) (see Ch.II. § 1.2.) were encapsulated by EVOH or EVOH/NZL nanocomposite films with both EVOH44 and EVOH27. In order to obtain the best device stability, two different adhesives and substrates were tested. The influence of the following factors on OSCs stability has been studied and reported in this paragraph:

- ethylene content of the EVOH copolymer (EVOH44/EVOH27)
- adhesive (epoxy or acrylic)
- substrate (flexible / glass plate)
- encapsulation (single EVOH film or multistacks of EVOH sandwiched with PET film(s)).

The composition of the encapsulation layers on flexible and glass substrates studied in this paragraph is described in Table 5.2.

Table 5.2. The composition of substrate and encapsulations used in the current experiments

	Substrate	Encapsulation layer(s)		
		Layer 1	Layer 2	Layer 3
1	Flexible	PET		
2	Flexible	EVOH44(27)		
3	Flexible	EVOH44(27)/NZL-20		
4	Glass	PET		
5	Glass	EVOH44		
6	Glass	EVOH44	PET	
7	Glass	PET	EVOH44	PET
8	Glass	PET	EVOH44/NZL-20	PET

a. Flexible OSC

In this experiment, organic solar cells deposited on PET substrate were encapsulated by PET, EVOH or EVOH/NZL-20 films (Table 5.2. # 1-3), using acrylic-based UV-curable adhesive. The performance of OSCs under damp heat conditions is represented by the plots of average power conventional efficiency (PCE) as a function of damp heat exposure time, which are shown in Fig.5.9.

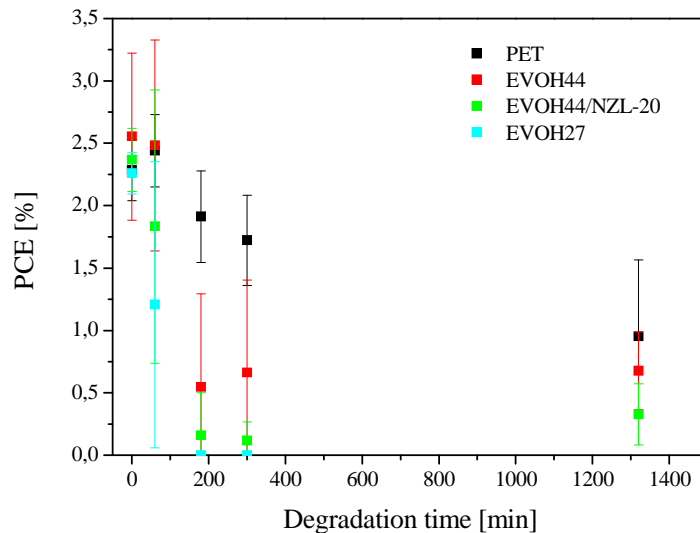


Fig.5.9. OSCs power conversion efficiency as a function of time under damp heat conditions. Materials: encapsulation (PET, EVOH44, EVOH44/NZL-20, EVOH27); acrylic adhesive; 3M flexible substrate.

The devices sealed with EVOH27/NZL-20 and EVOH27/NZL-20-PET multistacks were destroyed immediately after the contact with humid environment of the climatic chamber, no result can be obtained.

Fig.5.9. displays that the PCE of devices encapsulated by EVOH based materials is between 2 and 3 %, which is in the range of values previously obtained for P3HT:PC60BM based OSCs ^[297]. However, PCE of these devices significantly drops after only 200 min of exposure. The PCE decrease of PET encapsulated OSCs was not so significant after 200 min of experiment but reached similar value after 1300 min of exposure as those of the EVOH44-encapsulated cells.

In order to understand why PCE drops, the photos of OSCs after first 1.5 hours of damp heat exposure are given in Fig.5.10.

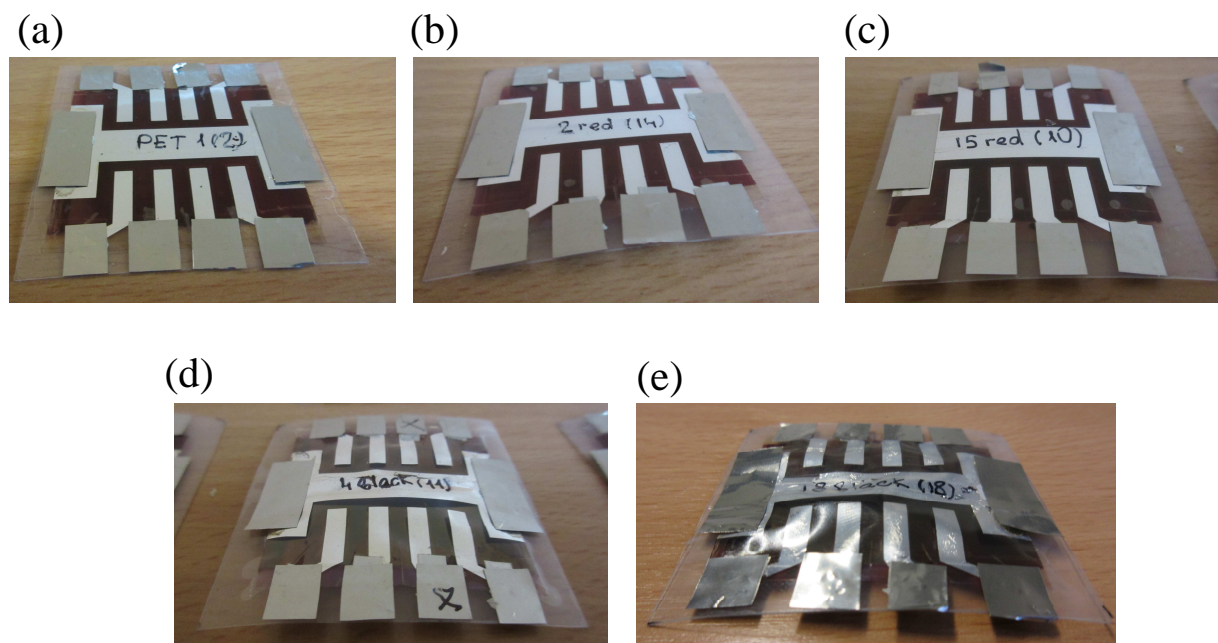


Fig.5.10. Organic solar cells after 1.5 h at damp heat conditions. Encapsulation layer: (a) PET, (b) EVOH44, (c) EVOH44/NZL-20, (d) EVOH27, (e) EVOH27/NZL-20.

These photos show that the decrease of device performance is related to delamination processes appearing in the devices. The cells encapsulated with EVOH27 and its nanocomposite (Fig.5.10.d-e.) show significant delamination after 1.5 h. In case of the EVOH44 based materials, delamination was not so significant but then, further damp heat exposure also resulted in delamination inside the device. Encapsulation failure can be observed in Fig.5.11. as shown in the photos of the devices after the experiment.

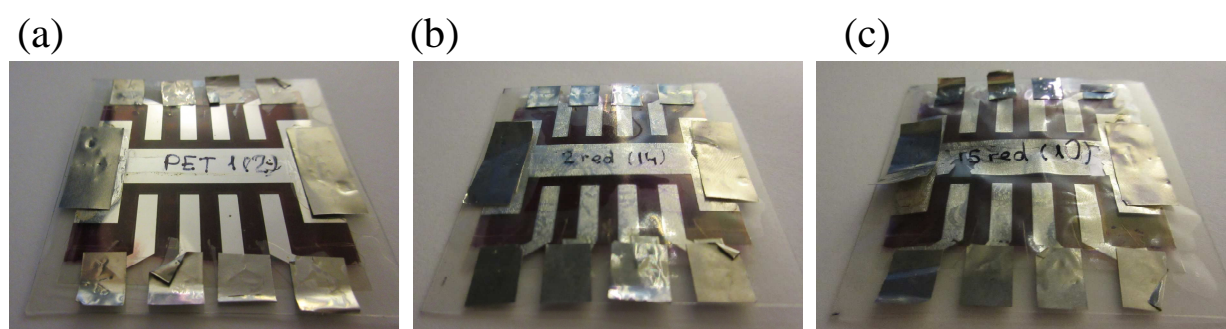


Fig.5.11. Organic solar cells after damp heat degradation experiment. Encapsulation layer: (a) PET, (b) EVOH44, (c) EVOH44/NZL-20.

In contrast to EVOH, the device sealed with PET did not exhibit any delamination problems and the PCE decrease, observed in Fig.5.9., is indeed related to the barrier performance of this polymer.

In general, all devices suffered from the delamination of encapsulation layer, EVOH44, EVOH27, and their nanocomposites. Thus, these devices were destroyed after 1300 min (~22 h) (Fig.5.10.-Fig.5.11.). After visual examination of the failed samples, it was concluded that the delamination mainly occurred in the area of the active part of the cell, at PEDOT:PSS active layer interphase. At the same time, no notable delamination problems were detected at the edges of the device, where encapsulation is in direct contact with the substrate.

It has already been reported that, due to its high hygroscopicity ^[29, 35, 38, 298-300], degradation of PEDOT:PSS is associated with the degradation of solar cells exposed to ambient humidity. Moreover, the failure mechanisms in inverted devices have been related to chemical changes at the PEDOT:PSS interface with the active layer ^[35]. Based on the literature and the results of current experiment, we can assume that delamination in OSC devices sealed with EVOH-based encapsulation layers is caused by both, high water uptake of EVOH films and high hygroscopicity of PEDOT:PSS. When EVOH leads to the penetration of water into the cell, then the PEDOT:PSS layer results in the rapid delamination.

b. OSC on glass substrate

Based on the results given above, it was considered to change the adhesive from acrylic glue to epoxy-based (from DELO) and to use a rigid substrate to improve the stability of the samples. All the studied encapsulation foils were based on EVOH44, because of the lower stability of EVOH27 encapsulated devices. Additionally, different multistacks layers of EVOH44 and PET (shown in Table 5.2. #4-8) were used in order to avoid the fast EVOH expansion due to direct contact with humid environment. Deposition of PET layer over EVOH will also model the use of EVOH nanocomposite layer as a water scavenger, as it is supposed to be introduced in encapsulation multilayer stacks as an internal layer.

The modifications of the device performance are shown in Fig.5.12.

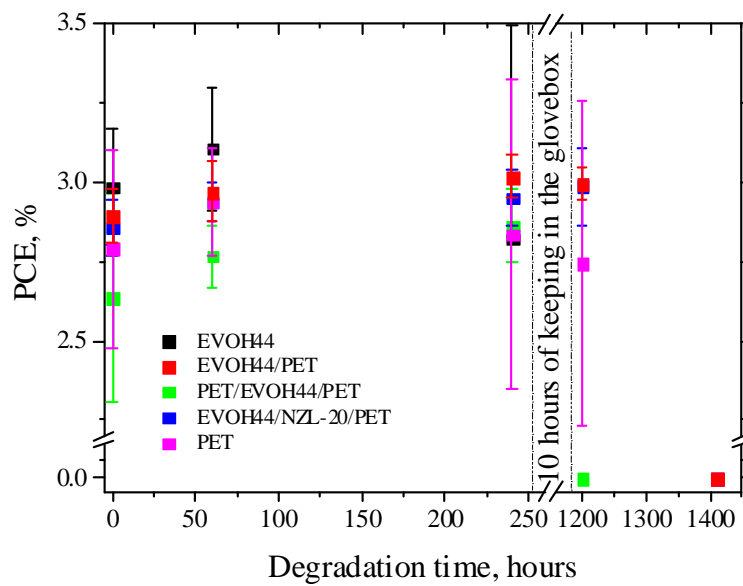


Fig.5.12. OSCs power conversion efficiency as a function of time under damp heat conditions. Materials: encapsulation (PET, EVOH44 and EVOH44/NZL-20 based foils) epoxy adhesive; rigid glass substrate.

During the first 4 h, all the cells show no significant changes of PCE values. However, keeping samples in the glove box during 10 h leads to the full or partial delamination of the samples encapsulated by EVOH44, PET/EVOH44/PET. Then samples were placed back to the climatic chamber. After 200 min of damp heat exposure (total experiment time 1400 min) all the devices with EVOH-based layers in their encapsulation were delaminated or exhibited zero efficiency.

This experiment suggests that these modifications did not bring any improvement, in particular, did not solve the delamination problem.

The delamination can be observed on the photos of device before the experiment (Fig.5.13.a) and after complete delamination (Fig.5.13.b).

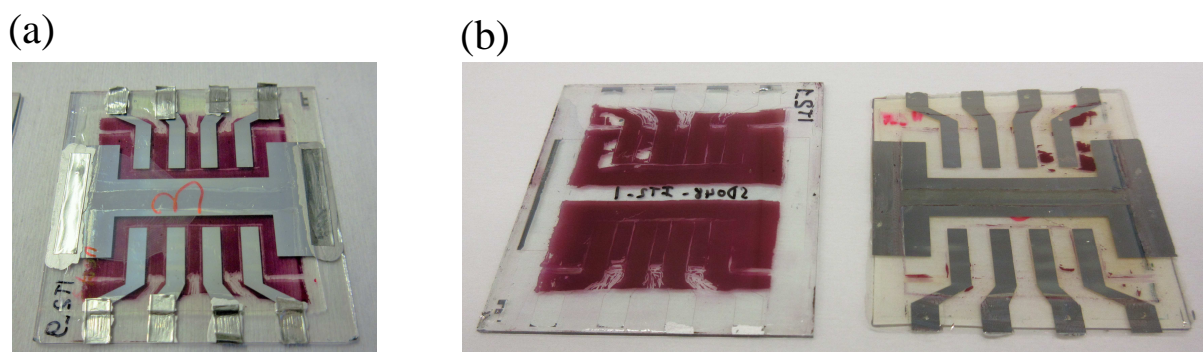


Fig.5.13. (a) Device before damp heat exposure (bright part at the active part displays the delamination); (b) Device after delamination: (left) glass substrate/ITO/ZnO/P3HT:PCBM, (right) PEDOT:PSS/electrodes/encapsulation.

The delamination in the devices before damp heat exposure (Fig.5.13.a) can be indicated by brighter color in cell area. The delamination of the devices before experiment appeared mostly in the devices with bi- and three layer systems included EVOH based films. It might indicate high stress created by different viscoelastic behaviour of each layer after UV curing of the adhesive.

As it is seen after complete device delamination (Fig.5.13.b), the active layer remains on the substrate and the electrodes on the encapsulation. This indicates that the weak point is the PEDOT:PSS active layer interface.

Concluding, the experiment of device performance in damp heat conditions failed due to delamination that mainly appeared at the PEDOT:PSS active layer interphase. This delamination was caused by the bending/expansion of encapsulation layers, in particular by EVOH based materials and high hygroscopicity of PEDOT:PSS. The main reason of polymer expansion was suggested to be the high polymer water uptake and a plasticiser effect of absorbed water.

3. Testing of multistacks in damp heat conditions

In order to better understand the mechanism of calcium sensors and OSCs devices failure, different combinations of material layers were simply stacked together using UV-curable adhesive and then tested in damp heat conditions.

The various multilayer stacks including the use of two different glues (epoxy or acrylic) and two substrates (a glass plate or a flexible ultra-barrier (UB)) were tested. EVOH44 or EVOH27 or PET were deposited on a substrate using adhesive glue and then flowed through a

laminator in order to remove excess adhesive. In some cases, stacks consist not only in a single layer that was deposited as “an encapsulation coating”, but also in the combinations of EVOH-PET and PET-EVOH-PET layers deposited on a substrate. Then all the samples were cured for 20 min. All procedure was carried out in air.

All the studied combinations of substrate-polymer layer stacks are summarised in Table 5.3.

Table 5.3. The structures of layer multistacks tested in damp heat conditions.

	Substrate	Polymer (multi) layers		
		Layer 1	Layer 2	Layer 3
1	Glass	PET		
2	Glass	EVOH44/27	PET	
3	Glass	PET	EVOH44/27	PET
4	Flexible UB	PET		
5	Flexible UB	EVOH44/27	PET	
6	Flexible UB	PET	EVOH44/27	PET

** two sets of samples were made, one using acrylic-based adhesive, and the other one using epoxy-based adhesive*

After UV-curing, the samples were placed into the climatic chamber at 65 °C/85 RH % for 3 weeks. After this period of storage in damp heat conditions, we did not observe any bending, shrinking, expanding, delamination between the layers. The samples were considered to be in the same state as they were before the damp heat exposure.

Taking into account this information, the delamination, which was observed for calcium sensors and OSC devices during their testing in damp heat conditions, is initiated by not sufficient adhesion between encapsulation and cell part in the devices. In contrast, the adhesion force bonding EVOH (or EVOH/NZL) based encapsulation with the substrate was strong enough to hold all the layers in the stack and to prevent any bending, shrinking or expanding of EVOH or EVOH/NZL films.

CONCLUSIONS

This chapter was dedicated to the search for a proof of concept of the developed EVOH nanocomposites as materials for OSCs encapsulation. Two main experiments were performed, damp heat degradation test analysed with an electrical calcium corrosion test and ageing test of encapsulated organic solar cells under damp heat conditions. In both cases EVOH and EVOH/NZL nanocomposite played the role of encapsulation layer. In order to optimise the systems, different materials were tested.

The main conclusions of this chapter are:

- the water barrier properties of the EVOH based encapsulation layers could not be measured due to failure of the test caused by delamination under damp heat conditions.
- the main causes of delamination was water uptake by the polymer leading to subsequent layer expansion and bending, and also the hygroscopicity of PEDOT:PSS;
- OSCs delamination appears in the active part of the cell and mainly takes place at PEDOT:PSS interface. At the same time, no significant delamination was observed at the device edges, between the encapsulation and the substrate.
- EVOH27 leads to even faster device delamination than EVOH44 and EVOH44/NZL nanocomposite;
- the obtained results suggest that the flexibility of the substrate, the nature of the adhesive, and even an additional top layer do not solve the main problem of device failure: delamination under damp heat environment.

In order to integrate the developed EVOH nanocomposite into encapsulation for OSCs more additional investigations have to be performed.

GENERAL CONCLUSIONS AND OUTLOOK

GENERAL CONCLUSIONS AND OUTLOOK

The ongoing research on organic solar cells (OSCs) has led to a significant improvement of the cell efficiency, bringing the organic photovoltaic technology closer to commercialisation. Nevertheless, ageing processes in the cell, caused mainly by sunlight and ingress of water and oxygen, lead to a loss in cell efficiency due to a drop in charge carrier transport, worsen light absorption, morphology changes and delamination. Ageing thus limits the cell lifetime, which is a current issue for OSCs market.

One strategy to address this problem is utilisation of effective encapsulation in order to prevent the permeation of water vapour and oxygen, and thus, degradation of organic devices. Different approaches have been proposed to achieve sufficient barrier properties of OSC encapsulation. One of the most efficient techniques, that is currently being used to establish ultrabarrriers, is based on alternation of thin layers with different nature and properties. However, the high manufacturing costs are an issue limiting progress in OSCs commercialisation. As an alternative, low-cost solution for improvement of performance of encapsulation, the introduction of functional nanofillers into the polymer matrix was employed in our research. The processing and characterisation of new nanocomposites based on ethylene vinyl alcohol (EVOH) copolymers and zeolite (nano)particles have been described in this manuscript.

The research approach was consisted of several steps. Firstly, the most appropriate composite materials were identified based on their initial functional properties such as morphology, transparency, surface roughness, thermo-mechanical, thermal, and water sorption properties. Then, the durability of chosen candidates was examined under accelerated weathering conditions. This allowed us to identify the photooxidation mechanism of EVOH polymer and its possible modifications with particle addition. Consequently, the impact of zeolite nanofiller on polymer durability was estimated on the different levels; the modification of molecular structure, and influence on the relevant material properties. Finally, the long-term stability of properties of chosen nanocomposites was investigated in order to assess their suitability as OSC encapsulants.

Two kinds of zeolite particles, with nano-(NZL) and micro-dimensions (DISC), and two EVOH copolymers based on different ratios of units in their compositions were used for composite processing with aim to identify the most suitable material in terms of target application.

Microscopy observation of films morphology detected homogenous distribution of particles just for the NZL nanofiller while the DISC addition resulted in the particle sedimentation during the film processing leading to poor overall dispersion. Additionally, all EVOH/NZL nanocomposites with the filler concentration up to 20 wt % exhibited good optical transparency in the visible range allowing their use for the encapsulation layer. However, particles had a significant influence on the surface morphology of the films, in particular, increasing the surface roughness.

Due to observed advantages of NZL nanofiller over the DISC particles, the main attention was then focused on EVOH/NZL nanocomposites characterisation. It has been shown that nanofiller addition does not cause any significant changes of the thermal properties and crystallinity of EVOH polymers, suggesting no considerable nucleation effect of the NZL zeolite. However, nanocomposite films exhibited reinforced mechanical properties indicating the desired maintaining of structural support of OSC encapsulation. Particular interest was focused on nanofiller acting as an adsorbent of permeant molecules, especially with regard to moisture ingress as one of the main issues for the cell durability. The performed water uptake experiment highlighted the increased capacity and adsorption rate by nanocomposite films with 20 wt % particles addition, indicating the reinforcement of water scavenger properties.

The studies dedicated to initial material properties showed that 20 wt % of NZL zeolite dispersed in EVOH44 creates the films with required film transparency, mechanical and water sorption properties, nevertheless, EVOH27 films achieve smoother layer surface.

The research interest was also focused on the photochemical behaviour of EVOH copolymers and the nanocomposites. In order to fully understand the particles influence, the photooxidation mechanism of EVOH was determined. It was indicated as being based on the classical sequence of hydroperoxidation/decomposition of hydroperoxides/ β -scission of alkoxy radicals. The analysis of gas and solid phase of photoxidised EVOH film indicates the formation of the products inherent for PVA and PE oxidation as well as the products characteristic just for EVOH. These photoproducts were found to be generated by photooxidation of different unit sequences of copolymer chain. The oxidation of EVOH occurred either on the tertiary and/or on the secondary carbon in α - and β -positions to hydroxyl groups. The comprehensive photooxidation mechanism of EVOH44 and EVOH27 was proposed in a schematic form.

Regarding the photooxidation mechanism of EVOH/NZL nanocomposites, the particles addition did not modify the photooxidation mechanism of the polymer but, the prodegrading effect of nanofiller was clearly showed through monitoring of infrared spectra of polymer and nanocomposite with 5-20 wt % of nanoparticles during the ageing process. This effect was considered to be mainly caused by the iron impurities, which are known to be involved in the photodecomposition of hydroperoxides, and thus accelerate oxidation rate of the polymer. Even though the nanocomposites displayed higher photooxidation rates than the pristine polymers, good transparency of films in the visible domain was still maintained after the irradiation, supporting the applicability for the OSC encapsulation materials.

The surface smoothing was observed for EVOH44 as well as for nanocomposite during the photoageing. The SEM and ToF-SIMS analysis of nanocomposite films revealed the loss of polymer matrix while the particles remained on the surface. However, no significant impact of particles on the evolution of viscoelastic properties and polymer crystallinity during EVOH and EVOH/NZL-20 photoageing was found. The preliminary studies of water uptake showed increase of water diffusion rate with the progressing polymer degradation. This highlights importance of good material photostability in order to ensure durability of encapsulation.

To conclude the study, a preliminary testing of selected materials as encapsulants for OSCs was performed at BELECTRIC OPV. The electrical calcium test, performed in order to estimate the water barrier properties of EVOH and EVOH/NZL nanocomposites, showed the issues of EVOH film application in the damp heat conditions (65 °C/85 % RH). The tested films bend and delaminate due to high film water uptake and water plasticising effect. This film behaviour did not allow measurement of water barrier properties of the films. Further testing of EVOH/NZL as encapsulation of OSCs indicated the same drawback, leading to delamination between the cell and the encapsulation layer. The observed delamination took place mainly at PEDOT:PSS and active layer interface and was initiated by the hydroscopicity of the hole transport layer. Unfortunately, the optimisation of the device composition using two different adhesives, glass or flexible polymeric substrates and deposition of additional PET encapsulation layers did not lead to any considerable improvement of the device stability. In addition, EVOH27 and EVOH27/NZL nanocomposites were found to be affected by humid environment even more than EVOH44 based films due to higher molecule polarity of the polymer matrix. Thus, the integration of EVOH/NZL nanocomposite into encapsulation for OSCs remains a challenge, which will require further investigation.

To summarise, EVOH27/NZL can be considered to be more suitable choice in terms of polymer photostability and film surface properties. However, regarding the applicability and operation in damp heat conditions, this nanocomposite suffers from low dimensional stability leading to consequent failure of encapsulated OSC device. At the same time, EVOH44/NZL is more promising to reach the structural stability in humid environment after additional material optimisation. On the other hand, it might not achieve the appropriate encapsulation lifetime due to faster photodegradation of EVOH44.

The continuation of this work should be focused on the two research aims. One is the introduction of EVOH/NZL nanocomposite layer into the encapsulation system and its further optimisation in terms of barrier performance and applicability. At the same time, the attention should be paid to further studies of OSCs encapsulated with developed materials, monitoring the performance of encapsulated devices. The water uptake properties need to be investigated in more detail upon EVOH/NZL ageing in order to obtain more information with regard to durability of its barrier properties. At the same time, additives acting as a metal deactivator can be introduced during the nanocomposite processing for sake of deactivation of zeolite iron impurities and improvement of material stability. However, the ultimate evaluation of the proposed materials should be made on the basis of their introduction into the encapsulation multilayer stack. This approach will allow for evaluation of EVOH/NZL films from the point of view of their main purpose - trapping the water molecules that already passed through the barrier layers structure in the encapsulation multilayer stack.

APPENDIX

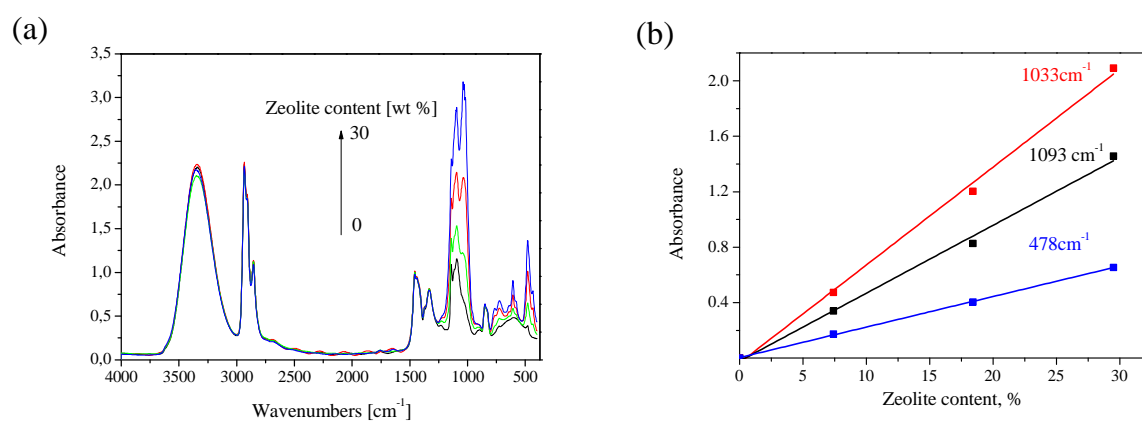


Fig.A.1. (a) FTIR spectra of pristine EVOH27(A) and EVOH27/NZL(A) nanocomposites with different particle contents (7-30 wt %); (b) absorbance evolutions at 1033 cm⁻¹, 1093 cm⁻¹, and 478 cm⁻¹ as a function of particle content in EVOH44/NZL(A) nanocomposites.

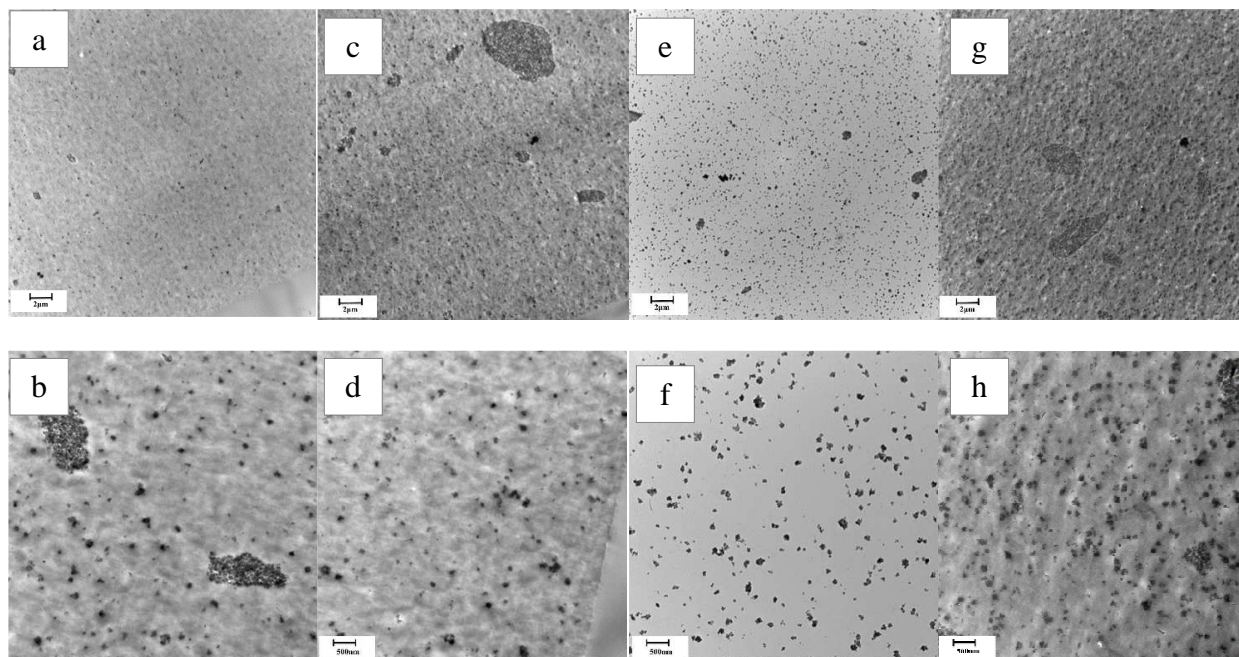


Fig.A. 2. TEM images of cross-sections of EVOH44/NZL-20 nanocomposite films processed by melt-mixing. NZL loading, wt %: (a,b) 5, (c,d) 10, (e,f) 15, (g,h).

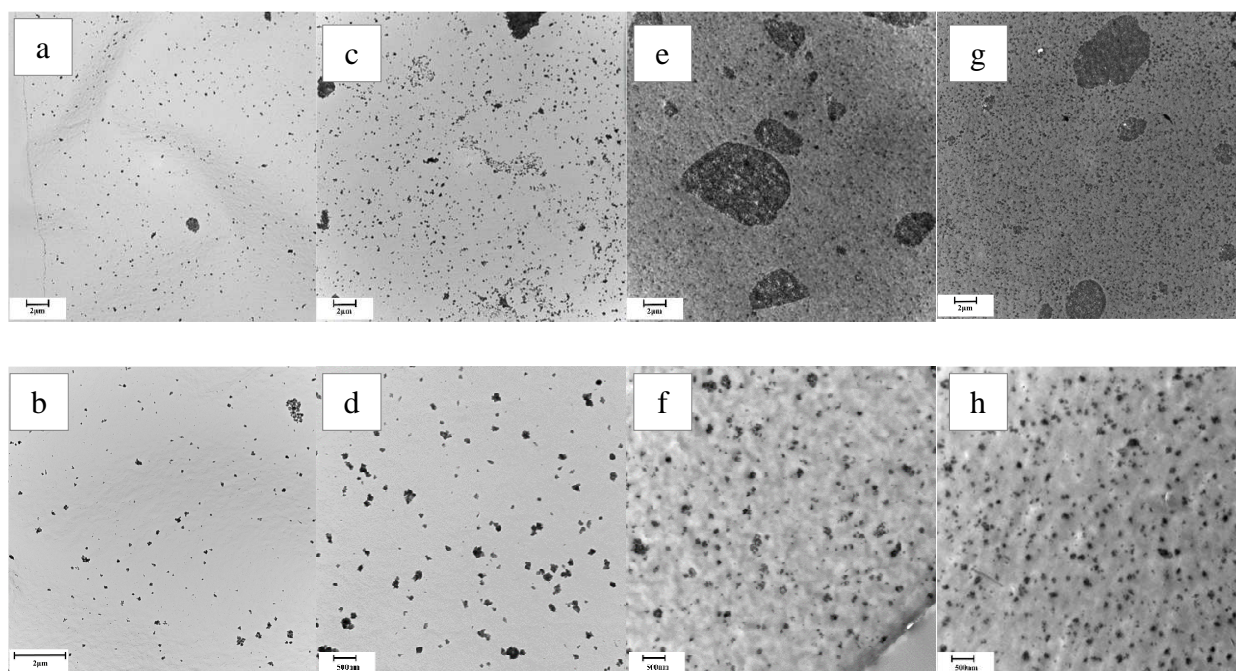


Fig.A. 3. TEM images of cross-sections of EVOH27/NZL-20 nanocomposite films processed by melt-mixing. NZL loading, wt %: (a,b) 5, (c,d) 10, (e,f) 15, (g,h).

REFERENCES

-
- [1] Becquerel AE. *Comptes Rendus de L'Académie des Sciences*. **1839**;9:145-9.
- [2] Fritts CE. *American Journal of Science*. **1883**;26.
- [3] Ohl RS. US 2,402,662, **1946**.
- [4] Chapin DM, Fuller CS, Pearson GL. *Journal of Applied Physics*. **1954**;25:676-7.
- [5] Jørgensen M, Norrman K, Krebs FC. *Solar Energy Materials and Solar Cells*. **2008**;92:686-714.
- [6] Krebs FC. *Refocus*. **2005**;6:38-9.
- [7] Grimes C, Varghese O, Ranjan S. In: *Light, Water, Hydrogen*. Springer, US; **2008**. p. 485-516.
- [8] Krebs FC, Gevorgyan SA, Alstrup J. *Journal of Materials Chemistry*. **2009**;19:5442-51.
- [9] Krebs FC. *Solar Energy Materials and Solar Cells*. **2009**;93:394-412.
- [10] Nelson J. *Materials Today*. **2011**;14:462-70.
- [11] Grossiord N, Kroon JM, Andriessen R, Blom PWM. *Organic Electronics*. **2012**;13:432-56.
- [12] Deibel C, Dyakonov V. *Reports on Progress in Physics*. **2010**;73:1-38.
- [13] Lattante S. *Electronics*. **2014**;3:132.
- [14] Su Y-W, Lan S-C, Wei K-H. *Materials Today*. **2012**;15:554-62.
- [15] Zhang F, Xu X, Tang W, Zhang J, Zhuo Z, Wang J, et al. *Solar Energy Materials and Solar Cells*. **2011**;95:1785-99.
- [16] Kotlarski JD, Blom PWM. *Applied Physics Letters*. **2012**;100:013306.
- [17] Gilot J, Wienk MM, Janssen RAJ. *Applied Physics Letters*. **2007**;90:143512.
- [18] Song QL, Wang ML, Obbard EG, Sun XY, Ding XM, Hou XY, et al. *Applied Physics Letters*. **2006**;89:251118.
- [19] Cao H, He W, Mao Y, Lin X, Ishikawa K, Dickerson JH, et al. *Journal of Power Sources*. **2014**;264:168-83.
- [20] Hoppe H, Sariciftci NS. *Journal of Materials Chemistry*. **2006**;16:45-61.
- [21] Schmidt C. In: Gerlach G, Wolter K-J, editors. *Bio and Nano Packaging Techniques for Electron Devices*. Springer, Heidelberg; **2012**. p. 581-99.
- [22] Motaung D, Malgas G, Arendse C. *Journal of Materials Science*. **2011**;46:4942-52.
- [23] Jeon SO, Lee JY. *Solar Energy Materials and Solar Cells*. **2012**;101:160-5.
- [24] Jørgensen M, Norrman K, Gevorgyan SA, Tromholt T, Andreasen B, Krebs FC. *Advanced Materials*. **2012**;24:580-612.

- [25] Rivaton A, Chambon S, Manceau M, Gardette J-L, Lemaitre N, Guillerez Sp. *Polymer Degradation and Stability*. **2010**;95:278-84.
- [26] Rivaton A, Tournebize A, Gaume J, Bussière P-O, Gardette J-L, Therias S. *Polymer International*. **2014**;63:1335-45.
- [27] Chambon S. Thesis: *Etude du vieillissement de cellules solaires photovoltaïques plastiques*. Clermont-Ferrand, Blaise Pascal University; **2006**.
- [28] Manceau M. Thesis: *Impact de la lumière sur la couche active des cellules photovoltaïques organiques*. Clermont-Ferrand, Blaise Pascal University; **2009**.
- [29] Voroshazi E, Verreet B, Buri A, Muller R, Di Nuzzo D, Heremans P. *Organic Electronics*. **2011**;12:736-44.
- [30] Norrman K, Larsen NB, Krebs FC. *Solar Energy Materials and Solar Cells*. **2006**;90:2793-814.
- [31] Cao H, Ishikawa K. *Solar Energy Materials and Solar Cells*. **2013**;109:215-9.
- [32] Ishii H, Seki K. *IEEE Transactions on Electron Devices*. **1997**;44:1295.
- [33] Habuchi H, Nitta S, Han D, Nonomura S. *Journal of Applied Physics*. **2000**;87:8580-8.
- [34] Hamza AV, Dykes J, Mosley WD, Dinh L, Balooch M. *Surface Science*. **1994**;318:368-78.
- [35] Norrman K, Madsen MV, Gevorgyan SA, Krebs FC. *Journal of the American Chemical Society*. **2010**;132:16883-92.
- [36] Hermenau M, Riede M, Leo K, Gevorgyan SA, Krebs FC, Norrman K. *Solar Energy Materials and Solar Cells*. **2011**;95:1268-77.
- [37] Norrman K, Gevorgyan SA, Krebs FC. *ACS Applied Materials & Interfaces*. **2009**;1:102-12.
- [38] Kawano K, Pacios R, Poplavskyy D, Nelson J, Bradley DDC, Durrant JR. *Solar Energy Materials and Solar Cells*. **2006**;90:3520-30.
- [39] Adams J, Salvador M, Lucera L, Langner S, Spyropoulos GD, Fecher FW, et al. *Advanced Energy Materials*. **2015**; DOI: 10.1002/aenm.201501065.
- [40] Dupont S, Voroshazi E, Heremans P, Dauskardt R. *Photovoltaic Specialists Conference - PVSC*. Austin, USA, **2012**. p. 3259-62.
- [41] Drakonakis VM, Savva A, Kokonou M, Choulis SA. *Solar Energy Materials and Solar Cells*. **2014**;130:544-50.
- [42] Chen S, Manders JR, Tsang S-W, So F. *Journal of Materials Chemistry*. **2012**;22:24202-12.

- [43] Giroto C, Voroshazi E, Cheyns D, Heremans P, Rand BP. *ACS Applied Materials & Interfaces*. **2011**;3:3244-7.
- [44] Shrotriya V, Li G, Yao Y, Chu C-W, Yang Y. *Applied Physics Letters*. **2006**;88:073508.
- [45] Choi H, Kim B, Ko MJ, Lee D-K, Kim H, Kim SH, et al. *Organic Electronics*. **2012**;13:959-68.
- [46] Kettle J, Waters H, Horie M, Chang SW. *Journal of Physics D: Applied Physics*. **2012**;45:125102.
- [47] Zhang ST, Zhou YC, Zhao JM, Zhan YQ, Wang ZJ, Wu Y, et al. *Applied Physics Letters*. **2006**;89:043502.
- [48] Brabec CJ, Shaheen SE, Winder C, Sariciftci NS, Denk P. *Applied Physics Letters*. **2002**;80:1288-90.
- [49] Wang M, Xie F, Du J, Tang Q, Zheng S, Miao Q, et al. *Solar Energy Materials and Solar Cells*. **2011**;95:3303-10.
- [50] Lee K, Kim JY, Park SH, Kim SH, Cho S, Heeger AJ. *Advanced Materials*. **2007**;19:2445-9.
- [51] Giannouli M, Drakonakis VM, Savva A, Eleftheriou P, Florides G, Choulis SA. *ChemPhysChem*. **2015**;16:1134-54.
- [52] Sun H, Weickert J, Hesse HC, Schmidt-Mende L. *Solar Energy Materials and Solar Cells*. **2011**;95:3450-4.
- [53] Krebs FC. *Solar Energy Materials and Solar Cells*. **2006**;90:3633-43.
- [54] Lungenschmied C, Dennler G, Neugebauer H, Sariciftci SN, Glatthaar M, Meyer T, et al. *Solar Energy Materials and Solar Cells*. **2007**;91:379-84.
- [55] Kim N, Potscavage Jr WJ, Sundaramoorthi A, Henderson C, Kippelen B, Graham S. *Solar Energy Materials and Solar Cells*. **2012**;101:140-6.
- [56] Gupta SK, Dharmalingam K, Pali LS, Rastogi S, Singh A, Garg A. *Nanomaterials and Energy*. **2012**;2:42 –58.
- [57] Erlat AG, Yan M, R. Duggal A. In: Wong W, Salleo A, editors. *Flexible Electronics*. Springer US, **2009**. p. 413-49.
- [58] Ahmad J, Bazaka K, Anderson LJ, White RD, Jacob MV. *Renewable and Sustainable Energy Reviews*. **2013**;27:104-17.
- [59] Kaltenbrunner M, White MS, Glowacki ED, Sekitani T, Someya T, Sariciftci NS, et al. *Nature Communications*. **2012**;3:770.

- [60] Sachs-Quintana IT, Heumüller T, Mateker WR, Orozco DE, Cheacharoen R, Sweetnam S, et al. *Advanced Functional Materials*. **2014**;24:3978-85.
- [61] MacDonald WA. *Journal of Materials Chemistry*. **2004**;14:4-10.
- [62] Adam C, Lacoste J, Lemaire J. *Polymer Degradation and Stability*. **1989**;24:185-200.
- [63] Wolf R, Sparavigna AC. *Engineering* **2010**;2:397-402.
- [64] Dennler G, Lungenschmied C, Neugebauer H, Sariciftci NS, Labouret A. *Journal of Materials Research*. **2005**;20:3224-33.
- [65] Kim N. Thesis: *Fabrication and characterization of thin-film encapsulation for organic electronics*. Georgia, Georgia Institute of Technology; **2009**.
- [66] Cros S, de Bettignies R, Berson S, Bailly S, Maise P, Lemaitre N, et al. *Solar Energy Materials and Solar Cells*. **2011**;95, Supplement 1:S65-S9.
- [67] Hanika M, Langowski HC, Moosheimer U, Peukert W. *Chemical Engineering & Technology*. **2003**;26:605-14.
- [68] Schuller S, Schilinsky P, Hauch J, Brabec CJ. *Applied Physics A*. **2004**;79:37-40.
- [69] Ketola B, McIntosh KR, Norris A, Tomalia MK. *23rd European photovoltaic solar energy conference*. Valencia, Spain **2008**. p. 2969-73.
- [70] Leterrier Y. *Progress in Materials Science*. **2003**;48:1-55.
- [71] Lipiński M. *Archives of Materials Science and Engineering*. **2010**;46:69-87.
- [72] Masuda A, Umemoto H, Matsumura H. *Thin Solid Films*. **2006**;501:149-53.
- [73] Potscavage WJ, Yoo S, Domercq B, Kippelen B. *Applied Physics Letters*. **2007**;90:253511.
- [74] Carcia PF, McLean RS, Reilly MH, Groner MD, George SM. *Applied Physics Letters*. **2006**;89:031915.
- [75] Schlothauer J, Jungwirth S, Köhl M, Röder B. *Solar Energy Materials and Solar Cells*. **2012**;102:75-85.
- [76] van Dyk EE, Audouard A, Meyer EL, Woolard CD. *Solar Energy Materials and Solar Cells*. **2007**;91:167-73.
- [77] Le Donne A, Dilda M, Crippa M, Acciarri M, Binetti S. *Optical Materials*. **2011**;33:1012-4.
- [78] Yin J, Zhu H, Wang Y, Wang Z, Gao J, Mai Y, et al. *Applied Surface Science*. **2012**;259:758-63.
- [79] Hayes RA, Lenges GM, Pesek SC. US 2,008,019,0481, **2008**.
- [80] Leterrier Y. *Progress in Materials Science*. **2003**;48:1-55.

- [81] Houbertz R, Domann G, Cronauer C, Schmitt A, Martin H, Park JU, et al. *Thin Solid Films*. **2003**;442:194-200.
- [82] Haas KH, Wolter H. *Current Opinion in Solid State & Materials Science*. **1999**;4:571-80.
- [83] Charton C, Schiller N, Fahland M, Hollander A, Wedel A, Noller K. *Thin Solid Films*. **2006**;502:99-103.
- [84] Cabedo L, Gimenez E, Lagaron J, Gavara R, Saura JJ. *Polymer*. **2004**;45:5233-8.
- [85] Haas K-H, Rose K. *Reviews on advanced materials science*. **2003**;5:47-52.
- [86] Carcia PF, McLean RS, Groner MD, Dameron AA, George SM. *Journal of Applied Physics*. **2009**;106:023533-1-3.
- [87] Chen TN, Wu DS, Wu CC, Chiang CC, Chen YP, Horng RH. *Journal of The Electrochemical Society* **2006**;153 :F244-F8
- [88] Dameron AA, Davidson SD, Burton BB, Carcia PF, McLean RS, George SM. *The Journal of Physical Chemistry C*. **2008**;112:4573-80.
- [89] Heuer H, Wenzel C, Herrmann D, Hubner R, Zhang ZL, Bartha JW. *Thin Solid Films*. **2006**;515:1612-7.
- [90] Sarkar S, Culp JH, Whyland JT, Garvan M, Misra V. *Organic Electronics*. **2010**;11:1896-900.
- [91] Meyer J, Görrn P, Bertram F, Hamwi S, Winkler T, Johannes H-H, et al. *Advanced Materials*. **2009**;21:1845-9.
- [92] Meyer J, Schmidt P, Kowalsky W, Riedl T, Kahn A. *Applied Physics Letters* **2010**;96 :2433080-3.
- [93] Seo S-W, Jung E, Chae H, Cho SM. *Organic Electronics*. **2012**;13:2436-41.
- [94] Affinito JD, Gross ME, Coronado CA, Graff GL, Greenwell IN, Martin PM. *Thin Solid Films*. **1996**;290-291:63-7.
- [95] Burrows PE, Graff GL, Gross ME, Martin PM, Shi MK, Hall M, et al. *Displays*. **2001**;22:65-9.
- [96] Nisato G, Kuilder M, Bouten P, Moro L, Philips O, Rutherford N. *Symposium Digest of Technical Papers*. **2003**;34:550-3.
- [97] Kim TW, Yan M, Erlat AG, McConnelee PA, Pellow M, Deluca J, et al. *Journal of Vacuum Science Technology A*. **2005**;23:971-7.
- [98] Olsen LC, Kundu SN, Bonham CC, Gross M. *31st Photovoltaic Specialists Conference*. Lake Buena Vista, FL, USA, **2005**. p. 327-30.

- [99] Moro L, Rutherford NM, Visser RJ, Hauch JA, Klepek C, Denk P, et al. *Proceedings of the SPIE*. **2006**. p. 63340M-M-9.
- [100] Dennler G, Lungenschmied C, Neugebauer H, Sariciftci NS, Latreche M, Czeremuszkin G, et al. *Thin Solid Films*. **2006**;511-512:349-53.
- [101] Wu C-Y, Liao R-M, Lai L-W, Jeng M-S, Liu D-S. *Surface and Coatings Technology*. **2012**;206:4685-91.
- [102] Chiang CC, Wu DS, Lin HB, Chen YP, Chen TN, Lin YC, et al. *Surface and Coatings Technology*. **2006**;200:5843-8.
- [103] Wu DS, Chen TN, Wu CC, Chiang CC, Chen YP, Horng RH, et al. *Chemical Vapor Deposition*. **2006**;12:220-4.
- [104] Chen T-N, Wu D-S, Wu C-C, Chiang C-C, Chen Y-P, Horng R-H. *Plasma Processes and Polymers*. **2007**;4:180-5.
- [105] Madakasira P, Inoue K, Ulbricht R, Lee SB, Zhou M, Ferraris JP, et al. *Synthetic Metals*. **2005**;155:332-5.
- [106] Kim N, Potscavage WJ, Domercq B, Kippelen B, Graham S. *Applied Physics Letters*. **2009**;94:163308.
- [107] Priolo MA, Gamboa D, Holder KM, Grunlan JC. *Nano Letters*. **2010**;10:4970-4.
- [108] Ramadas SK, Shanmugavel S. EP 2,771,182 **2014**.
- [109] Auch M, Ramadas S. *Films Close to Commercializing Nanoparticle Protective Film for Plastic Electronics*. <http://www.ineffableisland.com/2009/11/tera-barrier-films-close-to.html>. *Tera-Barrier*.
- [110] http://www.aip-worldcongress.org/member_terabarrier-films-pte-ltd-_169.php.
- [111] Zhu J, Morgan AB, Lamelas FJ, Wilkie CA. *Chemistry of Materials*. **2001**;13:3774-80.
- [112] Alexandre M, Dubois P. *Materials Science and Engineering: R: Reports*. **2000**;28:1-63.
- [113] Samyn F, Bourbigot S, Jama C, Nazare S, Biswas B, Hull R, et al. *European Polymer Journal*. **2008**;44:1631-41.
- [114] Kiliaris P, Papaspyrides CD. *Progress in Polymer Science*. **2010**;35:902-58.
- [115] Zhu A, Cai A, Zhang J, Jia H, Wang J. *Journal of Applied Polymer Science*. **2008**;108:2189-96.
- [116] Chandrakala HN, Ramaraj B, Shivakumaraiah, Lee JH, Siddaramaiah. *Journal of Alloys and Compounds*. **2013**;580:392-400.
- [117] Gaume J, Taviot-Gueho C, Cros S, Rivaton A, Therias S, Gardette J-L. *Solar Energy Materials and Solar Cells*. **2012**;99:240-9.

- [118] Seethamraju S, Ramamurthy PC, Madras G. *RSC Advances*. **2013**;3:12831-8.
- [119] Bussière P-O, Peyroux J, Chadeyron G, Therias S. *Polymer Degradation and Stability*. **2013**;98:2411-8.
- [120] Beyer G. *Plastics, Additives and Compounding*. **2002**;4:22-8.
- [121] Tronto J, Bordonal AC, Naal Z, Valim JB. In: Mastai Y, editor. *Materials Science - Advanced Topics*. InTech, **2013**.
- [122] Choudhary V, Gupta A. In: Yellampalli S, editor. *Polymer Nanocomposites*. InTech, **2011**. p. 65-90.
- [123] Bellucci F, Fabiani D, Montanari GC, Testa L. In: Nelson JK, editor. *Dielectric Polymer Nanocomposites*. Springer US, **2010**. p. 31-64.
- [124] Breck DW. *Zeolite molecular sieves: structure, chemistry, and use*. Wiley, New York; **1973**.p. 771.
- [125] Ng E-P, Mintova S. *Microporous and Mesoporous Materials*. **2008**;114:1-26.
- [126] Bekkum VH, Flanigen EM, Jacobs PA, Jansen JC. In: *Studies in Surface Science and Catalysis*. Elsevier, Amsterdam; **1991**.
- [127] Zheng Y, Li X, Dutta PK. *Sensors*. **2012**;12:5170-94.
- [128] Auerbach SM, Carrado KA, Dutta PK. *Handbook of Zeolite Science and Technology*. Taylor & Francis, New York; **2003**.p. 1204.
- [129] Fawaz J, Mittal V. In: Mittal V, editor. *Synthesis Techniques for Polymer Nanocomposites*. Wiley, Weinheim; **2015**. p. 1-30.
- [130] Rehab A, Salahuddin N. *Materials Science and Engineering: A*. **2005**;399:368-76.
- [131] Sinha Ray S, Okamoto M. *Progress in Polymer Science*. **2003**;28:1539-641.
- [132] Kawasumi M, Hasegawa N, Kato M, Usuki A, Okada A. *Macromolecules*. **1997**;30:6333-8.
- [133] Lan T, Kaviratna PD, Pinnavaia TJ. *Chemistry of Materials*. **1995**;7:2144-50.
- [134] Okada A, Fukushima Y, Kawasumi M, Inagaki S, Usuki A, Sugiyama S, et al. US 4,739,007, **1988**.
- [135] Kumar AP, Depan D, Singh Tomer N, Singh RP. *Progress in Polymer Science*. **2009**;34:479-515.
- [136] Pavlidou S, Papaspyrides CD. *Progress in Polymer Science*. **2008**;33:1119-98.
- [137] Paul DR, Robeson LM. *Polymer*. **2008**;49:3187-204.
- [138] Durmus A, Woo M, Kasgoz A, Macosko CW, Tsapatsis M. *European Polymer Journal*. **2007**;43:3737-49.

- [139] Schmidt DF, Giannelis EP. *Chemistry of Materials*. **2009**;22:167-74.
- [140] Li P, Kim NH, Hui D, Rhee KY, Lee JH. *Applied Clay Science*. **2009**;46:414-7.
- [141] Ebina T, Mizukami F. *Advanced Materials*. **2007**;19:2450-3.
- [142] Nenna G, De Girolamo Del Mauro A, Massera E, Bruno A, Fasolino T, Minarini C. *Journal of Nanomaterials*. **2012**;2012:7.
- [143] Kim H, Abdala AA, Macosko CW. *Macromolecules*. **2010**;43:6515-30.
- [144] Choudalakis G, Gotsis AD. *European Polymer Journal*. **2009**;45:967-84.
- [145] Di Maio E, Iannace S, Sorrentino L, Nicolais L. *Polymer*. **2004**;45:8893-900.
- [146] Bilotti E, Fischer HR, Peijs T. *Journal of Applied Polymer Science*. **2008**;107:1116-23.
- [147] Mu B, Wang Q, Wang H, Jian L. *Journal of Macromolecular Science, Part B*. **2007**;46:1093-104.
- [148] Li L, Li CY, Ni C, Rong L, Hsiao B. *Polymer*. **2007**;48:3452-60.
- [149] Xu D, Wang Z. *Polymer*. **2008**;49:330-8.
- [150] Fornes TD, Paul DR. *Polymer*. **2003**;44:4993-5013.
- [151] Supova M, Martynkova GS, Barabaszova K. *Science of Advanced Materials*. **2011**;3:1-25.
- [152] Mittal V. *Optimization of Polymer Nanocomposite Properties*. Wiley, Weinheim; **2009**.p. 175-195.
- [153] Bharadwaj RK. *Macromolecules*. **2001**;34:9189-92.
- [154] Zimmerman CM, Singh A, Koros WJ. *Journal of Membrane Science*. **1997**;137:145-54.
- [155] Kenyó C, Kajtar D, Renner K, Krohnke C, Pukanszky B. *Journal of Polymer Research*. **2013**;20:1-8.
- [156] Kenyó C, Renner K, Móczó J, Fekete E, Kröhnke C, Pukánszky B. *Polymer Composites*. **2014**;35:2112-20.
- [157] Le Van Mao R, Sjiariel B, Dunnigan J. *Zeolites*. **1991**;11:804-9.
- [158] Foster RH. In: Tracton AA, editor. *Coatings Materials and Surface Coatings*. CRC Press, **2006**. p. 12-1--5.
- [159] Foster RH. In: Tracton AA, editor. *Coatings Technology Handbook, (Third Edition)*. CRC Press, **2005**. p. 57-1--5.
- [160] Artzi N, Narkis M, Siegmann A. *Journal of Polymer Science Part B: Polymer Physics*. **2005**;43:1931-43.
- [161] Schirmer HG. US 4,928,474, **1990**.
- [162] Schroeder GO. US 4,254,169 **1981**.

- [163] Cerisuelo JP, Alonso J, Aucejo S, Gavara R, Hernandez-Munoz P. *Journal of Membrane Science*. **2012**;423-424:247-56.
- [164] Ratto JA, Froio B, Schirmer S, Bernacconi M, Vanderwalker D, Thellen C, et al. *ANTEC, Society of Plastics Engineers*. **2011**. p. 2-6.
- [165] Lee KM, Han CD. *Macromolecules*. **2003**;36:7165-78.
- [166] Lee SS, Kim KR, Han S-H, Jeong YS, Kim M-N, Park E-S. *Journal of Reinforced Plastics and Composites*. **2011**;30:932-44.
- [167] Jeong H, Kim B, Kim E. *Journal of Materials Science*. **2005**;40:3783-7.
- [168] Lucciarini JM, Ratto JA. *ANTEC, Society of Plastics Engineers*. **2002**.
- [169] Sang Shin Lee, Kyu Ryn Kim, Han S-H, Yeun Sug Jeong, Kim M-N, Park E-S. *Journal of Reinforced Plastics and Composites*. **2011**;30:932-44.
- [170] Moyo L, Focke WW, Heidenreich D, Labuschagne FJWJ, Radusch HJ. *Materials Research Bulletin*. **2013**;48:1218-27.
- [171] Yang J, Bai L, Feng G, Yang X, Lv M, Zhang Ca, et al. *Industrial & Engineering Chemistry Research*. **2013**;52:16745-54.
- [172] Fernando KAS, Lin Y, Zhou B, Grah M, Joseph R, Allard LF, et al. *Journal of Nanoscience and Nanotechnology*. **2005**;5:1050-4.
- [173] Martínez-Sanz M, Lopez-Rubio A, Lagaron JM. *Journal of Applied Polymer Science*. **2012**;128:2197-207.
- [174] Chiba Y, Tominaga Y. *Journal of Power Sources*. **2012**;203:42-7.
- [175] Lee E-J, Yoon J-S, Park E-S. *Polymer Composites*. **2011**;32:714-26.
- [176] Mailhot B, Morlat S, Gardette J-L, Boucard S, Duchet J, Gérard J-F. *Polymer Degradation and Stability*. **2003**;82:163-7.
- [177] Artzi N, Narkis M, Siegmann A. *Polymer Engineering & Science*. **2004**;44:1019-26.
- [178] Aleperstein D, Artzi N, Siegmann A, Narkis M. *Journal of Applied Polymer Science*. **2005**;97:2060-6.
- [179] Lee E-J, Yoon J-S, Park E-S. *Journal of Applied Polymer Science*. **2012**;125:E691-E704.
- [180] Yang J, Lin Y, Wang J, Lai M, Li J, Liu J, et al. *Journal of Applied Polymer Science*. **2005**;98:1087-91.
- [181] Morlat-Therias S, Mailhot B, Gonzalez D, Gardette J-L. *Chemistry of Materials*. **2005**;17:1072-8.

- [182] Redhwi HH, Siddiqui MN, Andraday AL, Hussain S. *Journal of Nanomaterials*. **2014**;2014:5.
- [183] Morlat-Therias S, Fanton E, Gardette J-L, Dintcheva NT, La Mantia FP, Malatesta V. *Polymer Degradation and Stability*. **2008**;93:1776-80.
- [184] Morlat-Therias S, Mailhot B, Gardette J-L, Da Silva C, Haidar B, Vidal A. *Polymer Degradation and Stability*. **2005**;90:78-85.
- [185] Morlat-Therias S, Fanton E, Tomer NS, Rana S, Singh RP, Gardette J-L. *Polymer Degradation and Stability*. **2006**;91:3033-9.
- [186] Lonkar SP, Kumar AP, Singh RP. *Polymers for Advanced Technologies*. **2007**;18:891-900.
- [187] Qin HL. *Chemical journal of Chinese Universities*. **2004**;25:197-8.
- [188] Sloan JM, Patterson PH, Hsieh A. *Polymer Materials Science & Engineering*. **2003**;88:354-5.
- [189] Singh RP, Khait M, Zunjarrao SC, Korach CS, Pandey G. *Journal of Nanomaterials*. **2010**;2010:13.
- [190] Woo RSC, Chen Y, Zhu H, Li J, Kim J-K, Leung CKY. *Composites Science and Technology*. **2007**;67:3448-56.
- [191] Gaume J, Rivaton A, Therias S, Gardette J-L. *Polymer Degradation and Stability*. **2012**;97:488-95.
- [192] Morlat-Therias S, Mailhot B, Gonzalez D, Gardette J-L. *Chemistry of Materials*. **2004**;16:377-83.
- [193] Osawa Z. *Polymer Degradation and Stability*. **1988**;20:203-36.
- [194] Dintcheva NT, Al-Malaika S, La Mantia FP. *Polymer Degradation and Stability*. **2009**;94:1571-88.
- [195] Qin H, Zhang Z, Feng M, Gong F, Zhang S, Yang M. *Journal of Polymer Science Part B: Polymer Physics*. **2004**;42:3006-12.
- [196] La Mantia FP, Dintcheva NT, Malatesta V, Pagani F. *Polymer Degradation and Stability*. **2006**;91:3208-13.
- [197] Leroux F, Meddar L, Mailhot B, Morlat-Therias S, Gardette J-L. *Polymer*. **2005**;46:3571-8.
- [198] Lonkar SP, Therias S, Caperaa N, Leroux F, Gardette J-L. *European Polymer Journal*. **2010**;46:1456-64.

- [199] Zhu H, Feng Y, Tang P, Cui G, Evans DG, Li D, et al. *Industrial & Engineering Chemistry Research*. **2011**;50:13299-303.
- [200] Bocchini S, Morlat-Therias S, Gardette JL, Camino G. *European Polymer Journal*. **2008**;44:3473-81.
- [201] Magagula B, Nhlapo N, Focke WW. *Polymer Degradation and Stability*. **2009**;94:947-54.
- [202] Morlat-Therias S, Fanton E, Gardette J-L, Peeterbroeck S, Alexandre M, Dubois P. *Polymer Degradation and Stability*. **2007**;92:1873-82.
- [203] Guadagno L, Naddeo C, Raimondo M, Gorrasi G, Vittoria V. *Polymer Degradation and Stability*. **2010**;95:1614-26.
- [204] Patterson PH, Sloan J, Hsieh A. *ANTEC, Society of Plastics Engineers*. **2003**. p. 3604-7.
- [205] Najafi E, Shin K. *Colloids and Surfaces A: Physicochemical and Engineering Aspects*. **2005**;257-258:333-7.
- [206] Ghasemi-Kahrizsangi A, Shariatpanahi H, Neshati J, Akbarinezhad E. *Applied Surface Science*. **2015**;353:530-9.
- [207] Grigoriadou I, Paraskevopoulos KM, Karavasili M, Karagiannis G, Vasileiou A, Bikiaris D. *Composites Part B: Engineering*. **2013**;55:407-20.
- [208] Zan L, Tian L, Liu Z, Peng Z. *Applied Catalysis A: General*. **2004**;264:237-42.
- [209] Shang J, Chai M, Zhu Y. *Journal of Solid State Chemistry*. **2003**;174:104-10.
- [210] Valadez-Gonzalez A, Cervantes-Uc JM, Veleza L. *Polymer Degradation and Stability*. **1999**;63:253-60.
- [211] Morreale M, Dintcheva NT, La Mantia FP. *Polymer International*. **2011**;60:1107-16.
- [212] Li J, Yang R, Yu J, Liu Y. *Polymer Degradation and Stability*. **2008**;93:84-9.
- [213] Sumino K-I, Taniike T, Terano M, George GA. *Macromolecular Reaction Engineering*. **2008**;2:135-41.
- [214] Grigoriadou I, Paraskevopoulos KM, Chrissafis K, Pavlidou E, Stamkopoulos TG, Bikiaris D. *Polymer Degradation and Stability*. **2011**;96:151-63.
- [215] Yang R, Christensen PA, Egerton TA, White JR. *Polymer Degradation and Stability*. **2010**;95:1533-41.
- [216] Yang R, Li Y, Yu J. *Polymer Degradation and Stability*. **2005**;88:168-74.
- [217] Therias S, Gardette JL. *Unpublished results*.
- [218] Nakayama N, Hayashi T. *Polymer Degradation and Stability*. **2007**;92:1255-64.

- [219] Therias S, Larche J-F, Bussiere P-O, Gardette J-L, Murariu M, Dubois P. *Biomacromolecules*. **2012**;13:3283-91.
- [220] Man C, Zhang C, Liu Y, Wang W, Ren W, Jiang L, et al. *Polymer Degradation and Stability*. **2012**;97:856-62.
- [221] Liu M, Horrocks AR. *Polymer Degradation and Stability*. **2002**;75:485-99.
- [222] Horrocks AR, Mwila J, Mirafatab M, Liu M, Chohan SS. *Polymer Degradation and Stability*. **1999**;65:25-36.
- [223] Bastani D, Esmacili N, Asadollahi M. *Journal of Industrial and Engineering Chemistry*. **2013**;19:375-93.
- [224] Han W, Cheung CT, Poon HY, Yeung KL. *Catalysis Today*. **2012**;193:194-9.
- [225] Mthombeni NH, Mbakop S, Onyango MS. *International Journal of Environmental Science and Development* **2015**;6:602-5.
- [226] Zadaka-Amir D, Nasser A, Nir S, Mishael YG. *Microporous and Mesoporous Materials*. **2012**;151:216-22.
- [227] Gascon J, Kapteijn F, Zornoza B, Sebastien V, Casado C, Coronas J. *Chemistry of Materials*. **2012**;24:2829-44.
- [228] Macrae D. US 1,626,682, **1927**.
- [229] Shores AA. US 5,244,707, **1993**.
- [230] Shores AA. US 5,304,419, **1994**.
- [231] Shores AA. US 5,591,379, **1997**.
- [232] Wu C-S, Liao J-Y, Fang S-Y, Chiang AT. *Adsorption*. **2010**;16:69-74.
- [233] Belibi PC, Daou TJ, Ndjaka J-MB, Michelin L, Brendle J, Nsom B, et al. *Journal of Food Engineering*. **2013**;115:339-46.
- [234] Baerlocher C, McCusker LB, Olson DH. In: *Atlas of Zeolite Framework Types (Sixth Edition)*. Elsevier Science, Amsterdam; **2007**. p. 196-7.
- [235] Lemaire J, Arnaud R, Gardette JL. *Revue Générale des Caoutchoucs et du Plastique*. **1981**;613:87-92.
- [236] Peike C, Hoffmann S, Hulsmann P, Thaidigsmann B, Weiß KA, Koehl M, et al. *Solar Energy Materials and Solar Cells*. **2013**;116:49-54.
- [237] Wilhelm C, Gardette J-L. *Journal of Applied Polymer Science*. **1994**;51:1411-20.
- [238] Lin-Vien D, Colthup NB, Fateley WG, Grasselli JG. *The Handbook of Infrared and raman Characteristic Frequencies of Organic Molecules*. Academic Press, San Diego, CA; **1991**.

- [239] Jaffrezzo JL, Calas N, Bouchet M. *Atmospheric Environment*. **1998**;32:2705-8.
- [240] Mironov VL. *Fundamentals of Scanning Probe Microscopy*. NT-MDT, Nizhniy Novgorod; **2004**.p. 97.
- [241] Schön PM, Gosa M, Vancso GJ. *Imaging & Microscopy*. **2013**;15:43-6.
- [242] Luckenbach TA. *DMTA: Dynamic Mechanical Thermal Analysis*. Rheometrics; **1990**. p. 13.
- [243] Menard KP. *Dynamic mechanical analysis: a practical introduction, second edition* CRC Press; **2008**.p. 240.
- [244] Lobo H, Bonilla JV. *Handbook of Plastics Analysis*. Marcel Dekker, New York; **2003**.p. 656.
- [245] Franco Urquiza, A. E, Santana Pérez, Onofre O, Gámez Pérez J, Martínez AB, et al. *Express Polymer Letter*. **2010**;4:153-60.
- [246] Cerrada ML, Perez E, Perena JM, Benavente R. *Macromolecules*. **1998**;31:2559-64.
- [247] Tock RW. *Advances in Polymer Technology*. **1983**;3:223-31.
- [248] Siracusa V. *International Journal of Polymer Science*. **2012**;2012:1-11.
- [249] Crank J. *The Mathematics of Diffusion*.(Second edition). Oxford University Press, New York; **1979**.p. 414.
- [250] Carter HG, Kibler KG. *Journal of Composite Materials*. **1978**;12:118-31.
- [251] Popineau S, Rondeau-Mouro C, Sulpice-Gaillet C, Shanahan MER. *Polymer*. **2005**;46:10733-40.
- [252] La Saponara V. *Composite Structures*. **2011**;93:2180-95.
- [253] Silva L, Tognana S, Salgueiro W. *Polymer Testing*. **2013**;32:158-64.
- [254] Merdas I, Thominette F, Tcharkhtchi A, Vendu J. *Composite Science and Technology*. **2002**;62:487-92.
- [255] Miller-Meskamp L, Fahlteich J, Krebs FC. In: Krebs FC, editor. *Stability and Degradation of Organic and Polymer Solar Cells*. Wiley & Sons; **2012**. p. 269-329.
- [256] Paetzold R, Winnacker A, Henseler D, Cesari V, Heuser K. *Review of Scientific Instruments*. **2003**;74:5147-50.
- [257] https://fas.dsi.a-star.edu.sg/equipments/tof_sims.aspx.
- [258] Vickerman JC, Briggs D. *ToF-SIMS: surface analysis by mass spectrometry*. IM Publications; **2001**.
- [259] Weng L-T, Chan C-M. *Applied Surface Science*. **2006**;252:6570-4.

- [260] Baerlocher C, McCusker LB, Olson DH. *Atlas of zeolite framework types*, (Sixth Revised Edition). Elsevier, Amsterdam; **2007**.p. 405.
- [261] Shikunov BI, Lafer LI, Yakerson VI, Mishin IV, Rubinshtein AM. *Bulletin of the Academy of Sciences of the USSR, Division of chemical science*. **1972**;21:201-3.
- [262] de Man AJM, van Santen RA. *Zeolites*. **1992**;12:269-79.
- [263] Flanigen EM, Khatami H, Szymanski HA. In: Flanigen EM, Sand LB, editors. *Molecular Sieve Zeolites-I*. American Chemical Society, **1974**. p. 201-29.
- [264] Ko YS, Ahn WS. *Bulletin of the Korean Chemical Society*. **1999**;20:1-6.
- [265] Holland-Moritz K, Hummel DO. *Journal of Molecular Structure*. **1973**;19:289-300.
- [266] Jiang H, Wu P, Yang Y. *Biomacromolecules*. **2003**;4:1343-7.
- [267] Siesler WW, Holland-Moritz K. *Journal of Polymer Science: Polymer Letters Edition*. **1980**;19:389.
- [268] Hu G-S, Ding Z-Y, Li Y-C, Wang B-B. *Journal of Polymer Research*. **2009**;16:263-9.
- [269] Lagaron JM, Giménez E, Saura JJ. *Polymer International*. **2001**;50:635-42.
- [270] http://www.easyfairs.com/uploads/tx_ef/Dynamar_12p_PCG_WEB_navi.pdf.
- [271] Cerrada ML, Perena JM, Benavente R, Perez E. *Polymer*. **2000**;41:6655-61.
- [272] Djezzar K, Penel L, Lefebvre J-M, Seguela R, Germain Y. *Polymer*. **1998**;39:3945-53.
- [273] Cerrada ML, Benavente R, Perez E, Perena JM. *Polymer*. **2001**;42:3127-38.
- [274] Popli R, Glotin M, Mandelkern L, Benson RS. *Journal of Polymer Science: Polymer Physics Edition*. **1984**;22:407-48.
- [275] Cabedo L, Lagaron JM, Cava D, Saura JJ, Gimenez E. *Polymer Testing*. **2006**;25:860-7.
- [276] Gardette M, Perthue A, Gardette J-L, Janecska T, Fodes E, Pukanszky B, et al. *Polymer Degradation and Stability*. **2013**;98:2383-90.
- [277] Sugimoto M, Shimada A, Kudoh H, Tamura K, Seguchi T. *Radiation Physics and Chemistry*. **2013**;82:69-73.
- [278] Pilichowski JF, Lacoste J, Mallegol J, Michel E, Delor F. *European Polymer Journal*. **1997**;33:1591-9.
- [279] Rivaton A. *Polymer Degradation and Stability*. **1993**;41:297-310.
- [280] Manceau M, Rivaton A, Gardette J-L, Guillerez S, Lemaitre N. *Polymer Degradation and Stability*. **2009**;94:898-907.
- [281] Sugimoto M, Shimada A, Kudoh H, Tamura K, Seguchi T. *Radiation Physics and Chemistry*. **2013**;82:69-73.

- [282] Gaume J, Wong-Wah-Chung P, Rivaton A, Therias S, Gardette J-L. *RSC Advances*. **2011**;1:1471-81.
- [283] Gaume J. Thesis: *Etude du photovieillissement de matériaux nanocomposites pour l'encapsulation de cellules solaires organiques*. Clermont-Ferrand, Blaise Pascal University; **2011**.
- [284] Gardette J-L, Rivaton A, Therias S. In: Allen NS, editor. *Photochemistry and Photophysics of Polymer Materials*. Wiley & Sons; **2010**. p. 569-601.
- [285] David C, Trojan M, Daro A, Demarteau W. *Polymer Degradation and Stability*. **1992**;37:233-45.
- [286] Ranby B, Rabek JF. *Photodegradation, photo-oxidation and photostabilization of polymers*. Wiley & Sons, New York; **1975**.p. 573.
- [287] Scott G, Sheena HH, Harriman AM. *European Polymer Journal*. **1978**;14:1071-7.
- [288] Tidjani A, Wilkie CA. *Polymer Degradation and Stability*. **2001**;74:33-7.
- [289] Qin H, Zhao C, Zhang S, Chen G, Yang M. *Polymer Degradation and Stability*. **2003**;81:497-500.
- [290] Kumanayaka TO, Parthasarathy R, Jollands M. *Polymer Degradation and Stability*. **2010**;95:672-6.
- [291] Chi TC. *Journal of Physical and Chemical Reference Data*. **1979**;8:439-97.
- [292] Graff GL, Williford RE, Burrows PE. *Journal of Applied Physics*. **2004**;96:1840-9.
- [293] van der Wel GK, Adan OCG. *Progress in Organic Coatings*. **1999**;37:1-14.
- [294] Schubert S, Klumbies H, Muller-Meskamp L, Leo K. *Review of Scientific Instruments*. **2011**;82:094101.
- [295] Mokwena KK, Tang J. *Critical Reviews in Food Science and Nutrition*. **1080**;52:640-50.
- [296] Zhang Z, Britt IJ, Tung MA. *Journal of Polymer Science Part B: Polymer Physics*. **1999**;37:691-9.
- [297] Dang MT, Hirsch L, Wantz G. *Advanced Materials*. **2011**;23:3597-602.
- [298] Yamanari T, Taima T, Sakai J, Tsukamoto J, Yoshida Y. *Japanese Journal of Applied Physics*. **2010**;49:01AC2.
- [299] Bulle-Lieuwma CWT, van Gennip WJH, van Duren JKJ, Jonkheijm P, Janssen RAJ, Niemantsverdriet JW. *Applied Surface Science*. **2003**;203–204:547-50.
- [300] de Jong MP, van IJzendoorn LJ, de Voigt MJA. *Applied Physics Letters*. **2000**;77:2255-7.

Abstract: The goal of this work was to develop EVOH/zeolite nanocomposites based on inorganic fillers such as zeolites for potential encapsulation of OSCs and to investigate their photochemical behaviour. The research was focused on the photooxidation mechanism of pristine EVOH copolymers and on the impact of the filler addition on this mechanism. EVOH/zeolite nanocomposites functional properties were characterised taking into account different particle sizes and filler contents.

Properties of EVOH copolymers and EVOH/zeolites nanocomposites such as optical transparency, surface morphology, mechanical and thermal properties, and water uptake properties were investigated. On the basis of obtained results, the best candidate(s) for encapsulation of organic solar cells has been proposed. The chemical degradation mechanism of pristine polymers has been proposed, the materials photostability and the impact of the zeolite particles on the photochemical behaviour of the polymer have been studied. Electrical calcium test and performance of encapsulated OSCs were carried out in order to evaluate the ability of the studied materials to be used as potential candidates for efficient and stable encapsulation coatings for OSCs applications.

Keywords: EVOH, nanocomposite, zeolite, photodegradation, OSCs, encapsulation.

Résumé: L'objectif de ce travail était le développement des nanocomposites d'EVOH/zéolites à base de charges telles que les zéolites pour l'encapsulation des cellules solaires organiques, et l'étude de leur comportement photochimique. Ce travail a porté sur l'étude du mécanisme de photooxydation des copolymères d'EVOH puis sur l'impact des zéolites sur ce mécanisme. Les propriétés fonctionnelles des nanocomposites d'EVOH/zéolites ont été étudiées en prenant en compte le taux de charge et la taille des particules.

Les propriétés des copolymères d'EVOH et des nanocomposites d'EVOH/zéolites comme la transparence optique, la morphologie de surface, les propriétés mécaniques et thermiques, et les propriétés d'absorption de l'eau ont été étudiées. Sur la base des résultats obtenus, les meilleurs candidats pour l'encapsulation des cellules solaires organiques ont été proposés. Le mécanisme de photooxydation des copolymères a été proposé, la photostabilité des matériaux et l'impact des zéolites sur le comportement photochimique du polymère ont été étudiés. Le test électrique de calcium et le suivi des performances des cellules solaires organiques encapsulées ont été effectués afin d'évaluer l'efficacité des matériaux étudiés comme candidats potentiels pour une encapsulation efficace et stable des cellules solaires.

Mots-clefs: EVOH, nanocomposite, zéolite, photodégradation, cellule solaire organique, encapsulation.